

X-320-63-264

TM X-55015

**FINAL REPORT
OF THE GODDARD
SUMMER WORKSHOP PROGRAM
IN
MEASUREMENT AND SIMULATION
OF THE SPACE ENVIRONMENT**

FACILITY FORM 802	N64-28201	N64-28222
	(ACCESSION NUMBER)	(THRU)
	302	1
	(PAGES)	(CODE)
	Jmx-55015	23
	(NASA CR OR TMX OR AD NUMBER)	(CATEGORY)

JUNE 18 TO SEPTEMBER 18, 1963



**GODDARD SPACE FLIGHT CENTER
GREENBELT, MARYLAND**

(5)

PGT-15381

**FINAL REPORT OF
THE GODDARD SUMMER WORKSHOP PROGRAM
MEASUREMENT AND SIMULATION
OF THE SPACE ENVIRONMENT**

JUNE 18 TO SEPTEMBER 18, 1963

"... To raise new questions, new possibilities,
to regard old problems from a new angle, re-
quires creative imagination and marks real ad-
vances in science."

--Albert Einstein

GODDARD SPACE FLIGHT CENTER
Greenbelt, Maryland

FOREWORD

When the first Goddard Summer Workshop was set up in 1962, it was considered an experimental venture, a sort of gamble. At its opening session we expressed doubt and misgivings that a short summer experimental effort, with a diverse outside group, could produce solutions to in-house problems. But we did hope that, in time, the Workshop participants would be encouraged to help in the solution of spaceflight problems. The venture was a definite success. And, for that reason, this year's Workshop was launched with solid confidence and great expectations.

The 1963 Final Report amply justifies the trust we placed in the hands of the several working teams. The university scientists together with Goddard permanent staff members obtained useful results in their conduct of in-house advanced research and technology (ART). Indeed, this Workshop approach promises to develop methods for carrying out in-house ART and obtaining needed technical information in a relatively short time and with limited Goddard personnel.

But of even greater significance to the future of Goddard is the intangible but marked progress which is achieved in the interrelationships between Goddard and numerous universities. During the three-month interval in which professors, graduate students, and Goddard technical staff investigate problems of immediate interest to the Center, there is a constant interchange of knowledge and understanding. There is learning and teaching. There is mingling of academic scientists with permanent practical staff who are kept abreast of new knowledge and are thus aided in coping with new problems.

At the same time, faculty members from different universities became acquainted with the practical engineering viewpoint of today. Moreover, the professors are made aware of Goddard's current and future requirements in human resources. They begin to realize that modern space technology requires a new type of engineer, and that the universities must develop curriculums to fit the needs of the coming generations.

All indications are that the different aspects of the Summer Workshop are progressing, and that its threefold mission is being accomplished.

Harry J. Smith

PREFACE

Goddard's first Summer Workshop was created last year by an urgent need to develop methods for effective utilization of new facilities. This year, the 1963 Workshop was organized with the hope that basic studies would provide greater reliability for satellites in orbit. The 3-month effort brought us closer to the fulfillment of that hope. We are nearer the mark not only because of the various investigations which were conducted, but also by the virtue of the interrelationships which were established. Again this year, studies were conducted by teams of university scientists and Goddard technical staff. Ultimately such working partnerships will have far-reaching effects upon our achievements in the space program. These interdisciplinary working teams of the Summer Workshop bring to the task newly acquired knowledge from widely dispersed sources. They generate new ideas. This type of association enhances individual capabilities at Goddard and raises the standards of the group as a whole.

This Final Report describes the actual studies conducted by four Summer Workshop teams. The problems they tackled were suggested by various Goddard activities. All scientific groups within GSFC were invited to submit problems which they desired to be investigated in-house by the Summer Workshop. The groups met with the principal investigator (a visiting professor) of each team in a pre-Workshop conference held in May. Priorities were assigned to the many items submitted and a study program was formulated. Among the principal factors which determined the areas selected for investigation were: the time element, the availability of professor-specialists representing particular disciplines, and the Center's ability to support the effort in providing needed facilities and work space.

A variety of needed information was obtained from the study projects investigated. Each category of effort represents progress though in a different form of advancement. In some cases the gap between theory and practice was bridged. For example, in Project A - Solar Radiation and Simulation - the calibration of the thermopiles for the measurement of total energy, there were available long established standards and theory which led directly to practical results. In other projects, the subject was explored on the periphery of existing information, as in the study of the filter-differential method for spectral irradiance determination. Here, a brand-new technique had to be explored.

Practically all aspects of Project B - Heat Transfer and Cryogenic Pumping in Vacuum Technology - were concerned with vacuum measurement and gauge calibration. From the start, it was the consensus of the group that top priority be assigned to the different methods of vacuum gauge standardization and comparison. However, few quantitative data are included in the results, because efforts were concentrated on developing means and techniques for obtaining data. The technology of vacuum-gauge calibration, particularly as applied to ultrahigh vacuum, is still weak. Hence, the Workshop has taken a forward step which will make possible the generation of more fundamental knowledge later on.

From Project C - Magnetic Environment and Simulation - may have come the most practical and immediately useful results, which will be applied to Goddard's new magnetic test facility. A number of coil systems were analyzed and calculations made to help the design of the planned installation. The task of demagnetizing a satellite component so as to reduce its field to zero has been achieved by a specially designed gimbal system. Team C also tackled other aspects of the magnetic problems related to environment simulation, with excellent results.

The several topics investigated under Project D - Causes and Effects of Radiation Damage - are mostly of long-range possibilities. The cooperative effort of Goddard and USNRDL in the task of calculating the energy-time beta spectra of fission products will provide values of quantities which have not been determined before. Effects of radiation on metal whiskers have been explored. Some experiments have been performed to determine the changes (if any) produced by proton bombardment in polyurethane foam or in the encased electrical circuitry.

The Summer Workshop committee is gratified to be able to include in this report the participation of four National Science Foundation High-Ability Secondary School Students. These young men worked for eight weeks, and each did an outstanding job in helping the particular team to which he was assigned. A paper prepared by one of them is included in this report. The participation by these students in this team effort indicates tremendous promise of their future capabilities and potentials.

Elias Klein

WORKSHOP PARTICIPANTS

SENIOR FACULTY MEMBERS

- BEYER, Gerhard H., Dr.**—Professor and Chairman of Chemical Engineering Department in the University of Missouri. Member of numerous scientific societies. Author of many publications in chemical engineering, thermodynamics and energy balance. During 1962-63 visiting professor in chemical engineering in University of Wisconsin.
- GAVIS, Jerome, Dr.**—Associate professor in chemical engineering at Johns Hopkins University. Member of numerous honor and scientific societies. Author of fifteen technical publications in chemistry and rheology. Specialist in dynamic properties of viscoelastic materials.
- HELLER, Robert B. Dr.**—Professor of applied science, George Washington University. Member of numerous scientific and honor societies. Author of many publications in nuclear reactor physics, Beta-Ray spectroscopy and nuclear counting techniques.
- MOHR, Eugene I. Dr.**—Professor and Head of Physics Department, Columbia Union College. Member of numerous honor and scientific societies. Author of some publications in Spectroscopy.
- OJALVO, Morris S., Dr.**—Professor of engineering and applied science at George Washington University. Member of numerous honor and scientific societies. Author of many publications in heat transfer and transient temperature distribution. Consultant to National Science Foundation in engineering energetics.
- THEKAEKARA, Matthew P., Dr.**—Associate professor of physics at Georgetown University. Belongs to numerous honor and scientific societies. Author of fifteen publications in physics and astrophysics. Participated in Goddard 1962 Summer Workshop.
- WAIDELICH, Donald, Dr.**—Professor of Electrical Engineering, University of Missouri. Formerly visiting Professor at University of New South Wales, Kensington, NSW, Australia on Fulbright grant. Member and fellow of numerous professional engineering and scientific societies. Many awards and listings in honor societies. Author of numerous scientific publications and co-author of book entitled "Transients in Electrical Circuits". Participated in Goddard 1962 Summer Workshop.

JUNIOR FACULTY MEMBERS

- JOHN, James E. A.**—University of Maryland PhD candidate 1963 in Aero Mechanical Engineering. Instructor in mechanical engineering. BSE Princeton University 1955, MSE Princeton University 1956. Participated in Goddard 1962 Summer Workshop.
- JOHNSTON, Richard L.**—Physics-Assistant Professor, Science Department United States Naval Academy. BS Carnegie Institute of Technology. MS University of Maryland. Working toward PhD in physics at the Catholic University of America.
- PICK, George S.**—The Catholic University of America-Graduate student and instructor in Mechanical Engineering. MME Catholic University 1962-Diploma Engineering Technological University of Budapest 1956. Participated in Goddard 1962 Summer Workshop.
- RINARD, George A.**—University of Missouri graduate student. Instructor in Electrical Engineering. BS 1959; MS 1961 University of Missouri.
- WATSON, John D.**—The Catholic University of America-Graduate student. Instructor in Electrical Engineering. BEE (cum Laude) 1960; MEE 1962 Catholic University.

GRADUATE STUDENTS

- AKINS, Daniel L.**—Howard University-Physical Chemistry. BS Howard University 1963.
- ANDERSON, John A.**—Howard University-Physical Chemistry. BS South Carolina State College 1961; MS Howard University 1963.
- BAUMGARDNER, Carl A.**—Michigan State University. Physics, BS Michigan State 1962. Working toward PhD in Physics.
- CANTER, Joseph M.**—Carnegie Institute of Technology. Physics, BS Yale University 1962. Teaching assistant in physics and studying for PhD at Carnegie Institute of Technology.
- CROOKS, Jonathan B.**—Johns Hopkins University-Chemical Engineering. BSE Johns Hopkins University 1962. Working toward PhD on University Fellowship. Participated in Goddard 1962 Summer Workshop.
- GALLI, Anthony J.**—Georgetown University-physics. BS Louisiana State University 1960. Working toward PhD in Physics at Georgetown University.
- LEVY, Edward K.**—University of Maryland-Mechanical Engineering. Expects to receive BSME in June 1963 from University of Maryland.
- MOHR, Lester L.**—Loma Linda University-Biochemistry and medicine. BA Columbia Union College 1962.
- OWENS, F. J.**—University of Connecticut-Physics. BS Manhattan College 1962. Working toward MS at University of Connecticut.
- SHARP, Robert L.**—University of Maryland. Mathematics, BEE Ohio State University 1959. Working toward PhD in Mathematics University of Maryland.
- SPEISER, Mario**—University of Maryland-Theoretical Physics. BA University of California Berkeley 1961. Working toward PhD in Physics University of Maryland.

THE GODDARD WORKSHOP PLANS AND PROCEDURES

Elias Klein

INTRODUCTION

The Goddard Space Flight Center was dedicated in March 1961. Immediately, the engineering staff faced the task of effectively utilizing new and unprecedented technical facilities for simulating space environments. This staff, already playing a significant role in the preparation, testing, launching, and data gathering of scientific satellites, found it necessary at the same time to develop new test methods and techniques for assessing reliability of spacecraft performance. The Goddard engineers and scientists had to monitor the expanded work of contractors, and in addition to train and educate the less skilled contractor personnel. Thus, Goddard in-house talent had not only to update its own technical information and keep abreast of newly acquired skills, but also to monitor contracts in terms of present-day engineering practices. The available manpower was extended beyond its capabilities and resources. The Summer Workshop program was inaugurated in 1962 to provide urgently needed help.

Generally, all the diversified summer studies lasting from 6 to 12 weeks arise out of a shortage of research personnel qualified to carry out the rapidly expanding technology of this country. New knowledge is unfolding at an enormous rate. There are not enough able scientists to keep pace with it and carry it forward. In certain fields of endeavor we dare not fall behind. This is especially true in modern space-science programs where, to achieve our national goals, special skills and talents are required. For this reason, NASA and its various centers have attempted to utilize campus faculties during periods when their teaching loads are at a minimum.

BASIC AIMS AND CONCEPTS

The Goddard Summer Workshop differs from the usual summer studies or summer institutes conducted in various scientific fields at universities, government research activities, or industrial laboratories. It was designed to accomplish three primary objectives:

1. To provide answers and solutions to specific problems of immediate interest to GSFC. These research and development tasks are carried out in-house. The investigations are undertaken by teams or working groups composed of senior professors, graduate students and Goddard permanent staff. In the various disciplines, the university faculties serve as experts and special consultants.

2. To arrange and organize each team project so that the collaborative academic-Goddard effort will be mutually beneficial, all participants having full opportunity to learn from each other and to teach one another. The interchange of ideas regarding different aspects of the problem helps to upgrade their competence. At the same time, the academic people are made aware of Goddard's various problems in application.

3. To acquaint and indoctrinate the teaching profession with Goddard's requirements for manpower qualifications and skills, so that the universities can provide adequate and suitable training. Working with the permanent staff members, during a 3-month stay at Goddard, the professors are made aware of the exceptional capabilities that will be demanded of future graduates in science and engineering in order to conquer outer space.

To implement this threefold plan so that Goddard could achieve its immediate and long-range objectives was the purpose of the undertaking. Its basic aims have been to alleviate the present shortage of scientific manpower by increasing the effectiveness of existing human resources at Goddard and by indoctrinating the teaching profession as to the skills and talents needed for progress in space science today. These aims were to be accomplished thru actual problem-solving in-house by collaborative team effort.

Perhaps the greatest benefit to be derived from this plan is the possibility of creating among the technical workers of Goddard a climate in which each can recognize his full capabilities and make better use of his human resources. Nowhere is there enough ready talent today to fulfill the technological requirement of the space age. But, "there are substantial reservoirs of talent in the population that have never been developed, and they will not be developed without special attention and help." That is a conclusion of John W. Gardner, president of Carnegie Corporation of New York, in its annual report of 1962. A means to help the Goddard technical worker utilize his full capabilities is, in my opinion, provided by the Goddard Workshop. At least, the opportunity is available to those who have not kept abreast of the swiftly changing space technology, to acquire new knowledge and to recapture the vigor necessary to recognize continuous change and innovation. According to President Gardner, "It is a sad but unarguable fact that most human beings go through life only partially aware of the full range of their abilities. For the self-renewing man, the development of his own potentialities and the process of self-discovery never end." Goddard should make the most of the opportunity to demonstrate that re-education and self-development are possible at almost any age.

Regarding the special skills, until now little was to be expected from new graduates of engineering schools. Their curriculums had been too specialized in old branches of engineering. The universities are just becoming aware of the training requirements that are needed by the engineer or applied scientist who deals with the problems of space exploration. Many schools are now providing more basic physics and mathematics in the engineering courses. Prospects are encouraging for the improvement and modernization of engineering curricula at the undergraduate level as well as in the graduate schools of this country. Even so, indications are that the shortage will continue to increase, unless

larger numbers of capable students are attracted to the engineering professions. The need for improvement in the quality of engineering education as well as in the quantity of well-trained personnel is more urgent today than ever before.

THE 1962 WORKSHOP

The threefold objective was implemented and tested in the Goddard Summer Workshop of 1962, with emphasis on the joint Goddard-university team effort as the keystone of the workshop plan. Teamwork produced the substantial and useful results of the 1962 workshop which would not have been obtained by the existing human resources at Goddard working alone. Nor would the results have been achieved if a number of academic men worked at Goddard for the summer, each on a project of his own and in different areas. The visiting professors' insight into Goddard's function in the space-science field and their favorable response to the effects of this program upon university courses are worthy achievements in themselves. In addition, at the close of the 1962 Workshop, substantially all graduate students expressed a willingness to return the following summer. Five of the 1962 academic participants worked in the 1963 Summer Workshop. There is also promise of a number of desirable applicants for permanent Goddard employment.

The 1962 Summer Workshop was organized into six teams. The program as a whole was devoted to simulation of space environment and proposed to pursue both theoretical and experimental work. It was sponsored by the Test and Evaluation Division. Various aspects of the following topics were studied:

- A. Solar Simulation and Albedo Effect on Spacecraft
- B. Heat Transfer and Cryogenic Pumping in Vacuum Technology
- C. Corona and Discharge Effects Inside Spacecraft at Low External Pressure
- D. Magnetic Simulation
- E. Response of Vehicle Structures to Acoustic Fields
- F. Relating Damage and Reliability to Environmental Data

Problem areas of this kind had been accumulating at Goddard as the Center was being built and developed. There was an immediate need for their study and solution. The results obtained from the 1962 Workshop were rewarding, and encouraged the expansion of the 1963 Summer Workshop to include the entire Goddard Space Flight Center.

On the basis of previous experiences and results, it was possible to plan the 1963 program with greater effectiveness. Again, special emphasis was placed on interdisciplinary participation and interaction of the academic scientists with Goddard technical personnel. An attempt was made to have in each team a variety of specialists collaborating on a given project area. A dominant factor in the final results of each group is the team captain or principal investigator. In addition to being a topflight scientist, he must have adaptability, courage, motivation, and resolute direction in order to accomplish at

least certain phases of the team's mission within the 12-week period. Goddard has been reasonably fortunate in procuring its team leaders.

SELECTION OF TECHNICAL AREAS AND PRE-WORKSHOP CONFERENCES

Early in the preparation for the 1963 Summer Workshop, all scientific groups within GSFC were canvassed (in December 1962) on problem-topics which they wished to be studied in-house by Workshop teams. It was also necessary to know the extent of participation planned by the different groups. The number and type of problems together with their scope and substance had to be determined before the program could be formulated. Sufficient working space and facilities had to be arranged. The availability of permanent Goddard staff members to work on the different teams had to be ascertained. In fact, the success of the overall Summer Workshop program depends considerably on the completeness of detailed preparations made many months before the opening session.

A variety of engineering and scientific subjects was submitted to the Committee for consideration as a result of the December request. These subjects were categorized into different technical areas, which were kept open for additional suggestions and further discussions. The material gathered was sufficiently diverse to indicate the various disciplines involved and the kinds of university specialists that would be required to carry out the investigations. The submitted material also intimated the goals expected from the Summer Workshop. To integrate these numerous suggestions into a single program without delay was now of paramount importance, particularly in the light of previous experiences which indicated the need to contact the desired senior university professors and promising graduate students before the start of Christmas vacations. Hence, a search was promptly instituted in the local and more distant universities for suitable participants of the 1963 Summer Workshop.

By April 1963, twenty-three university scientists (listed on page iv) were recruited. Also, by this time, the program plan was described to each of the Summer Workshop participants. Each was aware of the teams that were to be formed and of the technical areas to be investigated, namely:

- A. Solar Radiation and Simulation
- B. Heat Transfer and Cryogenic Pumping in Vacuum Technology
- C. Magnetic Environment Simulation
- D. Causes and Effects of Radiation Damage

At this stage no decision had been made on the priorities of the different subject-items within each technical area, nor was there an indication of the most suitable approaches and methods for tackling the various individual tasks. However, a recognized university expert for each technical area had been chosen to serve as principal investigator for all subject matter within that area, and also to act as team captain for the entire group investigating that area. Accordingly, a one-day preworkshop conference was scheduled

early in May to discuss each project or technical area. The discussion leader for each day was the principal investigator of the project announced for that day. Goddard personnel interested in any aspect or item of a given project were invited to discuss their preferences of the work to be carried out. Additional topics were offered for comment and discussion at the conference. Cooperating with the principal investigator at each conference was an appointed Goddard staff advisor who helped the visiting professor to orient the various items under consideration.

This was the schedule of the pre-workshop conferences:

PROJECT TEAM	PRE-WORKSHOP CONF. DATE	CONF. LOCATION BLDG. 7	PRINCIPAL INVESTIGATOR
A	Tuesday, May 7	Room 231	Dr. M. P. Thekaekara
B	Thursday, May 9	Room 110	Dr. G. H. Beyer
C	Friday, May 10	Room 110	Dr. D. L. Waidelich
D	Wednesday, May 8	Room 110	Dr. R. B. Heller

In each case the meeting began at 9 a. m. EDT.

These meetings helped to formulate the arrangements for conducting in-house studies. Priorities and procedures for carrying out the investigations were settled to the satisfaction of the groups concerned. A wholesome relationship was established between the principal investigators and participating Goddard personnel. The idea of university faculty and Goddard permanent staff working cooperatively as teams was crystallized. The meeting served to prepare the way for allocating specific equipment and facilities to the different teams. Most importantly, it provided an opportunity for Goddard personnel to participate in certain phases of advanced research and technology with the likely prospect of achieving some immediately needed results.

THE 1963 WORKSHOP

The real test of all the planning came when the several teams were ready to start their respective investigations. In June 1963 there were some 23 university participants from 14 different academic campuses located in 7 states. Most of them had not met each other before coming to Goddard. All seemed eager to get on with their tasks. A team composed of, say, three professors, three graduate students, and an equal number of technical workers from GSFC undertook a series of studies on a number of problems which appeared formidable, especially with the knowledge that definite and useful results were expected in 12 weeks. Yet, by the middle of September, the four teams not only produced a surprising number of tangible and useful solutions to the problems, but also provided several in-house continuing investigations for Goddard-university collaboration. These studies will be prosecuted at Goddard during this college year with the cooperation of academic specialists working on a part-time basis.

Aside from the specific problem-solving accomplished by each team, as recorded in the Final Report, team activity exerted a challenging influence upon its members. Because certain tasks had to be accomplished within a given time, each member of the team responded to the challenge by suggesting ways and means for completing the job. The interchange of ideas and the desire to achieve results on schedule spurred the individuals into action. This type of motivation enhances in-house competence and updates scientific know-how among the permanent workers. It also indoctrinates the visiting participants with the practical aspects of space science and technology. By contrast, the individual professor who visits Goddard during the summer months as a specialist usually concentrates on his main problem and seldom becomes involved in a group or team effort with the permanent staff.

A CONTRACT-IN-REVERSE

Even though the Goddard Summer Workshop has been considered a new venture in NASA-university relationships, it could be regarded as a normal government research contract to a university, but in reverse. A government-supported university contract is usually established for a period of 1 to 3 years. The sponsor (e.g., ONR, the National Science Foundation or NASA) has a contract supervisor, or scientific officer, or monitor, as he is variously called, who periodically visits the university to check on the progress of the contract. He is also responsible for the technical orientation of the scientific project which the university professors and graduate students are investigating on-campus. In his visits to this university group, the monitor can bring to the working scientists helpful information which will also benefit the project as a whole. For example, in the field of solar simulation, NASA may have several university contracts to study different aspects of the problem. The monitor in his visits obtained from another contractor the information that source-intensity measurements can now be made with considerable accuracy by a newly developed sensor. Here at this university the group is struggling with a traditional sensor and the results are not very reliable. In this manner it is possible to provide useful information among those engaged in similar work and to allow a maximum interchange of ideas. And, the monitor served effectively as a catalyst for both NASA and its contractors.

In the above case, the university engaged in a government research project was doing the job on-campus with its own manpower, which usually consists of a principal investigator with one or more of his professional associates. Often a number of graduate students, part-time workers, are included in the study group. Equipment and facilities are for the most part supplied by the university. Occasionally funds are made available by the sponsor for special instrumentation and services, in order to expedite the project and its results. Most such contracts with universities are in the category of basic sciences and are conducted on-campus for the benefit of the entire nation.

Similarly, the Summer Workshop at Goddard is an attempt to have university groups conduct studies at the Center in advanced research and technology in order to achieve

national goals in space exploration. There is a major difference, however, in the selection of the research project: When a university submits a proposal for scientific work to be undertaken, it is generally a type of basic research which is relevant to a particular department on the campus, and may deal with a subject of long-range possibilities; at Goddard, on the other hand, the investigations may be fundamental in nature and may be essential to future progress, but many of the summer studies require prompt answers both for immediate applications and for guidance to further development. Hence, the Workshop study areas are laid out in advance, and any professor who is invited to participate in the Workshop must choose to investigate some facet in the technical area selected.

Otherwise, the operation of the contract-in-reverse is accelerated, condensed, and concentrated from 3 years to 3 months with many advantages and benefits to Goddard and the participating universities. The new and unprecedented facilities, with highly specialized services and support, including the ferreting out of new knowledge in the various fields, provide exceptional opportunities for accomplishing the manifold purposes of the Workshop in spite of the time limitations. There are daily "monitor visits" to the university group of each team by the Goddard participants instead of one visit in 3 or 6 months. The program is under constant review by discussion and interchange of ideas between the academic personnel and their teammates of the permanent staff. Here, the graduate students as well as the younger NSF science prospects have an opportunity to contribute to the team planning and discussion. This frequent contact and the working together toward a common end-result encourage and promote understanding among the team members. In this way, the senior professors on the team can guide and help the younger students, while the latter are stimulated to further study in the space sciences. Together as a team they prosecute a given scientific program for a limited period in a manner which offers many advantages over other Goddard-university contracts.

CONCLUSION

It is generally agreed that progress in space exploration depends almost entirely upon university participation in the scientific program and in the supply of creative manpower. There are many types of cooperative Goddard-university scientific activities, particularly summer studies, which provide substantial and useful results. But, considering the accomplishments of the Goddard Summer Workshop during the past two summers, it is evident that the Workshop as planned and conducted at Goddard is of great promise and significance to the future advancement of space research and development, under the present manpower situation.

PROJECT A: SOLAR RADIATION AND SIMULATION

CONTENTS

	<u>Page</u>
SOLAR RADIATION AND SIMULATION	A-1
INTRODUCTION	A-1
I. SOLAR SIMULATION: THEORETICAL CONSIDERATIONS	A-5
II. SPECTROGRAPHIC MEASUREMENTS OF SOLAR SIMULATION SOURCES	A-11
III. THE FILTER-DIFFERENTIAL METHOD FOR SOLAR SIMULATION SOURCES	A-41
IV. CALIBRATION OF THERMOPILES	A-53
M. P. Thekaekara, M. S. Ojalvo, and A. J. Galli	
CALIBRATION OF THE FIVE-CHANNEL TIROS SATELLITE RADIOMETER	A-65
E. I. Mohr and F. J. Owens	

ILLUSTRATIONS

<u>Figure</u>		<u>Page</u>
A-1	Optical Schematic of Perkin-Elmer Monochromator	A-12
A-2	Double Monochromator with Cover Removed	A-13
A-3	Log Scale	A-24
A-4	Spectral Irradiance of a 2740-Candlepower Lamp	A-31
A-5	Spectrum of the Mercury-Xenon Arc and Carbon Arc Compared to the Solar Spectrum	A-37
A-6	Spectrum of the Carbon Arc: National Orotip Cored Carbon Rods (Range 4000A to 5000A)	A-39
A-7	Transmission Coefficient of Color Glass Filters, Eppley Filter Wheel	A-45
A-8	Mercury-Xenon Arc Spectrum: Histogram of Spectral Irradiance . . .	A-51
A-9	Mercury-Xenon Arc Spectrum from the Collimation Module: Histogram of Spectral Irradiance	A-51
A-10	Carbon Arc Spectrum: Histogram of Spectral Irradiance	A-52
A-11	A & M Standard Tungsten-Ribbon Lamps	A-59
A-12	Calibration Curves: Eppley Thermopile	A-59
A-13	Five-Channel Satellite Radiometer	A-66
A-14	Dimensions of Lenses	A-66

<u>Figure</u>		<u>Page</u>
A-15	Annulus of Radiating Surface	A-69
A-16	Energy Incident on Lens Aperture	A-69
A-17	Output of Channel 3, Radiometer No. 303, vs. Energy Incident on Detector	A-72
A-18	Output of Channel 5, Radiometer No. 303, vs. Energy Incident on Detector	A-72

TABLES

<u>Table</u>		<u>Page</u>
A-1	Wavelength Calibration of Leiss Double Monochromator with Flint Glass Prisms	A-19
A-2	Wavelength Calibration of Leiss Double Monochromator with Quartz Prisms	A-20
A-3	Wavelength Calibration of Perkin-Elmer Monochromator, Model 99 . .	A-21
A-4	Wavelength Calibration of Perkin-Elmer Monochromator, Model 112-U	A-22
A-5	Response Characteristics of Perkin-Elmer Spectrograph with a 1P28 and Thermocouple Detector	A-25
A-6	Perkin-Elmer Spectrograph Conversion Table for Signal Strengths at Varying Values of Gain Factors	A-26
A-7	Spectral Irradiance of Secondary Tungsten-Ribbon Standard Lamps . .	A-28
A-8	Spectral Irradiance of the 2740-Candlepower Lamp	A-30
A-9	Spectral Irradiance of the Mercury-Xenon Arc	A-35
A-10	Spectral Irradiance of the Carbon Arc	A-40
A-11	Fractional Energy Absorbed by Filters	A-49
A-12	Energy Distribution in Wavelength Ranges for the Carbon Arc and Hg-Xe Arc	A-50
A-13	Spectral Irradiance of Tungsten-Ribbon Lamps	A-58
A-14	Calibration Table for Thermopiles	A-61
A-15	Calibration for Power Five-Channel Radiometer No. 303	A-71
A-16	Calibration for Energy per Unit Area of Five-Channel Radiometer No. 303	A-71
A-17	A&M Division Calibration of Radiometer No. 303	A-73

SUMMER WORKSHOP 1963

Program Outline and Team Participants

PROJECT A: Solar Radiation and Simulation

Study Topics

- A-1 Precision measurements of total energy and spectral distribution
- A-2 Analysis and handling of solar simulation data
- A-3 Reliability and response characteristics of solar cells
- A-4 Calibration and data analysis of infrared sensors of weather satellites

TEAM A

<u>Academic Personnel</u>	<u>Goddard Personnel</u>	<u>Code</u>
*Dr. Thekaekara	Dr. W. W. Wolman	600
PRINCIPAL INVESTIGATOR	STAFF ADVISOR	
Dr. Ojalvo	Arthur R. Winker	322
*Dr. Mohr	Neil P. Zylich	322
Mr. Owens	Luther W. Slifer	636
*Mr. Galli	Brian T. Cunningham	636
Mr. Sharp	Dr. William Nordbert	651
	Andrew W. McCulloch	650
	NSF Summer Science Student George W. Williams	

*Continuing part-time work at Goddard on Project A.

SOLAR RADIATION AND SIMULATION

M. P. Thekaekara, M. S. Ojalvo, and A. J. Galli

INTRODUCTION

The area of research and development for Team A of the Summer Workshop was defined as Solar Simulation and Radiation. Precise measurement of radiant energy is important in many areas of the space program. For those engaged in prelaunch testing of space vehicles through solar simulation, the problem is of special significance.

Measurement of energy is an art and a science. The physical concept of energy is in itself very simple: It is work done or work potentially available. It appears in many forms, easily interacts with matter, is conserved in all changes. It is measured as the vector product of a force and the distance through which the point of application of the force moves. The dimensions of the unit of energy are (length² mass/time²). Although length, mass, and time have internationally accepted standards and can be measured with the utmost precision, amounting to few parts in a billion, the measurement of energy leaves large uncertainties. As a result, there is no international standard for energy with accepted limits of accuracy. Similarly, for one of the more fundamental constants of nature, the solar constant, different values are current in different countries, and the accepted values have frequently been revised. These two facts serve to illustrate the difficulties in energy measurement.

The problem of energy measurement involves a knowledge of many phenomena of fundamental physics related to the production of energy, its propagation through space and matter, and its interaction with energy-sensing devices. The new physics – physics of the twentieth century initiated by the quantum theory of Max Planck – would not have been possible except for the very extensive measurements made in earlier years on the spectral irradiance of a blackbody. In blackbody radiation, the irradiance in any spectral region is obtained by multiplying two functions, one denoting the number of degrees of freedom in a given wavelength range, and another denoting the average energy per degree of freedom. All high-temperature sources bear a certain resemblance to blackbody radiation.

On the other hand, significant departures from the Planck radiation law occur because emissive coefficients of surfaces may be less than unity, or because of emission and absorption lines. The energy in an emission line is the product of the Planck's constant, the frequency of the radiation, and the number of atoms undergoing a given transition in unit time. Hence, the intensity of a line leads to a determination of the number of atoms

involved in a transition between two levels. This, in turn, provides information about the number of atoms in a given upper state and about the transition probability. Transition probability is an important parameter in atomic and molecular physics. Many of the successes of the quantum theory are due to the well-established relationships between wave functions and transition probabilities.

Spectral lines have finite linewidths. The width of a line is due to many contributing causes: finite resolution of the spectrograph, graininess of the photographic emulsion, natural width of the line as given by the Heisenberg uncertainty relation, Doppler effect, vibrations in crystal lattices, collisions between atoms and ions, electric and magnetic fields in the plasma. An investigation of linewidths and line profiles leads to many interesting conclusions about the physics of the atom, molecule, and plasma, and also about the techniques of instrumentation.

These basic considerations of physics, important as they are from a theoretical standpoint, have additional significance for an applied physicist. They show what precautions should be taken, what instrumentation should be applied, how data might best be processed in any concrete situation. The metallurgical industry has long relied upon relative intensities of lines to test the chemical composition of its alloys and to control the quality of its products. The many industries in the areas of color and illumination need reliable monitoring techniques for total intensity and spectral irradiance. Those engaged in solar simulation and testing of spacecraft models for thermal balance have a great deal to learn from the techniques developed and the experience gained by other highly exploited areas of applied optics and spectroscopy.

The Test and Evaluation Division of Goddard Space Flight Center is interested in the measurement of energy, not because of its intrinsic physical significance, but because these techniques and their results are needed in current calibration and testing procedures. High degrees of precision will often have to be sacrificed for ease of measurement and rapidity of data processing. However, it is necessary to guard against major systematic errors, and to know the degree of accuracy in any set of measurements.

There are many different types of energy sensors: (1) phototubes like the 1P28 or lead sulfide cell, thermistor bolometers, silicon cells and other sensors depending on the semiconducting properties of crystals; (2) thermopiles and thermocouples of various kinds, air-cooled and water-cooled, with or without windows, depending on the Peltier and Thomson coefficients of conductors; and (3) large-area grids depending on the temperature coefficient of resistance of conductors. Team A has studied the sensitivity, linearity of response, and wavelength dependence of several of these energy sensors. In the course of our work we developed a reliable method for calibrating thermopiles.

Spectral-energy distribution of the high-energy sources currently used for solar simulation is a topic of considerable interest. Last year's Summer Workshop began these studies; during this year's Summer Workshop, a number of sources were examined over a wide spectral range. Several secondary tungsten-ribbon standard lamps were calibrated for

current use in the laboratory; this calibration ensures a more reliable standardization and a longer life for the primary standards calibrated at the National Bureau of Standards. We also have developed an alternate procedure for rapid determination of spectral energy distribution, one which we refer to as the Filter-Differential Method.

I. SOLAR SIMULATION: THEORETICAL CONSIDERATIONS

The essential information needed for simulating solar radiation is the total energy and the spectral distribution of the solar radiation for zero air mass, as well as those of the radiation from the mercury-xenon lamp or the carbon arc incident on the test floor.

The solar energy for zero air mass is usually considered to be sufficiently well known. Most workers in the field of solar simulation assume that the best value available at present is 2.00 calories per cm^2 per minute, as deduced by Francis S. Johnson at the Naval Research Laboratory in 1954.¹ This value is based on revisions of data collected for over 30 years by the Smithsonian Institution, on later data collected by Dunkelman and Scolnik,² and on a reevaluation of the correction factors for the infrared and ultraviolet ranges.

It is interesting to observe that the value of solar constant has frequently been revised, and each new revision has increased its value. P. Moon³ in 1940 published a detailed analysis of the data of the Smithsonian Institution and derived the value $1.896 \text{ cal cm}^{-2} \text{ min}^{-1}$. A revision in 1952 by Aldrich and Hoover⁴ raised the value to $1.946 \text{ cal cm}^{-2} \text{ min}^{-1}$. C.W. Allen⁵ in 1955 gave a value $1.97 \pm 0.01 \text{ cal cm}^{-2} \text{ min}^{-1}$. Francis S. Johnson's value of 1954 as quoted above was $2.00 \pm 0.04 \text{ cal cm}^{-2} \text{ min}^{-1}$. An independent set of measurements by Ralph Stair and Russell G. Johnston⁶ in June 1955 at an altitude of 9200 feet yielded a preliminary value of $2.05 \text{ cal cm}^{-2} \text{ min}^{-1}$; this value was later scaled down⁷, due to further correction factors, to a value very close to that of Francis S. Johnson.

Extensive data on the spectral-energy distribution of solar energy are available in the publications of Moon, Johnson, and Stair. These data have been collected together and critically evaluated by P. R. Gast in the "Handbook of Geophysics."⁸

The spectral irradiance of the sun in the visible and infrared spectra is approximately that of a blackbody at 6000°K . The blackbody temperature of solar radiation is so high that obviously no terrestrial source of radiation can be an exact spectral match to solar radiation. The melting point of tungsten, the most refractory metal, is 3370°C and that of tantalum is 3000°C ; these temperatures are nearly half that of the sun, and the energy distribution curve would therefore have the maximum at a wavelength of about one micron. A tungsten coil lamp of very high intensity, measurements on which are reported later in this paper, operates at a temperature of 2840°K and has maximum energy at 9500\AA .

To understand how this discrepancy can be overcome and a satisfactory degree of solar simulation achieved, it is helpful to recall a few basic concepts of radiation theory.

The Planckian theory of radiation assumes a state of energy equilibrium between the heated walls of an enclosure and the stationary waves of electromagnetic radiation within the enclosure. In other words, the average energy per degree of freedom in matter and radiation is the same. The new concept introduced by Planck's theory is that the energy transfer can occur only in integral multiples of a fundamental unit, frequency times a constant h . Therefore, the average energy per degree of freedom of all stationary waves of wavelength λ is

$$\frac{e^{hc/\lambda}}{e^{hc/\lambda} kT - 1} \quad (1)$$

instead of the value kT given by the classical kinetic theory of gases. The total number of degrees of freedom in the wavelength range λ to $\lambda + d\lambda$ is $8\pi\lambda^{-4}d\lambda$. From this arises Planck's law of radiation,

$$\psi_{\lambda} d\lambda = \frac{8\pi}{\lambda^5} \frac{hc}{e^{hc/\lambda} kT - 1} d\lambda \quad (2)$$

When the expression on the right-hand side is differentiated with respect to λ and equated to zero, one obtains the wavelength at which ψ is maximum. The equation

$$\frac{d\psi_{\lambda}}{d\lambda} = 0,$$

can be simplified to give

$$e^{hc/\lambda} kT \left(1 - \frac{hc}{\lambda kT}\right) = 1.$$

Hence

$$\frac{hc}{\lambda kT} = 4.965114. \quad (3)$$

The Wien's displacement law constant $\lambda_{\max} T$ is $0.289776 \text{ cm } ^{\circ}\text{K}$.

Our prime concern is with the energy radiated from a surface or that received on a surface, rather than with the energy density within an enclosure. The energy density is the radiant energy per unit volume of a stream of radiation. When energy radiates from the sun, the stream of radiation in the neighbourhood of the earth is parallel. The energy received by unit area is that contained in a cylindrical volume of space, of length equal to the velocity of light, and cross-section unity. Dividing the solar constant by the velocity of light produces the energy density. $\psi = \frac{\mathcal{J}}{c}$, where \mathcal{J} is the solar constant, c is the velocity of light, and ψ is the energy per unit volume due to solar radiation.

A different condition exists in an enclosure where the radiation streams back and forth in all directions. There is a simple relation between the intensity of radiation from a surface A , and the energy density ψ , provided the surface obeys the cosine law: that is,

equal amounts of energy are radiated in all directions. It can be shown that

$$E = \frac{1}{4} C \psi \quad (4)$$

The quantity E is related to the temperature by the well-known Stefan-Boltzman law of radiation. The energy radiated in unit time from unit surface of a blackbody is

$$E = \sigma T^4,$$

where σ is a constant and T is the absolute temperature. The value of σ can be obtained by rewriting the Planck's law of radiation in terms of the frequency ν , and integrating the expression to give the total energy density for all values of frequency.

$$\begin{aligned} \psi &= \int_0^{\infty} \psi_{\nu} d\nu = \int_0^{\infty} \frac{8 \pi h \nu^3}{c^3 (e^{h\nu/kT} - 1)} d\nu \\ &= \frac{8}{15} \frac{\pi^5 k^4}{c^3 h^3} T^4. \end{aligned} \quad (5)$$

Substituting for E from (4)

$$E = \frac{2}{15} \frac{\pi^5 k^4}{c^2 h^3} T^4, \quad (6)$$

which gives the value of σ to be

$$\sigma = \frac{2}{15} \frac{\pi^5 k^4}{c^2 h^3}.$$

The best spectral match to solar radiation is obviously the radiation issuing from an enclosure at about 6000°K . But such an enclosure presents great experimental difficulties.

An alternate procedure is to make use of the line spectrum of the elements. The strong emission lines of most elements lie in the visible and near-infrared region, because the energy required to transfer an electron in an atom from a lower bound state to a higher excited state is of the order of 1 to 10 electron volts. The wavelength corresponding to 5 electron volts of energy is about 6170\AA . The excited state has a very short half-life, and the atom makes a spontaneous transition to a lower state. The difference in energy between the two states is emitted as radiant energy.

The energy radiated in unit time due to a given transition is

$$E = N_n A_{n,j} h\nu \quad (7)$$

where N_n is the number of atoms in an upper energy state n , $A_{n,j}$ is the probability of transition in unit time from state n to state j , h is the Planck's constant, and ν is the frequency corresponding to this transition.

Increasing the pressure and temperature of the gaseous discharge causes the spectral lines to broaden. Raising the temperature also increases the relative population of the higher energy states, as shown by the Boltzman equation or the Saha ionization equation. In this way the relative energy is increased in the spectral lines of the lower wavelength range. Many of the lines which are practically absent in a low-temperature discharge (namely, the higher members of any of the Rydberg-Ritz series) appear strongly in a high-temperature discharge. These many lines, all broadened and coalescing into each other, make a large contribution to the continuum.

Another contributing factor may be understood by studying any of the series in line spectra; the Balmer series in hydrogen is the most familiar, and from a theoretical point of view the most readily understood. Each line of the series is due to a transition to the level $j = 2$ from the upper levels of $n = 3, 4$, etc. As the temperature is increased, not only does the intensity increase in the higher members of the series between 6563A and 3646A, but also a continuum on the shorter wavelength side of 3646A is observed, which is caused by transitions from positive energy states, the parabolic orbits, to the state of $j = 2$. The hydrogen spectrum has only one series in the visible region. A complex spectrum like that of mercury or xenon has many overlapping series, each obeying the Rydberg-Ritz combination principle and each having a continuum proper to the series. Xenon has 34 such series due to the transitions to the lowest levels only of the s , p , d and f states of the atom.

This mechanism of energy emission from a radiating source has certain advantages and disadvantages from the point of view of solar simulation. The major part of energy of the spectral lines and of the continua is in the visible and near-infrared region, the same spectral region where the solar energy is the greatest, so that a spectral match can be obtained even though the temperature of the radiant source is only half that of the sun. The spectral irradiance curve of the sun is just the reverse of those of high-energy laboratory sources like the mercury-xenon arc or the carbon arc. The solar irradiance curve is approximately a Planckian curve with a large number of narrow absorption lines arising from the sun's reversing layer. The other two curves have strong peaks of the emission lines superimposed on a continuum, those of mercury-xenon being much higher than those of carbon. This essential dissimilarity between the curves poses no special problem for solar simulation, because the important parameter is not the spectral distribution of the incident energy but the total energy absorbed. The absorption coefficient of surface coatings, though dependent on wavelength, does not show the very rapid variations over narrow wavelength bands which characterize the spectral-energy distribution curve.

The major disadvantage is that the spectral-energy distribution depends on many contributing factors, each of which in turn depends on variable parameters of the arc. Temperature, and therefore the total emissive power and the spectral irradiance, vary at

different locations in the arc. The highest temperature is in the vicinity of the anode. The input power, the rate of flow of the coolant air outside the lamp, the relative proportion of mercury and xenon, the change in pressure due to the aging of the lamp, the distance between the electrodes, and a few other indefinable factors, all affect the radiant-energy output of the mercury-xenon lamp.

Other factors control the output of the carbon arc. The hot spot of the arc wanders slightly around the positive crater and hence the percentage of the total energy collected by the optical system undergoes small fluctuations. In order to increase the energy in the visible and ultraviolet regions of the spectrum, the carbon rods are often enriched with rare earths. The relative proportion of these rare earths affects the spectral irradiance. Positive rods from different manufacturers or from different shipments by the same manufacturer do not necessarily have the same spectral distribution. The rate of feeding of the rods, the length of the arc, the velocity and direction of the air jet which stabilizes the arc, and the power input are other factors which affect the total energy and the spectral irradiance of the carbon arc.

II. SPECTROGRAPHIC MEASUREMENTS OF SOLAR SIMULATION SOURCES

PRISM SPECTROGRAPHS

The conventional technique for measuring spectral-energy distribution is sufficiently well known. It was discussed in detail in the Final Report of the Summer Workshop of 1962.⁹ The image of a given source is focused on the slit of a suitable spectrograph, and the intensity of a narrow spectral range is recorded using a detector, an amplifier, and a chart recorder. Next the given source is replaced by a standard tungsten-filament source. The spectral irradiance of the standard source is known through previous calibration. If \mathcal{I}_x and \mathcal{I}_c are the intensities in a given wavelength band λ to $\lambda + \Delta\lambda$ due to the unknown source and the standard of comparison, and s_x , s_c are the corresponding signal strengths, assuming that the signal is proportional to the intensity $\mathcal{I}_x = \mathcal{I}_c \times s_x/s_c$.

In our current investigations we were interested not merely in measuring the spectral irradiance of a few given sources, but principally in evaluating the method and in setting up a procedure for operating the available spectrographic equipment with maximum speed, efficiency, and accuracy. Certain preliminary studies were made and the results are briefly discussed below.

Three high-dispersion spectrographs were used in these studies of spectral irradiance of high-energy sources. Two of these are single-prism monochromators manufactured by Perkin-Elmer Corporation; the third is a double-prism monochromator manufactured by the Leiss Company, West Germany.

Figure A-1 is the optical schematic of the Perkin-Elmer spectrograph. Radiation from any of the standard instrument sources, S_0 , S_p , S_q , or from an outside source is focused on the variable width entrance slit S_1 by the spherical mirror M_2 . The portion of the beam passing through S_1 is collimated by the paraboloid mirror, M_3 , and refracted by the prism P. The Littrow mirror, M_4 , returns the radiation which is refracted again by the prism. A portion of the dispersed field is intercepted by the mirror, M_5 , and comes to a focus between the halves of a split mirror, M_6 . The energy is modulated by the slightly displaced rotating chopper, CH, and returned for a second pass through the paraboloid-prism-Littrow combination, wherein it receives a second dispersion.

After the second pass the beam is reflected by the mirror, M_7 , and brought to a focus in a spectrum falling across the exit slit S_2 . The exit slit passes chopped radiation of a narrow wavelength range whose bandwidth depends on the width of S_2 , and whose midband wavelength depends on the Littrow angle setting. This energy is reflected by the mirror, M_8 , and is collected and focused on the thermocouple detector, T, by the ellipsoid, M_9 ,

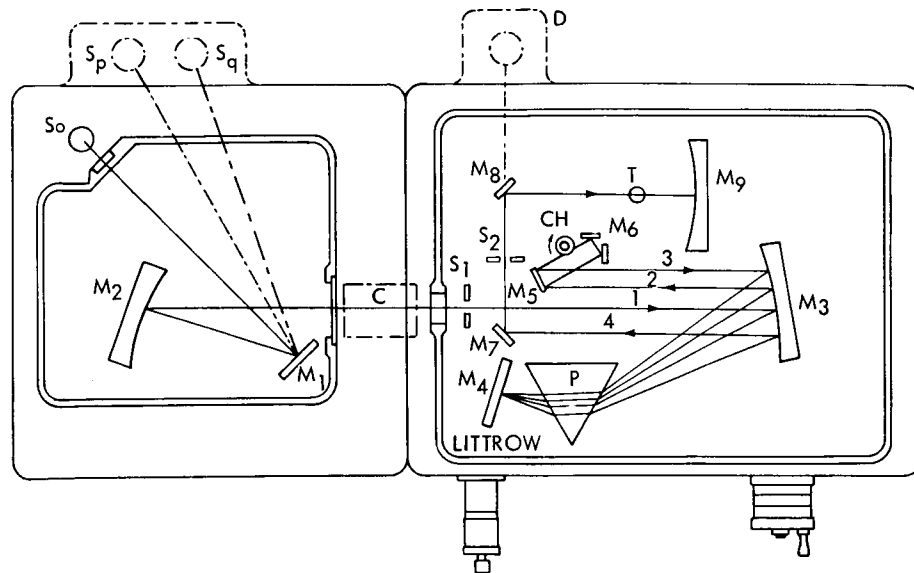


Figure A-1—Optical schematic of Perkin-Elmer monochromator.

producing a pulsating signal. This signal is amplified, and is shown as a pen deflection of a recorder. Other detectors, such as a lead sulfide cell or a 1P28 photomultiplier tube, may be used at position D when mirror M_8 is removed.

The position of the Littrow mirror is denoted by a drum reading on the instrument, and a calibration must be made relating the drum reading to the wavelength of the radiation falling on the detector.

The standard instrument sources, S_0 , S_p , S_q , are a hydrogen discharge tube, a tungsten-ribbon lamp, and a globar. The plane mirror, M_1 , reflects the beam from one or the other of these sources to the spherical mirror, M_2 . When the instrument is used to analyze an outside source such as the standard tungsten-ribbon lamp or the solar-simulator sources, an auxiliary image of the source is focused by a lens or a mirror at some point at the same distance from M_1 as the standard instrument sources. Since the standard tungsten-ribbon lamp is frequently used for energy calibration, we found it necessary to add an extra mount which ensures sufficient stability and accurate focusing. This mount, not shown in Figure A-1, is attached to the spectrograph base near the mirror, M_2 , on the side opposite to that of the three standard instrument sources.

The Leiss double-prism monochromator with cover removed is shown in Figure A-2, a photograph of the optical parts of the instrument. Light entering at the entrance slit, S_1 , is deflected by a plane mirror, A_1 , and is collimated by a concave mirror, H_1 . The parallel beam from the concave mirror is refracted by the first 30- 60- 90-degree prism, P_1 , which has a mirror coating on its rear surface. The spectrally dispersed light returning from the prism is focused on a second slit, S_2 , by means of another concave mirror, H_2 . After passing through the second slit, the light traverses a similar path of reflection at a

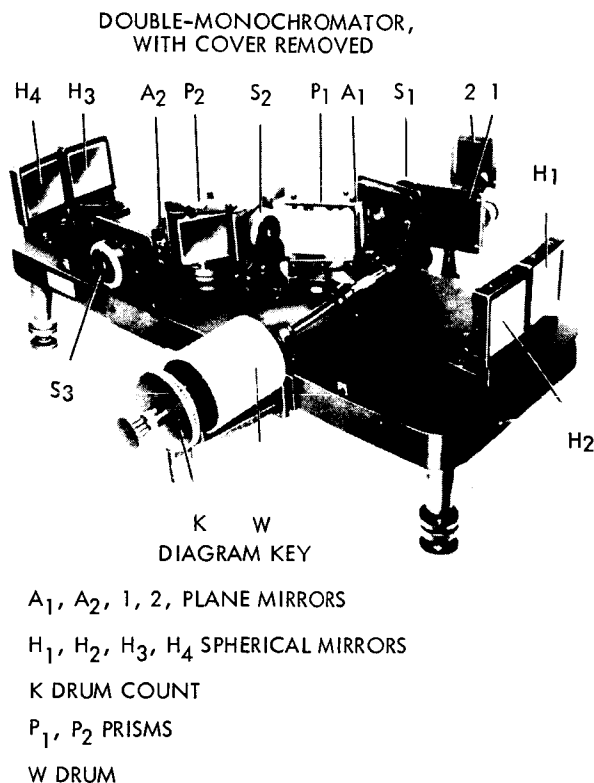


Figure A-2—Double monochromator with
cover removed.

concave mirror, refraction through a prism, reflection at a fourth concave mirror, and reflection at a plane mirror. The refracted beam is focused on the exit slit, S₃ beyond which is the detector, a 1P28 phototube, a thermocouple or a lead sulfide tube.

The prisms are mounted on two turntables which are coupled by gears to a graduated drum, W. Each complete turn of the drum produces a rotation of 1 degree. Prism positions can be reproducibly adjusted with an accuracy of ± 10 seconds. In using flint-glass prisms, this corresponds to an accuracy of the wavelength adjustment to 5Å at the center of the visible range, 6000Å, and of 1.6Å at 4500Å.

In a recent modification of the instrument, the flint-glass prisms were replaced by fused quartz prisms. This gives a wider transmission range of 0.25 to 3.0 microns, whereas the transmission range of the flint-glass prism is 0.365 to 2 microns. There is a corresponding loss in dispersion and resolving power, especially in the visible range, as both these depend on the rate of change of refractive index with wavelength. For the flint-glass prism, the change of refractive index ($\times 10^6$) per angstrom wavelength increment is 22.0 at 0.5 micron and 1.5 at 1.5 micron. The corresponding change for the fused quartz prism is 5.9 at 0.5 micron and 1.1 at 1.5 micron.

Another significant modification is the use of an improved detector, a Barnes Research radiometer, which is mounted at a distance of about 2 feet from the exit slit. A cassegrainian telescope focuses the image of the exit slit on the photosensitive surface of a lead sulfide detector. This arrangement gives a higher sensitivity and a wider coverage of the spectral range.

It is necessary to recall a few of the basic equations of physical optics which govern the refracting properties of prism instruments. A more complete discussion of the topic may be found in standard textbooks of optics.¹⁰

Let i_1 , r_1 , be the angles of incidence and refraction of a ray of light at the first refracting surface of a prism, r_2 , the angle of incidence in the glass at the second surface, i_2 , the angle of emergence, A , the vertex angle of the prism, w , the width of the refracting face of the prism, δ , the angle of deviation, D , the dispersion or the rate of change of δ with wavelength λ , R the resolving power $\frac{\lambda}{\Delta\lambda_m}$, where $\Delta\lambda_m$ represents the smallest change in wavelength that can be resolved, and n the refractive index.

The deviation is related to the angles of incidence and refraction by the equation

$$\delta = (i_1 - r_1) + (i_2 - r_2) \quad (9)$$

and the angle of the prism,

$$A = r_1 + r_2. \quad (10)$$

As i_1 is varied, δ passes through a minimum. The condition for minimum deviation is that

$$\frac{d\delta}{di_1} = 0 = 1 + \frac{\delta i_2}{\delta i_1}$$

Since by Snell's law $\sin i_1 = n \sin r_1$ and $\sin i_2 = n \sin r_2$, differentiation of i_2 with respect to i_1 gives

$$\frac{di_2}{di_1} = - \frac{\cos r_2}{\sqrt{1-n^2 \sin^2 r_2}} \cdot \frac{\cos i_1}{\sqrt{1-\sin^2 i_1/n^2}} = -1.$$

Multiplying out and squaring the second and last terms produces

$$r_2 = r_1.$$

Hence, for the position of minimum deviation,

$$n = \frac{\sin \frac{A + \delta}{2}}{\sin \frac{A}{2}}. \quad (11)$$

The variation of n with λ is not expressed by any exact formula. A useful approximation containing only two constants is the Cauchy formula

$$n = n_0 + \frac{B}{\lambda^2} \quad (12)$$

A more accurate approximation, with three constants n_0 , λ_0 , and C , is the Hartmann formula,

$$n = n_0 + \frac{C}{\lambda - \lambda_0} \quad (13)$$

The dispersion of a prism instrument is

$$D = \frac{d\delta}{d\lambda} = \frac{di_2}{d\lambda}$$

Sometimes linear dispersion is given in terms of centimeters per angstrom unit; it is the angular dispersion D multiplied by the focal length of the concave mirror which focuses the refracted light on the exit slit. The magnitude of D is related to the angle of the prism and the variation of n with λ .

To find D , begin with the equation,

$$\sin i_2 = n \sin r_2$$

to obtain

$$\frac{di_2}{d\lambda} = \frac{1}{\cos i_2} \left(\frac{\cos r_2 \sin r_1}{\cos r_1} + \sin r_2 \right) \frac{dn}{d\lambda}$$

This reduces to

$$D = \frac{di_2}{d\lambda} = \frac{\sin A}{\cos i_2 \cos r_1} \frac{dn}{d\lambda} \quad (14)$$

At the position of minimum deviation for a 60-degree prism, assuming Hartmann's dispersion formula for n , the dispersion of the prism is

$$D = \frac{C}{(\lambda - \lambda_0)^2 \sqrt{1 - n^2/4}} \quad (15)$$

The resolving power R of a spectrograph is defined as the ratio of the wavelength, λ , to the smallest change, $\Delta\lambda_m$, of wavelength that can be resolved. Thus

$$R = \frac{\lambda}{\Delta\lambda_m}$$

If $\Delta\theta_m$ represents the smallest angle that can be resolved at the exit slit, we may write

$$\Delta\lambda_m = \Delta\theta_m / D,$$

so that

$$R = D \frac{\lambda}{\Delta\theta_m}.$$

The value of $\Delta\theta_m$ depends on the width of the entrance slit and exit slit, on the residual aberrations of the optical components, and on the diffraction effects of light. In a properly designed spectrograph, the effect of the first two factors can be made small when compared to that of diffraction. The diffraction theory applicable in this case is that of Fraunhofer diffraction at a single slit. For a rectangular aperture of width a , the value of $\Delta\theta_m$ is λ/a , and it follows that $R = Da$. The equivalent width of the slit is the projection of the second refracting face of the prism on the emergent wavefront, and is equal to $w \cos i_2$.

Thus it is found that

$$R = \frac{w \sin A}{\cos r_1} \frac{dn}{d\lambda}. \quad (16)$$

At the position of minimum deviation, this reduces to

$$R = 2w \sin \frac{A}{2} \frac{dn}{d\lambda}. \quad (17)$$

For normal dispersion, the index of refraction increases as wavelength decreases. The rate of increase $dn/d\lambda$ becomes greater at shorter wavelengths. For different substances, the curve of n versus λ is steeper at a given wavelength if the index of refraction is greater. As wavelength increases towards one of the absorption edges of the material of the prism, the refractive index decreases abruptly.

WAVELENGTH CALIBRATION OF THE SPECTROGRAPHS

The wavelength calibration of the spectrograph is an essential preliminary step in operating a prism spectrograph. The results of the calibration may be presented either as a calibration curve of wavelength on the y-axis and counts on the x-axis, or as a table of wavelengths for small increments of the count. The count is read from the graduated drum geared to the Littrow mirror of the Perkin-Elmer spectrographs or to the prisms of the Leiss spectrographs. For precision work, the tabular form of presenting the results is preferable to a calibration curve. A linear interpolation between two pairs of values on the table gives the wavelength for any given count more accurately than can be read from a graph.

Data for the calibration table can be obtained by scanning any known spectrum. The most convenient spectrum for our purpose was the mercury-xenon arc.

This spectrum is very rich in lines extending over the whole spectral range from 2500A to 20,000A. Most of the lines are of atomic mercury; a few are of atomic xenon. Several lines, of which the origin is still obscure, have not been identified with the lines in any published literature. The wavelengths of these lines are, however, known to a high degree of accuracy from our earlier spectrographic charts of the mercury-xenon arc, made with a high-dispersion Jarrell-Ash grating spectrograph.

Other calibration points were obtained from a set of eight spectral lamps, low-pressure discharge tubes which emit a relatively pure spectrum of the following elements: Hg, Cd, Cs, K, Na, Tl, Zn, and Rb.

In the long-wavelength range beyond 1.8 micron there are few easily identified lines in any of the above sources.

A set of nine dielectric film filters, manufactured by the Optics Technology, Inc., and labeled "Spectracoat Monopass Filters," were available for this infrared range. Characteristics of these filters are discussed later in this report. According to the manufacturer's data, the peak transmission of the filters occurs at the wavelengths 1.815, 1.905, 2.020, 2.135, 2.225, 2.330, 2.435, 2.515 and 2.605 microns. The transmission peaks are known to be dependent on temperature, and the calibration of the spectrograph is less accurate in this range than in the shorter wavelength ranges.

The counter readings of the Perkin-Elmer spectrograph were registered on a recorder chart by an automatic marker. The spectrograph produced a short pen deflection of about half an inch at each tenth count, and an extra mark at five minus each hundredth count. For the Leiss spectrograph, counter marks were made manually, either by shielding off the light or by shining extra light for a very brief interval of time when the drum rotated past known counter readings. The relation between counter readings and positions of the recorder chart is strictly linear, so that the counter reading corresponding to any known wavelength was readily determined by a linear interpolation formula.

Several records of the spectra were made and the counter readings for known lines were averaged between these. In this way it was possible to correct for the backlash of the gears and the lack of uniformity of the chart drive. A graph was drawn of wavelength versus count on large-size graph paper to rule out any wrong identification of the lines.

The following procedure was adopted to obtain the calibration table from the given set of data points: The spectral range is divided into about five overlapping regions. In each region, three lines are chosen as standards. We assume that a quadratic equation,

$$\lambda_i = a + bx_i + cx_i^2, \quad i = 1, 2, 3. \quad (18)$$

gives approximately the relation between wavelength λ and count x . A small Burroughs E101 computer is used to calculate the values of a , b , and c from the set of three equations (18). The computer also finds the calculated value of λ , λ_{ca1} , for all known values of x , and the difference $\Delta\lambda = \lambda_{lit} - \lambda_{ca1}$ between the values listed in literature and those calculated from the quadratic equation. A smooth graph is drawn with count, x , on the x-axis and correction factor $\Delta\lambda$ on the y-axis. Values of λ_{ca1} are also found for counter readings at equispaced intervals of five counts or two counts. By adding the appropriate value of $\Delta\lambda$ to λ_{ca1} , we obtain the wavelength corresponding to each count.

For some of the earlier calibration tables a more simplified technique of data reduction was used. Instead of the quadratic equation, a linear equation of the form

$$\frac{\lambda - \lambda_1}{x - x_1} = \frac{\lambda_2 - \lambda_1}{x_2 - x_1}, \quad (19)$$

was employed. This gives rather large values of $\Delta\lambda$ in the wavelength range of the near-infrared, but has the advantage that the data can be processed with a desk calculator.

If a computer is available, the more accurate method of a second-degree equation should be used. Errors in the experimental determination of the count x for given λ are eliminated by this method. If the total number of data points is N , the accuracy of the final calibration table is \sqrt{N} times the accuracy of individual measurements.

The results are given in Tables A-1, A-2, A-3, and A-4. Tables A-1 and A-2 are for the Leiss double monochromator (Leiss catalog No. 9100; Serial no. 1214, Goddard property No. 26629) with flint-glass prisms and with quartz prisms. With the quartz prisms a wider spectral range is covered, but the counter readings are from 370 to 800, whereas the flint-glass prisms of greater dispersive power give a range 320 to 900 for the counter readings. Table A-3 is for the Perkin-Elmer spectrograph, Model 99 (Serial No. 130, Goddard property No. 24488) of the Aeronomy and Meteorology Branch; Table A-4 is for the Perkin-Elmer spectrograph, Model 112-U (Serial No. 305, Goddard property No. 28551) of the Test and Evaluation Division. Both spectrographs have quartz prisms.

All four tables give the wavelengths corresponding to a stepwise increment of count. It is significant that $d\lambda/dx$ increases as λ increases until λ is about 2 microns, and thereafter $d\lambda/dx$ decreases. A graph drawn with λ on the y-axis and count on the x-axis is convex to the x-axis over most of the wavelength range, and is concave to the x-axis at the extreme infrared. It is also seen that the flexion point of the graph occurs earlier for the Leiss spectrograph with the flint-glass prism. This is obviously an illustration of the anomalous dispersion of the material of the prism in the vicinity of an absorption band. The effect was first demonstrated in 1904 by R. W. Wood in a striking experiment with sodium vapor.¹¹

Table A-1
Wavelength Calibration of Leiss Double Monochromator
with Flint Glass Prisms,
(Leiss Catalog No. 9100)

Drum Reading	Wavelength $\lambda \text{ \AA}$	Drum Reading	Wavelength $\lambda \text{ \AA}$	Drum Reading	Wavelength $\lambda \text{ \AA}$
320	3540	575	4557	808	10128
325	3551	580	4588	810	10319
330	3561	585	4621	812	10526
335	3572	590	4654	814	10720
340	3584	595	4690	816	10920
345	3596	600	4728	818	11080
350	3608	605	4770	820	11251
355	3620	610	4812	822	11435
360	3633	615	4858	824	11639
365	3646	620	4905	826	11844
370	3660	625	4956	828	12048
375	3674	630	5010	830	12263
380	3688	635	5064	832	12487
385	3702	640	5121	834	12717
390	3717	645	5179	836	12952
395	3732	650	5239	838	13202
400	3747	655	5301	840	13448
405	3763	660	5364	842	13713
410	3779	665	5429	844	13984
415	3796	670	5496	846	14260
420	3812	675	5563	848	14545
425	3829	680	5633	850	14836
430	3847	685	5704	852	15133
435	3864	690	5770	854	15427
440	3882	695	5830	856	15742
445	3901	700	5895	858	16057
450	3919	705	5970	860	16352
455	3938	710	6060	862	16642
460	3957	715	6150	864	16921
465	3977	720	6243	866	17199
470	3997	725	6364	868	17469
475	4017	730	6504	870	17769
480	4038	735	6659	872	18051
485	4059	740	6800	874	18342
490	4080	745	6960	876	18630
495	4099	750	7121	878	18928
500	4121	755	7291	880	19206
505	4145	760	7467	882	19490
510	4167	765	7646	884	19780
515	4192	770	7855	886	20125
520	4219	775	8068	888	20451
525	4245	780	8307	890	20758
530	4272	785	8569	892	21045
535	4301	790	8845	894	21312
540	4331	794	9080	896	21610
545	4362	796	9193	898	21889
550	4394	798	9303	900	22148
555	4425	800	9439	902	22338
560	4460	802	9591	904	22559
565	4492	804	9759	906	22810
570	4526	806	9933	908	23060

Table A-2
Wavelength Calibration of Leiss Double Monochromator
with Quartz Prisms,
(Leiss Catalog No. 9100)

Drum Reading	Wavelength $\lambda \text{ \AA}$	Drum Reading	Wavelength $\lambda \text{ \AA}$	Drum Reading	Wavelength $\lambda \text{ \AA}$
370	2532	535	3430	680	10414
375	2540	540	3486	682	10734
380	2551	545	3545	684	11056
385	2563	550	3607	686	11381
390	2576	555	3672	688	11709
395	2589	560	3743	690	12039
400	2601	565	3818	692	12371
405	2614	570	3897	694	12706
410	2627	575	3979	696	13052
415	2642	580	4063	698	13400
420	2661	585	4155	700	13768
425	2680	590	4253	702	14117
430	2699	595	4362	704	14467
435	2726	600	4484	706	14819
440	2752	605	4610	708	15173
445	2776	610	4758	710	15516
450	2797	615	4922	712	15844
455	2820	620	5103	714	16167
460	2848	625	5304	716	16471
465	2880	630	5524	718	16775
470	2913	635	5764	720	17080
475	2946	640	6024	722	17389
480	2979	645	6304	724	17697
485	3012	650	6655	726	18007
490	3045	655	7100	728	18317
495	3080	660	7630	730	18626
500	3116	665	8230	740	20050
505	3155	670	8890	750	21430
510	3196	672	9180	760	22700
515	3237	674	9485	770	23940
520	3280	676	9792	780	25030
525	3325	678	10100	790	25940
530	3375			800	26690

Table A-3
Wavelength Calibration of Perkin-Elmer Monochromator,
Model No. 99

Drum Reading	Wavelength λ Å	Drum Reading	Wavelength λ Å	Drum Reading	Wavelength λ Å
1800	2510	790	10420	490	23590
1700	2615	780	10920	480	23920
1600	2755	770	11420	470	24250
1500	2910	760	11920	460	24590
1400	3135	750	12420	450	24920
1300	3395	740	12920	440	25240
1250	3555	730	13420	430	25570
1200	3730	720	13920	420	25880
1150	3980	710	14420	410	26180
1100	4265	700	14920	400	26470
1080	4395	690	15420	390	26750
1060	4530	680	15920	380	27030
1040	4700	670	16420	370	27320
1020	4895	660	16920	360	27610
1000	5100	650	17370	350	27900
980	5315	640	17830	340	28190
960	5585	630	18300	330	28480
940	5860	620	18730	320	28730
920	6210	610	19160	310	28970
900	6680	600	19590	300	29230
890	6930	590	20000	290	29490
880	7200	580	20360	280	29740
870	7485	570	20710	270	30000
860	7780	560	21080	260	30250
850	8090	550	21450	250	30520
840	8410	540	21800	240	30770
830	8770	530	22170	230	30990
820	9150	520	22530	220	31170
810	9550	510	22900		
800	9970	500	23260		

Table A-4
Wavelength Calibration of Perkin-Elmer Monochromator,
Model No. 112-U

Drum Reading	Wavelength $\lambda \text{ \AA}$	Drum Reading	Wavelength $\lambda \text{ \AA}$	Drum Reading	Wavelength $\lambda \text{ \AA}$
1050	2755	750	3755	450	10490
1040	2775	740	3810	440	11130
1030	2795	730	3870	430	11770
1020	2815	720	3935	420	12410
1010	2835	710	4010	410	13050
1000	2860	700	4090	400	13720
990	2885	690	4170	390	14410
980	2910	680	4260	380	15090
970	2935	670	4350	370	15740
960	2960	660	4455	360	16360
950	2985	650	4565	350	16980
940	3010	640	4680	340	17560
930	3035	630	4800	330	18140
920	3060	620	4930	320	18700
910	3085	610	5070	310	19260
900	3115	600	5220	300	19810
890	3145	590	5380	290	20360
880	3180	580	5555	280	20910
870	3215	570	5745	270	21460
860	3250	560	5950	260	22000
850	3285	550	6180	250	22540
840	3325	540	6490	240	23030
830	3365	530	6810	230	23490
820	3410	520	7160	220	23900
810	3455	510	7580	210	24290
800	3500	500	8000	200	24680
790	3545	490	8420	190	25060
780	3595	480	8860	180	25435
770	3645	470	9360	170	25800
760	3700	460	9920	160	26150
				150	26485

LOG SCALE

The log scale is an aid to processing data from recorder charts. Its widest use is in spectral-energy measurements. The conventional method of determining the energy of a spectral line or a narrow band of a continuum is to compare the output signals due to the unknown source with those due to a standard comparison source.

The output is microamps from a photomultiplier, microvolts from a thermocouple, or some similar physical quantity. The magnitude of the output is measured by the deflection of a recording pen on uniformly moving chart paper. The chart paper is usually 10 inches wide and is divided into 100 equal parts.

In most cases of measuring signals from charts, in spectroscopy as elsewhere, one is interested in the ratios of the signals on two charts rather than in their absolute values. Often one has to determine the average value of the signal as given by different charts. These averages are weighted averages, each chart weighted according to its gain setting or amplification factor; therefore, the logarithm of the signal is more convenient for processing the data. Signals of one chart can be brought to the same scale as those of another by adding a constant to the values of log signal. The log of the ratio of two signals is the difference between the logarithm of the signals.

Figure A-3 is a reproduction made on reduced scale from a log scale prepared on transparent film. Several copies of the log scale, made by direct photographic process, have been found to greatly facilitate data processing for spectral irradiance of sources, for standardization of tungsten ribbon lamps, and for similar measurements.

The numbers opposite the thick lines give the logarithm to the base 10 of the signal strength. The base line marked $-\infty$, is placed over the zero or null reading of the recorder chart; this does not necessarily coincide with the zero of the chart paper. One observes that the number opposite the ten-inch or topmost line is 2.00, which is $\log_{10} 100$, and the number opposite the one-inch line is 1.0. Thus

the numbers on the film are $\log s$, where s is measured in units of tenths of an inch.

The log scale was prepared primarily for use with chart paper 10 inches wide. It may be used equally well with chart paper of any smaller width (for example, with Leeds Northrup Co. chart paper No. 742 of 9.5-inch width). The log-scale reading for maximum deflection would be 1.978, which is 0.22 less than 2. The log values of all other signals would also be less than those on a chart of 10-inch maximum deflection by the constant amount 0.022. This constant difference does not affect the final result, since one is interested in the ratios of the signals or the differences of logarithms.

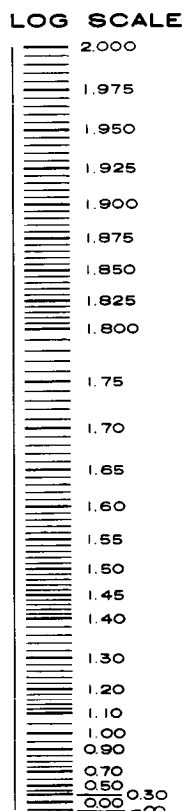


Figure A-3—Log Scale

In order to ensure the maximum possible accuracy in making the log scale, the following procedure was followed: A table of anti-logarithms correct to the fifth decimal place was first prepared. The rulings were made on paper by a ballpoint pen. The positions for the rulings were set by using a large comparator which is usually employed for measuring spectroscopic plates of over 10-inch length. The comparator has a high-precision screw which permits readings accurate to 1/10,000 of an inch. The numbers which are the logarithms of the comparator settings were written at the thicker lines. A photographic negative of the original was made at magnification exactly equal to unity. To ensure an exact copy without distortion, a Robertson copy camera of the kind used for miniaturized printed circuits was used. Positives on extra-thick film were made by contact printing from this negative. These copies of the log scale are now being used by different groups which for routine data processing rely on a large number of recorder charts.

Subsequent Sections describe results of several types of measurements in which the log scale proved to be a factor for time-saving and increased accuracy.

SIGNAL-STRENGTH CALIBRATION

In a photoelectric recording spectrograph, the input which is the radiant energy in a given narrow wavelength band is measured from the output which is the pen deflection of the recorder chart. The input energy may vary by a factor of 10^{10} or more from the weak continuum in the ultraviolet of the standard tungsten lamp to the strong peaks of the mercury-xenon emission lines. The output signal is limited to a maximum of about 10 inches; signals below 1 inch cannot be read with sufficient accuracy. The serious limitation in accuracy imposed by the recorder chart may be readily seen from the log scale, Figure A-3, which shows a 13 percent difference between adjacent rulings for log s equal to 0.5 and a 1.2 percent difference between adjacent rulings for log s above 1.8. It is necessary therefore to adjust the signal-to-energy ratio in order to bring the pen deflection within the narrow range of the recorder chart.

The ratio of signal-to-energy depends mainly on four factors: the f-number of each of the optical components in the spectrograph; the energy losses due to reflection, refraction, and scattering; the wavelength dependent sensitivity of the phototube or thermocouple; and the amplification of the recorder electronic circuitry.

The first two factors are fixed for any given spectrograph. The sensitivity of phototubes and other energy sensors varies with wavelength. The signal-to-energy ratio can be adjusted to a certain extent by choosing the right type of sensor for the range, or by changing the input voltage of the phototube. Two energy sensors most frequently used with the Perkin-Elmer spectrograph are the 1P28 photomultiplier tube and the thermocouple. Response characteristics of these energy sensors are presented in Table A-5. The input energy is from a tungsten-ribbon lamp operated at 30 amp. The spectral-energy

Table A-5
Response Characteristics of Perkin-Elmer Spectrograph
with a 1P28 and Thermocouple Detector.

$\Delta\lambda$ input energy from a 30 amp tungsten ribbon lamp (microwatts per steradian, 100 A, mm² of source); S in inches of chart paper.

Wavelength A	Energy input $\Delta\lambda$	Signal Output	
		1P28	Thermocouple
2800	.25	.2	.02
3115	.3	2.0	.043
3500	5.6	56.0	.065
3800	8.0	200.0	.40
4090	17.0	480.0	.79
5220	111.0	580.0	10.5
6000	231.0	210.0	30.0
7160	465.0	2.8	89.0
8000	621.0	2.0	117.0
13720	745.0	1.7	316.0
19810	371.0	0	372.0
24680	204.0	0	49.0
26480	159.0	0	.63

distribution curve of the lamp has a maximum at wavelength about 11.5 micron, and the spectral irradiance at this wavelength is 817 microwatts per (steradian, 100A bandwidth, 1 mm² of source). The input energy varies by a factor of 4000 over the range of measurement.

The output signal was measured at discrete wavelengths on a series of charts and average values were taken. All signals were reduced to a common scale with the aid of the log scale and of the conversion table described later in this section (Table A-6). The phototube, although apparently a more sensitive detector, is effective over a relatively narrow wavelength range of 3500A. The thermocouple gives a readily measurable signal over the range 8000 to 24,000A. At 19,000A, thermocouple sensitivity is maximum, but the signal-to-energy ratio is only one-sixth of that of the 1P28 tube at its maximum sensitivity range around 5200A.

The value of the output signal varies from a very low value of 0.02" to a maximum of about 600", that is, by a factor of 30,000. The useful range of the recorder chart is between 1" and 10". All signals can be brought within this useful range by choosing a suitable gain factor for the amplifier. It is important to know whether the response is strictly linear within the whole range of the amplifier, and what is the exact value of the signal-to-energy ratio for the different gain factors on the control panel of the amplifier.

Several tests were made on both the Perkin-Elmer and Leiss spectrographs for linearity of response. The data from the Leiss spectrograph showed that the electronic circuitry of the new research radiometer needs further adjustments. The signals from the Perkin-Elmer showed a sufficient degree of reproducibility. The control panel of the

Table A-6
 Perkin-Elmer Spectrograph Conversion Table for Signal Strengths at Varying Values of Gain Factors
 (If m and n are two values of gain factors, $m > n$, and $\log s_m$, $\log s_n$ are the respective logarithms (to the base 10) of the signals for a given input energy, then $\log s_m - \log s_n$ is a constant independent of the wavelength and input energy.

(The values of the constant are given in the following table, e.g., $\log s_2 - \log s_1 = 0.161$, $\log s_{16} - \log s_5 = 2.087$, etc.)

m n	2	3	4	5	6	7	8	9	10	11	12	13	14	15	16	17	18
1	.161	.338	.522	.710	.908	1.101	1.300	1.493	1.681	1.876	2.070	2.257	2.447	2.626	2.796	2.970	3.134
2		.176	.361	.548	.747	.940	1.139	1.332	1.519	1.715	1.908	2.096	2.286	2.465	2.635	2.808	2.972
3			.185	.372	.571	.764	.962	1.156	1.343	1.539	1.732	1.920	2.110	2.289	2.459	2.632	2.796
4				.188	.386	.579	.778	.971	1.158	1.354	1.547	1.735	1.925	2.104	2.274	2.447	2.612
5					.199	.392	.590	.783	.971	1.167	1.360	1.547	1.738	1.917	2.087	2.260	2.424
6						.193	.392	.585	.772	.968	1.161	1.349	1.539	1.718	1.888	2.061	2.226
7							.199	.392	.579	.775	.968	1.156	1.346	1.525	1.695	1.868	2.032
8								.193	.381	.576	.770	.957	1.147	1.326	1.496	1.670	1.834
9									.188	.383	.576	.764	.954	1.133	1.303	1.476	1.641
10										.196	.389	.576	.767	.946	1.116	1.289	1.453
11											.193	.381	.571	.750	.920	1.093	1.258
12												.188	.388	.557	.727	.900	1.064
13													.190	.369	.540	.713	.877
14														.171	.349	.522	.687
15															.170	.343	.508
16																.173	.337
17																	.164

Perkin-Elmer
 Amplifier Model 107
 Serial No. 614
 Part No. 107-0001

Perkin-Elmer amplifier is provided with a step-switch for selecting the gain factor, and the steps are given integral numbers 1 through 18. If m and n are two values of the gain factor, $m > n$, and $\log s_m$, $\log s_n$ are the respective logarithms (to the base 10) of the signal for a given input energy, then $\log s_m - \log s_n$ is a constant. The constant is independent of the wavelength, as is to be expected; it is also independent of the input energy, which shows that the response is linear. This test for linearity was made at different values of input energy and gain setting. Given sufficient time for warmup of the circuit and an adequate signal-to-noise ratio, the linearity of response was within the range of the accuracy of the measurements.

But it was also observed that a one-step increase in gain factor does not increase the signal by the same ratio at all the steps; for a change of gain factor from 1 to 2, the signal increases by 45 percent, whereas for a change from 7 to 8, the increase is by 58 percent. It was found necessary, therefore, to determine experimentally the ratio of the signals for constant input energy and varying settings for the gain factor. The results of these measurements are presented in Table A-6 as a conversion table for signal strengths. All values in the conversion table are logarithms to the base 10. The data for these tables taken at different periods during the Summer Workshop showed a high degree of consistency. Data were reduced using the log scale, by means of which the readings of charts recorded at any gain setting convenient for accurate measurement can readily be converted to a common scale.

SECONDARY TUNGSTEN-RIBBON STANDARD LAMPS

The tungsten-ribbon lamp is frequently employed as a standard of comparison for spectral irradiance. Considerable research has been done in many laboratories on the spectral emissivity of tungsten, and it has been established that the emissivity of tungsten remains fairly constant throughout the life of the tungsten lamp. A major advantage of the tungsten lamp is that it can be operated at a higher temperature than the carbon-filament lamps which long served as radiation standards. The spectral irradiance of the incandescent tungsten ribbon in the visible and ultraviolet is considerably higher than that of the carbon filament.

A special type of the lamp, developed for standardization purposes at the National Bureau of Standards,^{1,2} has a mogul bipost base and a cylindrical bulb. The radiant energy is viewed through a fused quartz window of about 1.25-inch diameter. The window is attached to the bulb by a graded seal, and is at a distance of 3 to 4 inches from the incandescent ribbon. The quartz window transmits a greater percentage of the ultraviolet radiation; as the window is at a greater distance than the rest of the bulb, the metallic deposit on the window due to the aging of the lamp is reduced. The General Electric Company produces this lamp commercially as Type GE 30A/T24/7. The lamps are usually operated at 6 volts, with current 25 amp, 30 amp, or 35 amp.

The spectral irradiance of these lamps may be determined from the observed color-temperature or brightness-temperature of the incandescent ribbon, making use of the published values of the emissivity of tungsten. However, the assumption that all samples of tungsten are identical in emissivity is not sufficiently accurate; the current practice in most laboratories is to have the lamp calibrated at the National Bureau of Standards with reference to one or more other calibrated standard lamps, or to a blackbody at known temperature.

The calibrated standard lamp is a fairly expensive item, considering its limited life-time (about 40 hours) and the cost of calibration. It is therefore advisable to have on hand several other lamps to serve as secondary standards. These may be calibrated with reference to one of the NBS primary standard lamps.

The Summer Workshop performed the calibration of several secondary standards. The results are presented in Table A-7.

Table A-7
Spectral Irradiance of Secondary Tungsten-Ribbon Standard Lamps
Operated at 25 amp and 30 amp in Microwatts per (ster. nm. mm²)

λ nm	SW 190		SW 191		SW 192		SW 188		SW 185		SW 1&2
	25 a	30 a	30 a								
500	1.49	7.11	0.96	4.43	1.16	5.64	2.06	9.83	1.21	7.01	7.62
550	3.19	13.3	1.98	8.65	2.52	10.8	4.20	17.8	2.66	12.7	14.5
600	5.88	21.0	3.66	14.5	4.68	17.3	7.42	28.1	4.89	20.2	23.1
650	8.98	30.1	5.87	21.5	7.46	25.6	11.6	39.6	7.81	28.9	33.3
700	12.8	39.6	8.67	31.5	10.9	33.9	16.4	51.1	11.4	38.0	43.6
750	17.1	49.1	11.9	36.9	14.9	42.3	21.7	62.4	15.6	47.1	53.5
800	21.7	57.4	15.2	44.1	19.0	50.7	26.8	72.3	19.7	54.5	62.1
900	28.7	63.2	21.7	57.3	25.2	60.3	28.9	69.1	29.2	60.3	74.6
1000	33.0	67.1	29.4	65.1	30.2	65.8	32.3	68.7	31.4	67.1	81.1
1100	34.5	69.3	33.1	67.8	34.1	68.6	35.5	70.2	35.2	70.7	82.8
1200	36.2	69.1	35.1	67.7	36.2	74.6	37.2	69.7	36.9	69.1	81.5
1300	36.5	67.0	35.4	66.0	36.5	72.9	37.5	67.6	37.2	67.0	77.8
1400	35.7	63.5	34.6	62.6	35.7	63.5	36.7	65.0	36.4	63.4	73.3
1500	33.9	59.0	32.9	58.1	33.9	58.4	34.3	59.7	34.6	59.0	67.6
1600	31.7	53.5	30.9	52.7	31.7	53.0	32.3	54.1	32.3	54.6	61.0
1700	29.1	47.6	28.4	47.0	29.1	47.1	29.7	48.3	29.7	47.6	54.2
1800	26.1	41.4	25.4	41.0	26.2	41.4	26.9	43.0	26.4	41.9	67.5
1900	23.4	36.1	22.7	35.7	23.4	36.1	24.1	37.8	23.4	36.1	41.4
2000	20.7	31.6	20.3	31.3	21.1	31.6	21.7	33.2	21.1	31.6	35.9
2100	18.5	28.3	17.8	26.8	19.1	28.0	20.0	29.4	18.3	27.7	31.2
2200	16.5	25.1	15.0	24.4	17.2	25.1	18.0	32.4	16.1	23.6	27.6
2300	14.7	22.2	14.4	22.2	14.9	22.2	17.6	27.2	14.0	19.1	24.6
2400	13.2	20.3	12.5	19.4	14.3	20.0	15.3	23.9	12.4	18.9	21.9
2500	11.5	17.7	11.8	18.5	12.1	17.7	13.8	22.9	10.9	17.7	19.6
2600	10.0	15.9	10.5	16.9	11.3	16.2	12.5	21.1	10.2	16.3	

The Perkin-Elmer spectrograph was used for these measurements. Two or more primary standards were available for intercomparison. For each of the primary and secondary standards, the complete spectrum was scanned at least twice. The deflections of the recorder were measured at intervals of ten counts. A computer program was developed to calculate the ratio of the signals s_x , (due to each of the secondary standards) to the signals s_c (due to each of the primary standards). Graphs were drawn for the ratio s_x/s_c for each pair of readings. From these graphs, two or more independent values of the spectral irradiance were obtained at all wavelengths for which NBS tables supplied primary calibration values.

Table A-7 presents the calibration data on seven lamps measured by the Summer Workshop. Five of these (SW 190, SW 191, SW 192, SW 188, and SW 185) were calibrated at current 25 amp and 30 amp. Two other lamps, SW 1 and SW 2, were calibrated at 30 amps only; as both of these have practically the same spectral irradiance, their values are entered in one column.

A coiled coil high-intensity lamp of 2740 candlepower frequently used as a standard of radiation in the A&M Division was also calibrated with reference to a standard tungsten-ribbon lamp. The lamp was placed at a certain distance from the slit of the spectrograph without any intervening optics to focus the image, and the distance of the coil from the slit was accurately measured. The slitwidth was made sufficiently large to give measurable signals throughout the spectral range. The complete spectrum was scanned. Next the spectrum of the standard tungsten-ribbon lamp was scanned, keeping the distance of the ribbon from the slit the same as that of the coil in the previous scan. A small correction factor is necessary because the areas of the coil and of the ribbon are not the same. The correction factor can be determined as follows:

If I_x , I_c are the spectral irradiance due to the coiled lamp and the ribbon lamp at a given wavelength, and s_x , s_c are the corresponding signals,

$$I_c = k_1 s_c$$

and

$$I_x = k_2 s_x, \quad (20)$$

where k_1 and k_2 are constants depending on the response of the spectrograph and the solid angles subtended by the two sources at the slit; k_1 and k_2 are not necessarily equal, but the ratio k_1/k_2 is independent of wavelength.

If the total energy radiated by the lamp is known, the value of I_x can be determined in absolute units.

An independent method of determining the spectral irradiance can be developed from an evaluation of the temperature of the coil:

Table A-8
Spectral Irradiance of the
2740-Candlepower Lamp
(in watts per steradian in direction
normal to the filament per 1000Å)

Wavelength (μ)	Intensity (watts)
.2	
.3	.03
.4	.71
.5	2.43
.6	5.19
.7	7.67
.8	10.35
.9	11.35
1.0	11.09
1.2	10.12
1.4	8.22
1.6	6.38
1.8	4.96
2.0	3.67
2.2	2.92
2.4	2.21
2.6	1.50
2.8	1.14
3.0	.54
3.2	.34
3.4	.17
3.6	.09
3.8	.04
4.0	.01

From equation (20)

$$\log I_c = \log I_c + \log (k_2/k_1) + \log (s_x/s_c) \quad (21)$$

Since k_2/k_1 is unknown, $\log I_x$ can be determined not in absolute units, but in relative units.

From known values of the spectral irradiance of a blackbody, the emissivity of tungsten and the transmission coefficient of the pyrex envelope of the bulb, the spectral irradiance of the coil lamp can be calculated for different temperatures. The values of I_x calculated from the equation,

$$\log I_x = \log I_c + \log (s_x/s_c)$$

will differ by a constant amount for all wavelengths from the calculated values of $\log I_x = \log (N_\lambda \epsilon_n \tau_p)$ for one particular temperature. (N_λ = spectral irradiance of a blackbody; ϵ_n = emissivity of a tungsten coil; τ_p = transmission coefficient of pyrex.) The procedure adopted in these calculations is explained more fully in the Section IV Calibration of Thermopiles.

Thus the temperature is determined, as also the value of k_1/k_2 .

From the known value of temperature, extrapolated values of spectral irradiance are obtained in the wavelength range below 0.4 micron and above 2.4 micron. The results of the calibration are presented in Table A-8. Figure A-4 is a graph of spectral energy distribution based on the data in Table A-8.

SPECTRAL IRRADIANCE OF THE MERCURY-XENON ARC

The spectral irradiance of the mercury-xenon arc was rightly considered as the area of greatest importance among those which Team A of the Summer Workshop selected for its investigations. The Space Environment Simulator now nearing completion in Building 10 of the Goddard Space Flight Center uses a honeycomb array of 127 mercury-xenon lamps, each of 2500-watt input, to produce simulated solar radiation on the test floor.

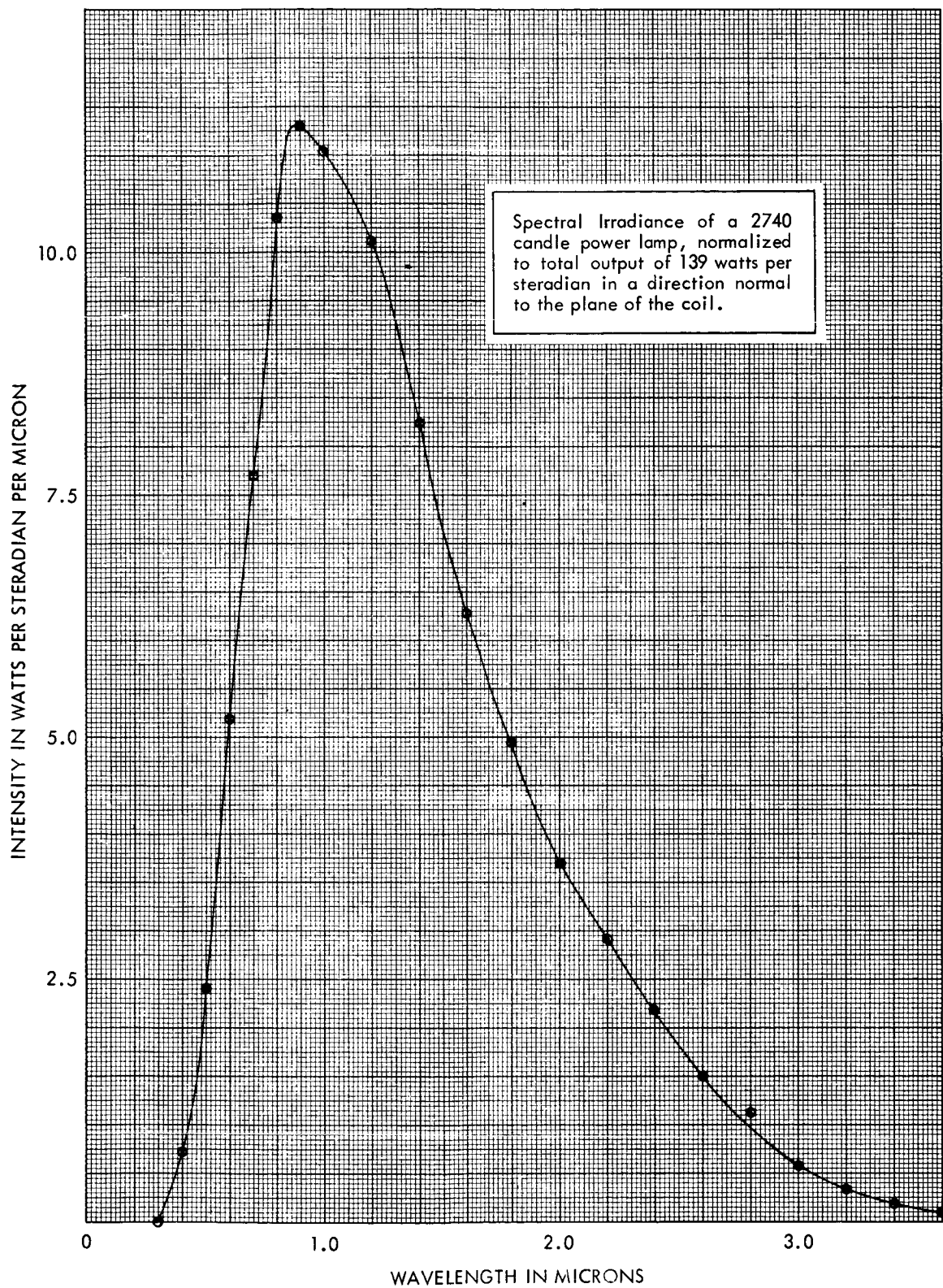


Figure A-4—Spectral Irradiance of a 2740-Candlepower Lamp

The main advantage of the mercury-xenon lamp is that it operates for long periods of time with apparently constant energy output. Intensity can be easily adjusted to any required level by changing the input power. Each lamp is a compact unit and can be replaced without undue delay in case of burnout. The energy-distribution curve, when integrated over sufficiently large wavelength regions, is a satisfactory spectral match for the solar energy of outer space. The efficiency of the lamp, measured by the ratio of the input electric energy to the output radiant energy in the visible and ultraviolet, is relatively high. A high percentage of the radiant energy comes from a well-defined spot near the anode so that a high degree of collimation can be achieved. The arc burns steadily without showing any tendency to wander around the anode.

On the other hand, the lamp has a certain instability characteristic of all high-energy sources. The spectral-energy distribution both of the continuum and of the emission lines is subject to fluctuations caused by the temperature and pressure of the gas mixture. These fluctuations are of importance if the absorption coefficients of the test surfaces are highly wavelength-dependent. Because the discharge takes place in a mixture of two gases, the fluctuations in spectral distribution are more pronounced.

Two kinds of information are required for solar simulation by a high-energy source like the mercury-xenon arc: detailed and accurate information about a "typical" lamp; also, integrated energy profiles over wide wavelength bands for different lamps and varying conditions of operation. A very large percentage of the energy of the mercury-xenon lamp is due to the strong emission lines; most of these are lines due to mercury and a few in the range 0.8 to 1.0 micron are due to xenon. The wavelengths of these lines are fixed to a high degree of precision, but the intensities of these lines depend on the relative population of the upper levels and are subject to change. A high-resolution slow-scanning spectrograph is needed for obtaining detailed information on the spectral irradiance. Once such data have been gathered, more rapid scanning devices can be employed to give the necessary parameters for meaningful solar simulation.

In our investigations of the spectral energy distribution of the mercury-xenon lamp, we have used three high-resolution spectrographs. The earlier studies were made with a Jarrell-Ash grating spectrograph, a 1P28 phototube, a vacuum-tube voltmeter, and a digitizer printout unit. The wavelength range 3600 to 6500A was covered. The principal results concerning the large number of emission lines and the self-reversal of the strong lines were reported earlier.⁹ The more recent studies were made with the Leiss double-prism monochromator and the Perkin-Elmer single-prism double-pass monochromator, described earlier on page A-11.

Three detectors were used, a 1P28 tube for the range 0.3 to 0.7 μ , a lead sulfide tube for the range 0.8 μ to 2.5 μ , and a thermocouple for the whole spectral range but with less sensitivity. In the ultraviolet range 0.25 to 0.35 μ , the Barnes Research radiometer with a lead sulfide detector was found to give measurable signals for all the emission lines. A total of 60 spectrum charts was available for analysis and measurement. The wavelength

dispersion on the charts varied from 50A per inch at 3000A, to 1000A per inch at 25,000A. The charts were taken with varying values of amplification; some of them with the lowest gain showed the high-energy peaks and hardly any continuum, and others with maximum gain brought out the faintest emission lines on a very strong continuum but gave all major emission lines completely off-scale.

For analyzing the data, the pen deflections s were measured on a log scale at each of the flexion points of the charts. The points for measurement were chosen so that, if a graph were drawn joining successive points by straight lines, the area under the graph would be very nearly the same as under the actual curve of the recorder pen. An alternate method of directly measuring the area under the curve by means of a planimeter was attempted, but was abandoned because of the length of time required for sufficiently accurate results. The values of $\log s$ of one chart differed from those of another for the same wavelengths by a constant, provided both charts were made with same operating conditions of the lamp and same setting for the spectrograph. The difference in $\log s$ is equal to the difference in the gain factors of the amplifier in the respective charts. In this way it was possible to reduce to a common scale all charts made under identical operating conditions.

Measurements were similarly made on charts of a standard tungsten-ribbon lamp. From the known spectral irradiance of the standard source and values of $\log s$ reduced to the same common scale as the Hg-Xe charts, an energy-calibration curve of the spectrograph is drawn. This curve is used to convert signal strengths of the Hg-Xe charts to energy in absolute units: namely, microwatts per (steradian, nanometer wavelength range, mm^2 of radiating source).

For purposes of solar simulation, the energy incident on unit area from a given source is of greater interest than the energy radiated from unit area of the source. Independent measurements, as explained later in Section III, have shown that the radiant energy from a 2500-watt Hg-Xe lamp is about 1740 watts. By integrating the spectral-energy distribution curve and measuring the distance of a given surface from the lamp, one can determine the conversion factor needed for calculating the energy incident on the surface in a given wavelength range.

A highly useful way of presenting the data on solar simulation sources is to normalize the spectral-irradiance curve of the source to that of solar energy for zero air mass. Our earlier work in this line was done on a desk calculator. In the later stages of our research, when data from several sources and under varying conditions of operation had been accumulated, we found it more convenient to develop a computer program. Two such programs have been successfully used in our data analysis. A simple version of the program, designed for a Burroughs E101, prints out the following results from a given set of a spectral irradiance data of \mathcal{I} for λ : i, wavelength range $1/2(\lambda_3 - \lambda_1) = \Delta\lambda$; ii, Average energy \mathcal{I} in the wavelength range $\Delta\lambda = 1/8 \mathcal{I}_1 + 3/4 \mathcal{I}_2 + 1/8 \mathcal{I}_3$; iii, Energy $\mathcal{I}\Delta\lambda$ in the range $\Delta\lambda$ at λ_2 ; iv, Integrated total energy in the range 0 to λ_2 ; v, Energy in the range $\Delta\lambda$ as a fraction of the solar constant; vi, Integrated energy up to λ_2 as a fraction of the solar energy.

A more detailed program, designed for an IBM 7094, computes the total area under the spectral-irradiance curve of a given set of points, normalizes the area to the solar constant, and calculates the area under the normalized curve for each small spectral range between data points, as well as for equal wavelength ranges of 50A for visible, 100A for near-infrared and 1000A for distant infrared. The program also gives the integrated fractional energy for these wavelengths, so that it is possible to make a point-by-point comparison with the solar spectrum.

This program is readily adaptable to detailed calculations of energy absorbed by surfaces and of energy transmitted by filters.

The present report contains only a small portion of the results on spectral irradiance of mercury-xenon lamps. More detailed information is available in a series of charts and tables which are too bulky to be given here.

The spectral-irradiance values of mercury-xenon lamps averaged over a large number of lamps and varying operating conditions are given in Table A-9. This might well be called the spectrum of a "typical" Hg-Xe 2500-watt lamp. Intensity values are given at 406 discrete wavelengths. The units for intensity are microwatts per cm², nanometer. These wavelengths, as stated earlier, are the flexion points of the energy-distribution curve. The very small peaks due to the faint emission lines, which number several hundreds, have been omitted because their contribution to the total energy is well below the percentage error of these results. All the major lines, as well as the self-absorption effect at the peaks of the strongest lines, are clearly seen in the table of intensity values.

The intensities have been normalized to one solar constant: that is, a curve drawn taking λ on the x-axis and \mathcal{I}_λ on the y-axis has the same area bounded between the curve and the x-axis as the solar-irradiance curve of air mass zero at earth's mean distance from the sun. The area is 0.1396 watts. In other words, Table A-9 gives the spectral irradiance incident on unit area placed normal to the rays of light at such a distance that the total energy received is 0.1396 watts; this distance is about 31.5 cm for a 2500-watt lamp emitting 1740 watts of radiant energy over a solid angle 4π . It should be noted that the values of \mathcal{I}_λ do not represent the area under curve for a distance of λ equal to 10A, but the ordinate of the curve for the given values of λ ; that is, the area of a rectangular strip of height equal to \mathcal{I}_λ and width equal to 10A.

The data presented in Table A-9 are taken from different sources and do not claim the same accuracy throughout the spectral range. The most accurate and detailed information is in the range 3550 to 6065A, where some 30 charts from the Jarrell-Ash spectrograph and the Leiss monochromator were analyzed. Data of almost equal accuracy were available in the range 6700 to 23,430A, where some 20 charts of the Leiss monochromator with flint-glass prisms and a lead sulfide detector were analyzed. For the intermediate range, only 5 charts taken with the Leiss quartz prism PbS combination and with the Perkin-Elmer quartz prism thermocouple combination were available. This range, however, produces hardly any emission lines and the continuum is of nearly uniform intensity.

Table A-9

Spectral Irradiance of the Mercury-Xenon Arc
 (Wavelength λ in angstroms; Intensity \mathcal{I} in microwatts per (cm², nanometer),
 Normalized to one solar constant)

λ	\mathcal{I}																
1900	0	3385	107	3747	87	4080	425	4960	85	6065	31	8952	162	12560	39	18130	28
2000	2	3400	32	3753	138	4082	122	4970	34	6182	71	8975	72	12623	43	18200	23
2100	5	3420	32	3755	87	4085	81	4980	23	6200	46	9010	58	12700	38	18310	19
2200	10	3429	42	3760	66	4088	64	5020	20	6400	47	9035	91	13100	36	18350	20
2300	15	3450	33	3767	58	4100	51	5030	20	6500	37	9045	208	13240	40	18550	18
2400	21	3460	33	3769	81	4110	55	5035	22	6550	37	9070	77	13400	40	18670	17
2500	25	3400	38	3773	58	4128	43	5045	25	6595	73	9100	61	13440	50	18820	20
2600	26	3520	21	3780	56	4160	36	5064	25	6615	36	9130	74	13520	46	18930	20
2700	27	3540	53	3782	63	4230	31	5146	20	6700	60	9162	93	13570	91	19000	18
2752	16	3542	107	3789	193	4268	40	5202	23	6716	268	9190	75	13620	60	19590	22
2754	1	3543	256	3795	61	4280	50	5310	22	6748	64	9274	75	13673	134	19700	28
2780	2	3545	91	3800	53	4305	72	5376	28	6885	79	9374	79	13780	36	19750	23
2790	45	3547	70	3806	60	4313	52	5386	31	6907	129	9420	58	13830	25	19850	21
2800	29	3552	87	3810	52	4320	79	5395	49	6970	75	9560	67	13890	36	20050	20
2803	40	3555	89	3812	56	4327	144	5406	39	7040	72	9620	61	13950	75	20150	21
2810	8	3559	186	3819	122	4345	315	5424	43	7086	98	9799	154	14020	36	20250	20
2840	2	3560	107	3822	56	4356	587	5427	69	7136	74	9863	66	14070	49	20850	20
2848	12	3568	91	3830	46	4358	361	5439	131	7215	74	9923	147	14660	36	20900	20
2880	2	3570	102	3842	45	4360	705	5455	560	7346	79	9984	64	14700	29	21000	19
2894	23	3585	131	3850	51	4372	330	5461	445	7400	66	10050	105	14732	34	21300	18
2900	5	3597	162	3858	79	4382	158	5468	674	7560	67	10139	477	14780	30	21600	23
2925	49	3607	255	3863	70	4406	91	5475	388	7620	67	10230	98	14830	29	22410	20
2940	7	3613	345	3870	50	4418	70	5479	173	7642	83	10310	70	15040	29	22499	23
2967	138	3622	523	3878	50	4435	73	5500	69	7660	63	10430	60	15170	29	22590	23
2970	31	3630	867	3893	55	4500	36	5570	43	7730	63	10550	61	15295	99	23110	22
2975	44	3640	855	3900	55	4505	141	5604	43	8190	56	10640	55	15420	29	23160	30
3000	11	3650	1043	3908	77	4545	28	5670	35	8205	56	10800	55	15540	28	23253	43
3021	77	3653	1019	3930	52	4580	29	5706	43	8231	345	10838	64	15930	28	23340	28
3023	69	3655	658	3940	43	4613	24	5725	61	8260	107	10890	59	16060	28	23430	18
3026	89	3657	274	3948	38	4660	25	5750	141	8280	151	10990	61	16120	28	24000	15
3050	18	3658	573	3950	75	4671	32	5761	239	8310	61	11030	59	16370	28	25000	13
3060	20	3659	510	3953	37	4675	28	5770	548	8346	102	11060	64	16620	28	26000	12
3090	8	3665	722	4000	37	4720	28	5771	573	8366	60	11100	61	16740	36	27000	10
3126	342	3667	848	4012	40	4726	30	5780	510	8409	72	11190	75	16850	59	28000	9
3128	107	3669	810	4020	59	4730	27	5791	609	8430	58	11287	466	16930	79	29000	8
3131	320	3673	560	4022	55	4792	25	5805	397	8569	70	11340	55	17010	64	30000	7
3200	18	3675	523	4030	81	4800	28	5814	288	8800	70	11400	53	17090	83	31000	6
3210	19	3676	739	4037	109	4812	28	5845	87	8819	466	11550	58	17190	58	32000	5
3220	16	3678	560	4040	239	4853	24	5859	56	8840	117	11700	59	17330	36	33000	4
3260	17	3683	388	4042	499	4895	26	5872	77	8850	87	11742	113	17370	31	34000	4
3300	18	3695	308	4046	353	4903	25	5893	59	8880	102	11940	100	17440	32	35000	3
3310	35	3700	262	4054	315	4916	98	5898	52	8908	147	12050	95	17560	28	36000	3
3320	31	3708	151	4062	102	4927	29	5966	36	8915	91	12090	120	17920	26	37000	2
3341	13	3720	115	4071	181	4940	28	6038	27	8930	64	12177	311	18020	25	38000	1
3375	36	3740	87	4075	122	4955	30	6050	40	8940	77	12460	42	18070	25	39000	1
																40000	0

In the ultraviolet range 2700 to 3500A, 5 charts of the Hg-Xe spectrum were made with the Leiss quartz prism PbS combination, but the tungsten standard did not give measurable signals. The intensity calibration was made with reference to earlier work of other investigators on mercury-xenon lamps.^{13, 14} In the distant infrared range beyond 23,430A which contains 7 percent of the total energy, the values were obtained from calculations based on the assumption of a Planckian distribution; this assumption is apparently valid, because the solar-energy curve in this range is also based on a similar assumption and lacks experimental confirmation. The range below 2700A which contains about 0.7 percent of the energy is also an estimate based on the Planckian distribution.

The internal consistency of the experimental data on which Table A-9 is based is such that we might claim an accuracy of 5 percent, the same as that of the NBS calibration tables of the standard lamp. However, it should be emphasized that the table refers to a "typical" lamp; variations as high as 30 percent have been observed in individual lamps in small ranges under extreme conditions of under-cooling or over-cooling.

The results of Table A-9 are presented graphically in Figure A-5. The data points of Table A-9 were plotted on a large sheet of graph paper, and the points were joined by a smooth curve in freehand drawing. The accuracy of the graph is therefore less than that of the table, and the finer details of the spectrum charts have been omitted. As the wavelength scale on the x-axis is highly condensed, the emission lines in the graph have a greater half-width than they actually have on the spectrum charts. The condensed wavelength scale also masks the strong self-reversal effect at the peaks of the emission lines in the visible range of the spectrum.¹⁵

The graph does however show a progressive increase of half-width in the longer wavelength range. From theoretical considerations, it can readily be shown that the half-width of the line is mostly due to quadratic Stark effect. Thus, a line of 15A half-width at 5000A corresponds to a width of the energy level of 60 cm^{-1} . A line from the same level has a half-width 9 times greater at 15,000A, and 16 times greater at 20,000A. This effect is seen clearly in the spectrum charts and to a certain extent also in the graph.

Figure A-5 also shows the spectral-energy distribution of the carbon arc, discussed in the next section, and of solar radiation of zero air mass based on Johnson's data.¹

SPECTRAL IRRADIANCE OF THE CARBON ARC

Techniques essentially similar to those described in the previous section were employed to measure the spectral irradiance of different carbon-arc sources. Measurements on only two of the carbon arcs are discussed in this report; detailed information on the other arcs investigated is available in a series of charts and tables.

Light from the positive crater of the arc is reflected by a concave mirror and is refracted by two planoconvex quartz lenses. The emergent beam spreads into a cone of

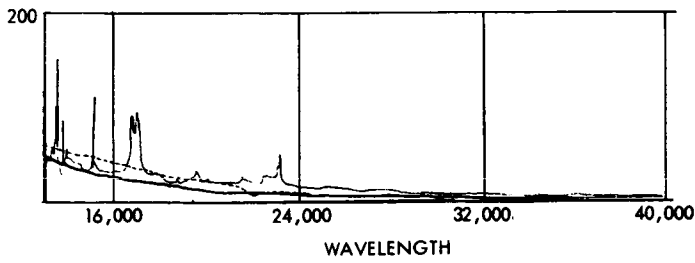
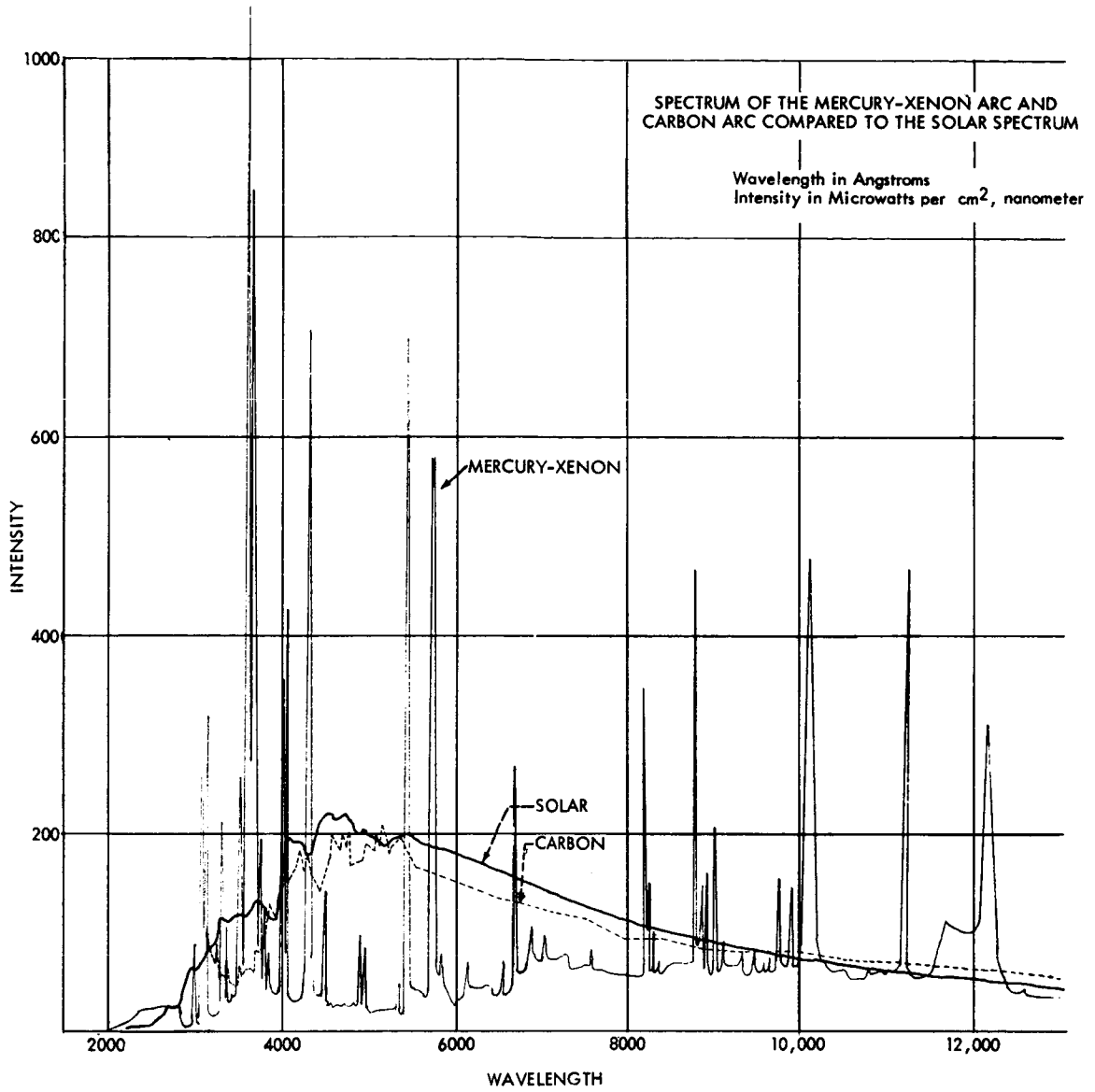


Figure A-5—Spectrum of the Mercury-Xenon Arc and Carbon Arc Compared to the Solar Spectrum

about 10 degrees half-angle. A small part of the beam is focused by a biconvex quartz lens on the slit of the spectrograph. The f-number of the lens is such that the beam of light falling on the first concave mirror of the spectrograph does not fully cover the mirror. Thus the scattered light within the spectrograph is reduced to a minimum.

The Perkin-Elmer quartz-prism double-pass monochromator was used for most of the charts of the carbon arc. All measurements of energy were made from these charts. For detailed study of the highly complex line structure in the visible region of the spectrum, a few charts were made using the high-dispersion Jarrell-Ash grating spectrograph.

The carbon-arc spectrum has in the range 3500 to 7000A many times more emission lines than the mercury-xenon arc. All lines have a finite half-width. The lines are so close together that, even with a high-dispersion instrument, only the peaks of the lines are distinguishable. Figure A-6 gives a typical portion of the chart made with the Jarrell-Ash spectrograph. As many as 400 lines may readily be counted in this 1000A range from 4000 to 5000A. The wavelength scale is linear. The intensity values on the y-axis were taken from Perkin-Elmer charts made in the same region on a similar but different carbon arc; these values are an approximation.

Beyond 5800A there are hardly any emission lines, and the spectrum chart is similar to that of a tungsten-ribbon lamp.

For measurement of energy, the charts were divided into short wavelength ranges, each corresponding to ten counts of the drum which controls the Littrow mirror. In each range a sloping line was drawn to indicate the average pen deflection of the range. Signal strengths were measured at the middle of these lines. The signal strengths of different charts and different gain factors were reduced to a common scale, using the conversion table for signal strengths previously noted (Table A-6).

For the other steps in data-reduction, energy calibration of the spectrograph, normalization to the solar constant, and integration of energy in wavelength ranges of 50, 100, 1000A, the procedure described for the Hg-Xe arc was followed.

The final results of two series of carbon-arc measurements are given in Table A-10. Wavelength is in angstroms. The intensity is in units of microwatts per angstrom range incident per cm^2 placed at such distance from the arc that the total energy received by the surface is 0.1396 watts.

Two columns of energy values are given in Table A-10 following the wavelength column. The first column refers to a new type of carbon rod, Lorraine Orlux, which only recently became commercially available. It is claimed that this type of rod gives relatively more energy in the visible and ultraviolet; our measurements show that the claim is justified to a certain extent. However, more reliable data in the range below 3100A are needed. The second column refers to the National Orotip cored carbon rods which are widely used in solar simulators.

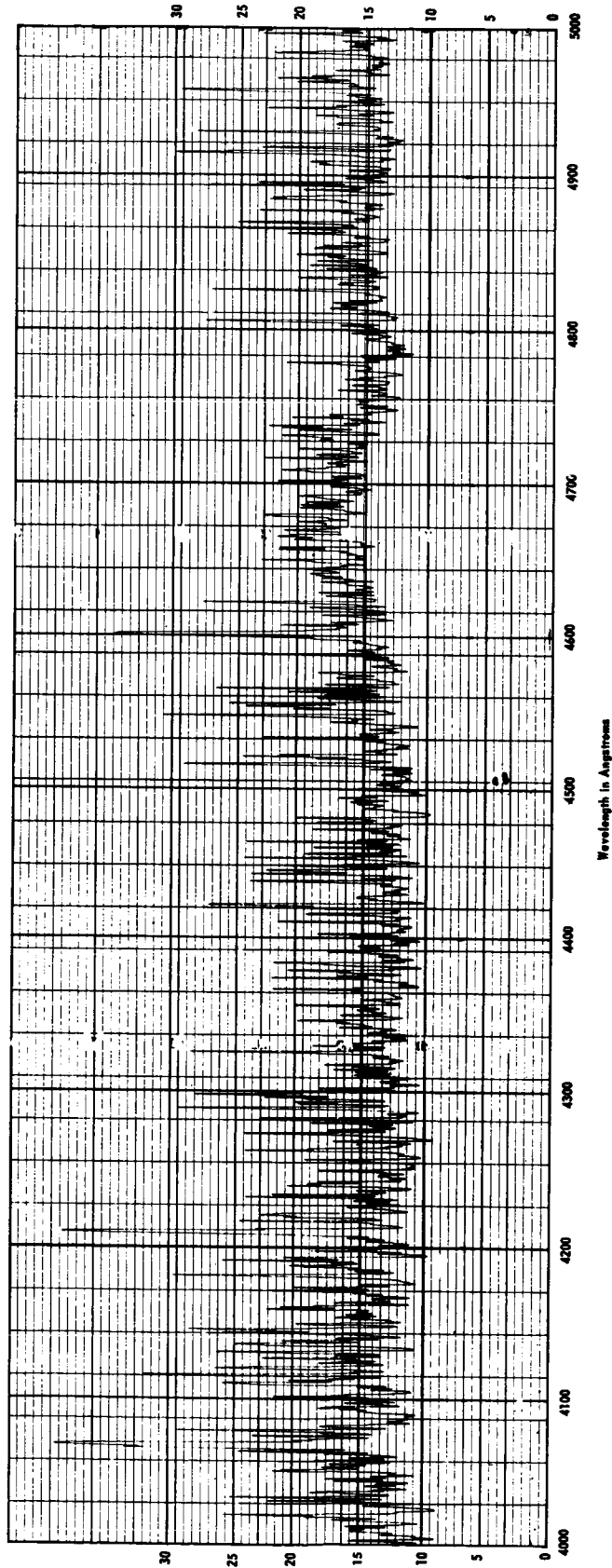


Figure A-6--Spectrum of the Carbon Arc: National Orotip Cored Carbon Rods (Range 4000 A to 5000 A)

Table A-10
Spectral Irradiance of the Carbon Arc (in microwatts/cm² Ångstrom,
normalized to one solar constant)

I_0 = Lorraine Orlux Carbon rods,
 I_n = National Orotip cored Carbon rods

λ	I_0	I_n	λ	I_0	I_n	λ	I_0	I_n
3145	10.0	5.50	4455	14.1	13.5	12410	6.03	6.03
3180	8.13	8.32	4565	17.4	17.0	13050	5.37	5.37
3215	7.59	8.51	4680	18.2	17.4	14410	4.47	4.37
3250	6.76	7.59	4800	16.6	15.9	15090	4.37	4.27
3285	5.50	6.03	4930	17.4	16.2	15740	3.89	3.72
3325	5.75	5.75	5070	18.2	17.0	16360	3.47	3.31
3365	5.50	5.37	5220	19.1	17.8	16980	3.24	3.09
3410	5.01	4.68	5380	19.5	18.6	17560	2.95	2.88
3455	4.68	4.68	5555	16.6	16.6	18140	2.46	2.51
3500	4.79	4.90	5745	15.9	15.5	18700	2.24	2.24
3545	5.50	6.61	6180	14.5	14.8	19260	2.14	2.14
3595	6.17	6.46	6490	13.5	14.5	19810	2.04	2.09
3645	6.31	6.17	6810	12.9	13.8	20360	1.82	1.82
3700	8.13	8.71	7160	12.0	12.9	20910	1.62	1.70
3755	7.94	9.12	7580	11.2	11.5	21460	1.38	1.45
3810	9.12	12.0	8000	9.33	10.7	22000	.550	.724
3870	12.9	12.9	8420	9.33	9.55	23030	.912	.309
3935	11.5	10.9	8860	8.32	8.91	23490	.794	1.00
4010	13.2	12.3	9360	7.94	8.91	23900	.794	1.00
4090	15.1	14.8	9920	7.94	7.94	24290	.646	.813
4170	16.6	16.6	10490	7.24	7.59	24680	.501	.589
4260	16.2	15.1	11130	7.08	7.24			
4350	15.9	14.8	11770	6.46	6.76			

The spectral irradiance of the Lorraine Orlux carbon rods is also shown graphically in Figure A-5, where the intensity values of the graph give energy per 10Å range, in order to conform to the units used for the mercury-xenon spectrum and the solar spectrum.

III. THE FILTER-DIFFERENTIAL METHOD FOR SOLAR-SIMULATION SOURCES

N64-28204

MEASUREMENT TECHNIQUES

The data analyzed in Section II show that neither the Hg-Xe arc nor the carbon arc is a perfect spectral match for solar radiation outside the atmosphere. Considering the energy distribution in very narrow bands of 10 to 50Å, the mismatch of the Hg-Xe arc is greater. Both spectra have a very large number of emission lines superposed on the continuum, but in the case of the Hg-Xe arc the lines are fewer and considerably stronger; this is readily apparent in Figures A-5 and A-6.

In solar simulation, the question of major importance is not the detailed structure of the spectrum but the energy absorbed by the test surface. Because the absorption coefficient of most materials changes but slowly with wavelength, a spectral match over wide wavelength ranges is adequate for solar simulation. However, it is necessary to monitor properly the spectral-energy distribution during a solar-simulation test. The monitoring system should be reliable, accurate, and rapid enough to give the spectral-energy distribution of the source before it has time to change significantly.

Team A of the Summer Workshop developed a new method for rapid scanning of the spectrum, by transmitting the total spectrum through a color glass filter or a dielectric film filter and measuring the energy by means of a total energy sensor (such as a thermopile). If $\mathcal{J}_\lambda d\lambda$ is the energy due to a source in a wavelength range $d\lambda$ at λ , τ_λ is the transmission coefficient of a given filter in the same range, \mathcal{J}_τ the total energy transmitted by the filter, and \mathcal{J}_0 the total energy incident on the filter,

$$\mathcal{J}_0 = \int_0^\infty \mathcal{J}_\lambda d\lambda, \quad \text{and} \quad \mathcal{J}_\tau = \int_0^\infty \mathcal{J}_\lambda \tau_\lambda d\lambda. \quad (22)$$

The experimental data are the integrals \mathcal{J}_0 with no filter and \mathcal{J}_τ with several filters. From these data we try to obtain the differential, or more precisely the value of the differential, averaged over relatively small wavelength ranges, and the method may therefore properly be called the "Filter-Differential Method."

The method may be illustrated by considering two ideal cases: (i), a narrow band-pass filter which has a transmission coefficient τ , a constant in the range λ_1 to λ_2 and is opaque below λ_1 , and above λ_2 ; (ii) a cutoff filter which is opaque below a wavelength λ and transparent above λ . In the first case,

$$\int_{\lambda_1}^{\lambda_2} \mathcal{J}_\lambda d\lambda = \frac{1}{\tau} \mathcal{J}_\tau \quad (23)$$

In the second case, if \mathcal{D}_{τ_1} , \mathcal{D}_{τ_2} are the energy transmitted by two filters which have cut-off limits at λ_1 and λ_2 respectively, $\lambda_2 > \lambda_1$,

$$\mathcal{D}_{\tau_1} = \int_{\lambda_1}^{\infty} \mathcal{D}_{\lambda} d\lambda; \quad \mathcal{D}_{\tau_2} = \int_{\lambda_2}^{\infty} \mathcal{D}_{\lambda} d\lambda;$$

and hence

$$\int_{\lambda_1}^{\lambda_2} \mathcal{D}_{\lambda} d\lambda = \mathcal{D}_{\tau_1} - \mathcal{D}_{\tau_2}. \tag{24}$$

Unfortunately no such filters exist. The transmission coefficient of filters is not a step function but changes slowly with wavelength. It requires a careful numerical analysis and several filters with overlapping ranges to obtain \mathcal{D}_{λ} as a function of λ . If the detailed characteristics of the spectral-energy distribution and the positions of the emission lines for a "typical" Hg-Xe arc or carbon arc are known, then, knowing the integrated energy profiles, $\int_{\lambda_1}^{\lambda_2} \mathcal{D}_{\lambda} d\lambda$, over different ranges in a particular case, we can readily determine the energy absorbed by the test surface.

Assume that integrated energy profiles are required over n discrete wavelength ranges, λ_0 to λ_1 , λ_1 to λ_2 , λ_{n-1} to λ_n . Let there be n filters, cutoff and wide-bandpass, whose average transmission coefficients are known over these wavelength ranges. Let τ_{ij} represent the transmission coefficient of filter i in the j^{th} range, \mathcal{D}_{τ_i} energy transmitted by the i^{th} filter, \mathcal{D}_{0j} energy incident on the filter in the j^{th} range.

The total energy incident on a filter is the sum of the energy incident in each of the n ranges.

$$\sum_{j=1}^n \mathcal{D}_{0j} = \int_0^{\infty} \mathcal{D}_{\lambda} d\lambda = \mathcal{D}_0 \tag{25}$$

The energy transmitted by the i^{th} filter is

$$\sum_{j=1}^n \tau_{ij} \mathcal{D}_{0j} = \mathcal{D}_{\tau_i} \tag{26}$$

There are n linear simultaneous equations of the form (26), with n unknowns, namely \mathcal{D}_{0j} . The equations can be solved by the matrix-inversion method using a computer, and \mathcal{D}_{0j} can be determined.

The accuracy of the final results depends on the accuracy with which the transmission coefficients of the filters and the energy transmitted by each filter can be determined. By

using more than one set of filters, the degree of accuracy can be improved. On the other hand, absorption characteristics of certain thermopile surfaces are not entirely independent of wavelength, and this introduces another set of coefficients, in the array of equations (26).

The ease and rapidity with which solar-simulation data can be monitored is the main advantage of the filter-differential method.

In a preliminary experiment for checking the method, measurements were made with a carbon arc as source, an Eppley thermopile as detector, and three Corning glass filters for transmitting selected wide bands. After waiting for the carbon arc to start controlling automatically, about 5 minutes after striking the arc, periodic measurements were made of the emf output of the thermopile, with and without the filters. Five sets of readings were taken with each filter. These values showed an average deviation of about 1 percent. The three filters were (i) 7-54 which transmits the range .23 to .42 μ and also partially in the range .66 to 2.75 μ ; (ii) 4-97 which transmits in the range .33 to .72 μ and also partially in the range 1.0 to 3.0 μ ; and (iii) 2-64, which is a cutoff filter transmitting in the range beyond 0.64 μ .

The transmission coefficient, $\mathcal{D}_T/\mathcal{D}_0$, of these three filters, averaged from 5 sets of values, was seen to be .168, .301, and .563, respectively.

A method of numerical integration was applied to determine the values of $\mathcal{D}_T/\mathcal{D}_0$ for incident solar energy of zero air mass. \mathcal{D}_T was evaluated from the manufacturer's data on the transmission coefficients of the filters and the known spectral irradiance values of the Johnson curve.¹ The respective values for the three filters were found to be .171, .314, and .457.

It appears that, for the visible and near-infrared, the fractional energy transmitted by the filter is less for the carbon arc than for solar radiation; for the distant infrared, the fractional energy transmitted for the carbon arc is greater. This result is substantially in agreement with our Perkin-Elmer measurements on the carbon arc. As is seen from Figure A-5, the carbon-arc spectrum is relatively stronger in the range beyond 9500A.

TRANSMISSION COEFFICIENT OF FILTERS

Filters currently used in spectroscopic work may be divided into three categories: Cutoff filters which transmit the spectrum beyond a certain wavelength; bandpass filters which transmit partially in one or more bands; and neutral-density filters.

A large variety of cutoff filters is commercially available from Corning Glass Co. The cutoff point varies between 2200A and 8000A, and at the cutoff point the transmission coefficient decreases slowly from a maximum of 85 or 95 percent and drops to zero at some wavelength 500 or 1000 A on the shorter wavelength side. In the infrared range beyond 2 microns, the filters have characteristic transmission curves.

Bandpass filters of Corning Glass, made of single glass plates, transmit over fairly large bands of 0.1 to 1.0 micron, and the transmission coefficients are strongly dependent on wavelength. Combinations of more than one bandpass filter are used to transmit over narrow bands of 200 to 500A. The transmission curves of these filters have an approximately Gaussian profile, and the peak transmission is about 10 percent.

We made a series of measurements to check the manufacturer's data on these filters. The results are available in the form of tables and charts which are too lengthy to be included in this report. Although our measurements on single glass-plate filters are in substantial agreement with manufacturers' data, the narrow-bandpass filters made of combinations of glass plates do not give consistent readings for transmission coefficients; the peak transmission seems to vary considerably, though the peak occurs at practically the same wavelength.

A special set of 12 filters mounted on a wheel has recently been supplied by Eppley Laboratories for monitoring the energy of the mercury-xenon lamp. The filters are of the narrow-bandpass type, but transmit a higher percentage of energy and have a steeper cutoff on both sides than the Corning Glass narrow-bandpass filters. They are also made of combinations of color glass plates mounted together. The measurements on these filters showed a certain degree of inconsistency both in the percentage transmission and in the wavelength at which maximum transmission occurs. This would seem to be a temperature effect. When high-energy radiation falls on the filters, the differential expansion of the glass and the filter mount changes the contact pressure between the components; this apparently causes changes in the transmission at the interfaces. Photochemical effects on the coloring agents in the glass may also occur, but these are probably of less significance.

Two complete sets of measurements were made on the transmission coefficients of the filters of the Eppley filter wheel. Total intensity (no filter) and transmitted intensity (with filter) were measured at close wavelength intervals. The source was a tungsten lamp in one set of measurements and a mercury-xenon arc in the other. A Perkin-Elmer spectrograph was used to select narrow spectral bands. The average of the results is given in Figure A-7. The experimental data on filter #1 are of very poor accuracy. The scatter of the points for most of the other curves was such that more elaborate measurements seem advisable.

Narrow bandpass filters depending on an entirely different principle are the dielectric film filters manufactured by Optics Technology, Inc. The transmission curves are approximately Gaussian, and peak transmission is about 30 percent. The main advantage of these filters is that they are totally opaque to all radiation outside that from a very narrow band. Several sets of measurements were made with the Leiss monochromator and a Beckman DK 2 to test the suitability of these filters for monitoring spectral irradiance. The degree of instability seems to be greater than in the case of the Eppley filters. Transmission curves from the manufacturers, those obtained with the Leiss, and those with the DK 2, all three differed from each other by as much as 50 percent, and

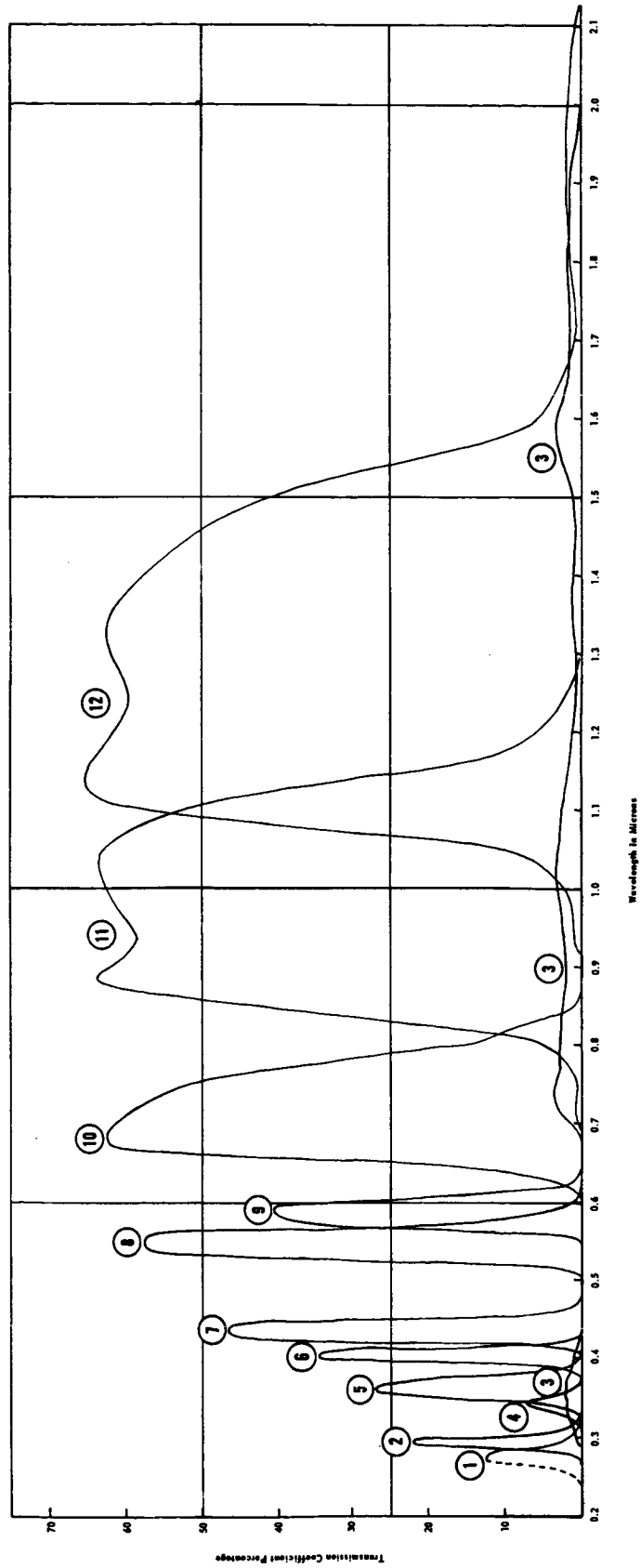


Figure A-7—Transmission Coefficient of Color Glass Filters, Eppley Filter Wheel

peak transmission wavelength showed a tendency to drift. It appears that this is a temperature effect and that the filters are not intended to be used with high-energy sources.

The neutral-density filters might well be thought of as a solution to this problem; if a filter can be found with a transmission coefficient strictly independent of wavelength, the spectral irradiance from any high-energy source can be reduced to a required lower level by using one or more of such filters.

Wire-gauze filters have long been used in optical spectroscopy as neutral density filters. The wire-gauze filter is a closely knit wire mesh placed far enough from the spectrograph slit to avoid all diffraction effects. Aluminum wire mesh is considered preferable to wire mesh of other metals like copper, brass, or steel, because the latter have selective color absorption or can change in transmission characteristics after aging or oxidation. Measurements were made with several wire-gauze filters which show that they are not truly neutral. A typical filter, No. 4, has an almost constant transmission coefficient of 19.2 percent in the visible range, but in the near-infrared between 0.6 and 0.9 μ , the percentage transmission is highly erratic, rising to 20.5 percent and falling to 18 percent. Beyond 0.9 μ up to 2.5 μ , the coefficient of transmission decreases gradually to a value of 15 percent at 2.5 μ .

A more satisfactory commercially available filter is the so-called "neutral-density filter," made of a thin aluminum film deposited on glass. The transmission coefficient is practically constant over a wide spectral range from 0.4 to 2.0 microns, except for a small dip at about 0.9 μ caused by the absorption of aluminum. The manufacturer's rating of the filter (which gives $\log_{10} (\mathcal{I}_0/\mathcal{I}_\tau)$, where \mathcal{I}_0 is the incident energy and \mathcal{I}_τ the transmitted energy) is only approximately true; there are significant aging effects, and in each case the transmission coefficient should be experimentally determined. One of the filters rated at 0.5, which corresponds to 31.6 percent transmission, was found to have a transmission coefficient varying between 30 and 32 percent in the range 0.4 to 2.0 μ . Below 0.4 μ , the transmission coefficient dropped rapidly, becoming zero at 0.3 μ . Beyond 2 μ , the value decreased slowly to a minimum of 22 percent at 2.47 μ , then rose to 27 percent at 2.65 μ . Beyond 2.65 μ , the absorption of glass becomes predominant.

Of the different neutral-density filters examined, the most satisfactory seems to be a quartz plate. The quartz window of a thermopile, for example, has a transmission coefficient between 92.8 and 93.5 percent in the range .3 to 2.5 μ . Beyond 2.5 μ the value decreases rapidly.

A general conclusion from these measurements is that the transmission coefficient of any filter is dependent on several factors, should be determined by an independent experiment, and should be rechecked periodically.

SPECTRUM MEASUREMENTS OF THE MERCURY-XENON ARC WITH AND WITHOUT MODULE AND OF THE CARBON ARC

Some preliminary measurements were made with color glass filters and a thermopile to compare the spectral energy distribution of a mercury-xenon arc without any intervening optical components; of the same arc with the collimating module of the Solar Environment Simulator; and of the carbon arc with its condensing optical components.

It has often been stated that in the ultraviolet the carbon-arc spectrum is weaker and that the Hg-Xe spectrum is stronger than the solar spectrum. An excess of energy can be removed by the use of suitable filters, but there is no ready means of making up a deficiency. It has also been stated that the optical components of the solar-simulator collimation module, consisting of three reflecting surfaces and four lenses, has the effect of removing the excess ultraviolet in the Hg-Xe spectrum and thus providing a closer spectral match to the sun. This is considered one of the strong arguments in favor of the Hg-Xe arc.

That the ultraviolet is considerably stronger in the Hg-Xe arc than in the carbon arc is well established experimentally. This is due to the very strong lines of mercury in the ultraviolet (those at 2536, 2653, 3131, and 3650A), and the total lack of such lines in carbon or in any of the rare earths currently employed to enrich the carbon-arc spectrum. Other factors which control the relative spectral irradiance (such as operating conditions of the arcs, the rare earth content of the carbon rods, or the pressure of the Hg-Xe lamp) have an influence much smaller than that of the strong emission lines of mercury. In low-pressure mercury discharge, the resonance line at 2536A emits 8900 microwatts of energy per steradian per mm^2 of source, which is 100 times greater than that of any of the other lines in mercury.¹⁶ In the high-pressure discharge this line is mostly self-absorbed and enhances the intensity of the other lines and the continuum.

The effect of the collimating module on the Hg-Xe spectrum needed to be studied experimentally. The completed module has recently been set up with due safety precautions above a darkroom facility, so that these measurements are now feasible. From the known values of the reflection coefficient of the mirrors and the transmission coefficient of the filters, the change in spectral irradiance can be calculated. The reliability of these values is, however, limited, since in the ultraviolet and far infrared where the spectral mismatch with the solar irradiance is most pronounced, the optical properties of the lenses and mirrors cannot be specified with sufficient accuracy.

The problem presents several difficulties if one attempts the conventional spectroscopic techniques of energy measurement described in section II. At the two extremes of the spectrum in the UV and IR, the ratio of signal to energy is very small, and further in the UV the energy of the standard tungsten-ribbon lamp decreases to the vanishing point. The Hg-Xe arc in the module gives a collimated beam, whereas the carbon arc with its built-in optics and the bare Hg-Xe arc give beams of unequal divergence. The additional optical parts needed to focus the light on the spectrograph slit is different in the three

cases, so that elaborate and rather uncertain correction factors are involved in determining the energy input from the signal output.

For these reasons, the filter-differential method was employed. A sensitive thermopile (Eppley thermopile No. 4702, calibrated according to the procedure discussed in Section IV) was used as the energy sensor. The emf of the thermopile was measured correct to one microvolt using a Rubicon potentiometer. The thermopile was mounted with its sensitive surface upwards. The light from the module was made to fall on the thermopile. The emf was measured without any filter and with each of 14 different Corning glass filters placed above the thermopile. Zero reading was taken with a piece of wood replacing the filter. Measurements were made four successive times. Similar sets of measurements were repeated using the bare Hg-Xe arc and the carbon arc. The light from the carbon arc is viewed after reflection from a parabolic mirror and refraction through two planoconvex quartz lenses. The light from the Hg-Xe arc is viewed directly through the spherical quartz envelope of the lamp. In these two instances, as the beam of light is horizontal, a mirror aluminized on the front surface received the light at a 45-degree angle to reflect it to the thermopile. The Hg-Xe lamp was a Westinghouse type SAHX-2500B lamp, and the same lamp was used with and without the module. The carbon arc was a strong electric arcomatic lamp, type 75 000-1, with national carbon rods.

As a preliminary check on the reliability of the method, measurements were made using an NBS-calibrated standard tungsten lamp as source. The values of emf showed an average deviation of one percent. A further check was the emf of the thermopile at a distance of 41 inches from the Hg-Xe arc and without any collimating optics. The emf corresponded to an irradiance of 12.91 milliwatts/cm². Earlier measurements had shown that the total energy output of the Hg-Xe arc operated at 2500 watts is 1740 watts. Assuming a uniform distribution of energy over a solid angle 4π , the energy at a distance of 41 inches should be 12.77 mw/cm², which is sufficiently close to 12.92 mw/cm² given by the thermopile.

The data were reduced by a method of successive numerical approximation. It is believed that a more accurate method using a computer will yield results rather close to those given below. The computer method was discussed earlier in Section III. It makes due allowance for the slope in the transmission curve of each filter. In the present calculations, the slopes are replaced by vertical lines and each transmission curve is assumed to be a step-function of the form:

$$\begin{aligned} \tau_{\lambda} &= 0 \quad \text{for} \quad \lambda_1 < \lambda < \lambda_2, \quad \text{and} \\ \tau_{\lambda} &= \tau, \text{ a constant for } \lambda_2 < \lambda < \lambda_1. \end{aligned} \tag{27}$$

Further, four of the filters, 9-54, 9-30, 0-53 and 0-54 were taken together and assumed to be wide-bandpass filters for the range 2810 to 32,750Å; three others, 0-52, 0-51 and

3-75 were similarly taken together as medium-bandpass filters, for the range 3860 to 29,000A. Finally the filter 2-64 was taken as transmitting in the range 6700 to 26,200A. Thus the filters divide the spectrum into seven wide ranges. These are the ranges of interest in solar simulation, since the absorption and reflection characteristics of most materials show wide differences when the incident energy passes from one of these ranges to another. The rest of the filters were narrow-bandpass filters, and data from them were not reduced. More elaborate computational techniques would be needed for these.

Table A-11 gives the fractional absorbed energy, $(1 - \mathcal{I}_\tau / \mathcal{I}_0)$, for the different filters and sources. \mathcal{I}_τ is the energy transmitted by the filter and \mathcal{I}_0 is the energy incident. The last column gives the fractional energy of the solar spectrum outside the range of the respective filters. These values are taken from the Johnson data. Table A-11 also gives the averages for the four wide-bandpass filters and the three medium-bandpass filters. The values of fractional energy absorbed by each of the seven filters, compared to the transmission curves of these filters and known spectral distribution of the sources, show a high degree of internal consistency. We conclude, therefore, that the averages in rows 5 and 9 are meaningful. Further data reduction is based on these averages and the values for filter 2-64. In particular, we observe that the average fractional energy absorbed by the four wide-bandpass filters, from the carbon arc and the Hg-Xe arc in the module, is 0.073 and 0.071. The corresponding value for the bare Hg-Xe arc is 0.194. We assume that the carbon arc and the Hg-Xe arc in the module emit no energy outside the range 2810 to 32,750A, and that the 7.2-percent absorption (average of .071 and .073) is all in the wide-bandpass range. In the "clear transmission" range, all filters absorb 7.2 percent, which is also confirmed by manufacturer's data on the filters.

Comparing the last column for the solar spectrum with the three earlier columns shows the degree of spectral mismatch for the three sources in each bandpass range. If the three sources were a perfect spectral match to the sun, the value in each row for the

Table A-11
Fractional Energy Absorbed by Filters

Filter No.	Wavelength Range Micron	Carbon Arc	Hg-Xe Arc without Module	Hg-Xe Arc with Module	Solar Spectrum
9-54	0.24 to 3.25	.068	.149	.043	.017
9-30	0.26 to 3.50	.052	.172	.055	.018
0-53	0.307 to 3.00	.078	.217	.092	.036
0-57	0.317 to 3.35	.095	.239	.095	.035
Average	0.281 to 3.275	.073	.194	.071	.021
0-52	0.360 to 2.9	.127	.304	.170	.077
0-51	0.389 to 2.8	.184	.408	.272	.105
3-75	0.410 to 3.0	.208	.414	.288	.123
Average	0.386 to 2.9	.173	.375	.243	.099
2-64	0.670 to 2.620	.478	.615	.535	.486

three sources would have been greater than the value for the solar spectrum in the same row by a constant amount 0.072.

If E is the fractional energy of the Hg-Xe without module outside the range 2810 to 32,750A, $E + 0.072 (1 - E)$ is the energy absorbed by the wide bandpass filters from the Hg- Xe without module; this value is experimentally seen to be 0.194. Thus $E + 0.072 (1 - E) = 0.194$, and $E = 0.132$. The same method can be used to find the energy outside the range 3860 to 29,000A, and that outside the range 6700 to 26,200A for each of the three sources. Each value thus obtained is the sim of two quantities, the energy in the short wavelength range and that in the long wavelength range. The relative apportionment to the two ranges is made from known spectral irradiance curves and module transmission curves.

The results of data reduction are presented in Table A-12. The first column gives the seven major wavelength ranges; the next three columns give the energy in these ranges from the three sources, in units of watts per meter². All values have been normalized to the solar constant, 1396 watts per m², so that the sum of the values in each of the three columns is 1396. The fifth column gives the solar energy in the same wavelength ranges. The next three columns give the average energy in the respective ranges in units of watts per meter² per micron. This is obtained by dividing the total energy in a given range by the width of the range in microns. For purposes of comparison, the average energy of the solar spectrum in each of the ranges is given in the last column.

A convenient graphical way of presenting these results is a histogram. Histograms of the spectrum of the Hg-Xe arc without the module, Hg-Xe arc with the module, and the carbon arc are given in Figures A-8, A-9 and A-10 respectively. The y coordinates of the histograms are the values in columns 7, 8 and 6 respectively of Table A-12. In a histogram a continuous curve of intensity versus wavelength is replaced by a step function which gives the average energy in watts per m², micron in the seven wavelength bands. The Johnson curve is superimposed on the histograms.

Table A-12
Energy Distribution in Wavelength Ranges for the Carbon Arc and Hg-Xe Arc
(Normalized to One Solar Constant)

Wavelength Range Microns	Energy in the Range in Watts per Meter ²				Energy in the Range in Watts per Meter ² , Micron			
	Carbon	Hg-Xe	Hg-Xe Module	Solar Spectrum	Carbon	Hg-Xe	Hg-Xe Module	Solar Spectrum
0 to 0.281	0	128	0	7.0	0	456	0	25
0.281 to 0.386	103	235	211	102	984	2234	2007	970
0.386 to 0.670	405	311	380	530	1425	1096	1337	1868
0.670 to 2.620	785	579	699	716	402	297	359	367
2.620 to 2.900	54	49	60	9.8	194	175	215	35
2.900 to 3.275	49	38	46	9.8	130	101	123	27
3.275 to 5.000	0	56	0	21	0	32	0	12.5

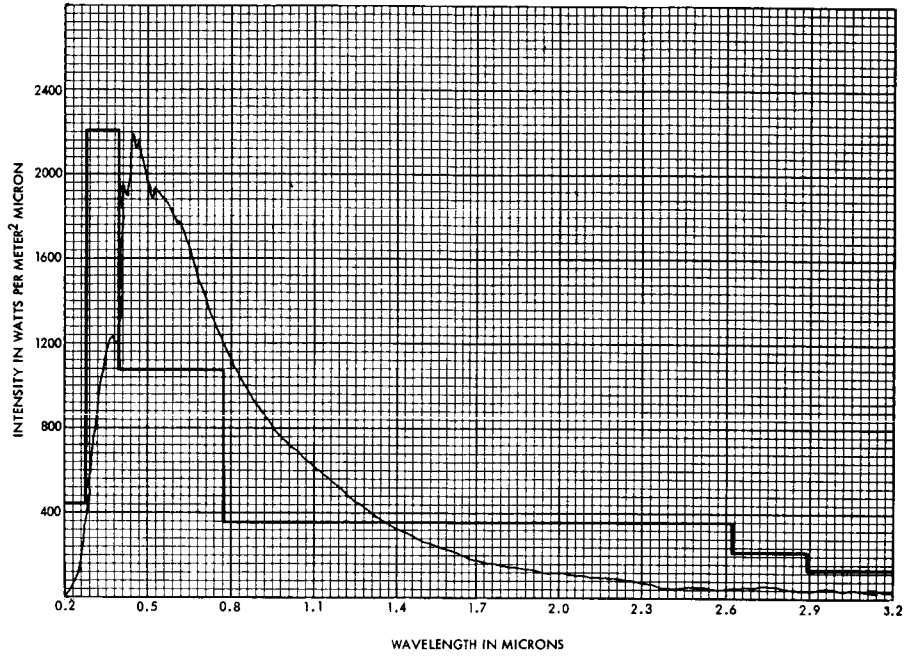


Figure A-8—Mercury-Xenon Arc Spectrum:
Histogram of Spectral Irradiance

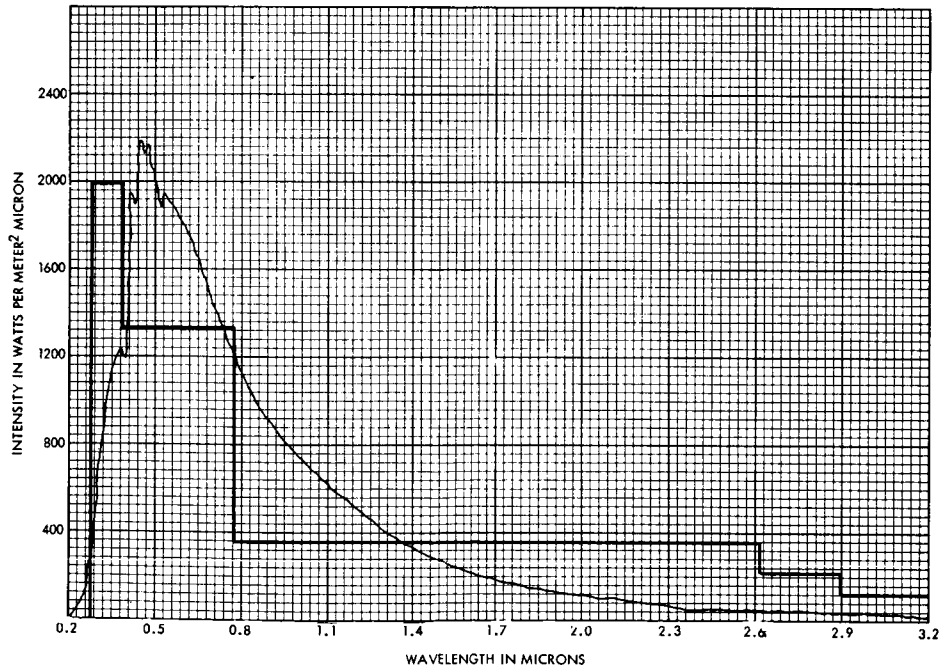


Figure A-9—Mercury-Xenon Arc Spectrum from the Collimation Module:
Histogram of Spectral Irradiance

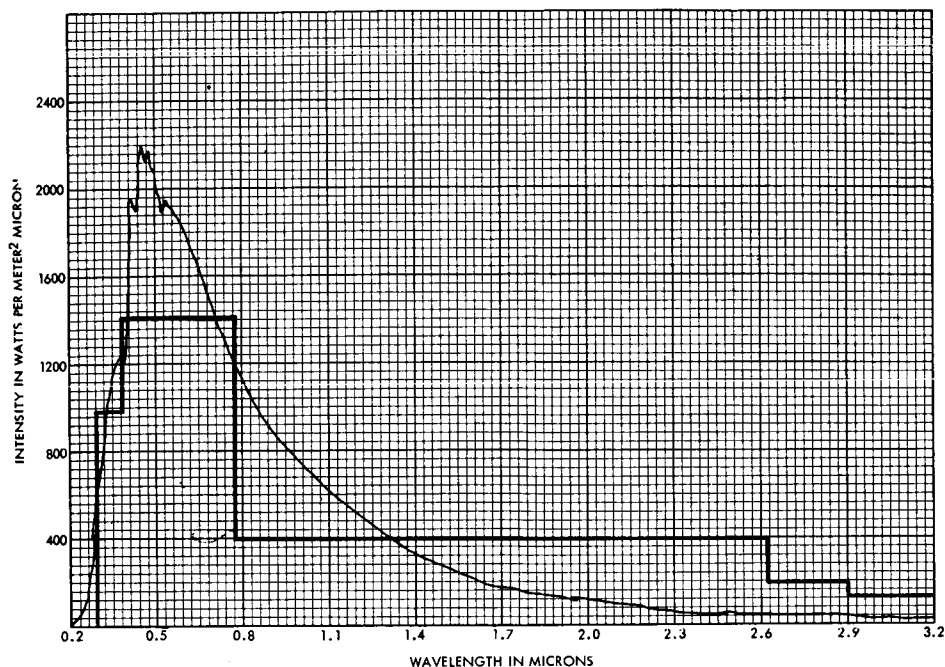


Figure A-10—Carbon Arc Spectrum:
Histogram of Spectral Irradiance

It is believed that available experimental data are capable of yielding more complete information if improved analytical tools are applied. Also, confirmation of these results by more precise and conventional spectroscopic methods is desirable. However, certain interesting conclusions may be drawn from these results: In the range 0.281 to 0.386μ the energy of the bare Hg-Xe arc is 2.3 times the solar energy, as apparent from columns 3 and 5 of Table A-12. The module brings the ratio down to 2.1. The carbon arc is a closer spectral match in this range. This is because the probability of atomic transitions is high in this range, whereas the blackbody radiation function decreases rapidly. In the visible range 0.386 to 0.670μ where the 6000μ blackbody has maximum energy, the energy of all three sources is less than that of the sun. However, if the visible and UV components are added, the Hg-Xe arc is a closer spectral match to the sun than the carbon arc. In the range 0.281 to 0.670μ , the solar energy is 670 watts/m^2 , whereas the energy of the carbon arc is 508 watts/m^2 and that of the Hg-Xe arc in the module is 591 watts/m^2 . In the near IR, the Hg-Xe arc in the module is a close spectral match; in the far IR, all three simulator sources are 4 to 6 times stronger than the sun. This is obviously due to the fact that in this range all four spectral irradiance curves are Planckian, and the temperature of the simulator sources is half that of the sun. However, the total energy in this range is small.

The main conclusions to be drawn from these studies seem to be that both the carbon arc and the Hg-Xe arc in the module are suitable for solar simulation, and that reasons for preferring one or the other in any given test cannot be based on considerations of spectral match to solar radiation. Lack of spectral match in all three cases requires that the spectral distribution be monitored during the test.

IV. CALIBRATION OF THERMOPILES

N64-28205

Determination of the total amount of energy incident on a surface is of great importance in space physics. Those engaged in the field of solar simulation are interested in knowing the energy incident on the test floor. Experiments on thermal balance of spacecraft cannot be successfully performed unless the experimenter knows to a high degree of accuracy the energy which falls on unit area of test surface. Total energy is of importance in the determination of absorption coefficients and emissivity of surfaces of space vehicles, calibration of solar cells, experiments on materials degradation due to radiation, etc.

An instrument frequently used for monitoring total energy is the Eppley thermopile. Its advantages are claimed to be a high degree of sensitivity, linearity of response over a wide range, facility in mode of operation, and stability of calibration. To a first approximation the response of the thermopile is independent of the spectral characteristics of the incident energy. However, calibration tables often provided with the instrument cover an energy range which is smaller by a factor of 10,000 than that used in solar simulation. It is frequently assumed that the response of the instrument is linear, no matter how wide the range over which it may be used.

The Summer Workshop decided to attempt an independent calibration of the thermopile in energy ranges needed for solar simulation.

THE EMF OF THE THERMOPILE

The Eppley thermopile used in the current investigations is of the circular type. The elements are silver and bismuth. There are eight junctions giving a total of 11.9 ohm resistance. The coating is lampblack. A thin quartz window of 1 mm covers the exposed surface. The calibration supplied by the manufacturers was made for ambient temperature of 24°C, relative humidity 21 percent. In the calibration table the variation in the emf output is from about 5 to 10 microvolts; in the measurements which we performed the range in emf was from 100 microvolts to 17,500 microvolts. It is important, therefore, to determine the relation between emf and temperature over these wide ranges.

The silver-bismuth thermocouple is not commonly used and a table of emf of the thermocouple as a function of temperature is not found in standard books of reference. The Handbook of the American Institute of Physics contains tables of the emf of important thermocouple materials with respect to platinum.¹⁷ The values obtained from these tables were compared by adding together the emf's of copper and constantan with the values given in standard tables (for example, in the "Handbook of Chemistry and Physics") for a

copper-constantan thermocouple. The calculated values and those given in standard tables were in close agreement. A similar comparison made in the case of the iron-constantan couple also showed that the agreement is sufficiently close to justify our using the tables in the A.I.P. Handbook for silver and bismuth.

For a silver-bismuth thermocouple, the emf (obtained by adding the emf of both elements) is 8.08 millivolts for 100°C and 15.34 millivolts for 200°C. The linearity of response is not as good as might be wished. When the reference junction is at 0°C and the other junction is at -100°C, the emf is 7.93 millivolts, a value which is sufficiently close to 8.08 millivolts for +100°C. The corresponding values for 8 pairs of junctions are 63.44 for -100°C and 64.6 for +100°C. This is the range in which our thermocouple has been used, and we have decided that no correction is needed for variations in ambient temperature.

On the other hand, a correction is needed if the temperature of the cold junction increases because of incident radiation. For a highly intense source which gives an emf of 42 millivolts, the temperature of the cold junction and of the case increases by as much as 4°C. In accurate determination of radiant energy, either a correction must be made for this increase in the temperature of the case, or a water-cooling arrangement must be employed to ensure a constant temperature for the case and the reference junction.

THE INTENSITY OF THE STANDARD SOURCE

In any calibration process it is of the utmost importance to have a radiation source whose output is accurately known. The conventional procedure employed in many laboratories is to use an incandescent carbon standard lamp supplied by the National Bureau of Standards. For our purposes this source has the disadvantage that it is operated at a fairly low temperature, with the maximum energy in the far infrared and the total energy output rather small. We need a more intense source whose maximum output lies closer to the visible range, because the thermopile is to be used for sources which simulate the solar radiation.

The best approximation seems to be the tungsten-ribbon lamps calibrated by the National Bureau of Standards for spectral energy distribution.^{1,2} The advantages of these lamps were discussed earlier in Section II. These lamps operate at temperatures between 2000°K and 2600°K. A fairly simple calculation shows that a standard lamp operated at 30 amps emits energy which, when received on a surface between 10 and 15 cm away from the ribbon, is equal to one solar constant. The lamp thus serves as a very convenient source for calibration.

Two different lamps were available: lamp E.U. #235 operated at 35 amperes, and lamp #185 operated at either 30 amperes or 25 amperes, giving three calibrated sources. For all three sources, tables of spectral irradiance are available at close wavelength ranges between 0.25 micron and 2.6 microns. We are interested in knowing the total energy radiated by these lamps per steradian per mm² of the source from the extreme

ultraviolet to the distant infrared. The extrapolation for the two ends of the spectrum can be made with a fairly high degree of accuracy.

Values of the energy radiated by a blackbody are available in a recent publication by Pivovonsky and Nagel.¹⁸ These values of E_λ , when multiplied by ϵ_w , the emissivity of tungsten, and τ_q , the transmission coefficient of the quartz window, should give the radiation emitted by the standard lamp. Tables were prepared for the computed values of $E_\lambda \epsilon_w \tau_q$, the spectral irradiance at close wavelength ranges, for the following temperatures: 1800, 2000, 2200, 2400, and 2600°K. When these values are compared with the values of spectral irradiance given by the calibration tables of the National Bureau of Standards, it appears possible to assign a temperature value to the tungsten ribbon. This is obviously the temperature at which the tungsten ribbon of the calibrated lamp operates. The close agreement at all wavelengths between the calibration tables of the NBS and of the calculated values of $E_\lambda \epsilon_w \tau_q$, for the assumed temperature is a confirmation of the validity of the method.

Values given in the NBS tables are in units of microwatts per (steradian, nanometer, mm² of source). Assuming the curve of spectral irradiance versus temperature to be a straight line over short wavelength ranges of 0.1 micron, (0.2 micron in the infrared), it is possible to calculate the total energy radiated from 1 mm² of the source per unit solid angle throughout the spectral range. The values are .0670, .1202, and .1908 watts respectively for lamp #185 at 25 amp., #185 at 30 amp., and lamp #235 at 35 amp.

There is obviously an element of uncertainty in these values. On the other hand, the values represent three different sources, each of which can be viewed either from the side of the quartz window or from the opposite side through the pyrex envelope of the bulb.

EXPERIMENTAL PROCEDURE

For the measurement of emf, the Eppley thermopile was mounted on a movable stand on an optic bench. At one end of the optic bench was mounted the tungsten ribbon lamp with the center of the ribbon at the same level as the center of the thermopile. The thermopile was placed at different distances, varying between 12 cm and 100 cm; in each position the distance was read accurately by a scale and vernier. Before taking each reading, an opaque screen was placed in front of the thermopile in order to find the zero reading. For each source, two sets of readings were taken, first with the distance increasing and next with the distance decreasing. The emf was read on a precision voltmeter reading correct to microvolts.

It was observed that the quartz window of the lamp protrudes some distance in front of the ribbon and is carried by a neck whose diameter is less than the height of the ribbon. When the radiation is viewed through the quartz window, a small fraction of the radiation is scattered in different directions by the neck; this introduces an error in the measurement. In order to correct for this error, measurements were first made with

the quartz window facing the thermopile. Later the lamp was rotated through 180° , and measurements were made through the pyrex envelope of the lamp.

The calibration tables supplied with the lamps give the spectral irradiance as viewed through the quartz window. For measurements made through the pyrex envelope, a correction factor is necessary because of the difference in the transmission coefficients of quartz and pyrex, especially in the ultraviolet and infrared.

The values of spectral irradiance, as stated earlier, are given in units of microwatts per (mm^2 of source, nanometer of spectral range, unit solid angle). It is important to check the agreement in units between the calibration tables of the NBS and the tables of black-body radiation functions given by Pivovonsky and Nagel.¹⁸ Take, for example, the value at 2200°K for a blackbody which, according to Pivovonsky and Nagel, amounts to 2.097×10^5 watts per (cm^2 of source, cm bandwidth, unit solid angle) at 1.4 micron. This is equal to 2.097×10^2 microwatts per (mm^2 of source, nanometer bandwidth, unit solid angle). The tungsten ribbon at 1.4 micron at 2200°K has emissivity 0.31,¹⁹ and the quartz window transmits 0.97 of the incident energy. Hence the spectral irradiance for a tungsten ribbon at 2200°K at 1.4 micron should be 60.4 microwatts per (mm^2 of source, nanometer, unit solid angle). The value given by the NBS calibration table for lamp #185 operated at 30 amp. is 75.1 microwatts per (mm^2 of source, nanometer, unit solid angle). This checks the agreement in units and permits computation of the value of the temperature of the filament.

The thermopile views the radiation from the whole filament. The width and the height of the filament were measured using a cathetometer. For calculating the area when the lamp is actually in operation, a correction must be made for the thermal expansion of the ribbon because the original measurements were made at room temperature.

Multiplying the spectral irradiance per mm^2 by the area (in mm^2) of the incandescent ribbon, produces the total irradiance from the ribbon. If the thermopile is at a distance very large compared to the dimensions of the ribbon, the inverse square law will be strictly verified. For small values of the distance between the ribbon and the thermopile, a correction has to be made for the oblique angle of the line-of-sight. Consider a length dx on the ribbon at distance x from the center: The projection of dx normal to the line-of-sight is $dx \cos \theta$, where θ is the inclination of the line-of-sight to the horizontal. If A is the area of the thermopile, the projection of that area normal to the line-of-sight is $A \cos \theta$. Let \mathcal{J}_0 be the energy received from unit length at the center of the ribbon. The energy received from element dx at distance x is $\mathcal{J}_0 dx \cos^2 \theta$ which $= \mathcal{J}_0 dx s^2 / (s^2 + x^2)$, where s is the distance between the filament and the thermopile. Integrating this expression over a half-length of the filament, we find the energy received from the half-length to be $\mathcal{J}_0 s \tan^{-1}(L/2s)$, where L is the length of the filament. The correction factor, though small, is not negligible; it decreases the equivalent length of the filament from 50.4 mm at large distances (namely, beyond 30 cm) to 49.56 mm at 12 cm distance.

Another correction factor involved in these measurements is the radiation from the envelope of the lamp. As the height of the lamp is large compared to the height of the ribbon, this part of the radiation is more sensitive to the distance of the thermopile. The radiation from the envelope is mostly in the extreme infrared and is easily absorbed by the atmosphere. When the measurements are taken with a 1-mm quartz window in front of the thermopile, this part of the radiation has considerably less effect. The error can be minimized by placing a screen with a tall slit in front of the lamp, but care should be taken lest the screen become heated and introduce a secondary source of radiation.

RESULTS

The spectral irradiance of the tungsten ribbon lamps is given in Table A-13. In the range 0.3 to 2.6 microns, the values for the three sources (#185 at 25 amp., #185 at 30 amp. and E.U. 235 at 35 amp.) under the subheading "quartz" are from the NBS calibration tables and give the spectral irradiance as viewed through the quartz window. The entries in the spectral ranges below .3 micron and above 2.6 micron are computed values of $E_{\lambda} \epsilon_w \tau_q$, based on the temperature of the ribbon. The spectral irradiance as viewed through the pyrex envelope is obtained by multiplying the value in the first column by τ_p / τ_q (where τ_p is the transmission coefficient of the pyrex envelope of the lamp). The last column gives the values for two secondary standard lamps, SW1 and SW2, whose spectral irradiance was determined by comparing them with lamp #185 operated at 30 amp. The area of the ribbon in mm^2 and the total irradiance in watts/steradian are given in the two final entries of each column. The data on the three Standard Sources are presented as a graph of \mathfrak{J} versus λ in Figure A-11.

The method of calibration was first tested on the air-cooled thermopile #4702 operated with and without a quartz window. The results of the measurements are shown in Figure A-12 as a graph of $\log v - \log I$ versus $\log I$. I is the intensity in watts per cm^2 incident on the surface of the thermopile. It is obtained from the area under the spectral irradiance curves of the standard lamps, that is, from the entries of the last row of Table A-13. The energy emitted per steradian in a direction normal to the plane of the ribbon, divided by the square of the distance from the thermopile, gives the intensity per cm^2 . If the thermoelectric emf v is strictly proportional to the incident energy I , the ratio v/I should be a constant, and hence $(\log v - \log I)$ should be independent of $\log I$. The results of measurement from the three sources are indicated in the figure. The upper and lower sets of points are respectively for the thermopile without and with the quartz window. The points lie on a smooth curve which slopes downwards for large values of intensity. This is as might be expected, since for high radiation level at the hot junctions, some of the heat is dissipated through conduction and re-radiation; hence, the sensitivity of the thermopile, v/I , decreases.

It is of particular interest that all the data points lie close to each other. The short vertical line on the lower curve shows the relative scatter of the points for a 5-percent variation of the ratio v/I . Most of the data points show a percentage variation well below

Table A-13
Spectral Irradiance of Tungsten-Ribbon Lamps
Microwatts per (steradian, nanometer, mm² of source)

λ (Microns)	E 185 (25 A)		E 185 (30 A)		EU 235 (35A)		SW 1 & 2
	Quartz	Pyrex	Quartz	Pyrex	Quartz	Pyrex	Quartz
0.2	9.8×10^{-8}		4.5×10^{-6}		7.1×10^{-5}		3.6×10^{-6}
0.3	.0025	9.3×10^{-4}	.029	1.1×10^{-2}	.226	8.4×10^{-2}	3.1×10^{-2}
0.4	0.9	0.9	1.12	1.1	5.15	5.0	1.1
0.5	1.97	1.9	8.81	8.6	25.7	25.1	7.6
0.6	7.19	7.0	25.4	24.8	62.0	60.5	23.1
0.7	15.7	15.4	46.9	45.8	102	99.8	43.6
0.8	25.5	24.9	65.9	64.4	132	129	62.1
0.9	33.7	33.0	78.6	76.7	145	141	74.6
1.0	39.7	38.2	84.7	82.7	147	143	81.1
1.2	45.0	43.9	84.2	82.0	132	129	81.5
1.4	42.9	41.9	75.1	73.5	111	108	73.3
1.6	37.5	36.6	62.0	60.5	87.7	80.5	61.0
1.8	30.4	29.7	48.0	46.9	66.6	65.0	47.5
2.0	24.0	23.4	36.2	35.2	49.3	48.2	35.9
2.2	18.9	18.9	27.8	27.0	38.1	37.2	27.6
2.4	15.1	14.8	22.1	21.6	30.1	29.4	21.9
2.6	12.1	11.8	17.7	17.3	24.0	23.4	17.5
2.8	7.9	7.7	11.2	10.9	15.0	14.6	11.2
3.0	7.5	4.7	10.3	6.5	14.0	8.8	10.3
3.2	6.1	3.0	8.5	4.2	11.2	6.3	8.4
3.4	4.8	1.8	6.8	2.5	8.8	3.2	6.8
3.6	3.9	0.8	5.4	1.1	7.1	1.5	5.4
3.8	2.4	0.1	3.3	0.4	4.3	0.6	3.3
4.0	1.8		2.5		3.2		2.5
4.2	1.3		1.8		2.3		1.8
4.4	0.9		1.2		1.5		1.2
4.6	0.5		0.7		0.9		0.8
Watts mm ² ster.	.0670	.0619	.1202	.1125	.1908	.1798	.1170
Area mm ²	152.97	152.97	153.47	153.47	152.74	152.74	45.08
Watts/ ster.	10.25	9.47	18.45	17.26	29.14	27.46	5.27

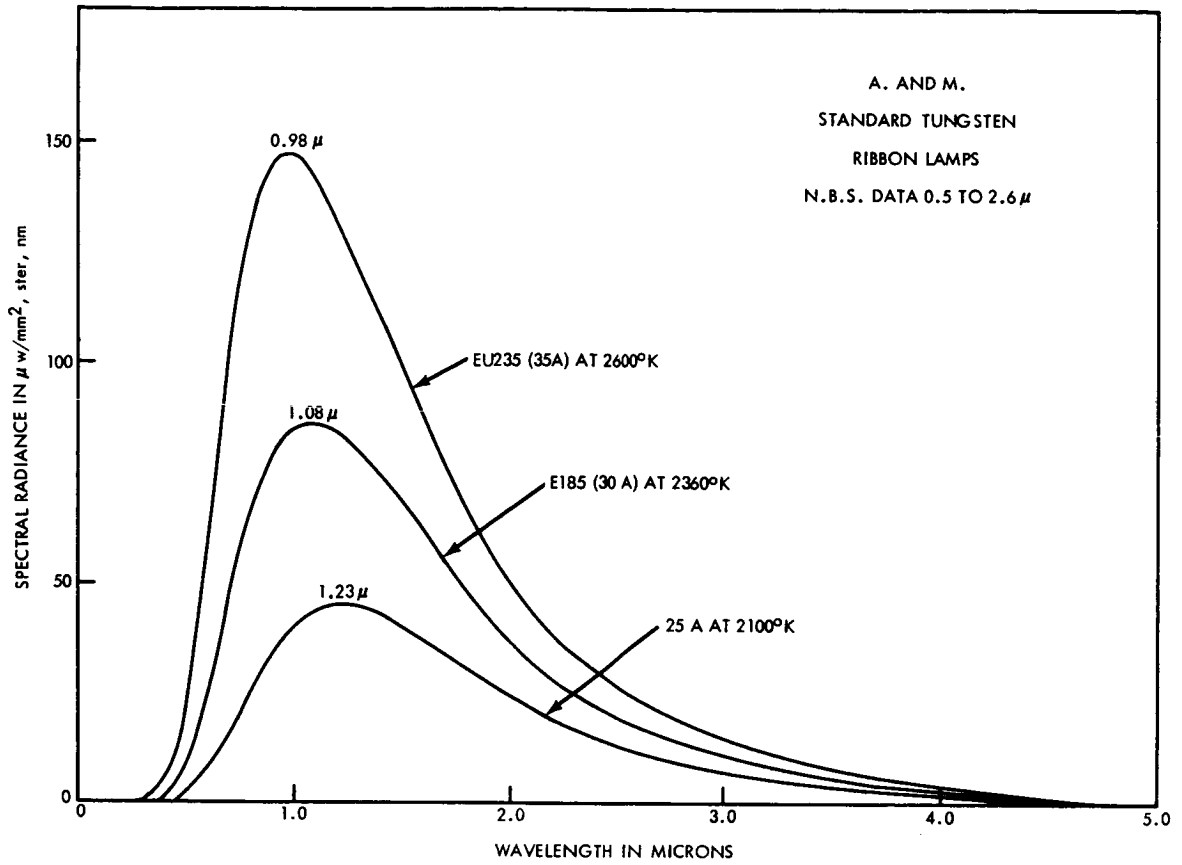


Figure A-11-A&M Standard Tungsten-Ribbon Lamps

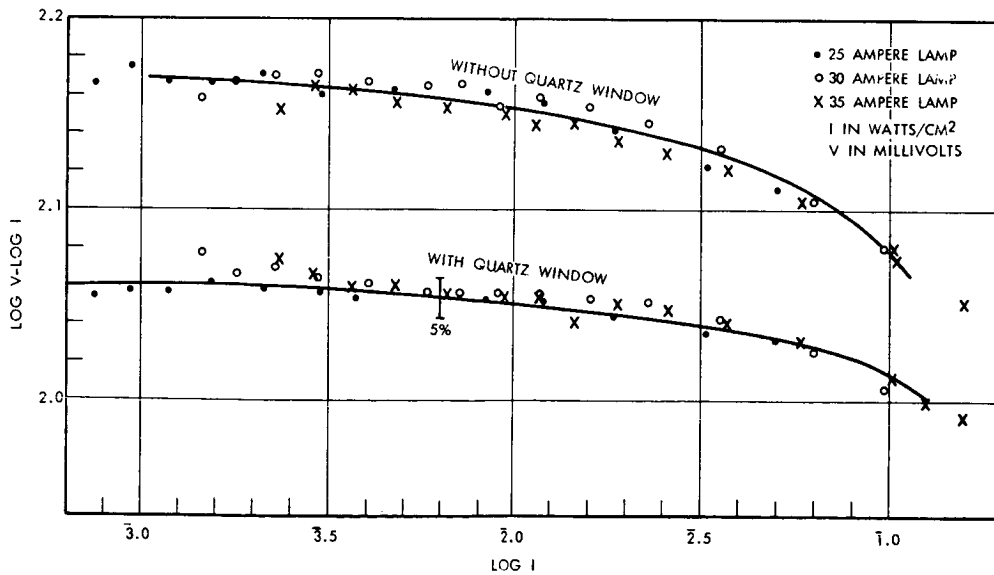


Figure A-12-Calibration Curves, Eppley Thermopile #4702

this. The NBS calibration tables of the standard lamps do not claim an accuracy of less than 5 percent; apparently the integrated values of total irradiance are considerably more accurate. Two different types of voltmeters were used for reading the emf. The least division of each was 10 microvolts, and the emf in the units of microvolts could only be estimated from the deflection of the null galvanometer. The percentage error in reading the emf varies from 0.03 percent at high intensities to 5 percent at the lowest intensity. In spite of these intrinsic sources of large error, the internal consistency of the observations is of the order of 2 percent. This, it would seem, is a strong argument for the reliability of this method of calibration.

The same method of calibration was later used for six other thermopiles which covered an intensity range from 640 to 250,000 $\mu\text{w}/\text{cm}^2$. Four other standard lamps were also used in the course of these measurements. The readings from all lamps show a high degree of consistency. Attempts were also made to use coiled filament lamps of rating 500 watts, 1000 watts and 1750 watts. The wide scatter of the data points seems to show that these lamps are subject to large intensity fluctuations and hence are not reliable standards.

Calibration data of the thermopiles have been prepared as individual calibration tables which have been distributed to the users of these thermopiles. The consolidated results of all the calibrations are presented in Table A-14. In this table, the first column gives the emf in microvolts; the other columns give the corresponding intensities for each of the thermopiles in microwatts per cm^2 . Four of the thermopiles have demountable windows of quartz or lithium fluoride. Measurements made with the window are so indicated in the table, and are followed in the next column by measurements made without the window.

Table A-14

Calibration Table for Thermopiles (V in Microvolts; \mathcal{J} in Microwatts/cm²)

\mathcal{J} V	4720 Quartz	4702	4814 Quartz	4814	4928 Quartz	4928	4966 LiF	4996	8554	Water Cooled T&E	G.E.
12.5											
15							829.9				
17.5							957.2			4121	
20							1059			4645	
22.5							1211			5152	
25							1340	975.0	2010	5649	
27.5							1466	1072	2660	6166	
30							1589	1172	2990	6668	
32.5							1715	1276	3120	7178	
35							1841	1374	3350	7674	
37.5							1928	1476	3660	8185	
40							2089	1578	3800	8690	
45							2333	1778	4253	9683	
50							2588	1982	4700	10720	
55							2831	2183	5150	11720	
60			912				3076	2388	5600	12710	875
65			989				3327	2594	6047	13740	948
70			1066	924			3573	2793	6480	14760	1018
75			1140	992			3811	2999	6920	15780	1088
80			1215	1061			4055	3221	7360	16750	1160
85			1305	1127			4305	3420	7795	17780	1230
90			1370	1195			4550	3622	8238	18840	1300
95			1445	1265			4797	3837	8663	19860	1430
100	889.2	642.7	1520	1330			5035	4046	9110	20890	1440
125	1102	799.8	1900	1665			6237	5093	11900	26060	1785
150	1315	957.2	2360	2065			7482	6138	13800	31260	2197
175	1528	1114	2665	2330			8690	7211	15510	36560	2470
200	1742	1274	3045	2665			9908	8279	17650	41880	2810
225	1954	1432	3425	2994			11140	9376	19750	47420	3160
250	2168	1596	3720	3330			12360	10450	21760	52840	3490
275	2382	1574	4195	3660			13580	11530	23900	58340	3835
300	2594	1914	4540	3995	2480		14830	12620	25950	63830	4165
325	2805	2080	4950	4330	2696		16040	13740	28000	69660	4530
350	3020	2239	5330	4660	2911	2463	17260	14830	30100	75160	4840
375	3243	2404	5711	4991	3126	2645	18490	15920	32190	80720	5177
400	3459	2569	6090	5325	3343	2859	19720	17060	34270	86500	5510
450	3882	2897	6850	5960	3778	3193	22130	19280	38200	98170	6170
500	4315	3228	7610	6615	4213	3558	24660	21580	42280	109900	6840
550	4753	3556	8360	7253	4650	3926	27040	23820	46240	121600	7490
600	5188	3899	9110	7903	5090	4294	29580	26060	50200	133700	8150
650	5636	4236	9860	8544	5530	4663	32060	28380	54260	145900	8820
700	6067	4560	10605	9180	5970	5034	34510	30690	58200	158100	9470
750	6501	4909	11350	9820	6413	5394	36980	32960	62220	170600	10130
800	6950	5248	12100	10460	6858	5776	39540	35240	66200	183200	10780
850	7379	5598	12800	11070	7302	6148	41980	37580	69100		11430
900	7834	5943	13600	11700	7749	6521	44570	39900	74050		12080
950	8279	6295	14230	12370	8194	6895	47100	42270	78000		12750
1000	8730	6637	15050	12970	8642	7269	49550	44570	81900		13200

Table A-14 (Continued)

Calibration Table for Thermopiles (V in Microvolts; λ in Microwatts/cm²)

V \ λ	4702 Quartz	4702	4814 Quartz	4814	4928 Quartz	4928	4996 Quartz	4996	8554	Water Cooled T&E	G.E.
1250	10990	8414	18350	16100	10890	9149	62230	56360	102300		
1500	13240	10210	22450	19250	13160	11040	74990	68550	120500		
1750	15560	12050	26150	22400	15420	12940	87900	80540	139700		
2000	17860	13870	29650	25500	17730	14850		92900	158500		
2250	20180	15740		28500	20030	16770			178000		
2500	22540	17700			24660	18680			196300		
2750	24890	19590			26990	20620			215000		
3000	27290	21530			29330	22550			233000		
3250	29720	23500			31670	24490			251000		
3500	32140	25530			34020	26430					
3750	34590	27480			36380	28390					
4000	37070	29510			41100	30340					
4500	41880	33570			45840	34260					
5000	46990	37760				38190					
5500	52000	41880				42130					
6000	57020	46240				46080					
6500	62230	50580									
7000	67300	54950									
7500	72440	59290									
8000	77800	63680									
8500	82790	68230									
9000	88310	72780									
9500	93760	77450									
10000	98860	82040									
12500	126200	105700									
15000		130000									
17500		155200									

REFERENCES

1. Johnson, Francis S., "The Solar Constant," *J. of Meteorology*, **11**, 431-439 (1954)
2. Dunkelman, L. and R. Scolnik, "Solar Spectral Irradiance and Vertical Atmospheric Attenuation in the Visible and Ultraviolet," *J. Opt. Soc. Am.* **49**, 356-367 (1959)
3. Moon, Parry, "Proposed Standard Solar Radiation Curves for Engineering Use," *J. Franklin Inst.* **230**, 583 (1940)
4. Aldrich, L.B. and W.H. Hoover, *Ann. Astrophys. Observatory, Smithsonian Inst.* **7** (1954)
5. Allen, C.W., "Astrophysical Quantities," Univ. of London, 1955
6. Stair, Ralph and Russel G. Johnston, "Preliminary Spectroradiometric Measurements of the Solar Constant," *J. Natl. Bur. Standards*, **57**, 205 (1956)

7. Stair, Ralph, private communication
8. Gast, P.R., "Handbook of Geophysics," Chapter 16.3, "Solar Radiation," pp. 16-14 to 16-30, McMillan Company, New York (1960)
9. Thekaekara, M.P., "Spectral Energy Distribution of a Mercury-Xenon Lamp," pp. 2-1 to 2-34, Part II, Final Report of the GSFC Summer Workshop Program, X-320-62-193, compiled by Elias Klein (1962)
10. Valasek, Joseph, "Introduction to Theoretical and Experimental Optics," John Wiley and Sons, Inc., New York (1956) pp. 91-98
11. Jenkins, Francis A. and Harvey E. White, "Fundamentals of Optics," McGraw-Hill Book Company, New York (1957) pp. 464-467
12. Stair, Ralph, Russell G. Johnston and W. W. Halbach, "Standard of Spectral Irradiance for the Region 0.25 to 2.6 Microns," J. Res. Natl. Bu. Standards, 64 No. 4, 291-296 (1960)
13. J.C.H., "Spectral Energy Distribution of the 2.5-Kilowatt Hg-Xe Short-Arc Lamp, SAHX-2500B," Westinghouse Electric Corporation, Bloomfield, N. J. (1962)
14. Mann, A.E., and Michael Dubey, "Solar Simulators," Space Aeronautics, March 1962
15. Thekaekara, M.P., "Mercury-Xenon Arc and the Carbon Arc as Sources of Solar Illumination," GSFC X-320-63-57, April 1963, p. 10, fig. 5
16. "American Institute of Physics Handbook," edited by Dwight E. Gray, McGraw-Hill Book Company, New York (1957) pp. 7-120
17. "American Institute of Physics Handbook," edited by Dwight E. Gray, McGraw-Hill Book Company, New York (1957) pp. 4-6
18. Pivovonsky and Nagel, "Tables of Blackbody Radiation Functions," McMillan Company, New York (1961)
19. DeVos, J.C., "A New Determination of the Emissivity of Tungsten Ribbon," Physica (Research Dept. of the N.V. Kama, Arnhem, Nederland)XX, pp. 690-713 (1954)

CALIBRATION OF THE FIVE-CHANNEL TIROS SATELLITE RADIOMETER

N64-28206

E. I. Mohr and F. J. Owens

INTRODUCTION

The TIROS meteorological satellites contain three radiometers, one of which is a five-channel medium-resolution scanning radiometer designed to collect radiation in five wavelength bands by optically filtering the radiation. Each of the five channels contains its own independent optical system and transistorized amplifier. Channels 3 and 5 are sensitive to the visible part of the spectrum; the filter in channel 3 transmits radiation in the range 0.2 - 5.5 microns, and that of channel 5 in the range 0.55 - 0.75 micron.

The Aeronomy and Meteorology Division at Goddard Space Flight Center calibrated channels 3 and 5, using a standard 2740-candlepower tungsten-filament lamp. Radiation from the lamp was diffusely reflected from a sheet of white paper; by placing this sheet at different distances from the radiometer, for varying intensities of radiation, the output voltage of a channel was measured.

The data received from TIROS on channels 3 and 5 did not appear compatible with the calibration of these channels and the known facts concerning the earth's albedo. The 1963 Summer Workshop was asked to seek a solution in collaboration with the A&M Division by calibrating channels 3 and 5, using the technique proven successful in calibrating thermopiles with standard tungsten-ribbon lamps.

PRINCIPLE OF THE RADIOMETER

Figure A-13 shows the optical components of one radiometer channel in cross section. Each channel is designed to have a 5- by 5-degree field-of-view. The optical axis of a given channel is bidirectional, 180 degrees apart. A 90-degree mirrored prism P is mounted in the optical path so that the energy incoming from either direction strikes one or the other half of the rotating chopper disk C and is reflected into the optical system. As the half-aluminized half-black chopper disk rotates, it becomes a scanning disk which is half absorbing, half reflecting; the disk alternately switches radiation from the scan beam pointed at the earth or radiation from the reference beam pointed at outer space into a small radiation receiver.

The radiation receiver consists of an optical filter f, a lens L, and a thermistor-bolometer D. The filter in channel 3 transmits radiation in the range 0.2 - 5.5 microns

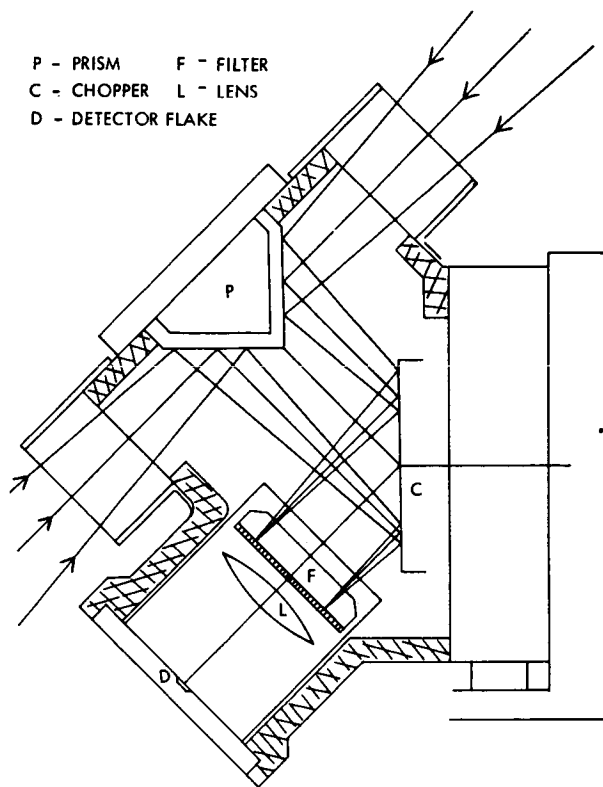


Figure A-13-Five-Channel Satellite Radiometer

and that of channel 5 in the range 0.55 - 0.75 micron. The lens is a doublet (f/1.0) with a clear aperture of 0.5-inch. Lens #1 in both channels 3 and 5, shown in Figure A-14a, is a planoconvex lens of sapphire; lens #2, shown in Figure A-14b, is composed of BaF₂ in channel 3 and of fused quartz in channel 5. These two lenses are combined as shown in Figure A-14c to form the doublet. This arrangement gives a clear aperture of 1.15 cm, and an area of 1.04 cm²; the chopper and prism receive radiation from opposite directions and send it into the lens system, so that only one-half this area (0.52 cm²) is really effective or usable area.

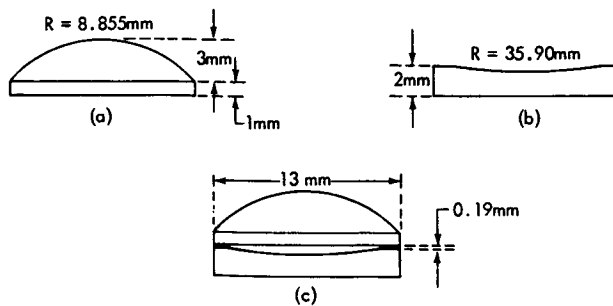


Figure A-14-Dimensions of Lenses

(More complete descriptions of the radiometer and optics have been published by R. A. Hanel and others.^{1, 2})

Because the prism and chopper serve only to change the direction of the incoming radiation, the optical properties of the doublet may be studied on the assumption that the source of radiation and the detector are located on the optical axis on opposite sides of the lens. The index of refraction of the lens material is known, as are the dimensions of the lenses; from these may be calculated the focal length of each lens and of the combined doublet. Using this information, the position and size of the image of the tungsten-ribbon source were calculated. Sample calculations for channel 3 with a wavelength of 1.2 microns are given here; the symbols used are those commonly used in optics.

$$1/f = (n-1)(1/r_1 - 1/r_2)$$

$$1/f_1 = (1.752 - 1)(1/0.8855 - 1/\infty) = 0.752/0.8855$$

$$f_1 = 0.8855/0.752 = 1.178 \text{ cm for the sapphire planoconvex lens}$$

$$1/f_2 = (1.468 - 1)(1/-3.59 - 1/\infty) = 0.468/-3.59$$

$$f_2 = -3.59/0.468 = -7.66 \text{ cm for BaF}_2 \text{ planoconcave lens}$$

$$F = f_1 f_2 / (f_1 + f_2 - t) = 1.178(-7.66) / (1.178 - 7.66 - 0.47) = 1.299 \text{ cm}$$

$$\alpha = f_1 t / (f_1 + f_2 - t) = 1.178 \times 0.47 / (1.178 - 7.66 - 0.47) = -0.079 \text{ cm}$$

$$\beta = -f_2 t / (f_1 + f_2 - t) = -(-7.66) \times 0.47 / (1.178 - 7.66 - 0.47) = -0.514 \text{ cm}$$

$$1/Q = 1/F + 1/P = 1/1.299 + 1/-155 = 0.763$$

$$Q = 1/0.763 = 1.31 \text{ cm}$$

$$q = Q + \beta = 1.31 - 0.51 = 0.80 \text{ cm}$$

$$P/Q = L_0/L_i; \quad 155/1.31 = 1.549/L_i; \quad L_i = 0.013 \text{ cm}$$

ANALYSIS OF IMAGE FORMATION AND DETECTOR POSITION

In analyzing the data available for the optical system of the radiometer, the image formed by the doublet is found to be considerably smaller than the detector "flake" in channel 5; the image is less than 0.2 mm long and about one-fifth as wide, and the flake is 1 by 1 mm. This is also true in channel 3 for wavelengths smaller than about 3 microns; here again the image formed is smaller than the detector surface. For wavelengths greater than about 3 microns, the image would form behind the surface of the flake so that, at the flake surface, the height of the beam is greater than the 1-mm dimension of the flake. As the amount of energy in the range of 3 microns or greater represents only 3.5 percent of the total energy, it appears that the fraction of the energy

which could not fall on the flake must certainly be less than 1 percent of the total energy seen by the effective aperture of the lens (0.52 cm² of lens surface).

POWER RECEIVED BY THE DETECTOR FROM THE TUNGSTEN RIBBON

The rate at which energy of a given wavelength is received from the tungsten ribbon by the detector is a function of I_w , the spectral irradiance of the source; $R_p(\lambda)$, the reflectance of the prism; $R_c(\lambda)$, the reflectance of the chopper; $R_d(\lambda)$, the responsiveness of the thermistor flake; $T_f(\lambda)$, the transmittance of the filter-and-lens combination; r , the distance between source and detector; A_1 , the area of the tungsten ribbon; A_2 , the effective area of the lens aperture; and $f(\Omega)$, the fraction of the radiation falling on the effective aperture of the lens which actually converges on the detector flake. The product of these factors must be integrated over the wavelength range to which the channel responds; the total power received by the detector, therefore, may be closely approximated by

$$P = \sum I_w R_p(\lambda) R_c(\lambda) R_d(\lambda) T_f(\lambda) \frac{A_1 A_2}{r^2} f(\Omega) \cdot \Delta\lambda . \quad (1)$$

Here I_w is determined by the expression

$$I_w = N_\lambda(\lambda, T) \cdot E_w(\lambda, T) \cdot T_q$$

where $N_\lambda(\lambda, T)$ is the spectral irradiance of a blackbody; $E_w(\lambda, T)$ is the emissivity of tungsten; and T_q is the coefficient of transmission of quartz. As the image of the tungsten ribbon which is formed by the lens is smaller than the detector flake, one may let $f(\Omega)$ equal unity.

POWER RECEIVED BY THE DETECTOR FROM AN EXTENDED SOURCE

Assuming that the energy falling on an extended white surface is diffusely reflected, let x watts/cm² be the energy diffusely reflected into the solid angle 2π , and y watts/cm²-steradian the radiation in the normal direction. Then the radiation given off at an angle θ is $y \cos \theta$ watts/cm²-steradian. Hence, the radiation through the annulus of radius $r \sin \theta$ and width $d\theta$ and area dA is

$$\begin{aligned} y \cos \theta \, dA/r^2 &= y \cos \theta \cdot 2\pi r \sin \theta \cdot r \, d\theta/r^2 \\ &= 2\pi y \cos \theta \sin \theta \, d\theta . \end{aligned}$$

The total radiation is obtained by integrating this expression from 0° to $\pi/2$. Thus we have (Figure A-15)

$$\begin{aligned}
 x &= \int_0^{\frac{\pi}{2}} 2\pi y \cos \theta \sin \theta \, d\theta \\
 &= - \int_0^{\frac{\pi}{2}} 2\pi y \cos \theta \, d(\cos \theta) \\
 &= - 2\pi y \left. \frac{\cos^2 \theta}{2} \right]_0^{\frac{\pi}{2}} \\
 &= \pi y \cos^2 \theta \Big|_0^{\frac{\pi}{2}} \\
 \therefore x &= \pi y, \text{ or } y = \frac{x}{\pi}
 \end{aligned}$$

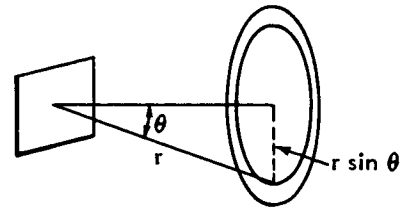


Figure A-15—Annulus of Radiating Surface

Therefore the diffuse radiation in the normal direction is $y = x/\pi$.

The energy dP falling on the effective aperture of the lens, dA' , from an annulus of area dA of the diffusely reflecting surface (Figure A-16) will be

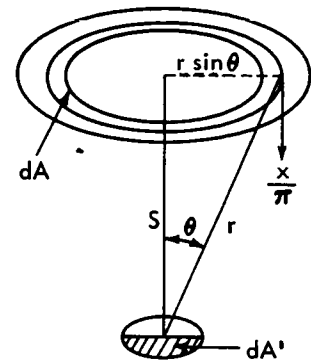


Figure A-16—Energy incident on lens aperture

$$dP = \frac{x}{\pi} \frac{dA \cos \theta \cdot dA' \cos \theta}{r^2}$$

where $dA = 2\pi r \sin \theta \cdot r d\theta$

$$\therefore dP = \frac{x}{\pi} \cdot \frac{2\pi r \sin \theta \cdot r d\theta \cdot \cos^2 \theta \cdot dA'}{r^2}$$

$$= 2x dA' \cos^2 \theta \sin \theta \, d\theta$$

$$P = - \int_0^{\theta} 2x dA' \cos^2 \theta \, d(\cos \theta)$$

$$= - 2x dA' \left. \frac{\cos^3 \theta}{3} \right]_0^{\theta}$$

Since $dA' = 0.52 \text{ cm}^2$,

$$P = \frac{2(0.52)}{3} x \cdot \cos^3 \theta \Big|_0^{\theta} = 0.347 x \cos^3 \theta \Big|_0^{\theta}$$

The value of the angle θ in the above expression may be calculated from the experimental curves which give the relation between the angle made by the incident ray with the optical axis and the output voltage of the radiometer. (See the graphs following page 3-8 in the instruction manual 14-420B.) The total area under this curve is evaluated. This area, divided by the maximum output voltage, gives in degrees the angular radius of an "ideal field-of-view," defined as one with an area such that all parts of it send energy to

the radiometer at an overall uniform rate which will give this maximum output voltage. The value of θ was found to be $2^\circ 9.3'$ for channel 3, and $2^\circ 6'$ for channel 5. Thus, for channel 3,

$$P = 0.347 \times \cos^3 \theta \Big|_{2^\circ 9.3'}^0 = 7.49 \times 10^{-4} \times \text{watts.} \quad (2)$$

For channel 5, this becomes

$$P = 0.347 \times \cos^3 \theta \Big|_{2^\circ 6'}^0 = 6.94 \times 10^{-4} \times \text{watts.} \quad (3)$$

Hence x (the power diffusely reflected by unit surface into the solid angle 2π) will be, for channel 3,

$$x = 1334 P \text{ watts/cm}^2 = 1.334 \times 10^7 P \text{ watts/cm}^2, \quad (4)$$

and for channel 5,

$$x = 1440 P \text{ watts/cm}^2 = 1.44 \times 10^7 P \text{ watts/m}^2. \quad (5)$$

As previously ascertained, the energy diffusely reflected in the normal direction is $y = x/\pi$ therefore the power received by channel 3 in the normal direction is

$$y = 425 P \text{ watts/cm}^2 = 4.25 \times 10^6 P \text{ watts/m}^2, \quad (6)$$

and by channel 5

$$y = 458 P \text{ watts/cm}^2 = 4.58 \times 10^6 P \text{ watts/m}^2, \quad (7)$$

where P is the power in watts received by the given channel from the tungsten ribbon used in calibrating the radiometer.

EXPERIMENTAL PROCEDURE

The five-channel radiometer to be calibrated was mounted on an optical bench so that it was free to rotate about both a vertical and a horizontal axis, as well as to slide along the optical bench. The tungsten-ribbon standard lamp was mounted on a table, with the ribbon vertical at a height which would align the center of the ribbon with the axis of the radiometer. The vertical and horizontal rotations of the radiometer were necessary to obtain proper alignment and to make the image of the ribbon fall on the detector flake. It was observed that a rotation of the axis of the radiometer through even 1 degree would cause the output voltage to drop to almost one-half the maximum value, as might be expected from the value of the angular radius of the ideal field-of-view.

The intensity of the radiation received by the radiometer was varied by moving the detector along the optical bench. The detector output was determined as a function of the

intensity and distance of the source. As this did not allow a range of intensities sufficiently large for the calibration, additional values were obtained by getting the detector output as a function of the distance from the source and of its intensity after the radiation passed through the neutral-density filter 0.5 (filter with $\log(1/T) = 0.5$).

REDUCTION OF THE DATA

Using equation (1), the value of the power P incident on the detector flake was calculated for each of the settings of the radiometer on the optical bench, for both channels 3 and 5. $\log v$, the logarithm of the output voltage was plotted against $\log(P/v)$, the logarithm of the ratio of power P and output voltage v . The best smooth curve was drawn through these points, and the values of P for various values of v were ascertained by means of this curve. Results are given in Table A-15.

Values of P for given values of v listed in Table A-15 were changed to corresponding values of X by means of equations (4) and (5) in order to get the calibration in terms of power input in watts per square meter (diffusely reflected from a plane surface) for the corresponding values of output voltage. Results are listed in Table A-16. Calibration data listed in Table A-16 is plotted in Figures A-17 and A-18.

As stated in the introduction, channels 3 and 5 were calibrated by the A&M Division, using light diffusely reflected from a sheet of white paper as the source. Data obtained by this method are given in Table A-17; in addition, they are plotted into Figures A-17 and A-18 for easy comparison with the calibration made by the Workshop team.

Table A-15

Calibration for Power of
Five-Channel Radiometer #303
(V in volts; P in microwatts)

V	P (Channel 3)	P (Channel 5)
11.00	18.5	3.04
10.00	16.8	2.77
9.00	15.3	2.51
8.00	13.7	2.24
7.00	12.1	1.97
6.00	10.4	1.71
5.00	8.80	1.44
4.00	7.15	1.17
3.00	5.46	0.90
2.00	3.76	0.61
1.00	2.02	0.33
0.75	1.56	0.26
0.50	1.09	0.18

Table A-16

Calibration for Energy per Unit Area
of Five-Channel Radiometer #303
(V in volts; X in watts/m²)

V	X (Channel 3)	X (Channel 5)
11.00	246	43.7
10.00	225	39.8
9.00	204	36.2
8.00	182	32.3
7.00	161	28.4
6.00	140	24.6
5.00	117	20.7
4.00	95.5	16.8
3.00	72.9	12.8
2.00	50.3	8.87
1.00	26.9	4.75
0.75	20.8	3.69
0.50	14.5	2.59

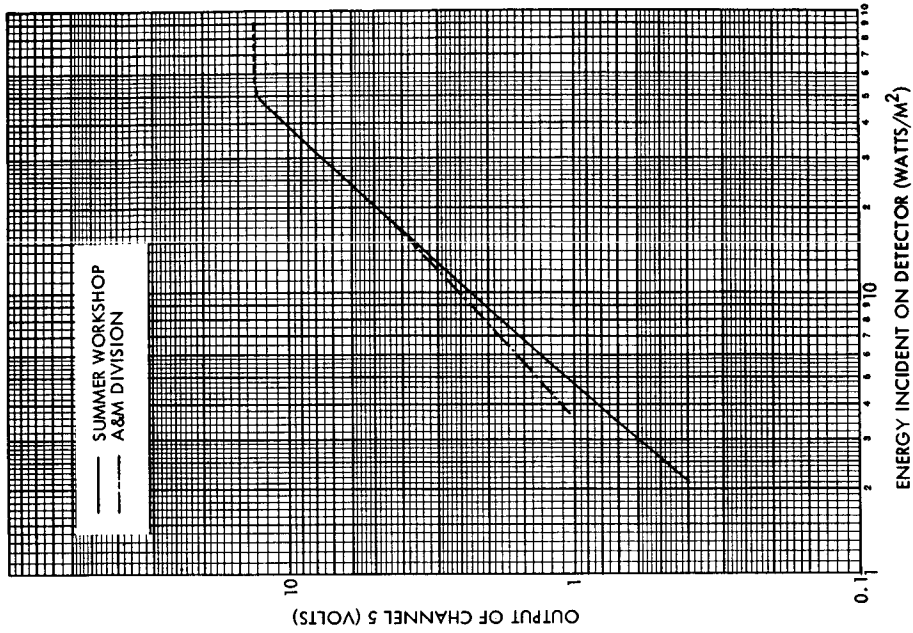


Figure A-18—Output of Channel 5 (Radiometer # 303) vs energy incident on detector

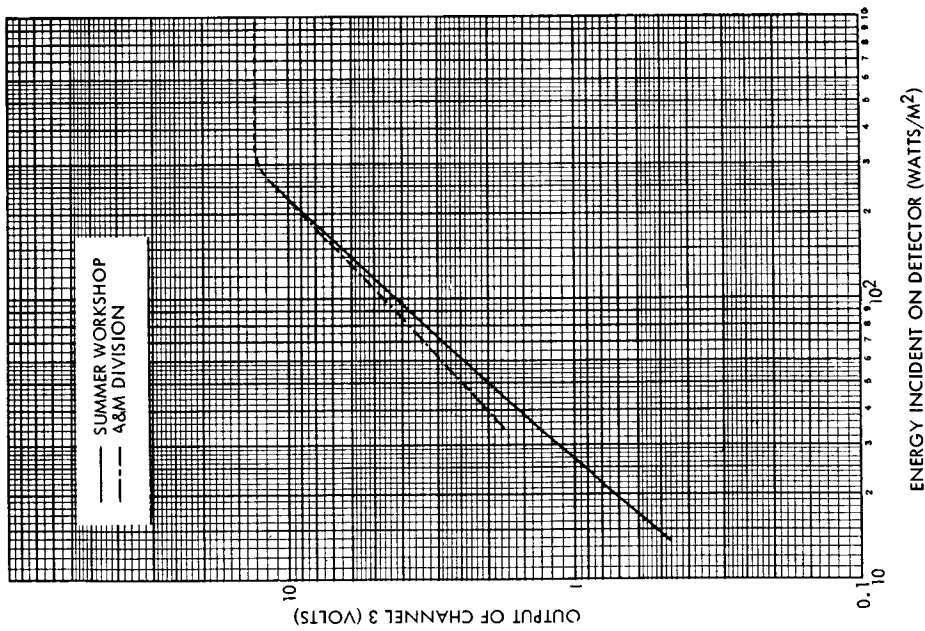


Figure A-17—Output of Channel 3 (Radiometer # 303) vs energy incident on detector

Table A-17

A&M Division Calibration of Radiometer #303
(V in volts; X in watts/m²)

V (Channel 3)	X (Channel 3)	V (Channel 5)	X (Channel 5)
10.3	233.2	4.92	20.6
9.55	210.1	4.45	18.6
8.57	189.6	4.10	16.8
7.80	172.2	3.70	15.2
7.26	157.2	3.44	13.9
7.42	159.8	3.43	14.1
6.82	146.4	3.15	12.9
5.93	124.0	2.73	11.0
5.03	106.4	2.39	9.41
4.39	92.3	2.10	8.16
3.88	80.7	1.85	7.13
3.29	67.1	1.58	5.94
2.85	56.7	1.38	5.02
2.34	46.2	1.15	4.08

DISCUSSION OF THE RESULTS

Saturation in the output voltage is reached at approximately 13 volts for both channels 3 and 5. Needing a fairly wide range of intensities to obtain a valid calibration of the radiometer, Team A of the Summer Workshop used a series of intensities which produced output voltages ranging from 0.5 volt to 11 volts for both channels. The A&M Division, in its calibration of the same channels, used a similar range of intensities to obtain output voltages varying from about 2 volts to 10 volts for channel 3, and from about 1 volt to 5 volts for channel 5.

A comparison of the results of the two methods of calibration shows that, for channel 3, an output of 10 volts (the maximum obtained in the A&M calibration) corresponds to an intensity of 224 watts/m² in the A&M calibration, and an intensity of 225 watts/m² in the Team A calibration. For channel 5, an output of 5 volts (the maximum obtained in the A&M calibration) corresponds to an intensity of 20.9 watts/m² for the A&M calibration and an intensity of 20.7 watts/m² for the Team A calibration. In other words, the results obtained by the two methods of calibration are in agreement at the maximum value of the output voltage used in the A&M Division's calibration.

However, the calibration curve for channel 3 (shown in Figure A-17) shows that the slopes of the curves obtained by the two methods are somewhat different; the slope of the curve obtained by Team A is 0.0463 volts-m²/watt, and that obtained by the A&M Division is 0.0423 volts-m²/watt. For a perfectly linear response, the output voltage should be directly proportional to the intensity; if this were true for these curves, the slope should be approximately 0.0444 volts-m²/watt, approximately halfway between the slopes of the curves obtained by the two methods.

Examination of the calibration curves for channel 5 (Figure A-18) gives similar results; the slope of the curve obtained by Team A is 0.253 volts-m²/watt, whereas that of the curve obtained by the A&M Division is 0.228 volts-m²/watt. For perfectly linear response, the expected slope would be 0.241 volts-m²/watt, and the corresponding curve would lie between the curves obtained by the two methods, as in the case of channel 3.

The departure from the expected slope in the A&M calibration curves represents an intensity increasing beyond the calculated value as the distance increases between the radiometer and the diffusely reflecting sheet of paper. This departure might be partially attributable to variations in the diffuse reflectivity of the paper as larger areas of the paper are "seen" at increasing distances; however, assuming that the sheet is uniformly illuminated and that the diffuse reflectivity is constant, a more likely explanation is suggested: It happens that the angle between the normal to the sheet of paper and the "line-of-sight" to the radiometer decreases from approximately 24 degrees to 17 degrees or less as the sheet of paper moves farther away; if there is specular reflection, the intensity of the energy reflected specularly would increase as the angle decreases. This would produce an incident energy greater than the calculated value, and would result in an output voltage slightly higher at the lower intensities than might be expected.

The contrary departure from the expected slope in the Team A calibration curve represents an intensity which gradually becomes smaller than the calculated value as the distance increases between the radiometer and the tungsten ribbon. This departure might be caused by small discrepancies in the size and position of the image of the tungsten ribbon relative to the size and position of the detector flake. The dimensions of the optics used to check these values, obtained from data given for an earlier model of the radiometer, might differ somewhat from those of the radiometer used in these calibrations (serial number 303). In addition, the calculations were made under the assumption that the doublet is composed of two thin lenses; the planoconvex lens, however, actually is not a thin lens. The discrepancies inherent in these assumptions may explain the decrease in response measured as the distance of the source was increased.

It was mentioned in the introduction that the A&M Division's calibration seemed to be incorrect by a factor of 2. Since Team A of the Summer Workshop began its independent calibration of the radiometer, some significant information has been obtained. An analysis by the A&M Division of data received from TIROS IV has revealed a significant amount of degradation in the five-channel satellite radiometer, especially large and relatively fast in channels 3 and 5, which seems to have occurred within about a week after the satellite was launched. This same degradation was detected in TIROS II and TIROS III after data from these satellites were corrected for asymmetry. Interestingly, if the data are extrapolated back to launch time, the degradation amounts to approximately the "factor of 2" discrepancy which had originally been observed in channels 3 and 5. The cause of this degradation is now under study by the A&M Division.

The authors of this report wish to thank Andrew McCulloch of the A&M Division and members of his staff for their help in this calibration.

REFERENCES

1. R.W. Astheimer, R. deWaard, and E.A. Jackson, Journal of the Optical Society of America, 51, 1386-93 (1961)
2. R.A. Hanel and D.O. Work, Journal of the Optical Society of America, 51, 1394-99 (1961)

PROJECT B: HEAT TRANSFER AND CRYOGENIC
PUMPING IN VACUUM TECHNOLOGY

CONTENTS

	<u>Page</u>
INTRODUCTION	B-1
G. H. Beyer	
CRYOSORPTION	B-3
G. H. Beyer	
Industrial Participation	B-7
J. E. A. John	
VACUUM GAGE SYSTEMS	B-11
J. Gavis	
Vacuum Gage Comparison by Pressure Division Method	B-12
J. Poynter	
SPACECRAFT VACUUM GAGE COMPARISON	B-17
C. A. Baumgardner	
PRELIMINARY DESIGN ANALYSIS FOR AN ULTRAHIGH-VACUUM SYSTEM	B-23
J. E. A. John	
FEASIBILITY OF LIQUID-METAL VACUUM SEALS	B-29
J. E. A. John, D. L. Akins, G. S. Pick	

ILLUSTRATIONS

<u>Figure</u>		<u>Page</u>
B-1	Adsorbed Volume Over Seven Decades of Pressure	B-5
B-2	Cryosorption Array	B-8
B-3	Schuhmann Apparatus for Calibration by Pressure-Division Method	B-13
B-4	Workshop Apparatus for Calibration by Pressure-Division Method	B-15
B-5	Results of a Series of Preliminary Runs Showing Ion Gage vs Calculated Pressure Utilizing Boyles Law: $P_f V_f = P_1 V_1 + P_2 V_2$	B-16
B-6	High-Vacuum Calibration System, Schematic Diagram	B-19
B-7	High-Vacuum Calibration System	B-21
B-8	Ultrahigh-Vacuum Cryogenic Pumping System, Schematic Diagram	B-24
B-9	Liquid-Metal Seal	B-29
B-10	Seal Test Apparatus, Structural Diagram	B-30
B-11	Seal Test Apparatus, Flow Diagram	B-30
B-12	Seal Test Apparatus, Interior View	B-31
B-13	Pumpdown Curve for Vacuum System with Liquid-Metal Seal	B-34

TABLES

<u>Table</u>		<u>Page</u>
B-1	Radiative Heat-Transfer Calculation	B-25
B-2	Properties of Liquid-Metal Scalant	B-30
B-3	Ultimate Pressures Using Liquid-Metal Seal	B-33

SUMMER WORKSHOP 1963

Program Outline and Team Participants

PROJECT B: Heat Transfer and Cryogenic Pumping in
Vacuum Technology

Study Topics

- B-1 Vacuum gauge calibration: two different set-ups
- B-2 Cryosorption materials
- B-3 Cryogenic shroud design
- B-4 New ideas for low-pressure measurements

TEAM B

Academic Personnel

Goddard Personnel

		<u>Code</u>
Dr. Beyer	Dwight C. Kennard	320
PRINCIPAL INVESTIGATOR	STAFF ADVISOR	
Dr. Gavis	William Hardgrove	322
*Dr. John	Harold Shapiro	322
Mr. Akins	James Poynter	323
Mr. Baumgardner	Charles Madison	322
Mr. Pick	Oliver B. Humble	322
	George Newton	651
	Leland Clark	651
	NSF Summer Science Student David B. Cook	

*Continuing part-time work at Goddard on Project B.

PROJECT B: HEAT TRANSFER AND CRYOGENIC PUMPING IN VACUUM TECHNOLOGY

G. H. Beyer

INTRODUCTION

Vacuum technology has developed so rapidly during the past decade that it is generally now agreed that our ability to produce low pressures has outstripped our ability to measure them.

Spacecraft testing has imposed ever more stringent requirements on cleanliness, and on increased pumping speeds for the noncondensable gases, particularly hydrogen. It is not surprising, therefore, that Project B of the Summer Workshop was asked to study vacuum technology and cryogenic pumping as they relate to the testing and evaluation of spacecraft.

Effort was divided among the following areas:

- Cryosorption - which holds considerable promise for pumping hydrogen outgassed from spacecraft in test chambers simulating conditions in outer space
- Vacuum-gauge calibration - for developing better equipment and procedures for measuring low pressures
- Cryogenic pumping - for achieving ultrahigh vacua where unusual surface phenomena can be studied

Also, some experimental tests were made on liquid-metal seals in an effort to assess their effectiveness in high-vacuum systems.

The reports which follow summarize Workshop activities in the fields of interest to Project B, and include recommendations which seemed important to the individual authors. Because of limitations of time and equipment, the reports are less complete than might be desired; however, the focusing of attention on those problems most deserving of continued effort is in itself a substantial step toward the gathering of significant experimental data. And a realistic appraisal of the time and talent that can be brought to bear on a problem is an essential first step in formulating an effective research program.

CRYOSORPTION

N64-28207

G. H. Beyer

It is well known that high vacua can be created by the use of cryogenic fluids such as liquid nitrogen, hydrogen, or helium. Condensation on surfaces cooled by cryogenic fluids results in the condensed molecules exerting their full vapor pressures at the existing temperature. For water at 90°K, this vapor pressure is 10^{-18} mm – so very small a number that water can be effectively removed by liquid-nitrogen-cooled surfaces. However, hydrogen even at 20°K has a vapor pressure of 760 mm, so large a number that hydrogen cannot be very effectively removed by condensation.

Cryosorption is of interest because the attraction between adsorbed gas molecules and a cold adsorbent surface effectively lowers the vapor pressure of the adsorbed gas. For example, 1 gram of charcoal at 20°K is reported to adsorb some 140 cm³ (STP) of hydrogen at an equilibrium pressure of only 10^{-7} torr. Cryosorption thus represents a potential means of removing hydrogen from regions of low pressure, not by condensation (attraction between like molecules) but by adsorption (attraction between unlike molecules, the gas and the surface of the adsorbent).

A price is paid for this unique behavior, however: The surface of the charcoal can accommodate only a limited number of hydrogen molecules before it becomes covered. The fact that a single layer of molecules seems to be all that can be adsorbed at equilibrium by a surface is a severe limitation on adsorption capacity, unless large areas of surface can be made available at low temperatures and periodically desorbed for reuse.

A vacuum system was designed at Goddard Space Flight Center to investigate cryosorption. While the system was being constructed, a report was issued by Linde Division of Union Carbide Corporation (under contract to Arnold Engineering Development Center) which prompted reappraisal of the experimental program at Goddard. The report contained equilibrium data on the adsorptive capacity of charcoal, silica gel, and molecular sieves for hydrogen and helium at temperatures between 20 and 40°K and at pressures in the range 10^{-3} to 10^{-8} torr.

Factors affecting the practical application of cryosorption will be discussed here under several headings: Equilibrium data, kinetic data, temperature control, effective adsorbent reuse, and industrial participation. Discussion of these topics will be followed by recommendations for the program at Goddard.

EQUILIBRIUM DATA

Equilibrium data represent the potential capacity of various adsorbents. From an analysis of such data may be derived a better understanding of low-temperature adsorption processes and of methods for correlating, interpreting, and extrapolating experimental observations. Considering the difficulty of obtaining reliable data under extremes of low temperature and low pressure, careful analysis of such data certainly seems warranted.

Physical adsorption of a gas on a solid surface involves relatively weak forces, the heat effects being of the same order of magnitude as the heat of condensation. Because diffusion of the gas to the adsorbent surface generally limits the rate of removal, it is important to minimize the resistance to mass transfer. As the adsorbent surface becomes covered with adsorbed molecules, the pressure of the gas in equilibrium with the adsorbent rises until – when the surface is fully covered – the gas exerts its full vapor pressure for the existing temperature.

For a given adsorbent exposed to a vacuum system in which hydrogen forms a substantial percentage of the gas to be removed, the amount of gas adsorbed at equilibrium is primarily a function of pressure and temperature. At the low temperatures associated with cryosorption, the isotherm relating the amount adsorbed to the pressure is approximately linear, following Henry's Law at low pressures.

An analysis was attempted of the Linde equilibrium data for the adsorption of hydrogen on charcoal. The method used presents serious inconsistencies, but it is given as an example of the approach to the problem rather than as a solution.

The work of Hobson^{3,7} with nitrogen adsorbed on glass suggested an application of the Dubinin-Radushkevitch equation (4) to the Linde data for hydrogen adsorbed on charcoal. The equation is:

$$\log V = \log V_{sat} - AT^2 \left[\log \frac{P_H}{P_{sat}} \right]^2$$

This equation relates the volume adsorbed, V , to the pressure of hydrogen, P_H , at absolute temperature T . The vapor pressure of hydrogen at T is P_{sat} ; the volume adsorbed when $P_H = P_{sat}$ is V_{sat} . The ratio V/V_{sat} may be interpreted as the fractional coverage of the adsorbent surface corresponding to any one value of p_H . When the surface is completely covered, the pressure of hydrogen is its saturation pressure at the existing temperature.

The equation was used by plotting $\log V$ vs $[\log (p_H/p_{sat})]^2$. The intercept was $\log V_{sat} = 2.60$; the slope of each isotherm was $-AT^2$, from which A was obtained. Perhaps fortuitously, the data at 20.2°K yielded $A = 1.03 \times 10^{-5}$, while the data at 30°K yielded $A = 1.02 \times 10^{-5}$. Using the constants, the equation was solved repeatedly by computer at temperatures of 6, 7, ... , 32°K , and pressures 1×10^{-3} , 1×10^{-4} , ... , 1×10^{-9} mm. In

this way a complete family of curves of volume adsorbed was established (Figure B-1) over seven decades of pressure from four experimental data points at 20.2°K and four experimental data points at 30°K. All curves were asymptotic at high pressures to $\log V_{sat} = 2.60$, or $V_{sat} = 398 \text{ cm}^3$ (STP). This asymptote may be interpreted as complete surface coverage of the charcoal used. It is interesting to note that, using Dushman's⁵ value of 15.22×10^{14} for the number of hydrogen molecules per cm^2 , a value may be estimated for $V_{sat} = 508 \text{ cm}^3$ (STP), indicating that about 80 percent of the surface reported for the charcoal is able to accommodate hydrogen molecules.

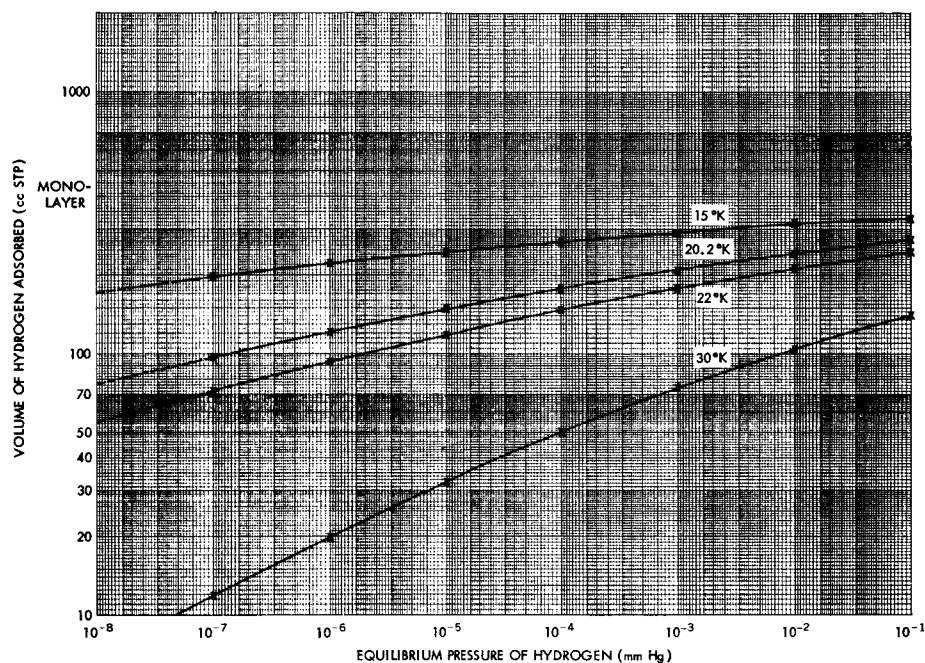


Figure B-1—Adsorbed volume over seven decades of pressure

KINETIC DATA

Whatever the method of rationalizing equilibrium data, it may be concluded that charcoal does have substantial equilibrium capacity for holding hydrogen at low pressures; however, the pumping speed of an adsorbent is of as much interest as its equilibrium capacity.

Linde reported kinetic data on the rate of hydrogen adsorption, using apparatus similar to that used for low-temperature calorimetry. Rates of adsorption were obtained from the variation of pressure with time when an increment of gas was introduced to a cell containing adsorbent. Also, by monitoring the pressure in an adsorption cell with a constant leak of hydrogen into the cell, a measure of the pumping speed was obtained.

A major conclusion drawn from the Linde data is that adsorption from a region of low pressure (where the mean free path of the gas molecules is large) results in poor penetration into any adsorbent; only that portion of the adsorbent directly exposed to the gas is effective. This was demonstrated by increasing the depth of the adsorbent fourfold with no substantial change in the amount of hydrogen adsorbed. Apparently, therefore, the exposed area per unit weight of adsorbent should be maximized, as the top layers of adsorbent tend to shield the lower layers, thereby reducing the equilibrium adsorptive capacity available to the gas at low pressures. To realize as much capacity as possible, the rate of adsorption must be encouraged by properly exhibiting the adsorbent to the gas.

TEMPERATURE CONTROL

Temperature is known to affect adsorptive capacity so greatly that temperatures above 30°K are considered too high to be of practical interest. It is essential to minimize temperature gradients within the adsorbent, and the design of cryosorption equipment demands careful attention. Even though the heat of adsorption is 1000 to 2000 cal/gram mole, the quantities of material are so small that the heat load is likely to depend primarily on the effectiveness of radiation shielding. Even color may influence choice of an adsorbent, white molecular sieves having an inherent advantage over black charcoal.

The thermal bond between an adsorbent and its heat sink is an important variable. A seven- to ten-fold loss of capacity accompanies a rise of 10°K in charcoal. For reasons affecting heat transfer, as well as for greater surface availability, shallow well-cooled beds of adsorbent are essential to the successful development of cryosorption pumping.

EFFECTIVE ADSORBENT REUSE

From the preceding discussion of equilibrium and kinetic data, it is apparent that careful design will be needed to realize a substantial amount of equilibrium adsorptive capacity. For example, specifying that hydrogen pressure shall not exceed 10^{-7} mm is equivalent to specifying that only 140/398 (about 35 percent) of the adsorbent surface, at most, will be used. For an appreciable rate of adsorption, an even lower percentage of coverage must be accepted, because the rate becomes zero as equilibrium coverage is approached. The net effect is that the cryosorbents probably will have to be effectively reused, preferably in situ and perhaps even during a test run:

Reuse of adsorbents involves temperature cycling: for example, from 20°K for adsorption to 77°K or higher for desorption. Some method must be provided for efficient disposal of the desorbed hydrogen; this might be collected on a cryopanel cooled with liquid helium, after decreasing the conductance between a vacuum chamber and the adsorbent. A satisfactory portion of the desorbed hydrogen might be pumped away; or, getting using evaporated molybdenum films⁶ may develop practical results. Temporary

isolation of the loaded cryosorbent from the region of high vacuum may be necessary in circumstances where the adsorbent has been contaminated by outgassing from a test item, or by residual gases other than hydrogen.

INDUSTRIAL PARTICIPATION

J. E. A. John

Team B, in the course of its activities on cryosorption, made contact with the Linde Company, which was known to be actively engaged in cryosorption research. From a visit to Linde by Drs. Beyer and John on August 23, 1963, and a formal presentation at Goddard on cryosorption, September 13, 1963, by Dr. Stern of Linde's Research Division, Team B found that considerable progress has already been made toward the ultimate goal of using cryosorption in a vacuum system.

Linde first considered cryotrapping, but the pumping speeds were inadequate. Although cryosorption appeared to offer possibilities for adequate pumping speeds, data were not available on adsorption properties of materials at low temperature (20°K). Linde therefore entered into a program to obtain the required data.

Charcoal was considered first because it appeared to have the highest adsorptive capacity; however, it was found that at the same low temperatures molecular sieves were actually more efficient than charcoal. Also, charcoal presented a potential safety hazard in that an explosion might develop if an air leak developed. Accordingly, molecular-sieve adsorbent was adopted.

Linde is presently able to furnish a panel consisting of a thin layer (1/64 inch to 1/8 inch) of Molecular Sieve 5A bonded to an aluminum or stainless steel surface. Two of the major problems associated with the application of cryosorption have thus been resolved: containment of the adsorbent in a vacuum chamber, and maintenance of the adsorbent bed at a uniform low temperature (the bed is thin enough to offer negligible thermal resistance).

Considerable work on a cryosorption array resulted in development of a special method for bonding the adsorbent to the surface. One method was to bond the molecular sieve in milled slots 1/8-inch wide and 1/64-inch deep. Now a uniform direct-bonding process has been developed.

It is important to shield the adsorbent both from radiation and from contamination by condensable gases within the chamber. Linde suggested an array (Figure B-2) consisting of the cryosorption panel enclosed by a chevron shield

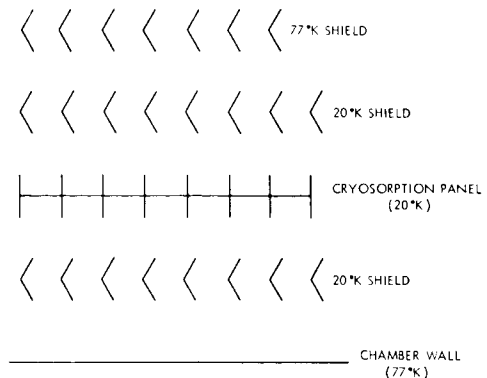


Figure B-2—Cryosorption Array

maintained at 20°K, which in turn is enclosed by chevron shields at 77°K. The cryosorption panel itself consists of parallel plates, in order to maximize capture probability.

Linde reports that pumping speeds of 7000 liters per second per square foot of frontal area had been measured for hydrogen at 10^{-8} torr, with a flat plate of adsorbent maintained at 20.2°K. Greater pumping speeds would be possible with improved geometric arrays. High pumping speeds should also be possible for helium, if the adsorbent were cooled at 4.2°K, although insufficient data are available for substantiating this claim.

Linde representatives plan to submit a proposal to furnish a cryosorption panel and accompanying cryogenic array for evaluation by Goddard. This panel would be tailored to use in a chamber 3 feet in diameter and 3 feet high, the cryosorption panel itself to operate at 20°K.

RECOMMENDATIONS

G. H. Beyer

1. Experimental research on cryosorption requires a sizeable group effort. Experimental measurements at low temperatures and low pressures require painstaking attention to detail; if necessary resources of time, talent, and money are not available at Goddard, it may be more practical to support cryosorption studies elsewhere.

2. Cryosorption pumping is of such potential importance that a person knowledgeable in this field should be assigned to follow up and assess developments in the field. Often there is a considerable lag between the obtaining and the reporting of data; to minimize this lag, and to benefit more substantially from the work of others, continual surveillance is necessary. Also essential are periodic visits to laboratories actively concerned with cryosorption.

3. Equilibrium data for the adsorption of hydrogen on charcoal and molecular sieves appear adequate for current needs; however, the area of correlation, interpretation, and extrapolation of such data (and data for other gases) deserves more attention than it has received. A project of this sort might well be done over a period of years at a university.

4. Kinetic data depend to a large extent upon adsorbent history and temperature control. Now that cryosorption panels appear to be available, a testing program should be seriously considered for panels furnished by industrial suppliers, using one of Goddard's small vacuum chambers.

5. Cryosorption is only one step in a sequence of operations all of which must be carried out within a small area if the adsorbent is to be used effectively. For space-chamber work, where continuous outgassing of a spacecraft serves as a source of gas throughout the test period, it is possible that regeneration of the adsorbent will be necessary. Therefore, the entire sequence of operations — including activation, shielding, cooling, adsorption, heating, and desorption — must be considered as a single compatible system.

6. Thermonuclear research is also vitally concerned with pumping hydrogen at low pressures. Experiments on gettering, using active metals such as molybdenum, may prove of interest.

7. Adsorbent capacity may be less important than pumping speed and operating convenience. Etched heat-exchange surface, for example, may prove attractive for reasons of cleanliness and temperature control; or, molecular sieves may be preferred to charcoal because available bonding techniques ensure better temperature control.

8. Finally, effective research is generally done by people whose primary interest is research. If responsibility is diluted with multitudinous other tasks, both the quantity and quality of research will suffer. This is true primarily because the definite tasks preempt the time of the undefined tasks.

REFERENCES

1. Pick, G. S., "A Vacuum System to Investigate Cryosorption," Goddard Space Flight Center Report X-320-63-67, February 1963
2. Stern, S. A. et al, "The Cryosorption Pumping of Hydrogen and Helium at 20°K (Interim Report)," Arnold Engineering Development Center Report AEDC - TDR - 62 - 200, October 1962
3. Hobson, J. P., "Physical Adsorption of Nitrogen on Pyrex at Very Low Pressures," J. Chem. Phys., 34, 1850 (1961)
4. Dubinin, M. M., and Radushkevich, L. V., Proc. Acad. Sci. U.S.S.R., 55 (1947)
5. Dushman, S., "Scientific Foundations of Vacuum Technique," 2nd ed., John Wiley, New York, 1962, p. 381
6. Hunt, A. L., et al., "Gettering of Residual Gas and the Adsorption of Hydrogen on Evaporated Molybdenum Films at Liquid-Nitrogen Temperatures," Advances in Cryogenic Engineering Vol. 8, Plenum Press, New York, 1963
7. Hobson, J. P., "Physical Adsorption in Ultra High-Vacuum Systems," Transactions of the Eighth Vacuum Symposium, Pergamon Press, New York, Vol. 1, p. 146, 1961

VACUUM GAUGE SYSTEMS

J. Gavis

N64-28208

INTRODUCTION

In discussing calibration methods for high- and ultrahigh-vacuum gauges, a careful distinction should be made between "absolute" and "relative" pressure measurements.

An "absolute" system is one in which a known absolute pressure is produced, against which a gauge may be checked. In a "relative" or comparison system, the gauge reading is checked against that of another arbitrarily chosen standard gauge whose readings are assumed to have certain values of pressure. Methods using comparison systems may be assumed to be well known and developed down to the limiting ranges of pressures which can be indicated by ionization gauges (about 10^{-4} to 10^{-12} torr).

The "absolute" calibration of gauges in the ultrahigh-vacuum region is a problem of another order of magnitude. Several reports have been published describing various schemes for these measurements;⁴⁻⁸ all the authors, however, admit to difficulties inherent in their methods and note that further work is being conducted.

In the August 1963 issue of Physics Today, there appeared an article by Daniel Alpert entitled "Ultra-high Vacuum: A Survey," which gave clearly and simply a critical evaluation of past and continuing research efforts in the field of ultrahigh-vacuum measurement.

The entire range of pressures below 1 atmosphere (vacuum pressures) may be conveniently divided at about 10^{-6} to 10^{-7} torr for purposes of investigation. In practice, it is relatively easy to produce a known absolute pressure above 10^{-6} to 10^{-7} torr; below this point, no really satisfactory method exists of obtaining known pressures, although pressures measuring as low as 10^{-12} torr have been obtained. The problem at these very low pressures (ultrahigh vacua) is to determine accurately the absolute value of the pressure or, alternatively, to determine accurately the number and kind of molecules present in a given volume.

TYPES OF VACUUM GAUGES

The pressure-division experiment was developed as a means of providing standardized vacua as a basis of comparing measurements from different types of vacuum gauges.

Modern ultrahigh-vacuum gauges may be classified into two broad groups: Those which measure numbers of molecules by some sampling means, and those which measure mechanical effects of the presence of molecules. The latter group measures

quantities closest to pressure itself, namely changes in momentum per unit time or force.

Use of the first group depends upon a knowledge of the particular molecular species present, and requires auxiliary means of identifying them. Although application of the second group would appear to require only absolute methods in which a knowledge of the molecular species present is not needed, this is not so for most methods classified within it.

Types in the first group include: Barnes' cold-cathode scintillation gauge; Lafferty's cold-cathode gauge; all other ionization-type gauges and mass spectrometers; Haller and White's surface microbalance.

Types in the second group are: Beams' spinning rotor drag gauge; Schwarz's resonance radiometer gauge; Micro-erg Laboratory's radiation-pressure radiometer gauge.

In practice, use of Beams' gauge requires knowledge of the molecular weight of the gas molecules present. Use of Schwarz's gauge requires knowledge of the accommodation coefficient of the gases present on the surfaces of the gauge. Only the last-named gauge can be used without reference to the type of molecule present in the gas.

It is immediately evident that measurement of ultrahigh vacuum is a most intricate and difficult research problem. Work already done by the investigators listed is enormous, and their investment of time, money, and energy would be difficult to duplicate.

As a recommendation at the end of the Workshop, therefore, the writer suggests that the Test and Evaluation Division at Goddard should not attempt an ultrahigh-vacuum research effort unless it is willing to provide experienced research people who have no responsibility other than nonscheduled and free research.

Finally, the writer recommends that the division, after careful consideration and consultation with experts in the field, support the research groups which appear most promising of ultimate success.

VACUUM-GAGE COMPARISON BY PRESSURE-DIVISION METHOD

A review of previous work, including that of the 1962 Summer Workshop,¹ led to the conclusion that a workable system for obtaining known absolute pressures above 10^{-6} to 10^{-7} torr could be constructed following the design (Figure B-3) of Shuford Schuhmann, National Bureau of Standards.

Schuhmann's method is basically the pressure-division method first suggested by Knudsen: that is, an accurately known small volume of gas at an easily measured pressure is expanded into a much larger, but accurately known, volume. By Boyle's law, the pressure in the system is proportional to the ratio of small volume and large volume and

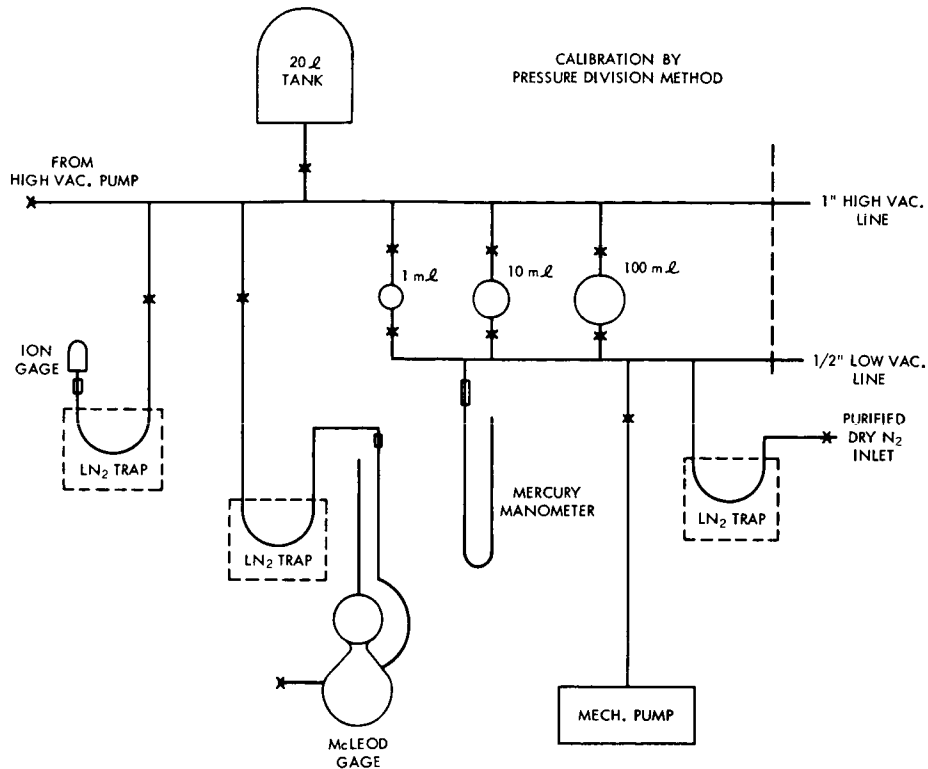


Figure B-3—Schuhmann apparatus for calibration by pressure-division method

to the original pressure. (If the volume ratio is 10^{-4} torr, for instance, it is possible to get down to 10^{-2} torr from 100 mm original pressure.) Intermediate pressures may be obtained by starting with other volume ratios and other original pressures. A second step, performed by opening the small volume to the system at the pressure obtained by the original expansion and using this as a new small volume, will serve to reduce the pressure (in the example, to 10^{-6} torr). Schuhmann found the practical limit of this procedure to be about 2×10^{-7} torr.

Advantages of the pressure-division method are the freedom from worry about adsorption, and the fact that the system does not have to be baked. Usually, as pressures are decreased to the 10^{-6} torr range, appreciable error is introduced by adsorption or desorption of condensable gases on or from the walls of the system, so that actual numbers of molecules in a given volume may differ widely from those thought to be present. Schuhmann's method avoids this situation by putting liquid nitrogen traps between all gauges being calibrated and the system.

To perform a calibration, the system is flushed with purified dry nitrogen passed through a liquid-nitrogen-cooled trap to assure that the only noncondensable gas present is nitrogen. After expansion, condensable gases will desorb; the total pressure in the system will rise above that thought to be present. However, because of the trap between

the system and the gauge being calibrated, the gauge will see only the partial pressure of the nitrogen, which is accurately and "absolutely" known.

Schuhmann's methods and apparatus, and their capabilities and limitations, have been described elsewhere in readily available form³ and therefore will not be described in detail here. Schuhmann's most important suggestions for improvement are that the system be constructed of metal, using the largest diameter tubing conveniently possible, and that the manometer for measuring original pressures be at least 1/2-inch in diameter to reduce capillarity errors in reading it.

A system incorporating the suggestions mentioned has been designed according to the schematic diagram, Figure B-1, and should present no difficulties in fabrication. A considerably modified system was constructed for the Summer Workshop so that the apparatus could be completed during the Workshop session; it was made from pyrex glass and incorporates a vac-ion pump. The apparatus was set up in the Standards and Calibration Laboratory of the Test and Evaluation Division, under the direction of James Poynter.

DESCRIPTION OF THE APPARATUS

J. Poynter

The apparatus is shown in Figure B-4. The vacuum system may be divided into two subsystems, the ultrahigh-vacuum system and the high-vacuum system.

The ultrahigh-vacuum system is used primarily as a pumping station for lowering pressure in the high-vacuum system. It consists of a vac-ion pump, vac-ion pump control, sump, vacsorb force pumps, nude ion gauge with control, thermocouple gauge, and the necessary high-vacuum valves and fittings.

The high-vacuum system is used to compare various gauges and to calibrate a vac-ion gauge by means of expanding various generated pressures. This system, composed entirely of glass, consists of:

20-liter reservoir	high-vacuum stopcocks
two 1-milliliter reservoirs	cold traps
10-milliliter reservoirs	two U-tube manometers
100-milliliter reservoirs	ion gauge with control
1/2-inch manifold	McLeod gauge
1-inch manifold	two mechanical forepumps

together with the required supports rack and necessary clamps and fittings.

The cold traps used in this apparatus are of the double symmetrical design developed by P. R. Yeager of Langley Research Center, NASA. All glass stopcocks are of the

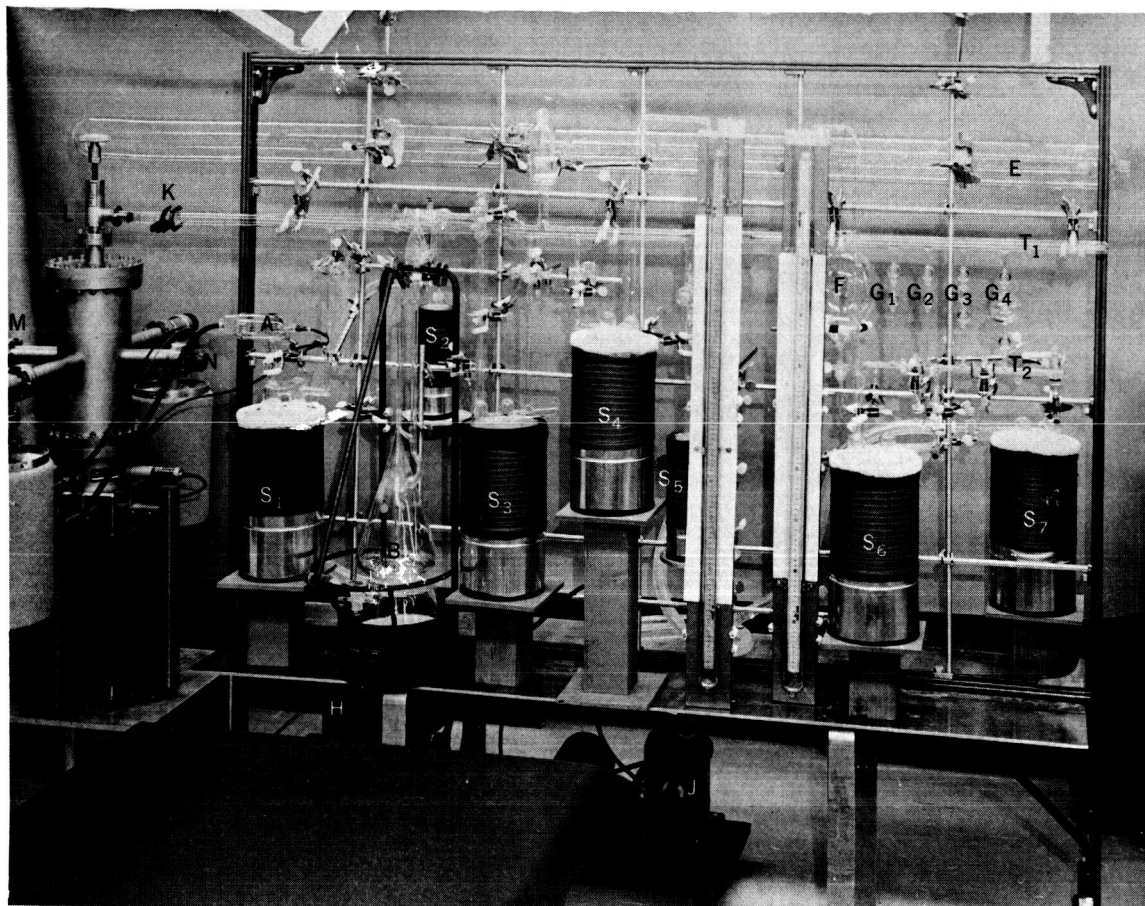


Figure B-4—Workshop apparatus for calibration by pressure-division method

high-vacuum type, and are lubricated with Apiezon L grease. The McLeod gauge used in this experiment is the extended-range Model GS-110 by Consolidated Vacuum Corporation.

The volumes of gas-storage reservoirs G_1 , G_2 , G_3 , G_4 , and F (see Figure 2) were calibrated before being assembled into the system. G_1 , G_2 , G_3 , and G_4 were weighed empty, filled with mercury, and reweighed; F was filled with water from a calibrated burette. The volumes of the various glass manifolds and the expansion reservoir were determined by the application of Boyle's law.

During the last few weeks of the Summer Workshop, the Calibration and Standards Laboratory completed three separate comparison runs using the pressure-division method (Figure B-5). These four runs provided enough data to establish confidence in the pressure-division method as a basis for the comparison of vacuum gauges. Refinement of the technique will continue after the Summer Workshop session has concluded.

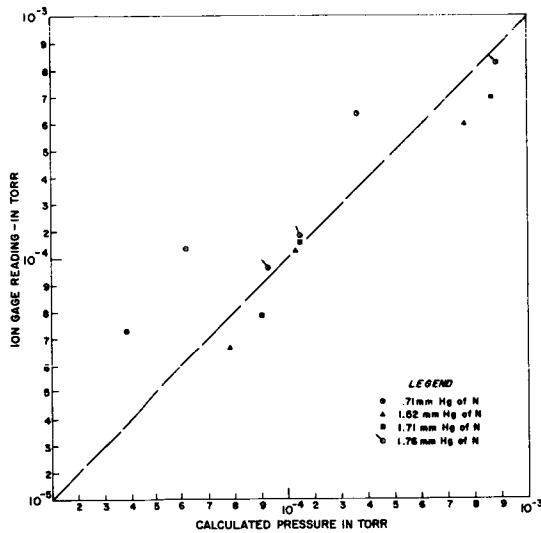


Figure B-5—Results of a series of preliminary runs showing ion gage vs calculated pressure utilizing Boyles law: $P_f V_f = P_1 V_1 + P_2 V_2$

REFERENCES

1. Report of 1962 Goddard Summer Workshop, pp. 3-26 - 3-31.
2. Knudsen, M., *Amm. Phys. (Leipzig)* 31, 633 (1910); *Am. d. Phys.* 44, 581 (1919)
3. S. Schuhmann, *proc.*
4. Beams, J.W., Spitzer, D.M., Jr., and Wade, J.P., Jr., *Rev. Sci. Inst.* 33, 151 (1962)
5. Schwarz, H., *Rev. Sci. Inst.* 31, 433 (1961)
6. Barnes, G., *Rev. Sci. Inst.* 31, 608 (1961)
7. Haller, I., and White, P., *Rev. Sci. Inst.* 34, 677 (1963)
8. Lafferty, J., *Rev. Sci. Inst.* 34 (1963)

SPACECRAFT VACUUM GAUGE COMPARISON

C. A. Baumgardner

INTRODUCTION

For a prompt start on Summer Workshop participation in the Aeronomy and Meteorology Division's vacuum-gauge calibration program, Team B decided to get some practical experience in the technical aspect of the program by working on some current problems. The work was divided in two parts: evaluating an ultrahigh-vacuum calibration system built for Goddard in 1961 by National Research Corporation, and designing and building a high-vacuum calibration system.

EVALUATION OF NRC-BUILT SYSTEM

The NRC system is a series of chambers separated by rotating plates in which there are openings of various accurately measured sizes. Pressure in each chamber can be reduced by pumping, and pressure ratios can be changed by magnetically rotating the plates between the chambers and above the pumps in order to expose different sizes of openings. As pressure is reduced in succeeding chambers, kinetic theory calculations can determine the pressure ratio between the first and last chambers. A McLeod gauge connected to the first chamber can be used to compare gauges on the last chamber in the ultrahigh-vacuum region. Reference 1 gives a more complete description of this system.

In order to make full use of this system, several questions needed answering. These included: evaluation of a McLeod gauge to be used with the system; determining whether leakage between stages was appreciable; determining pump speeds accurately; and studying the effect of adsorption phenomena in the last chamber. The group using the equipment was busy calibrating flight gauges, and the system was being used to compare the output of a secondary standard ionization gauge with the others being calibrated.

Even if time were available during which the equipment was not needed for comparing gauges, it would have taken many months to answer all the questions. Team B learned that NRC had built an improved version of the system being used at Goddard, and was offering to calibrate gauges with it. Upon investigation, it was found that the system had been generally simplified and the pressure range reduced. Five improvements were particularly noteworthy.

(1) One chamber was removed and the size of the chambers was reduced. This makes the system more reliable, but provides a smaller working range of pressures (between 10^{-4} and 10^{-8} torr).

(2) The plates above the pumps which previously rotated to change the size of the orifices were replaced by fixed plates with a single orifice; this minimizes leakage and helps in determining pumping speeds more accurately, but also serves to reduce the pressure range.

(3) Instead of the rotating-plate method of changing the orifices between chambers, a lever working through a stainless steel bellow operates to open or close the larger of two fixed orifices; this eliminates interstage leakage, but (as with the rotating plate) it does require an operator with a feeling for the system to manage the lever.

(4) Quartz lamps suspended inside the final chamber are used for bakeout instead of the clumsy oven arrangement in the Goddard system. This does not noticeably affect the normal calibration operation.

(5) Copper gaskets instead of O-rings are used to seal the orifice plates between stages.

In using the Goddard system, three points have been determined:

- The pressure ratio between stages is independent of the pressure in the molecular flow region. This was ascertained by using four ionization gauges, previously compared with one another, on different stages and changing pressures.
- The pressure ratio is as predicted by kinetic theory calculations; this was verified by interchanging the gauges between stages.
- To first order, the pressure ratio is independent of the molecule used.

The McLeod gauge, which is too time-consuming in operation, was not used constantly with the system; an ion gauge was used on the first stage.

After studying the system NRC built for Goddard, and in view of the points mentioned above, I have concluded that the system is not yet a practical "absolute" calibration system (the system is absolute when used with a McLeod gauge, which is impractical; when used with a secondary standard ionization gauge, it is more practical, but not absolute). The fact that pumping speeds can change radically does create uncertainties in the accuracy of the calibration, although this effect is minimized by the use of the orifices above the pumps. However, in view of the quick pressure response of the system, and the dearth of equipment available for doing the same job, I conclude that it would be advantageous to Goddard to improve the present equipment and put it to its intended use.

DESIGN OF HIGH-VACUUM SYSTEM

As use of a McLeod gauge on the orifice system is impractical, a system was designed and built which could calibrate a secondary standard ionization gauge for use on

the NRC-built system. This high-vacuum system can also be used for routine comparison and similar studies of other gauges.

Figure B-6 is a diagram of the system, which consists of a #304 stainless steel cylinder 17 inches long and 7 inches in diameter, pumped by a 36-liter-per-second oil-diffusion pump and forepump. Pressure is regulated by adjusting the gas inflow through a gas-inlet system consisting of a desiccant, a variable leak, and a cold trap. The pump and leak communicate with the cylinder through a manifold, a 3-inch length of 2-inch-diameter pipe; if the connection were direct, the pump and leak would affect the readings of the gauges on the cylinder.

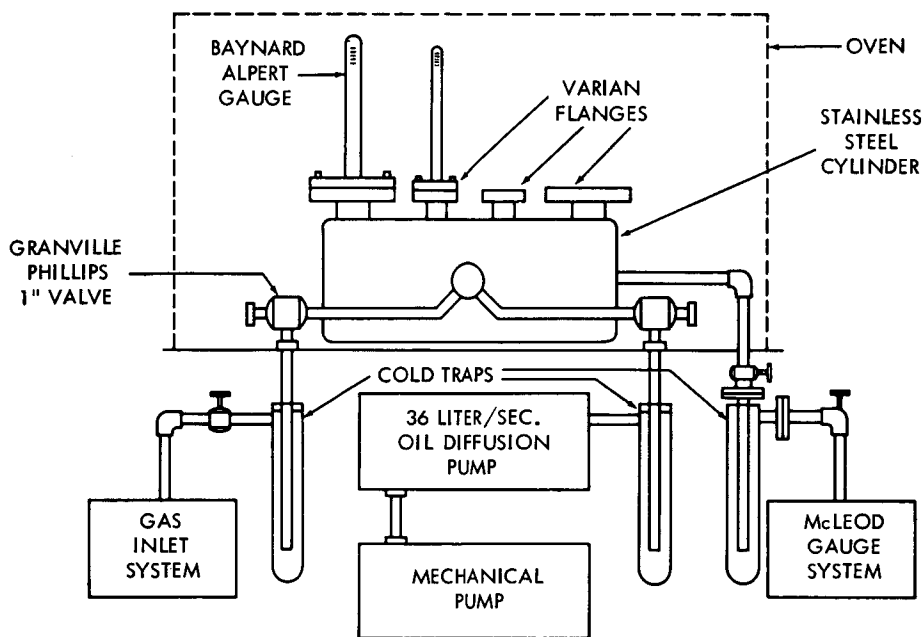


Figure B-6—High-vacuum calibration system, Schematic Diagram

The gauges for calibration are attached to the cylinder on four flanges welded to the cylinder; these flanges are the same type as those on the orifice system, so that the ionization gauges can easily be interchanged between systems. At one end of the cylinder is an outlet to the calibration standard, which can be a multiple-compression McLeod gauge as used by Kriesman,² requiring lengthy evaluation as do all McLeod gauges, or a pressure-division system as discussed in the article by Dr. Gavis in this report, if that system should prove more practical.

Several steps have been taken to reduce ultimate pressures. In addition to the usual cold traps between the cylinder and the diffusion pump and between the cylinder and the McLeod gauge, a cold trap is used to collect condensables (primarily water vapor and hydrocarbons) in the incoming gas. All parts of the system above the line in Figure B-6

are degassed by baking to 400°C. The cylinder and tubing have been electropolished. All valves are Granville-Phillips valves except the one immediately before the McLeod gauge, which is a Veeco stainless steel bellows valve with Teflon gaskets. All welds have been made on the inside except the final capping at one end of the cylinder. Figure B-7 shows the system with three of the flanges blanked off; the cold trap and the valve immediately before the McLeod gauge had not yet been installed.

The best way to point out some problems in calibration is to describe how a calibration run actually will be made. The gauges are attached with the system at atmospheric pressure. Any valving between the cylinder and the gauge would seriously affect the conductance and cause a pressure differential between the cylinder and the gauge. The system is then pumped down, checked for leaks, and baked out; bakeout time is proportional to the amount of time that the system was open to the atmosphere, and for dirty systems can be as long as 15 hours or more. Bakeout usually runs overnight, during which time a thermocouple located directly below the short manifold and attached to a relay will keep the temperature constant at about 200°C. The temperature is then raised in steps to 400°C and lowered again. After bakeout, the traps are filled, the system is pumped down, the electronic equipment is attached, and the gauges are degassed.

The calibration run begins at this point. The gas in which the gauges are to be calibrated is leaked into the system until the desired pressure is reached. The gauges are allowed to level out, showing that equilibrium has been reached; then another wait of about 5 minutes is required to ensure that the McLeod gauge has reached the same pressure, a time lag caused by the tubulation of the gauge. Measurements are taken at increasing pressures, then repeated at decreasing pressures. The writer had no opportunity to make a calibration run on this system, as time barely sufficed to complete the system itself.

Upon completion, the system pumped down to 10^{-6} torr in a few hours, and reached 2×10^{-8} torr after one bakeout. Although there was no evidence of any leakage, there appeared to be outgassing from a 10-inch length of stainless steel tubing connected directly to the main cylinder under the table, where it was not baked out but was heated with a hot-air gun. Electrical heating tape was wrapped around this tubing for use in future bakeouts, which should permit attainment of much lower pressures. This system, therefore, appears usable for ultrahigh-vacuum comparisons as well as for high-vacuum calibration.

Two improvements are possible in a system of this type. The pumping can be made more efficient by using a pump which does not have to be trapped from the system; this would reduce the ultimate pressures and time the time needed for pump-down, because pump speed is now limited by the cold trap and the connected tubing. Also, locating the McLeod gauge closer to the vacuum chamber than was possible in our arrangement would reduce the length of tubing necessary and thereby make measurements more reliable.

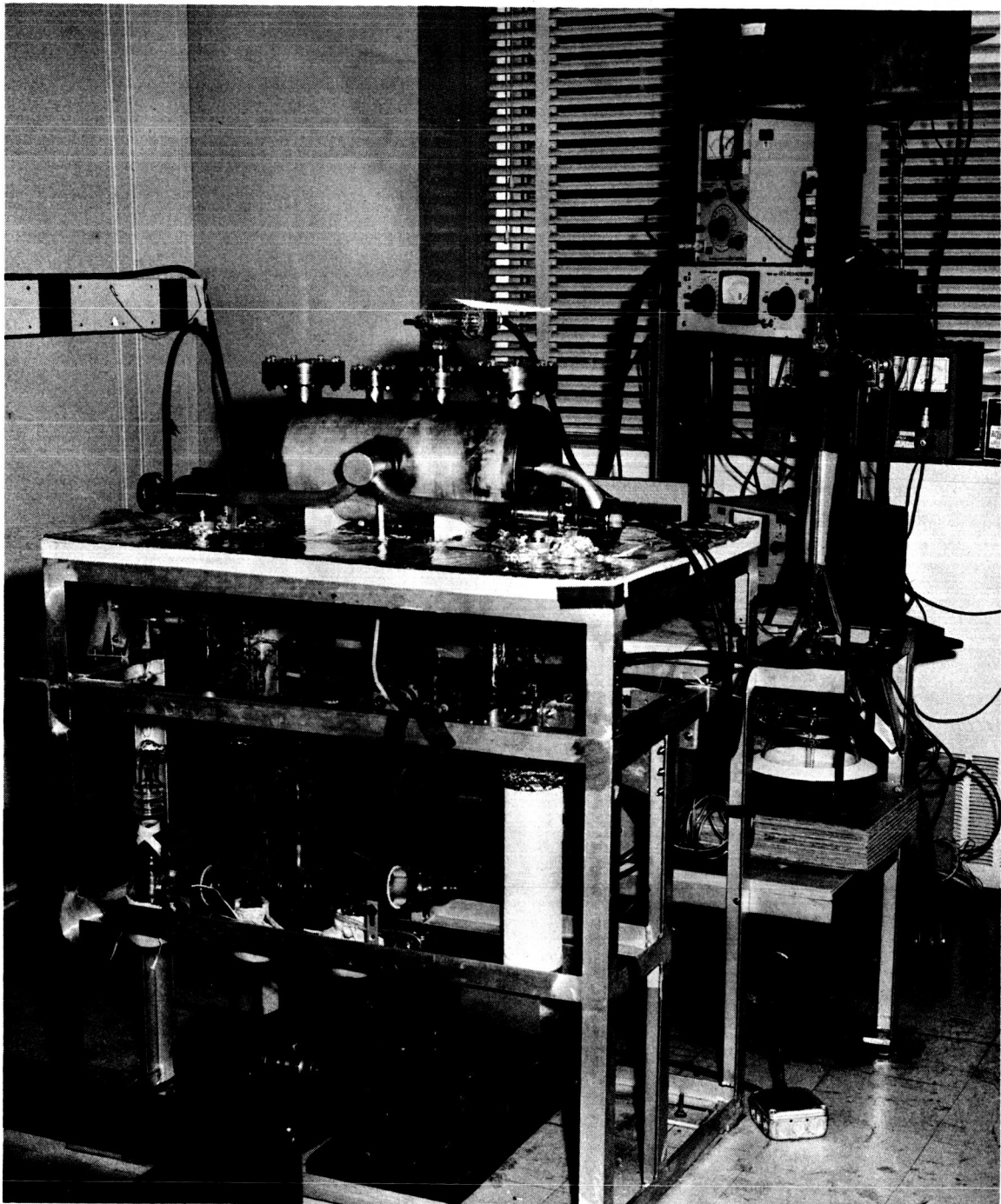


Figure B-7—High-vacuum calibration system

RECOMMENDATIONS

As no ultrahigh-vacuum gauge-calibration system suitable for use in the Test and Evaluation Division appears to be forthcoming, the present situation would, in my opinion, be considerably improved by building a comparison system similar to that just described. Standard gauges to be used with the system could be obtained from the Aeronomy and Meteorology Division if their present equipment is improved as recommended earlier in this report.

The writer's appreciation is extended to George Newton and his staff, Physics Branch, A&M Division, for their willing assistance, and to the Fabrication Division, especially the welding section, for their excellent work and cooperation. Thanks are also due to Frank Torney, National Research Corporation, for the discussions referred to in the report.

REFERENCES

1. Roehrig, J.R., and J.C. Simons, Jr., "Accurate Calibration of Vacuum Gauges to 10^{-9} Torr," 1961, Transactions of the American Vacuum Society Symposium, Vol. I.
2. Kriesman, W.S., "Extension of the Low Pressure Limit of McLeod Gauges," Geophysics Corporation of America, TR# 63-8-N.

N64-28209

PRELIMINARY DESIGN ANALYSIS FOR AN ULTRAHIGH-VACUUM SYSTEM

J. E. A. John

ABSTRACT

N64-28209

An analysis has been made to demonstrate the feasibility of using cryogenic pumping to obtain ultrahigh vacua. A chamber-within-chamber design was used to minimize real leak rates into the test chamber, the walls of the chambers being maintained at temperatures of 77°K, 20°K, and 4.2°K successively by means of cryogenic fluids. Estimates were made of ultimate pressures for such a system, with and without a test object in the inner chamber. Heat loads on the chamber walls were calculated, together with the resulting cryogenic-fluid flow rates required. As a cryogenic pumping system provides no facility for pumping noncondensable gases, it was suggested that a cryosorption panel be incorporated in the cryogenic pumping system, each system being complementary to the other.

John

INTRODUCTION

Most of our information on the effect of the space environment on materials, friction, surfaces, and so forth has been obtained from work in space-simulation chambers with pressure limits of the order of 10^{-9} to 10^{-10} torr. Actual pressures of space, however, are several orders of magnitude below this limit. Materials in this environment are likely to encounter unexpected effects at these lower pressures. It appears advisable, therefore, to provide as a testing environment an ultrahigh-vacuum chamber capable of reaching 10^{-14} to 10^{-15} torr, at least on a small scale.

High pumping speed must be provided to attain an ultrahigh vacuum, and at the same time initial and real leak rates must be minimized. The system described here, which uses cryogenic pumping, should be capable of attaining ultrahigh vacua in the 10^{-14} torr range; this report was written to demonstrate the feasibility of using a cryogenic pumping system for the task in question.

SYSTEM DESIGN AND OPERATION

Figure B8 is a schematic diagram of the chamber-within-chamber design which was chosen to decrease the real leak rate into the inner chamber. In operation, with all valves open, the entire system is first pumped down with a mechanical pump and an oil-diffusion

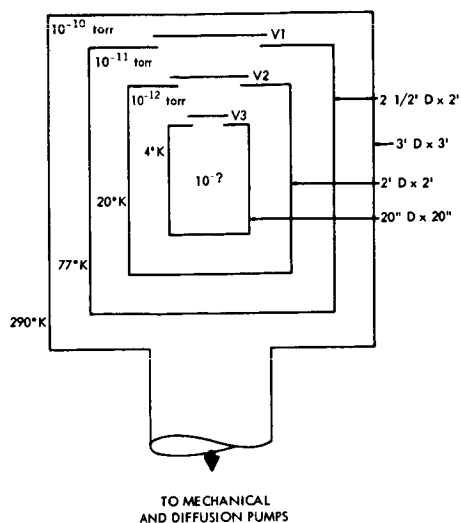


Figure B-8—Ultrahigh-vacuum cryogenic pumping system, Schematic Diagram

pump with LN² baffle; the first valve (V1) is closed and LN² is circulated through the outer chamber walls. Next, V2 is closed and the central chamber outer wall is cooled to 20°K with GHe. Finally, V3 is closed and the inmost chamber walls are cooled to 4.2°K with LHe.

The ultimate pressure obtainable in the inner chamber obviously depends upon the pressure in each of the other chambers; therefore, it would be desirable to begin with as low a pressure as possible in the outermost chamber. A 3- by 3-foot chamber and pumping system are now available; with double O-rings and guard vacuum, vacua of 5×10^{-8} torr have been reached, the limitation being due to penetration of gas through the elastomer O-rings. Farkass¹ claims that, in a similar system of 75 ft³ volume, vacua

of 10^{-11} torr have been achieved, the only difference being that the O-rings were cooled to -20°C to minimize gas permeation. It appears, therefore, that the present system should be equipped with cooling channels to improve the initial vacuum; an overall system pressure of 10^{-10} torr should be attainable.

HEAT LOADS

Heat loads on the cryogenic fluids must be calculated so that the required flow rates may be determined. As the system is to be pumped to 10^{-10} torr before the cryogenic fluids are introduced, heat transfer to the shrouds is due solely to radiation. An additional heat load is incurred from the latent heat of the gases being condensed in the chamber, but this is insignificant because of the relatively small amounts of gas present. Chamber dimensions assumed for the following calculations are those shown in Figure B8. Radiative heat transfer from one surface to another enclosing it is given by:

$$q = \frac{(0.1714 \times 10^{-8}) (T_1^4 - T_2^4)}{\frac{1 - E_1}{E_1 A_1} + \frac{1 - E_2}{E_2 A_2} + \frac{1}{A_1}}$$

where

q = heat transfer in BTU/hr

A₁ = surface area of enclosed surface (ft²)

A_2 = surface area of enclosing surface (ft²)

E_1, E_2 = emissivities of surfaces

T_1, T_2 = surface temperatures

The equation assumes that the absorptivity and emissivity of the surfaces are equal. It is assumed further that the emissivities of all surfaces are 0.5. This is a conservative estimate; fairly extensive data on the emissivity of condensate-coated surfaces is given by Moore.² Table B-1 gives the results of the radiative heat-transfer calculations. The outer chamber surface was assumed to be at room temperature (290°K), the inner chamber empty.

Table B-1
Radiative Heat-Transfer Calculation

Shroud	Surface Area (ft ²)	Surface Temperature (°K)	q (BTU/hr)
LN ₂	29.4	77	1390
GHe	18.9	20	4.53
LHe	13.0	4.2	.0014

The flow rate of liquid helium required is particularly interesting, as the capacity of the available ADL-Collins helium cryostat is limited to 6.5 liters per hour. The latent heat of LHe is 2.5 BTU/liter, so that the heat load given corresponds to a flow of .00056 liters per hour for an empty chamber. If an object is in the test chamber, the heat load on the LHe chamber walls is greatly increased; for example, if a 6-inch-diameter black sphere is maintained at 290°K, the LHe requirement goes up to 38 liters per hour.

Another consideration is the amount of LHe required for cooldown. If the inner chamber walls are made of aluminum 1/16-inch thick, the amount of heat that must be withdrawn to cool from 100°K to 4.2°K is given by:

$$Q = m C_p \Delta T$$

where

m = mass of aluminum (lbs)

Q = heat removed (in BTU)

C_p = mean specific heat of aluminum over the range 100°K to 4.2°K

For this system, Q was calculated to be 49.7 BTU, requiring 19.9 liters of helium. This calculation assumes the shroud to be precooled with LN_2 to $100^\circ K$; also, no allowance was made for the LHe feed lines, etc. The quantity of LHe needed for the cooldown will probably be greater than the amount calculated.

LEAK RATES

Two leak rates, real and virtual, must be considered, the virtual rate being attributable to outgassing. To estimate a real leak rate, assume as a worst possible case that an orifice of 1 cm^2 area exists in the inner chamber. The conductance of such an orifice is given by:

$$C = 3.64A \sqrt{\frac{T}{M}} \text{ liters/sec} \quad (\text{Reference 3})$$

where C = conductance
 A = orifice area (cm^2)
 M = molecular weight of gas

It is assumed that the majority of the residual gas at this point is hydrogen; all others (except He) would have been condensed at these temperatures. For the "worst possible" case being considered, $C = 5.15$ liters per second for hydrogen. The rate of leakage due to this real leak is given by:

$$Q = C\Delta P$$

where Q = inleakage in torr liters per second
 ΔP = pressure difference across orifice

The pressure inside the GHe chamber is of the order of 10^{-12} torr and that inside the test chamber somewhat less, so that

$$Q = 5.15 \times 10^{-12} \text{ torr liters per second}$$

This extremely small leak rate points up the value of the chamber-within-chamber design. Valve-operating problems at these high vacua are minimized; absolute closure is not required, because reduction of the conductance across the valve to a tolerable level is sufficient. A metal plate dropped by some external means (such as a magnet) would suffice.

For the virtual leak rate, there are two possibilities: clean and empty chamber, or test object in chamber. In the former situation, outgassing from walls would take place at 4.2°K. As outgassing rates decrease logarithmically with temperature,⁴ it can be assumed that, at 4.2°K, virtual leak rates are negligible. However, with a test object at 290°K, the outgassing rate cannot be ignored. Dayton⁴ gives data on outgassing rates for various metals. For stainless steel (polished, vapor-degreased), the outgassing rate is 1.4×10^{-9} torr liters sec^{-1} cm^{-2} after 10 hours' pumping. For a 6-inch-diameter sphere, this corresponds to a virtual leak rate of 1.0×10^{-6} torr liters per second.

PUMPING SPEEDS

Kinetic theory gives the number of liters per second of a gas striking the surface of a container per unit area:

$$S_1 = \frac{1}{4} (14551) \sqrt{\frac{T}{M}} \quad (\text{Reference 3})$$

For a cryopumping surface, pumping speed S is given by:

$S = f S_1$, where f = sticking coefficient, depending on surface temperature and vapor pressure of the gas being cryopumped.

Again, assuming that the majority of the residual gas in the inner chamber is hydrogen, it is necessary to obtain f for hydrogen at 4.2°K. Bachler, Klepping and Mascher⁵ give experimental values of approximately 0.01, yielding a pumping speed:

$$S = 0.0515 \text{ liters sec}^{-1} \text{ cm}^{-2} = 624 \text{ liters sec}^{-1}$$

ULTIMATE PRESSURE

The ultimate pressure obtainable in the test chamber is a balance between leak rate and pumping speed. For a clean and empty chamber,

$$P_{\text{ultimate}} = \frac{Q}{S} = \frac{5.15 \times 10^{-12}}{624} = 8.25 \times 10^{-15} \text{ torr}$$

For a test chamber with a 6-inch-diameter stainless steel test object, however, the ultimate pressure is not as low; assuming that most of the outgassing load is hydrogen (the worst case, because cryogenic pumping speeds for other gases would be higher),

$$P_{\text{ultimate}} = \frac{1.0 \times 10^{-6}}{624} = 1.6 \times 10^{-9} \text{ torr}$$

PUMPING OF NONCONDENSABLE GASES

The limitation on any cryogenic pumping system is the inability to pump the noncondensable gases hydrogen, helium, and neon. For example, the relatively low pumping speeds for hydrogen must restrict the ultimate pressure obtainable in the test chamber, as shown previously. As an extreme case, if the entire surface of the test chamber were coated with hydrogen condensate, the pressure in the chamber would be the vapor pressure of hydrogen at 4.2°K, approximately 5×10^{-7} torr.⁵ Another problem is that there is no provision for pumping helium gas, which may be present because of leakage from the LHe system through the chamber walls.

Two methods are suggested for overcoming these difficulties: First, pumping the LHe under vacuum, in order to reduce the chamber-wall temperature; second, installation of a cryosorption panel to take care of the noncondensable gases. The first method was tried by Bachler et al.,⁴ operating at 2.5°K; sticking coefficients for hydrogen gas were increased fiftyfold, similarly increasing pumping speeds. However, a system for pumping LHe under vacuum would be inherently expensive, and would not simultaneously provide a capability for pumping gaseous helium.

Installation of cryosorption panels appears to be the better method. Experimental work at Linde⁶ has shown that pumping speeds for hydrogen at 20°K and 10^{-8} torr of the order of 7000 liters/sec ft² can be obtained, along with similarly high speeds for helium at 4.2°K, using a panel consisting of molecular sieve bonded to an aluminum plate.

For the ultrahigh-vacuum system under consideration, then, the incorporation of a cryosorption system into the cryogenic pumping system appears to allow the pumping speeds necessary in areas where the cryogenic system alone would be insufficient.

REFERENCES

1. Farkass, I., Gould, P.R., and Horn, G.W., " 1×10^{-11} Torr in Large Metal Chambers," Trans. AVS, 1962
2. Moore, B.C., "Effect of Gas Condensate on Cryopumping," Trans. AVS, 1962
3. Dushman, S., "Scientific Foundations of Vacuum Technique," 2nd edition, John Wiley and Sons Inc., 1962
4. Dayton, B.B., "Relations Between Size of Vacuum Chamber, Outgassing Rate, and Required Pumping Speed," Trans. AVS, 1959
5. Bachler, W., Klepping, G., and Mascher, W., "Cryogenic Pump Systems Down to 2.5°K," Trans. AVS, 1962
6. Stern, S.A., et al., "The Cryosorption Pumping of Hydrogen and Helium at 20°K," (interim report) Arnold Engineering Development Center, AEDC-TDR-62-200, October 1962

abstract p B-35

N64-28210

FEASIBILITY OF LIQUID-METAL VACUUM SEALS

J. E. A. John, D. A. Akins, G. S. Pick

INTRODUCTION

A basic component of any ultrahigh-vacuum system is a seal capable of isolating a test chamber from its higher pressure surroundings.

Two of the most common vacuum seals now in use are the elastomer O-ring seal and the metallic shear seal. The former has the problem of outgassing and gas permeation; the latter requires a large force per unit seal-length to maintain the sealing action. The search for a seal which would provide minimal virtual and real leak rates in a chamber, without requiring a large force to consummate the seal, led to investigation of a liquid-metal seal.

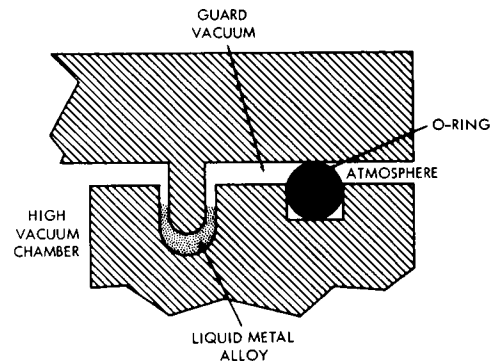


Figure B-9—Liquid metal seal

Figure B-9 shows the method of applying a liquid-metal seal to a high-vacuum system. A guard vacuum isolating the liquid metal from atmospheric pressure is necessary to prevent the atmospheric pressure from pushing the liquid metal into the chamber. The liquid can withstand a small pressure difference, because of the surface tension forces between the liquid and the solid metallic surfaces of the flanges.

Desirable properties for a liquid-metal sealant include: low vapor pressure, high surface tension, good wetting properties on metals, low melting point, and noncorrosive action with the flange materials (at least at room temperature, and preferably also at bakeout temperatures). An alloy of gallium, indium, and tin proposed by Milleron appears to satisfy these requirements to a degree. Table B-2 shows properties of this alloy.

Table B-2

Properties of Liquid-Metal Surface

Percent Composition of Alloy by Weight	Melting Point (°C)	Vapor Pressure (mm Hg)		Surface Tension (dynes/cm.)	
		(mm Hg)	(°C)	(dynes/cm.)	(°C)
62.5 Ga, 21.5 In, 16 Sn	10.7	< 10 ⁻⁸	500	> 500	500

EXPERIMENTAL APPARATUS AND TECHNIQUES

The experimental assembly for applying and testing the liquid-metal seal consisted of a cylindrical stainless steel chamber mounted on a 140-liter vac ion pump. The upper flange of the chamber contained the liquid-metal sealant reservoir. Copper shear seals were used between the top and intermediate sections, and between the intermediate section and the ion pump (Figure B-10). The top plate included a finger which protruded into the liquid-metal reservoir and effected the seal, as shown in Figure B-9.

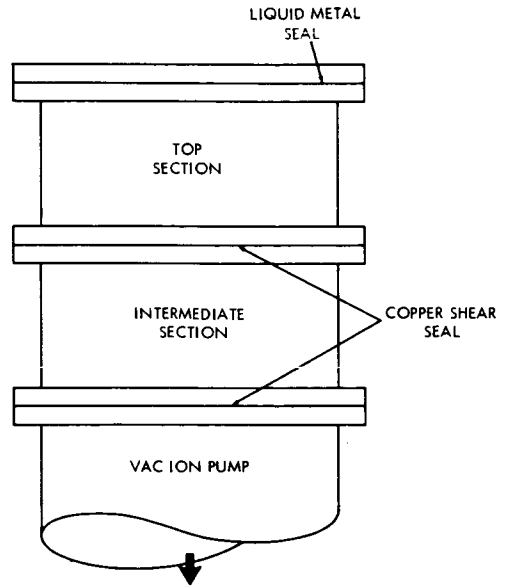


Figure B-10—Seal test apparatus, Structural Diagram

Figure B-11 is a complete flow diagram of the apparatus. Provision was made to cool the liquid metal in place below its freezing point, in order to investigate the feasibility of using the metal as a cast seal. Cooling channels were machined into the upper flange immediately above and below the seal area. Figure B-12 is a photograph of the apparatus.

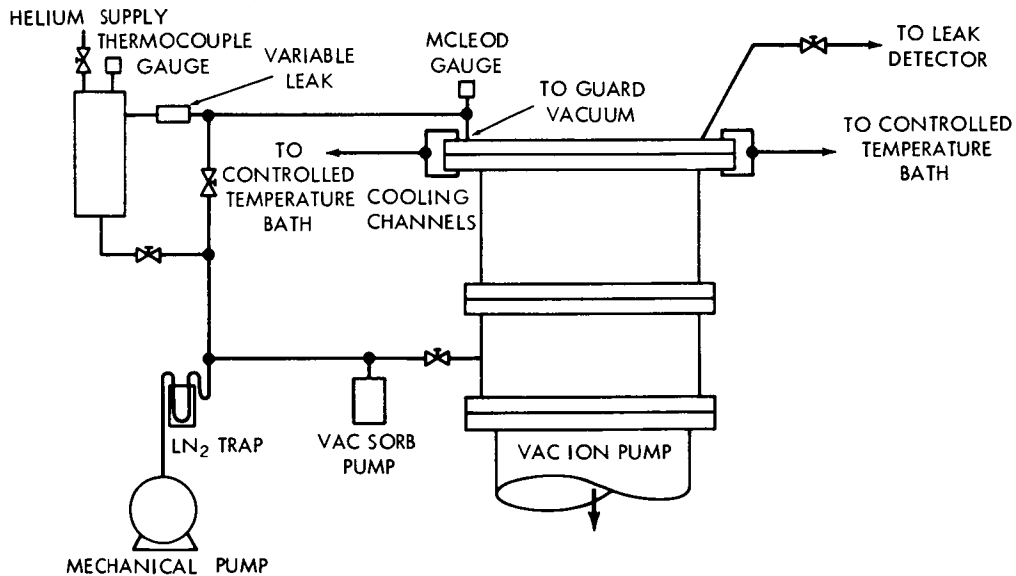


Figure B-11—Seal test apparatus, Flow Diagram

INSIDE VIEW OF EXPERIMENTAL SEAL

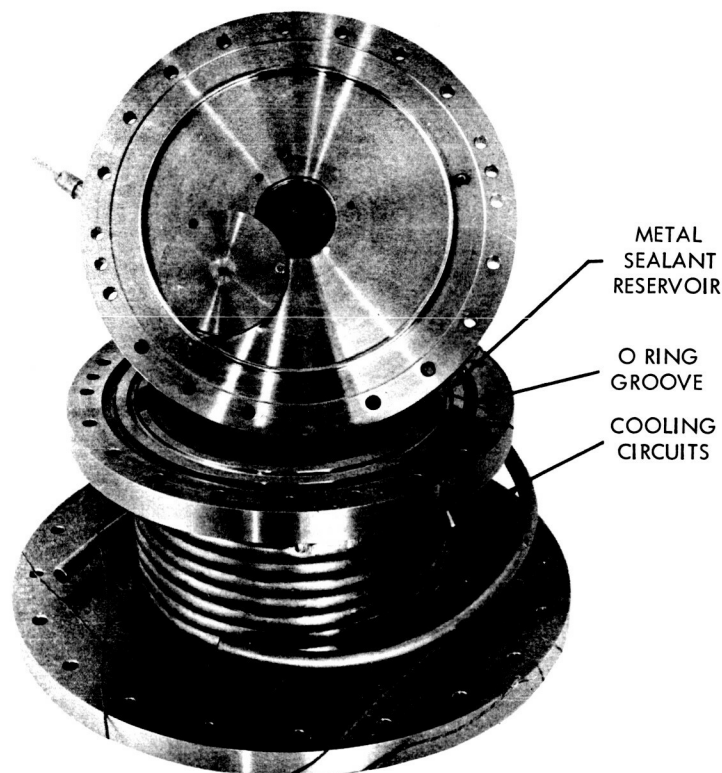


Figure B-12—Seal test apparatus, Interior view

PREPARATION OF SEAL

Before testing the sealant, it was necessary to carry through an extensive procedure to prepare the sealant and the contacting surfaces.

First, the alloy was vacuum-pumped for several hours to remove air bubbles trapped and dissolved in the liquid. Next, the metal surfaces to be in contact with the liquid were cleaned, to ensure wetting of the surfaces. The cleaning procedure involved removal of grease, by rinsing with acetone; polishing the surfaces with moist levigated alumina on a fine cloth; rinsing with tap water; rinsing with distilled water; rinsing with acetone to dry the surfaces. A small amount of gallium was then spread over the "finger" in the top plate and over the liquid reservoir. The flange containing the reservoir was levelled. Finally the reservoir was filled with gallium alloy, and the mating flange with top plate lowered gradually into place. Four C-clamps were used to provide the small amount of force needed to achieve the O-ring seal.

PUMPDOWN PROCEDURE

The guard vacuum and the chamber were first pumped down simultaneously with a mechanical pump, care being exercised that the pressure difference between the chamber and the guard vacuum was never great enough to blow the liquid metal into the chamber. A pressure difference of 150 mm of mercury across the seal could be tolerated.

To lower the pressure further in the guard vacuum and the chamber, a zeolite vac-sorb pump was used to reach a pressure of approximately 1 micron, read on a mercury McLeod gauge. At this point, the guard vacuum was shut off from the pump and helium gas was admitted into the guard vacuum up to a pressure of 500 microns. The chamber was connected to a mass-spectrometer leak detector with a sensitivity of 3×10^{-10} standard cc of helium per second. If no leaks were found at this time, the vac ion pump was turned on; the pressure in the system, as read on the vac ion pump cold cathode gauge, was recorded as a function of time. From the ultimate pressure on the pumpdown curve, the total of the real and virtual leak rate from the system can be found for a known pump speed. To separate the leak rate through the liquid-metal seal from that of the rest of the system, the test just described was repeated with the top section removed, using a blank plate and a copper shear seal on top of the intermediate section.

Any difference between the leak rates for the two experiments could be due only to outgassing from the walls of the top section (presumably very small) or leakage through the liquid-metal seal.

Next, the vac ion pump was baked out and the above experiments were repeated. The effect of the bakeout was limited, unfortunately, because heaters were not available to bake out the chamber itself.

As an additional experiment after the ultimate pressure had been reached with the liquid metal in place, the metal was frozen by passing cold nitrogen gas through the cooling channels. The effect on the ultimate pressure was noted for this case without using a guard vacuum.

RESULTS

With a helium pressure of 500 microns in the guard vacuum, no leakage was detected by the helium leak detector at a chamber pressure of 1 micron. Therefore, the leak rate through the seal was less than 3×10^{-10} standard cc of helium per second. This corresponds to 2.28×10^{-10} torr liters of helium per second.

Figure B-13 is a typical pumpdown curve. Ultimate pressures obtained for each case are given in Table B-3.

Table B-3
Ultimate Pressures Using Liquid-Metal Seal

Conditions	Ultimate Pressure (torr)
No bakeout (liquid metal)	3×10^{-8}
No bakeout (frozen)	3×10^{-8}
No bakeout (no liquid metal)	3×10^{-8}
Bakeout (liquid metal)	7×10^{-9}
Bakeout (no liquid metal)	7×10^{-9}

For each of the ultimate pressures given, a system leak rate was calculated from the expression $Q = SP$, where

Q = sum of real and virtual leak rates (torr liters per second)

S = pumping speed at ultimate pressure P (liters per second)

From the pump manufacturers' catalog (Varian Associates), data were obtained on pump speed vs. pressure down to 10^{-8} torr only; at this pressure, the pump speed was given as 100 liters per second, decreasing with a further decrease in pressure. Using this value (with the realization that it would be only approximate), leak rates were calculated. Without bakeout,

$$Q = 100 \times 3 \times 10^{-8} = 3 \times 10^{-6} \text{ torr liters/sec}$$

With bakeout,

$$Q = 100 \times 7 \times 10^{-9} = 7 \times 10^{-7} \text{ torr liters/sec}$$

As the addition of the liquid-metal seal did not increase the system leak rate, it can be concluded from this test that the leakage through the seal is somewhat less than 7×10^{-7} torr liters/sec.

For the type of application investigated, the liquid-metal seal presents several distinct advantages over the elastomer O-ring seal and the shear seals. Jordan² presents leak rates for elastomer seals as measured by a helium leak detector. For the best material tested, butyl, the leak rate was measured as 0.25×10^{-8} atm cc/sec/in., or 1.9×10^{-9} torr liters/sec/in. For the 5.5-inch-diameter seal tested, this would mean a leak rate of 3.3×10^{-8} torr liters per second. The liquid-metal seal yielded a leak rate at least two orders of magnitude below this on the helium leak detector. Wheeler and Carlson³ give data for the force required to make a metallic shear seal, values are approximately 2000 pounds per inch of seal circumference. For the 5.5-inch-diameter seal, this would

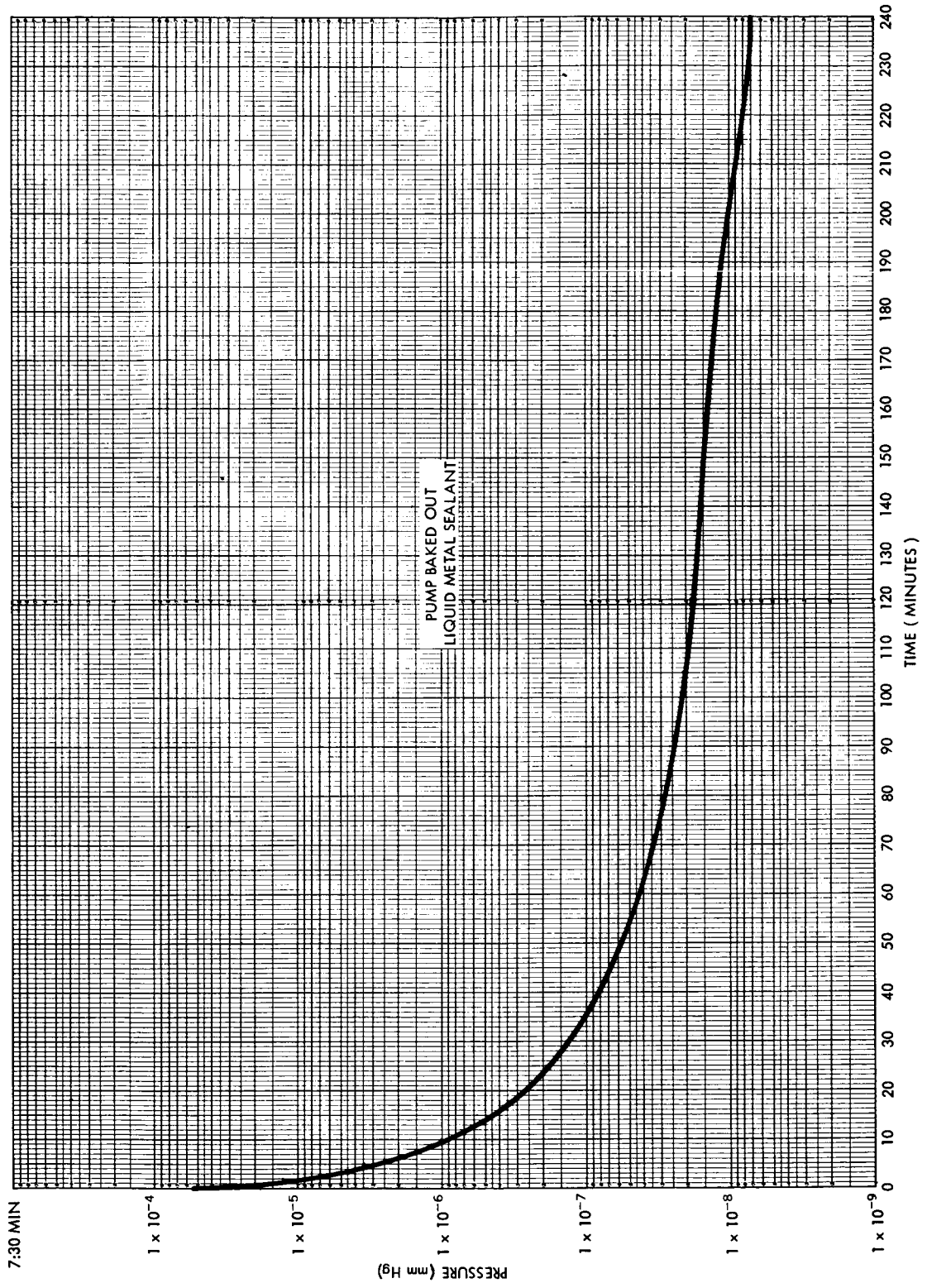


Figure B-13—Pumpdown curve for vacuum system with liquid-metal seal

require a force of 34,500 pounds, and consequently massive flanges. Liquid-metal seals are therefore more advantageous than the more conventional seals, especially those of larger diameter.

However, several problems are inherent in use of liquid-metal seals. The flange holding the reservoir must be horizontal; no misalignment can be tolerated. A guard vacuum is necessary for the liquid-metal seal; at no time, during pumpdown or during a test run, can the pressure difference between guard vacuum and chamber be more than about 150 mm/Hg, or the seal will be broken. The cast seal offers the advantage of eliminating the guard vacuum, but requires the use of cooling channels to keep the alloy solid. The alloy is extremely corrosive at bakeout temperatures; cooling would again be necessary during system bakeout to prevent corrosion of the stainless steel flanges. Finally, the procedure of preparing the liquid metal and the flanges for the sealing operation is a fairly extensive one, consuming several hours at least. The elimination of any step in the procedure would be sufficient to prevent a seal.

CONCLUSION *N64-28210*

A procedure was found for using a liquid-metal seal in an ultrahigh-vacuum system. Leak rates through a 5.5-inch-diameter seal were so small that, with a chamber pressure of 1 micron, there was no indication on a leak detector with a sensitivity of 3×10^{-10} standard cc of helium per second. Also, leakage was small enough to give no appreciable in-leak to a system at a chamber pressure of 7×10^{-9} torr.

The liquid-metal seal, essentially eliminating gas permeation and requiring a very small force per unit length to achieve a seal, has several advantages over the conventional O-ring and metallic shear seals. However, because of the extensive preliminary procedure required to prepare the flanges and liquid metal for the seal, the liquid-metal seal would be difficult to make use of on a routine basis.

Author

REFERENCES

1. Milleron, N., "Utilization of the Surface Tension of Liquid Metals in Making High-Vacuum Seals," American Vacuum Society Transactions (1957).
2. Jordan, J.R., "New Developments in Vacuum Sealing," American Vacuum Society Transactions (1961).
3. Wheeler, W.R., and Carlson, M., "Ultrahigh-Vacuum Flanges," American Vacuum Society Transactions (1961).

PROJECT C: Magnetic Environment Simulation

CONTENTS

INTRODUCTION	C-2
D. L. Waidelech	
AC DEMAGNETIZATION OF SATELLITE COMPONENTS	C-5
John D. Watson	
SURVEY OF THE LITERATURE ON NONMAGNETIC MATERIALS FOR USE IN SPACECRAFT	C-13
J. B. Crooks	
TESTING OF NONMAGNETIC MATERIALS	C-61
E. Levy	
THE FOUR-CIRCULAR-COIL SYSTEM	C-77
THE FOUR-SQUARE-COIL SYSTEM	C-91
THE SIX-CIRCULAR-COIL SYSTEM	C-113
D. L. Waidelech and M. Speiser	
ANALYSIS OF FOUR-COIL SYSTEMS OF FINITE COIL-WINDING AREA . . .	C-121
George Rinard	

ILLUSTRATIONS

<u>Figure</u>		<u>Page</u>
C-1	Artist's Concept of Tumbler and Coil	C-6
C-2	AC Demagnetization Apparatus, Structural Diagram	C-6
C-3	Tumbler Inside Coil	C-7
C-4	Tumbler Removed from Coil	C-7
C-5	Coil Calibration Curve	C-8
C-6	AC Demagnetization Apparatus, Schematic Diagram	C-8
C-7	Demagnetization of 3.5-Inch Steel Rod as a Function of Initial Field Strength	C-10
C-8	Astatic Magnetometer, Schematic Diagram	C-62
C-9	Astatic Magnetometer	C-62
C-10	AC Induction Primary and Secondary Coils	C-64
C-11	AC Induction Apparatus, Schematic Diagram	C-64
C-12	Magnetic Measurement Apparatus Used at NOL	C-64
C-13	DC Induction Coil System	C-65
C-14	Galvanometer, Lamp, and Scale	C-66
C-15	Preliminary DC Circuit, Schematic Diagram	C-66

<u>Figure</u>		<u>Page</u>
C-16	RC-Coupled Amplifier with DC Apparatus	C-67
C-17	Difference Amplifier, Schematic Diagram	C-68
C-18	Galvanometer Calibration Circuit, Schematic Diagram	C-75
C-19	Four-Circular-Coil System	C-78
C-20	Geometry for One Circular Coil	C-79
C-21	Geometry of the Four-Circular-Coil System	C-79
C-22	Plot of Magnetic-Field Intensity, Four-Circular-Coil System	C-80
C-23	Coil Geometry Used in Calculating (a) One Coil, (b) Two Neighboring Coils	C-81
C-24	Geometry of the Four-Square-Coil System	C-91
C-25	Geometry of One Square Coil	C-91
C-26	Geometry for the Field-Intensity Calculations for One Square Coil	C-96
C-27	Geometry for the Field-Intensity Calculations for Four Square Coils.	C-96
C-28	Plot of Magnetic-Field Intensity, Four-Square-Coil System ($\phi = 0^\circ$)	C-97
C-29	Plot of Magnetic-Field Intensity, Four-Square-Coil System ($\phi = 15^\circ$).	C-97
C-30	Plot of Magnetic-Field Intensity, Four-Square-Coil System ($\phi = 30^\circ$).	C-98
C-31	Plot of Magnetic-Field Intensity, Four-Square-Coil System ($\phi = 45^\circ$).	C-98
C-32	Dimensions for Inductance Calculation of (a) Four-Coil System, (b) Cross Section of Single Coil	C-99
C-33	Geometry of the Six-Coil System	C-113
C-34	Geometry for a Single Coil	C-113
C-35	Region of Possible Solutions	C-114
C-36	Cross Sectional View of Circular or Square Solenoid	C-123
C-37	Geometry for Square Solenoid	C-126

TABLES

<u>Table</u>		<u>Page</u>
C-1	Comparison of AC and DC Deperming	C-9
C-2	Eddy-Current Effects as a Function of θ	C-74
C-3	Electrical Resistivities	C-74
C-4	Parameters for the Braunbek Coil System	C-77
C-5	Parameters for Systems with Opposing Currents	C-79
C-6	Parameters for Systems with Currents in the Same Direction	C-94
C-7	Parameters for Systems with Currents in the Opposite Direction	C-95
C-8	Parameters for Systems with Integral Turn Ratios	C-95
C-9	Computed Solutions for the Six-Coil System	C-115
C-10	Comparison of Solenoid Dimensions to Those of the Ideal Case	C-128

SUMMER WORKSHOP 1963

Program Outline and Team Participants

PROJECT C: Magnetic Environment Simulation

Study Topics

- C-1 Analysis of six-coil system
- C-2 Analysis of four-coil system with finite coil dimensions
- C-3 Synthesis of the total field from that of components
- C-4 The testing of non-magnetic materials
- C-5 Properties of non-magnetic materials

TEAM C

Academic Personnel

Goddard Personnel

		<u>Code</u>
*Dr. Donald L. Waidelich	Chauncey L. Parsons	324
PRINCIPAL INVESTIGATOR	STAFF ADVISOR	
John D. Watson	William G. Brown	325
George A. Rinard	Catherine H. Evans	542
Mario Speiser	Robert E. Gebhardt	325
Jonathan B. Crooks	William D. Kenney	324
Edward K. Levy	Dr. Norman F. Ness	611
	NSF Summer Science Student Thomas B. Silliman	

*Continuing part-time work at Goddard on Project C.

MAGNETIC ENVIRONMENT SIMULATION

D. L. Waidelich

INTRODUCTION

Laboratory simulation of the magnetic environment in space is important in the testing of satellites and spacecraft for two principal reasons:

- The magnetic moment of the satellite will react with the magnetic field in space to produce a torque which tends to spin the satellite.
- The magnetic field of the satellite may interfere with the operation of magnetometers aboard the spacecraft which are designed to measure the magnetic field in space.

The Summer Workshop team working on magnetic environment simulation has been concerned with two principal aspects of the simulation problem: first, to make the magnetic moment of the satellite as small as possible; second, to produce as uniform a controlled magnetic field as possible for testing the spacecraft.

One problem is that of demagnetizing (or "deperming") the components of which a spacecraft is made. An apparatus was constructed that would produce a sizeable alternating field, and would at the same time rotate a component mechanically about each of three orthogonal axes in a motion closely approximating random rotation. First tests seem to indicate that the apparatus will perform successfully.

Another problem studied was that of taking the magnetic properties of several components, along with their location, and finding the magnetic properties of the facet of the spacecraft made up of these components; similarly, the properties of the facets constituting the spacecraft could be combined to produce the overall magnetic properties of the spacecraft. Some progress was made on this, but much remains to be done.

The materials of which a satellite is constructed should be as nonmagnetic as possible and at the same time must have good structural properties. A library search for references on nonmagnetic materials resulted in a bibliography of more than 300 citations; these were reviewed to determine the type of information available on each. Digesting the information led to selection and procurement of samples of nonmagnetic materials for testing and for use as standards.

Materials used in a satellite should be tested to determine just how nonmagnetic they are; for instance, ferromagnetic impurities may be present, or cold-working may cause

a normally nonmagnetic metal to become sufficiently magnetic to be unsatisfactory for the purpose. Various methods of testing for nonmagnetic properties of metals were investigated; these methods appeared to fall into two general categories—first, those involving the measurement of forces; second, those involving the measurement of induced voltages and the resulting currents.

It was desired to measure the materials at magnetic flux densities of the order of that at the surface of the earth (about 0.5 gauss, or 50,000 gammas) or less. In almost all cases, the measurement of forces required flux densities much higher than 0.5 gauss, whereas the measurement of induced voltages can be performed at 0.5 gauss or less; therefore, it was felt that the induction measurements probably would be more satisfactory. A pulsed type of circuit for making induction measurements was tested successfully, although more work needs to be done to improve its sensitivity and stability. An alternating-current circuit was also constructed, but testing was not completed.

In the production of uniform magnetic fields, the four-circular-coil system has been studied and has been used in practice. The system in which the ampere-turns of each coil are equal is called the Braunbek system, and some further calculations were made for it. Calculations were also made for systems in which the currents in one pair of coils are opposite to those in the other pair of coils; these systems have the advantage of large volume of uniformity and large access space, but have the accompanying disadvantage of having a small field constant. Calculations were made of the field intensity at various points both on- and off-axis in the four-circular-coil system; the inductance of the system was also calculated. The systems with opposing currents have the advantage of having lower inductances.

Coil systems with four square coils should have a considerable structural advantage over circular coil systems, but would have the disadvantage of introducing a circumferential variation in the field intensity. A complete analysis of the four-square-coil system was made, both for instances in which all currents flow in the same direction and for those in which two of the currents flow in a direction opposite to that of the other two coils. Results were similar to those for the four-circular-coil systems.

Several calculations were made for systems that would have equal currents and turns ratios that are the ratios of integers; the field intensity both on and off the axis was also calculated. From these calculated values, contour plots were made which showed the field variation in various planes through the axis of the system, indicating that the circumferential variation does in fact exist. The inductance of such a system was also calculated.

Further work on the six-circular-coil system was completed. Two successful computer programs were fashioned, and many complete systems were calculated. Some of the systems were found to have spheres of homogeneity greater than 50 percent, which is much larger than the values previously known. One pressing problem is that of finding a method to determine the boundaries within which possible solutions lie.

One difficulty common to all the coil systems is that the analyses assume zero cross section, whereas the actual cross sections are finite. This has the effect of changing the optimum dimensions, and the object of the work on coil systems with finite cross section is to find out how much of a change results. Work was done on four-circular-coil systems with solenoidal coils and with coils of rectangular cross section, as well as on four-square-coil systems with solenoidal coils. The preliminary results seem to indicate that, with the assumed cross sections close to those to be used, the effect on the dimensions of the system may be small enough to be negligible.

One interesting result was obtained in that it appears possible to make four coefficients zero in a four-coil system with a finite coil size compared to three coefficients zero in the same system with zero coil cross section. This appears to be possible, however, only with rather long coils, a fact which would result in making the access space comparatively small.

Several fluxgate magnetometers were constructed, tested, and calibrated during the Workshop period. In addition, an attempt was made to optimize experimentally the parameters of the magnetometer so that it was quite sensitive. These were constructed to measure the field near test specimens and to function as measuring devices for permeability.

Each of these phases of the magnetic environment simulation problem is discussed in further detail in the articles in this section.

AC DEMAGNETIZATION OF SATELLITE COMPONENTS

John D. Watson

INTRODUCTION

The magnetic field associated with satellite components, which arises from the magnetic materials used in construction, can be detrimental to satellite performance. This is particularly true if the satellite's primary mission is measurement of earth's magnetic field at several radii from the earth's surface; it may turn out that the magnetic field of the satellite, because of remanent magnetization of ferromagnetic materials used in its construction, is of the order of the field to be measured.

Most of the remanent magnetization in a satellite component may be removed by a demagnetization process. Demagnetization consists of a cycling of the hysteresis loops and, consequently, the remanent magnetization from some maximum value (depending upon the amplitude of the initial demagnetization field strength) to zero.

The maximum amplitude of the initial field strength must be of the order of the cohesivity of the material to ensure removal of saturated remanences.

The dc demagnetization system used at Goddard's magnetic test facility makes use of Helmholtz coils energized by alternate polarity pulses to produce the diminishing magnetic field essential to the cycling process. This system operates to measure the field of the component to be demagnetized, determine the direction of the maximum field intensity, align this direction with the axis of the Helmholtz coils, then demagnetize the component along this axis. Satisfactory results have been obtained with this method.

An objective of the Summer Workshop was to determine if an ac demagnetization process would be more effective than the process just described for reducing permanent magnetization to a minimum intensity.

Normal procedure in ac demagnetization^(1, 2) is to randomly rotate or tumble a component having an undesirable remanent magnetization in an alternating magnetic field which may be reduced smoothly to zero from a chosen maximum value. It is important that the rate at which the ac field is decreased be even and slow, compared with the rotation speed of the component. The motion of the component in the field should be as random as possible to ensure that all directions in the component are subjected to the demagnetization action of the alternating magnetic field.

An ac demagnetization system was built to satisfy the requirements stated.

THE AC DEMAGNETIZATION APPARATUS:

THE TUMBLING SYSTEM

A tumbling system (Figure C-1) was designed to provide random motion of the component. A diagram of the system is given as Figure C-2. The system provides rotation of a component about three mutually perpendicular axes with a single drive to the outer rectangular frame. The component to be demagnetized is placed inside the inner rectangular frame. The drive shaft turns the outer rectangular frame A. Pulley D is fixed to support F; as frame A rotates, belt G is wound around fixed pulley D. As this belt is also linked to pulley E, the latter rotates and turns the inner frame B, which rotates about an axis perpendicular to that of frame A. The same procedure is used to obtain rotation of the inmost frame; pulley H, fixed to frame A, serves to move belt J around as frame B rotates, turning pulley I to rotate frame C about an axis perpendicular to that of frame B.

It is evident from this description that there are always two mutually perpendicular axes of rotation; the axis of the inmost frame is continually travelling from a position parallel to that of the first axis to a position mutually perpendicular to both the other axes. The axes have speeds of rotation in the order of 18: 19: 20, the inmost frame turning at the fastest speed and the outer frame at the slowest speed. With this ratio,

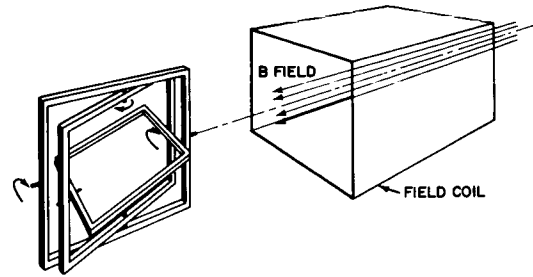


Figure C-1—Artist's concept of tumbler and coil.

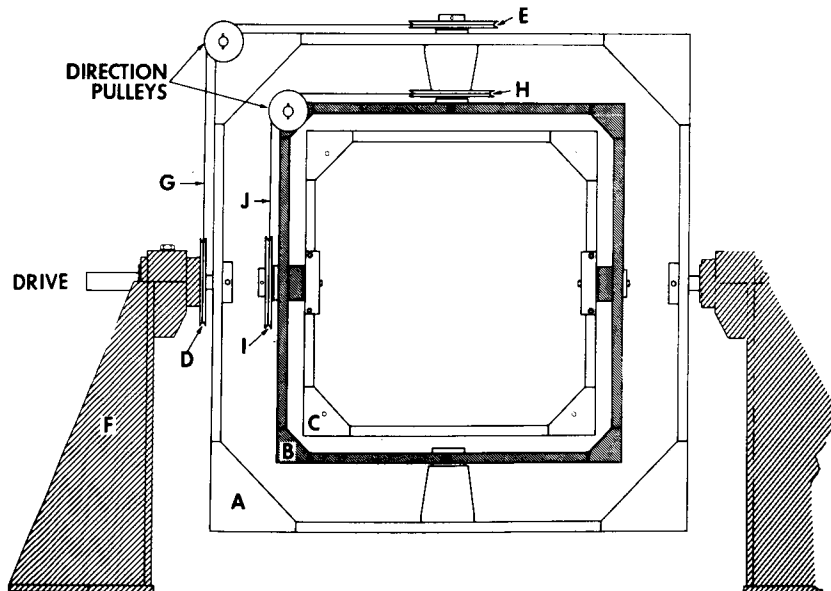


Figure C-2—AC demagnetization apparatus, structural diagram.

any direction in the component performs a Lissajou figure during rotation, and all directions of the component are subjected to the demagnetizing action of the field.

The inmost rectangular frame measures 24 inches to a side, providing 8 cubic feet of working volume. The belts are rubber O-rings which work reasonably well for the designed rotation speeds of the tumbler. All materials used in construction are nonmagnetic.

THE COIL

The coil which provides the magnetic field was designed and built at Goddard. It consists of a single layer of 280 turns of No. 8 double-cotton-covered square copper wire wound on a wooden frame in the shape of a cube. Figures C-3 and C-4 are photographs of the tumbler and the coil.

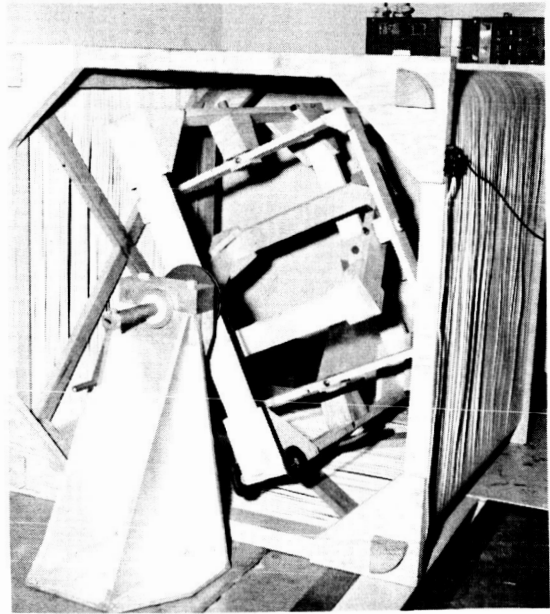


Figure C-3—Tumbler inside coil.

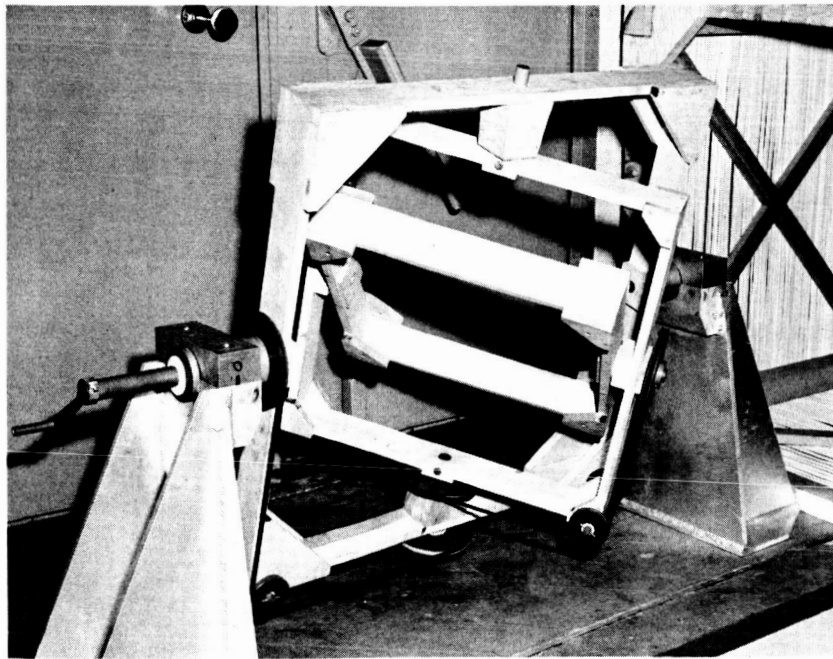


Figure C-4—Tumbler removed from coil.

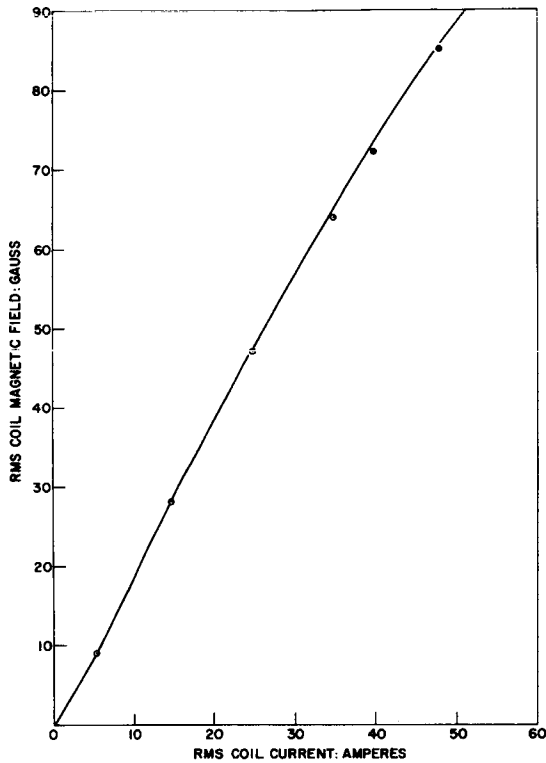


Figure C-5—Coil calibration curve.

The coil has a dc resistance of 2.14 ohms (measured hot, i. e. after reaching an operating temperature of 50°C) and an inductance of 62 millihenries. At 60 cps, the inductive reactance ($2\pi fL$) of the coil is 23 ohms. A supply voltage of 120 volts was sufficient to produce 50 amperes coil current when the coil was resonated with a series capacitor bank of 106 microfarads. The exact capacitance was determined by trial and error during tests; the coil was calibrated (Figure C-5) with an RFL Model 1890 gaussmeter and was found to produce 120 gauss (peak value) for an rms current of 50 amperes.

Figure C-6 is a schematic diagram of the ac demagnetization apparatus. The General Radio variac, source of the variable voltage, is driven by a variable speed dc motor through an 800:1 reduction gear.

THE AC DEMAGNETIZATION PROCEDURE

The desired maximum field is established in the coil. The component to be demagnetized is placed within the inmost rectangular frame of the tumbler apparatus (the frame being removable for convenient placement of the package). The variac wiper is set to the desired speed and the tumbling action begins. The component is tumbled until the variac wiper has completed its traverse from maximum voltage to zero.

In the Workshop operation, the outer frame of the tumbler was rotated at a speed of about 40 rpm for initial evaluation of the apparatus; the variac completed its traverse within a 10-minute period.

DESCRIPTION OF SAMPLES

Samples used in the tests were furnished by the Magnetic Test Section at Goddard, and consisted of:

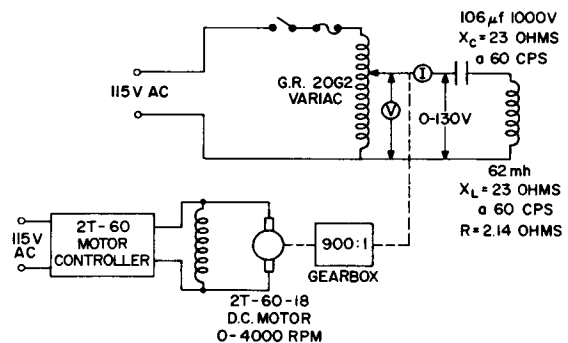


Figure C-6—AC demagnetization apparatus, schematic diagram.

- A cylindrical steel rod 3.5 inches long, 1 inch in diameter
- A cylindrical steel rod 12.5 inches long, 0.25 inch in diameter
- An amplifier chassis box containing transistors, transformers, potentiometers, capacitors, etc.

The samples were magnetized in a dc field of 25 gauss, and the axial component of the resulting remanent magnetization was measured at a distance of 24 inches from the center of the sample. Measured values are listed in Table C-1a.

DISCUSSION OF RESULTS

A comparison of the field intensity remaining in the samples after ac deperming and after dc deperming is shown in Tables C-1b and C-1c. For the steel rods, the ac deperming is more effective than the dc deperming by a factor of 6.

Table C-1—Comparison of AC and DC Deperming

Sample	12.5" rod	3.5" rod	Component Box
(a) All magnetic fields measured at 24" from center of sample.			
Original field (gammas) after 25-gauss exposure	1900	15	150
(b) After dc deperming			
Magnetic field remaining (gammas) after treatment at dc field strength of 50 gauss	5.6	3.0	7.3
Percentage field remaining (original field as base)	0.29	20	4.8
Percentage demagnetization (original field as base)	99.68	80	95.8
(c) After ac deperming			
Magnetic field remaining (gammas) after treatment at peak ac field strength of 120 gauss	1.0	0.5	1.4
Percentage field remaining (original field as base)	0.053	3.3	0.93
Percentage demagnetization (original field as base)	(approx.) 100	96.6	99

This comparison, however, is not strictly fair to either the dc or the ac technique, as it does not allow for the fact that the samples were depermed in an ac field strength of 120 gauss, whereas the maximum field available for dc deperming is 50 gauss. Likewise, in the dc process, the samples were demagnetized along a premeasured axis of maximum permanent field intensity; in the ac process, the rods were tumbled and all directions were subjected to the ac field. It is possible that an even larger percentage of the permanent field could have been removed if, in the ac process, the rods were also fixed with their axis of maximum field intensity aligned with the axis of the coil. The advantage of the tumbling action is not as great in demagnetizing rods as it would be in demagnetizing a component with a multipole field.

The third sample, the amplifier, is more representative of a satellite component with a highly irregular field. Deperming by the ac process decreased the residual field to 0.93 percent of its initial value, while dc deperming decreased the field to 4.8 percent of its initial value.

The graph shown in Figure C-7 is a fairer comparison of the two methods of deperming. A previous study of initial dc demagnetization field strength versus remanent field strength after dc deperming has been made by the Magnetic Test Section for the 3.5-inch rod; similar data were obtained by using ac deperming.

The rod was depermed in peak alternating fields of 120, 75, and 50 gauss (the 50-gauss points on the curves provide a comparison of the two methods). The field after dc deperming was 3.0 gamma; after ac deperming, 0.8 gamma. These data indicate that tumbling in an ac field is the more effective procedure.

Figure C-7 also shows data obtained by ac deperming at peak field strengths of 75 and 120 gauss. There is little decrease in the residual magnetism of the rod after the 50-gauss exposure.

No attempt was made to null the background field of the earth for these ac deperming experiments; a field-free facility was available for dc deperming.

CONCLUSIONS

1. Initial tests indicate ac tumbling is more effective than dc deperming.

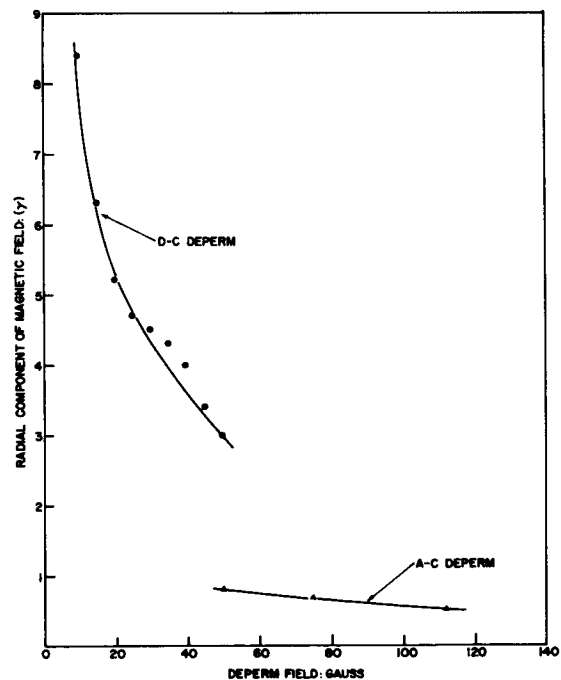


Figure C-7—Demagnetization of 3.5-inch steel rod as a function of initial field strength.

2. Tumbling of the component is an important factor in the demagnetization process.
3. A field-free space, though certainly helpful, is not a major requirement for demagnetization by ac tumbling.

SUGGESTIONS FOR FURTHER STUDY

Additional tests should be made using magnetic materials with larger coercive forces to determine the upper limit of effectiveness of this apparatus.

Effectiveness of the ac demagnetization should be analyzed as a function of

- speed of rotation of sample
- maximum initial demagnetization field
- rate of decrease of field

to determine optimum conditions for reduction of remanent magnetism to a minimum intensity.

All measurements in this report were made through the courtesy of C. Leland Parsons and the men of the Magnetic Test Section. Their cooperation, consultation, and encouragement are greatly appreciated by the author.

REFERENCES

1. Creer, K. M. , "AC Demagnetization of Unstable Triassic Keuper Marls," Geophys. Jour. 2, 261-275 (1959)
2. Irving, E. , Scott, P. , and Ward, M. , "Demagnetization of Igneous Rocks by Alternating Magnetic Fields," The Phil. Mag. 6, 225-241 (1961)

N64-28211

SURVEY OF THE LITERATURE ON NONMAGNETIC MATERIALS FOR USE IN SPACECRAFT

J. B. Crooks

INTRODUCTION

Magnetic materials pose at least two problems in spacecraft:

- Even a slightly magnetic material will have a torque exerted upon it by a uniform magnetic field, and will contribute to a tendency of the spacecraft to align itself with respect to the field.
- Magnetic materials will affect the field near a magnetometer which may have been intended for use at field strengths as low as one gamma.

For the present applications, two types of behavior are of concern: (1) distortion of the external field due to a susceptibility not equal to zero; (2) low-frequency hysteresis, with a residual induction in the material being possible in the absence of an externally applied field. Property 2 is characteristic of ferro- or ferrimagnetic materials, but not of truly paramagnetic or diamagnetic materials; however, because of ferromagnetic impurities (or minor phases), low-susceptibility materials frequently exhibit a small amount of hysteresis.⁹⁵ Hence, both properties 1 and 2 should be considered in determining whether or not a material is acceptable. With these considerations in mind, it was decided to gather information about possible nonmagnetic materials for use in spacecraft, or for other aerospace applications, and to include in the search the topics discussed in the sections which follow.

1: WEAKLY MAGNETIC MATERIALS

Information was collected at various temperatures and compositions on the magnetic properties of essentially nonmagnetic metal alloys and plastics (References 36, 47) that could be used for structural purposes. Low field-strength measurements were particularly desirable. These measurements are useful if only to indicate that a metal alloy does not become ferromagnetic (see discussion under III). Also, in instances where it is desired to make "completely" nonmagnetic alloys, composition vs. susceptibility data would be very useful. A large portion of the references in the bibliography belong to category I.

II: SUSCEPTIBILITY OF ORGANIC COMPOUNDS

Most articles from recent years are concerned with relatively minor deviations from rules of bond and atom additivity in the computation of susceptibility. Deviations of more than 20 percent are unusual and, when such deviations occur, acceptable explanations are usually available.²⁹⁶ As the proportion of the various types of bonds/atoms often does not vary greatly from one organic compound to another (or even the bonds and atoms contributions, provided nonmetallic elements are involved), the validity of the bond additivity method implies that the susceptibility of most organics should be about the same magnitude, and be very low (majority -0.6 to -0.7×10^{-6} e. m. u. /gr.).²⁷⁷

Organic materials must contain no unpaired electrons in order for the previous arguments to be strictly valid; these would give a strong paramagnetic contribution, and also would constitute a necessary condition for the existence of ferromagnetism or antiferromagnetism. However, only one reference was found that related to magnetic order in organic compounds, and this was at 1.5° K (antiferromagnetism). Thus it would seem that plastics, provided they are completely free of ferromagnetic impurities, could be selected without regard to magnetic properties for most applications.

III: FERROMAGNETISM AND ANTIFERROMAGNETISM IN NONFERROUS ALLOYS

An extensive amount of information was available on the magnetic behavior of ferromagnetic alloys of Fe, Co, and Ni. In order to determine how important a problem possible ferromagnetic phases involving the elements Cu, Mn, rare earths, and other transition metals would present, information was collected on ferromagnetic alloys containing these metals but not iron, cobalt, or nickel. Examples of structural alloys which fall into this category are the ferromagnetic Cu-Mn-Al²⁸¹ and Ag-Mn-Al Heusler alloys.¹⁸⁰

References pertaining to antiferromagnetism are included in the bibliography for three reasons:

1. There is a large variety of ferromagnetic nonferrous alloys, and more are continually being discovered (e. g., Cu_3Zr , ZrZn_2). In almost every case where an element is known to be ferromagnetic when in combination with other elements, antiferromagnetic combinations involving the same elements are also known. For nonferrous metals, the antiferromagnetic compounds predominate; therefore, if an antiferromagnetic alloy or compound of a questionable element is found, it seems conceivable that ferromagnetic alloys or compounds of the same element may also be eventually found.

2. Finely divided particles of some antiferromagnetics have been found to exhibit weak ferromagnetic properties,²⁶⁷ particularly remanence, and this is believed to be attributable to uncompensated moments around particle boundaries. It is possible that polycrystalline antiferromagnetic alloys would exhibit the same ferromagnetic effect, although it probably would be extremely small in magnitude.

3. For most applications, antiferromagnetic alloys would be satisfactorily nonmagnetic, as their susceptibility is about the same magnitude as that of a strong paramagnetic.

A recent review article by Crangle²⁵⁴ has been found on ferromagnetism and antiferromagnetism in nonferrous alloys, to which the reader is referred. It may be noted, however, that, in addition to alloys of Cu, Mn, and rare earths, the compounds BiU_3 ¹²², ZrZn_2 ¹⁶¹, and ScIn ²⁵⁴ have been reported as ferromagnetic, but all have Curie temperatures below room temperature.

IV: "COMPLETELY" NONMAGNETIC ALLOYS

It has been suggested that one might combine two or more alloys (for example, a diamagnetic such as copper with a paramagnetic such as aluminum) to obtain a completely nonmagnetic alloy. This technique certainly would seem feasible, and in fact one article was found which dealt with a successful application using nickel and copper¹⁶⁵ to produce an alloy for structural use in instrumentation. Some effort was spent in investigating this possibility. The following considerations seemed important:

1. The relative magnitudes of the various diamagnetic and paramagnetic contributions to magnetic susceptibility require that a large portion of the diamagnetic metal or phase be present²²²; e. g., the nickel/copper alloy was 96.3 percent Cu, 3.7 percent Ni. Therefore, part of the research time was spent in collecting information on the mechanical properties and physical properties of alloys of diamagnetic metals. Of these, only the alloys of beryllium, copper, cadmium, zinc, silver, and gold offered much promise.

2. It was decided that problems posed by ferromagnetic impurities would be especially important for these alloys, as the alloys would be useful only in applications requiring extremely nonmagnetic materials. Several references in the bibliography pertain to this problem. McClelland¹⁰² had to correct susceptibility measurements for ferromagnetic impurity concentrations (assumed to be iron) in copper as low as 0.2 - 0.3 parts per million. Also pertinent are several articles by Knappwost^{124, 125, 137, 139, 288} and others^{295B} on dilute alloys of Fe, Co, Cr in copper, and copper alloys (no ferromagnetism observed for Cr). Much work has also been reported on dilute alloys of manganese in copper.

Of the diamagnetic metals, the alloys of copper seem to have the best potential mechanical properties. Data from various handbooks indicate that tensile strengths exceeding 100,000 psi are possible with certain tin bronzes, manganese bronzes, and copper-nickel-silicon alloys^{310B}. Certain copper-beryllium alloys have tensile strengths of 150,000 psi. On the other hand, one disadvantage of the copper alloys is their high conductivity (eddy-current effect). Where tensile strength or hardness is important rather than strength-to-weight ratio, and where very good corrosion resistance is needed, some alloys of gold-platinum-zinc and other metals may find use. Tensile strengths of 150,000 psi have been claimed for these alloys^{310B}. Values quoted for the metals above represent

upper limits, however, and available data indicate that serious sacrifices will have to be made with regard to the best obtainable mechanical properties in order to make completely nonmagnetic alloys. Also, very ferromagnetic-impurity-free metals would have to be used in order to benefit from the alloy's being "completely" nonmagnetic.

Several references pertain to promising additives which might be used in making nonmagnetic plastics and glasses, by counteracting the normal diamagnetism associated with these substances. Pertinent to plastics are two references^{234, 240} dealing with paramagnetic ferrocene polymers, and the possibility of making from them useful rubbers or plastics; also, one reference³²³ dealing with hydrocarbon-soluble compounds of iron and cerium. The information in several references on the magnetic susceptibility of various glasses^{41, 45, 97, 295} suggests certain metal oxides that could be used to make these nonmagnetic. One possible drawback to these nonmagnetic plastics or glasses, however, is that the paramagnetism of the additives mentioned has a strong temperature dependence, which might make the useful temperature range of nonmagnetism too limited to be of much value.

V: MECHANICAL AND PHYSICAL PROPERTIES OF NONFERROUS METALS AND PLASTICS

Certain review articles, bibliographies, and articles of special interest on the mechanical and physical properties of alloys of essentially nonmagnetic metal elements were collected.

CONCLUSION

Several references not previously discussed should be mentioned. The NOL-EES reports by Gross and Gordon^{95, 282, 283, 285B} together constitute the most comprehensive body of information yet found dealing with the magnetic properties of low-permeability materials. These give the results of a large number of copper-base alloys and of stainless and other nonmagnetic steels, with the effects of various heat treatments, cold-working, and small amounts of Fe on permeability, coercive force, and remanence. Measurements were made at 0.3 Oe and 40 to 200 Oe. The authors concluded that the magnetic behavior of these alloys in strong fields could be used to predict their weak-field magnetic properties.

The review by Klemm and Vogt¹² on the magnetic properties of feebly magnetic materials might give information on German reports similar in nature to these NOL-EES reports. Two articles by Butts^{19, 89} deal with the magnetic properties of ten cast and ten wrought copper alloys, with reference to the effect of Fe content.

Some isolated measurements have been made of various useful commercial alloys: for example, measurements reported in Materials in Design Engineering²⁴⁸ on several

titanium alloys indicate a permeability of 1.00005. Titanium alloys have in general very good strength-to-weight ratios, with tensile strengths of 150,000 - 200,000 psi.

It is possible to infer magnetic properties of some commercial alloys indirectly from some of the references in the bibliography. References 110, 245, and 299 imply that the magnetic properties might be relatively insensitive to Fe, Cu, or Co additions; some aluminum-rich compounds of these elements were all paramagnetic. In contrast, the article by Knappwost^{124, 125, 137, 139} and others indicate that Fe or Co contamination might be very troublesome in copper. Similar conclusions might be drawn from the magnetic behavior of vanadium with other transition elements, from the article by Childs²⁷⁴, or from the behavior of commercial magnesium rare-earth alloys from the articles by Gaume-Mahn^{13, 28, 93}.

Appendix C-1 is a list of abstracts and journals and the extent to which they were searched.

APPENDIX C-1

JOURNALS AND ABSTRACTS, AND OTHER MATERIAL SEARCHED

1. Technical Abstract Bulletin, Armed Forces Technical Information Agency; June 15, 1963, to January 15, 1962 (except August 15, July 15, 1963); also Accession No. AD-1 to AD-75,000
2. Scientific and Technical Aerospace Reports; June 15, 1963 to January 1, 1963
3. International Aerospace Abstracts; June 15, 1963, to Sept. 1, 1963
4. Chemical Abstracts; December 1956 to January 1947
5. Engineering Index; June - January, 1963, 1962, 1961, 1960, 1954 through 1950
6. American Society for Metals; Review of Metal Literature (abstracts); 1961, 1960
7. Science Abstracts, Physics; June 1963 to January 1963, 1960, 1959, 1958
- *8. JPL Bibliography No. 186, "Magnetism, Magnetic Properties, and Magnetic Phenomena" (covers the Engineering Index, Science Abstracts, Physical & Electrical Engineering, and other literature collections); December 1959 to January 1955
9. Materials in Design Engineering, June 1962 to June 1963, also Materials Selector Issue, mid-October 1962

*The most important references from JPL 186 are included in the present bibliography, but appropriate headings in JPL 186 should be checked to ensure as complete coverage for years 1957-58 as for other years covered in present bibliography.

BIBLIOGRAPHY

MAGNETIC PROPERTIES (CYCLE A, REF. 1-274)

1. "Some recent metallurgical developments with special reference to engineering requirements," F. C. Thomson, Machinery Market 1938, 25-6.
Magnetic properties of an Al-Mg alloy described.
2. "Magnetic investigation of the ternary system aluminum-copper-chromium," Adolf Knappwost and Hans Nowotny, Z. Metallkunde, **33**, 153-7 (1941); Metals and Alloys **14**, 292 (1941)
Solubility of Cr in copper found to be 3.1 percent or greater. This value is considerably larger than that found by previous investigations.
3. "Diamagnetism of organic compounds and its additivity," Genyuro Hazato, Science (Japan) **14**, 162-6 (1944)
Review, 27 references.
4. "Magnetism and constitution of organic compounds," Wilhelm Klemm, Z. Elektrochem. **51**, 14-23 (1945)
Diamagnetic, paramagnetic, susceptibilities.
5. "Problem of the bent line in paramagnetism," I. Maxim, Bull. soc. roumaine phys. **47**, No. 84, p 33-40 (1946) (In French)
Break in the temperature-dependence plot of inverse susceptibility for Mn (2.6%) dissolved in B brass. From 0-800°C, data fall on two straight lines. Constant's given

$$X (\text{gram atomic Mn}) = \frac{C}{T-\theta} \text{ (supposed, not given in abstract)}$$

Low Temperature portion

θ	C
- 58.6°K	2.476
-228.1°K	3.031

6. "Magnetochemical studies," Adolphe Pocault, Ann. chim. [12] **1**, 527-87 (1946)
cf. C.A. 40 -1709

7. "Solubility of austenite in stainless steels," C. B. Post and W. S. Eberly, Trans. Amer. Soc. Metals, Preprint No. 5, 21 pp (1946)
Magnetic permeability measurements at 50, 100, 150, 200 Oe.
8. "The temperature dependence of magnetic susceptibility of annealed and cold-worked copper," T. S. Hutchison and J. Reekie, Nature 159, 537-8 (1947)
Measurements were made on specimens that were (I) cold worked, (II) annealed for 10 hours in H at 950°K and either (a) cooled slowly or (b) quenched in water. For both I and II, susceptibility changed linearly with temperature from 90 to 630°K. For II (a) and (b), the change was 21% over the temp. range. For I, the change was 12%. Result discussed in terms of Stoner's suggestion for paramagnetic metals.
9. "Temperature dependence of the diamagnetic susceptibility of the brasses," Jules A. Marcus, Phys. Rev. 71, 471 (1947)
Published in abstract form - paper given before the Am. Phys. Soc.
10. "Principles of magnesium metallurgy. (I) Physical Properties," Williamson W. Moss, Jr., Light Metal Age 5, No. 2, 8-15 (1947)
Magnetic properties included.
11. "The formation of σ phase in duplex chromium-nickel-molybdenum corrosion-resisting steels," H. W. Kirby and J. I. Morley, J. Iron and Steel Institute (London) 158, 289-94 (1948)
 σ phase results in loss of magnetism.
12. "Magnetic properties of nonferromagnetic substances," Walter Klem and Eckhard Vogt, FIAT Rev. German Sci. 1939-46, Physics of Solids PT II (1948) 1-26
Review with 77 references.
13. "A study of the cerium-magnesium alloy system," Françoise Mahn, Ann. Phys. [12] 3, 393-458 (1948)
No ferromagnetism observed.
14. "Effect of cold-working on the magnetic properties of pure metals," James Reekies and T. S. Hutchison, Phys. Rev 74, 610-20 (1948) (cf. R & H Nature 157, 807 (1946)
Paramagnetism of aluminum decreased by as much as 15% by cold working. Article maintains that the effect can not be explained by the presence of ferromagnetic impurities, but is "related to certain metallurgical changes which occur on cold-working."
15. "Theory of ferromagnetism of binary alloys," S. V. Vonsovskii, J. Tech. Physics. (U.S.S.R.) 18, 131-43 (1948)
Relation derived between Curie points by binary alloys.

16. "The superconductivity of lanthanum and cerium," W. T. Ziegler, J. Chem. Physics 16, 838 (1948) cf CA 42 1775g,
Variation of magnetic susceptibility with temperature detd. La and Ce.
17. "Rapid-state changes in aluminum mixed crystals," Herman Auer, Z. Naturforsch. 4a, 533-40 (1949)
Solid solutions of Al + 5 Cu, magnetic susceptibility.
18. "Thermal effect due to magnetization process in weak fields," L. F. Bates, J. de Physique et le Radium 10, No. 12 353-63 (Dec. 1949)
Bibliography. results of experimental studies at the University of Sheffield.
19. "Magnetism in copper alloys; effect of iron impurity," Allison Butts and Paul L. Reiber, Jr., Proc. Am. Soc. Test. Materials 49 857-83, 884-6 (1949)
Residual magnetic moment of 10 wrought copper alloys and 10 cast alloys (Be-Cu, Ni-silver, monel, etc.). Suggests that all but three of alloys would be usable for non-magnetic applications if Fe content is less than 0.01%. Discusses sensitivity of magnetic properties to Fe content. Quenching from 800° effective in lowering magnetic moment.
20. "Magnetic susceptibility of weakly paramagnetic substances," Juan D. Curet-Cuevas, Univ. Microfilms (Ann Arbor, Mich.) Pub. No. 1097 124 pp (microfilm \$1.54, paper enlarge \$12.40) Microfilm abstracts 9, No. 1, 14-15 (1949)
21. H. Fahlenbrach, Archiv. fur Eisenhüttenw. 20 No. 9-10, 293-0 (Sept - Oct 1949)
Magnetic studies of low carbon iron-chromium alloys. Permeability and cohesive force for 0-30% chromium, 0-5% silicon.
22. "Data furnished by magnetism on the state of ionization of metals of the iron family in compounds containing a single magnetic constituent," G. Foëx, Bull. soc. chim. France, (1949) p 157-60
Paramagnetic behavior of known compounds, V, Cr, Mn, Fe, Co, Ni with Si, N, P, As, Sb, O, S, Se, and Fe.
23. "Atomic magnetic moments of transition metals and alloys and the interaction distances of their lattice," F. M. Gal' perin, Isvest. Akad. Nauk. S.S.S.R., Ser. Fiz. 13, 574-95 See CA. 41, 1900c (1949)
Previous paper proposed formula for ferromag. alloys

$$M = M - K_1 (d_1 - D) + K_2 (d_2 - D) + K_3 (d_3 - D) + \dots + K_i (d_i - D)$$

M = experimental atomic magnetic moment.

d_i = distance to the "i" th layer of neighboring atoms.

K_i = arbitrary constant

D = sum of atomic radii of the s and d shells.

M = "the corresponding no of magnetons" (Bohr)

- Agreement with exper. for ferromagnetic alloys "good". Formula can be used to calculate the paramagnetic moment of Cr, Zr, Sc, Ti, Cu, Al and alloys. Can be applied to solid solutions and alloys such as Mn Cu Al, Ni₃ Mn, Ni₃ Fe, Cr Te.
24. "Paramagnetic susceptibility of alloys of transition metals with tellurium," F. M. Gal' perin and T. M. Perepalince, Doklady Acad. Nauk. S.S.S.R. 69, 19-22 (1949)
The magnetic susceptibility of VTe (50 at %) is given by the expression $\chi_m = 0.92/T$.
Magnetic moment is 1.7 Bohr magnetons per atom of vanadium.
The alloys Cr-Te from 25 to 70 atomic percent are ferromagnetic. Nickel-telluride has susceptibility independent of temperature, and whose magnitude indicates no unpaired delectrons. Cobalt-Telluride is antiferromagnetic.
25. "Magnetic properties of chromium telluride," F. M. Gal' perin and T. M. Berek alanei, Zhur. eksptl. teoret. fiz. 19, 470-2 (1949)
May sat. -196°C, 447 gauses
(I_S) 20°C, 314 guas.
above 50% at Te, I_S falls rapidly to zero.
For Te less than 50% - I_S approx. same as equimolar CnTe.
26. "Conditions for the occurrence of ferromagnetism in metal compounds," J. H. Gisolf, Physica 15, 677-8 (1949) (In english)
Theoretical; probably too old, too brief, to be of much use.
27. "Magnetic susceptibilities of the rare earth elements. I: Yttrium," O. M. M. Hilal and S. Sugden, J. Chem. Soc. 1949, 135-6
Purity of final product checked spectroscopically - magnetic analytical technique.
28. "Magnetic properties of cerium-magnesium alloys," F. Mahn, Revue de metallurgie 46 No. 6, 365-9 (June, 1949)
"Coefficient of magnetization" at const. temp. and as functions of field strength.
29. "Magnetic susceptibility of zinc at liquid hydrogen temperature," Jules A. Marcus, Phys. Rev., 76, 413-16 (1949) cf. CA 41, 4018c
30. "Temperature dependence of the susceptibility of zinc, cadmium, and gamma brass," Jules A. Marcus, Phys. Rev. 76, 621-3
Zn, Cd Single crystals polycrystalline γ -brass.
31. "Field dependence of diamagnetism at low temperature," D. Shoenberg, Bull soc. chim France, 1949, p 363-5 (In English) cf. C.A. 33 4337
Hg crystal: no D Haas - Van Alphen effects of 9000 gauss, Ga: - period of oscillation much smaller than in Zn or Bi; has degeneracy temperature 300°K.

32. "Magnetic properties of tin at low temperatures," B. I. Verkin, B. G. Fazarev, and N. S. Dudinko, Doklady Acad. Nauk, S.S.S.R. 69, 773-6 (1949)
Single crystals of tin show very strongly De Haas-Van Alphen effect at low temperature. 8000-12,000 Oe, frequency much greater than for Bi, Zn. Period and amplitude increase with H.
33. "Magnetic properties of palladium-base alloys," J. Wucher, Compt. rend. 229, No. 24, 1309-10 (Dec. 1949)
Alloys of Cu, Ag, Al, Sn, and Pb.
34. "The magnetic properties of uranium and uranium-iron alloys," L. F. Bates and J. R. Mallard, Proc. Phys. Soc. 63B 520-6 (1950)
Uranium, and 5 - 10% alloys of Fe no evidence of ferromagnetism. Temperatures investigated 20° - 35° C.
35. "Investigation of the magnetic properties of well-ordered alloys," F. M. Gal'perin, Doklady Acad. Nauk. S.S.S.R., 75, 647-56 (1950)
Ni₃Mn, Ni₃Fe, FeCo, MnBi, and CrTe- (applies formula for calculating magnetic moments to these compounds).
36. "Magneto-chemical study of polymerization," Jean Haurau, Bull. soc. chim. France (1950) 1152-4
Magnetic susceptibility of monomers and polymers of cyclopentadiene 2,3 dimethyl, 1,3 butadiene, styrene, and monomer of methacrylate.
Data in agreement with hypothesis of one double bond destroyed each step.
37. "Chemistry of transition elements," Wilhelm Klem, Naturwissenschaften 37, 150-6, 172-7 (1950)
Ti to copper - magnetism discussed (probably very briefly) - many references.
38. "Study of transformations of system platinum-iron," A. Kussmann and G. Von Rittberg, Z. Metallkunde, 41, 470-7 (1950)
94-98% Pt intermediate range where alloy is ferromagnetic below room temperature (less than - 80° C).
39. "Cast heat-resistant alloys of the 21% Cr 9 Ni nickel type," Howard S. Avery, Charles R. Wilks and John A. Fellows, Trans. Am. Soc. Metals No. 13, 24 pp (1951)
Presumably stainless steel.
Magnetic measurements included. - Different types of heat treatment.
40. "Ferromagnetism, paramagnetism, and cohesive energy of transition metals and their alloys," T. O. Beng, Colloques intern. centre, natl. recherche sci 27, ferromagnetisme et antiferromagnetisme (Pub. 1951) also J. Phys. Radium 12, 418-29 (1951) (In English)

Formulas for magnetic moment as function of no. of d. electrons - extended to include intermetallic compounds. - Eval. for paramagnetic susceptibility w. no arbitrary constants.

41. "The magnetic susceptibility and constitution of colored glasses. I-Theoretical considerations and experimental methods," +II. H. Cole, J. Soc. Glass Technol., 35, 5-40T (1951)
Believes there is no reasonable doubt that one can predict magnetic properties from composition and types of bond of coloring ions in glasses. "II. Glasses containing Iron Oxide." Ibid. 25-40T.
42. "The magnetic susceptibility of zinc at liquid hydrogen temperatures," J. W. Dare and J. A. Marcus, Phys. Rev. 84, 787-8 (1951)
Single crystal; mag. susc. oscillated about -186×10^{-6} (X_A ?).
43. "Ferromagnetism in the manganese-indium system," Walter V. Goeddel and Don M. Yost, Phys. Rev. 82, 555 (1951)
Ferromagnetism is due to Mn_2 In phase.
44. "An absolute measurement of the susceptibilities of tantalum and other metals," F. E. Hoare and J. C. Walling, Proc. Phys. Soc. (London) 64B, 337-41 (1951)
Measurements on Ta, Pt, Pd, Rh.
45. "Magnetic studies of glasses containing iron. Their color and constitution," H. Moore and S. Kumar, J. Soc. Glass Technol. 35 T 58-88, discussion 89-92 (1951)
Experiments were made on Fe in Ferrous (I) and Ferric (II) state. For I-mass suscept. of Fe approx 220×10^{-6} c.g.s., very close to that Fe^{++} . Glasses used $Na_2 O-CaO-SiO_2$. For II, χ varied from $210-350 + 10^{-6}$
Conclusions: 1) ferrous iron produces blue color, 2) Ferric iron is colloidal $Fe_2 O_3$ - yellow color, 3) Ferroso-Ferric iron exists in form of colloidal Ferroso-Ferric oxide.
46. "The problem of anomalous diamagnetism," H. Nowotny and H. Bitner, Monatsh. 81, 887-906 p [? 1950 ? 1951 ?]
Theory of anomalous diamagnetism outlined, published work on occurrence in Hume-Rothery γ phases reviewed - (variation of χ with composition).
Alloys of Cu with Zn, Cd, Hg, Si, Sn; Au with Zn; Ni with Zn, Cd; Mn with Zn; Pd with Zn, Cd; and of Pt with Zn, Cd.
47. "Diamagnetic anisotropy of polyethylene, polystyrene and poly 2-5, dichloro-styrene," E. M. Weir and P. W. Selwood, J. Am. Chem. Soc. 73, No. 7, 3484-7 (1951)
Fibers in several stages of elongation. Effect on susceptibility is very small. (Less than 20% of mean susceptibility of -100×10^{-6} per repeating unit 2-5 dichlorostyrene.)

48. "Effect of Brillouin zones on the physical-chemical properties of alloys," H. Witte, H. Klee, and K. H. Freier, Naturwissenschaften. 38, p 185-6 (1951)
Magnetic susceptibility of system Mg Cu₂ - Mg Zn₂ system, "Relative positions of Fermi body and Brillouin zones determine the course of susceptibility." (C. A., abstractor).
49. "Interactions between the d shells in the transition metals," C. Zener, Phys. Rev. 81 440-4 (1951)
Theoretical. Suggests that d-d-interaction same sign irrespective of separation. Relationship between ferromagnetism and s-d interaction.
[I believe that this might be pertinent to the problem: how dilute must a ferromagnetic component (in solid solution) be in order to be certain of no ferromagnetism?]
50. "Magnetic properties of metals at low temperature," G. E. Zilberman, Zhur. eksptl. teoret. fiz. 21, 1209-17 (1951)
Related to De Haas-Van Alphen effect.
51. "The systems platinum-zinc and platinum-cadmium," H. Nowotny, E. Bauer, A. Stamphl, and H. Bittner, Monatsch. 83, 221-36 (1952)
Microscopic X-ray, thermal analysis of phases in solid state after high-temp. quenching.
Phase Pt Zn₈ and Pt₃Zn exhibited anomalous diamagnetism.
- | | |
|--------------------------------|---------------------------------------|
| 62% Zn - 0.2x10 ⁻⁶ | pure Pt is paramagnetic; pure Cd, Zn, |
| 90% Zn - 0.68x10 ⁻⁶ | ~ 0.200x10 ⁻⁶ emu. |
52. "Magnetic behavior of intermediate phases in alloys of transition elements," P. A. Beck, J. Metals 4, 420 (1952). Sigma specimens of the following compounds were tested:
- (1) Fe 40, Cr 30, and Mo 20 at 2/0
 - (2) Fe 48.7 Cr 50, and W 1.1 at %
 - (3) Fe 25 or 35, and Mo 30 at %
 - (4) Co 40.7 and Cr 59.3%
- (may be nonmagnetic)
See A. H. Sully: "The sigma phase in binary alloys of the transition elements," Journal Inst. Metal (1951) 80 173.
53. "Magnetic measurements of Hume-Rothery γ -phases," H. Bittner and V. Nowotny, Monatsh. 83 1308-13 (1952)
- | |
|---|
| Cu - Al X = -0.9x10 ⁻⁶ at $\gamma - \gamma_1$ boundary |
| X = -0.2x10 ⁻⁶ at $\gamma_1 - \gamma_2$ boundary |
- Cu-In X ~ -0.3x10⁻⁶ (min value) Ag-Hg X ~ -0.3x10⁻⁶
States rule that anomalous diamagnetism with increasing at. wt. of metal [uncert. which component: seems to apply to both from data given.]

54. "Selection and processing of chromium-nickel stainless steels for magnetic applications," F. K. Bloom and T. S. White, Wire and Wire Products 27, 1036-1037, 28, 1126-7 (1952)

Composition ranges from 16-26% Cr and 6-22% Ni "Substantially nonmagnetic" in annealed condition.

AISI type	Permeability (after cold-drawing 100 Oersteds)
301	40.0
302	36.8
304	2.93
316	1.009
310	1.007

55. "Electronic structures and physical properties in the alloy system nickel-copper and palladium-silver," R. B. Coles, Proc. Phys. Soc. 65B, 221-9 (1952)
Pd-Ag - shows expected behavior
Ni-Cu - deviations; d band holes even as low as 5% Ni.
56. Ferromagnetic Properties of Metals and Alloys, Vol. XI, Oxford, Geoffrey Cumberledge (1952) 317 pp.
Book.
57. Eakin, C. T., "Non-Magnetic Steels." Electrical Manufacturing, pp 108-112, 268, 270, 272, (July 1952).
58. "The changes in some properties of vanadium sesquioxide near its transformation point," More Foex et al, Recherche centre natl. tech. sci. lab., Bellevue 21, 237-259 (1952)
 V_2O_3 is antiferromagnetic - 110-250°C.
59. "Effective magnetic distances in metals, alloys, and ferromagnetic and antiferromagnetic combination of the iron group," Robert Forrer, Ann. phys. 7, 605-621 (1952)
Analysis of published data on Cr, Mn, Fe, Co, Ni. Close distances - antiferromagnetism; intermediate dist. - ferromagnetism; large distances - variable paramagnetism (between d shells probably). 22 ref.
60. "Titanium-copper binary phase diagram," A. Joukainen, N. J. Grant and C. F. Floe, J. Metal, 4, No. 4 766-60 (July 1952)
Metallographic exam, X-ray and thermal analysis. Found intermetallic compounds. Ti_2Cu , $TiCu$, Ti_2Cu_3 , $TiCu_3$.
[Paramagnetic-diamagnetic]

61. "Magnetic susceptibilities of palladium-rhodium alloys from 20°K to 300°K," F. E. Hoare et al, Nature **170**, 537 - ∞ (1952) cf. CA 46 10726f.
Rh 1, 5, 10 at % and Pd-Ay 3 atomic %
62. "The magnetic susceptibilities of platinum, rhodium, and palladium from 20-290°K," F. E. Hoare and J. C. Matthews, Proc. Roy. Soc. A **212** 137-48. (1952)
63. "Nuclear resonance and electronic structure of transition metals," W. P. Knight and C. Kittel, Phys. Rev. **86** 373 (1952)
Theoretical. Zener (C. A. 45, 3706h, 46, 4293 e) suggests antiferromagnetic coupling exists in V, Cr, Nb, Mo, Ta, and W. Present authors find no evidence of "ordinary" antiferromagnetism in V, Nb or W.
64. "The magnetic susceptibility of uranium," C. J. Kriessman, Jr. and T. R. McGuire (NOL, White Oak), Phys. Rev. **85**, 71-2 (1952)
Body force method used to make measurements, -195°C -1.66x10⁻⁶ e.m.u. (g.)
1120°C -2.10x10⁻⁶, room temp. 1.72x10⁻⁶, abrupt changes at 698, 808°C.
65. "Magnetic properties of metallic uranium and uranium hydride," W. Trzbiatowski, H. Slwa and B. Stalinski, Rockzniki Chem **62**, 110-12 (1952) (English summary)
Pure U and UH₃ de + d - 80- 292°K, 80-462°K resp.

U - paramagnetic, independent of temperature

UH₃ - strong paramagnetism; below 173°K has ferromagnetic properties
66. "Thermomagnetic study of palladium hydride and alloys of palladium with diamagnetic metals," J. Wucher, Ann. Phys. **7**, 317-59 (1952)
Alloys of Pd with Ag, Al, Au, Cu, Pb, S6, and Sn. 0-800°C susceptibility measurements. Usually followed Curie-Weiss law, but same "sharp bends" in 1/x versus T plot. Correlates behavior with electron concentration.
67. "Magnetic properties of gadolinium metal," J. F. Elliot, S. Legvold, and F. H. Spedding, Phys. Rev. **91**, 82-30 (1953)
Saturation magnetization obeys T^{-3/2} law, 20-250°K. Zero temp. saturation corresponds to about 7 Bohr magneton.
68. "Magnetic properties and electron distribution in some alloys and definite compound," G. Föex, Helv. Phys. Acta. 199-206 (1953)
69. Washington conference on magnetism. Reviews of Modern Physics **25**, 331, (1953)
"Cohesive force of precipitation alloys," A. H. Geisher, p 316-22.
70. "Antiferromagnetic CuCl₂ · 2H₂O crystals," C. J. Gorter, Rev. Mod. Physics **25**, 232-7 (1953)
Temperatures investigated are in 0.6 - 4.1°K range. Fields up to 20,000 oe.

71. "Magnetic susceptibility of platinum, rhodium for 20 to 2900°K," K. F. E. Hoare, and J. C. Mathews, Proc. Roy. Soc. 213 No. 1108,

Results discussed in terms of collective electron theory.

72. "Magnetic study of high polymers-I. Diamagnetic anisotropy of natural rubber," Akera Ishihara, Hajime Kusumo, et al, J. Chem. Phys. 21, 1009-11 (1953)

Study of anisotropy of magnetic susceptibility. At second order transition, noted abrupt change in the slope of anisotropy versus temp. curve.

73. "Hardening of aluminum-silver alloys-VIII. Hall constant and magnetic susceptibility," Werner Kosler and Aldolf Frei, Z. Metallkunde 44, 495-502, (1953)

Measurement made on three aluminum alloys, Ag-38.8%, Cu 3.9%, and Si 0.5%. In all three instances, the "electron density" increased with second metal addition. "Mobility" of condition electrons decreased.

74. "High-temperature magnetic susceptibility of vandadium, niobium, tungsten, and molybdenum," C. J. Kriessman Jr. (U.S. Nav. Ord. Lab., White Oak,) Rev. Mod. Phys. 25, 122-6 (1953)

Spectroscopically pure. Measured with electrically compensated torsion balance, Corrections for ferromagnetic impurity. (.01 to .02x10⁻⁶ susceptibility units for Nb, Ta, Mo, W; for V, 0.25 x 10⁻⁶) [probably cgs units]

Element	Suscep (25 °C)	High Temp Suscep.
V	+5.0 x 10 ⁻⁶	4.57 x 10 ⁻⁶ (1700 °C)
Nb	+2.20 x 10 ⁻⁶	1.79 x 10 ⁻⁶ (1575 °C)
Ta	+0.827 x 10 ⁻⁶	0.668 x 10 ⁻⁶
Mo	+0.93 x 10 ⁻⁶	1.11 x 10 ⁻⁶ (1825 °C)
W	+0.32 x 10 ⁻⁶	0.37 x 10 ⁻⁶ (1850 °C)

75. "Magnetic and electric properties of gadolinium, dysprosium, and erbium metal,"

S. Legvold, F. H. Spedding, F. Boeson and J. F. Elliot, Rev. Mod. Phys. 25, 129-30 (1953)

Article gives magnetization curves of gadolinium, also measured electrical resistivity. Abrupt change, for Gd, Dy, and Er, at temperatures 300°K, 155°K, and 80°K (only slightly) respectively.

76. "The thermal and magnetic properties of palladium-silver alloys," F. E. Hoare, J. C. Mathews, and J. C. Walling, Proc. Roy. Soc. A216, 502-15 (1953).

Maximum value in susceptibility versus temp. plot of palladium persists to Pd Ag 2.25.

77. "The calculation of the diamagnetism of aromatic compounds," M. Mayot et al, J. chim. phys. 50, 176-82 (1953)

78. Materials and Methods Manual No. 93 - G. H. Stearly, Materials & Methods. 37, No 4 115-30 (1953)

Magnetic materials, with 2-page discussion of non-magnetic stainless steels.

79. "Effect of heat treatment on cold-worked 18-8 wire," Samuel Stockheim, Iron Age 172, No 14, 112-114 (1953)

Magnetic properties are unaffected up to 1100° F for cold-drawn wire. 1100 to 1400° F, change from magnetic to nonmagnetic properties. Between 1200° F and 1300° F there is a sharp drop in tensile properties ($4 \times 10^{+5}$ lbs sg in to $2.5 \times 10^{+5}$ lbs/sg in.)

Electrical resistivity.

Room Temp.	650 ohms	cir mil ft.
1280° F	490 ohms	cir mil ft.

80. "Neutron diffraction studies of various transition elements," C. G. Stull and M. K. Wilkinson, Rev. Mod. Phys. 25, 100-105 (1953)

Although Cr and Mn were found to be antiferromagnetic, with Neel temperatures of 475° K and 100° K respectively, neutron diffraction studies gave no evidence of antiferromagnetism for W, Mo, Nb, or V.

81. "Ferromagnetism of dysprosium," Felix Trombe, Bull. Soc. Chim. France (1953) 1073 cf. c. n. 47, 8435F

Curie point is dependent on field strength = about 85° K at field strengths approaching zero at high temperatures. Curie-Weiss law is obeyed (mag. moment 10.65 Bohr.) At intermediate temperatures (140-250° K) exhibits antiferromagnetic properties.

82. "Metallic dysprosium and its magnetic properties," Felix Trombe, Proc. XI Intern. Congr. Pure Appl. Chemistry. London, S, 951-2 (1947) (Pub. 1953) (In French)

From 250 to 730° K, strongly paramagnetic; has Curie point of 105° K

83. "The magnetic properties of metallic dysprosium, Felix Trombe, Compt. rend. 236, 591-3 (1953)

Above the ferromagnetic Curie point, the susceptibility has an antiferrous magnetic type temp dependence to 250° K. Also positive dependence on field strength noted. Region of interest, 153-178° K

84. "Ferromagnetism and the band structure of transition metals," F. Bakder, K. Ganzhorn, and U. Dehlinger, Z. Physik 13 7, 190-9 (1954)

85. "The magnetic susceptibility of metallic uranium," L. F. Bates and D. Huges, Proc. Phys. Soc. (London) 67B, 28-37 (1954)

15-920°C temp dependence. Sudden transitions noted. Associated with α -B, B- α transitions?

86. "Temperature dependent. De Haas-Van Alphen parameters in zinc," Ted G. Berlincourt, and M. C. Steels, Pys.. Rev. 95, 142--8 (1954) cf Ibid 96, 1344.

87. Heat Treating Austenite Steels, W. B. Breeler. U. S. Pat 2,696, 540. (1954?)

Alloy A	0.10%	16.97Cr	6.87 Vi
Alloy B	0.06%	18.84 Cr	8.46 Ni
Alloy C	0.07%	18.84 Cr	10.99 Ni

New treatment involves coiling to 0° F, then raising temp and deforming the material. Increases mechanical properties, but makes all three alloys considerably more magnetic.

	Conventional Treatment	New
A	18.76	35-45
B	2.92	19.38
C	1.004	1.979

Permeabilities of alloys A, B, and C

88. "Magnetic susceptibility of germanium," G. Busch and H. Helfer, Helv. Phys. Acta 27, 201-4 (1954)

Measurements on single crystal 26-1180°K. Below 900°, results depend on thermal history of the crystal.

89. "Magnetic properties of copper and copper alloys," Allison Butts, pp 501-7 Copper-The Science and Technology of the Metal, Its Alloys, its Compounds. Reinhold Publishing Co., N. Y. (1954)

90. "De Haas-Van Alphen effect in tin and tin-antimony alloys," G. T. Croft, W. F. Love, and F. C. Nix, Phys. Rev. 95, 1403-8 (1954)

91. Temperature and field dependence of the de Haas - van Alphen effect," F. J. Donahue and F. C. Nix, Phys. Rev., 95, 1395-402 (1954)

92. "New ferromagnetic substances in the rare-earth group," Francoise. Gaume-Mahn, Bull. Soc. Chim. France, (1954) 564-75 cf CA 47, 12189a. Temperature - magnetization plots.

93. "Magnetic and dilatometric study of the formation of Ce-Mg₂," Francoise Gaume-Mahn and M. Cohen, Compt. rend. 238, 1302-3 (1954)
Mention of "coefficient of magnetization." (susceptibility?)
94. "Paramagnetic susceptibility of Au-Cr alloy," Aldo Giansoldati, Arkiv. Fysik 8, 151-154 (1954)
2.35 at % and 6.75 at % Cr obey Curie-Weiss law. 21% Cr alloy has sharp break in 1/X versus T curve. at 500°-600°K.
95. "Magnetic permeability of so-called nonmagnetic metallic materials," M. R. Gross (Naval Engr. Exper. Sta., Annapolis, J. Am. Soc. Naval Engineers 60, 215-45 (1954)
This article summarizes the results of a very intensive study. Magnetic permeability, cohesive force, residual induction on large number of structural alloys; effect of cold-working heat treatment, etc.
96. "Transition metals and their alloys," W. Hume-Rothery, B. R. Coles, Advances in Physics (Supp. to Phil Mag.) 3, No 10, 149-243 (April 1954)
A review with bibliography.
97. "The influence of different elements on the color and magnetic susceptibility of glass: (I) Iron," J. de Jong, J. Soc. Glass Technol. 53, 57-83T (1954) Ratio of ferrous to ferric ions determined by measurement of magnetic susceptibility. Author believes bonding of Fe⁺⁺, Fe⁺⁺⁺ is ionic.
II. Titanium and chromium: magnetic measurements made.
98. "Progress in the field of dia- and paramagnetism," G. Joos, Zeit fuer Angew. Phys. 6, p 43-8 (1954)
Literature review on De Haas-Van Alphen effect, in crystals; paramagnetic resonance. Bibliography.
99. "Paramagnetism in the system copper-iron," Aldolph Knappwost, Z. Metallkunde 45, 137-42 (1954)
Solid solutions studied. Paramagnetism ascribed to Fe⁺⁺.
100. "The radical dissociation of aryl disulfides," H. Z. Lecher, Science 120, 220-222 (1954)
Paramagnetic susceptibility measured.
101. "Antiferromagnetism in metals," A. B. Libard, Pro. Roy. Soc. 244 No. 1157, 161-76 (1954)
Bibliography. Energy-band theory of antiferromagnetism. Both metals and compounds discussed.
102. "Effect of cold-work on the magnetic susceptibility of copper and aluminum," J. D. McClelland, Acta. Metallurgica 2, 406-408 (1954)
Spectroscopically pure samples used. No change was noted. Faraday method used to determine simultaneously susceptibility and ferromagnetic impurity.

103. "Ferromagnetism of certain manganese-rich alloys," E. R. Morgan, J. Metals 6, No. 9 AIME. Trans., 200 983-8 (1954)

Discussion of ($M_n X_4$) C face-centered cubic ferromagnetic phase. X = Al, In, Sn. Elements X have high positive valence and positive "size factor" with respect to M_n . Magnetic moment of at least one Bohr magneton.

104. "Antiferromagnetism of manganese," L. Patrick, Phys. Rev. 93, 370 (1954)

Notes resistance anomaly near Neel temperature. ($\sim 100^\circ K$)

105. "Magnetic susceptibility and electronic specific heat of transition metals in relation to their electronic structure," E. C. Stoner, Acta Metallurgica 2, 259-73 (Mar. 1954)

Theoretical

106. "How radiation affects structural materials," C. R. Sutton, Iron Age 174 No. 8, 128-131, NO. 9, 97-100 (1954)

Austenitic stainless steels, types 347 Nb - Ta, annealed and shot-peened, and type 329 annealed, showed large increase in suscep. after irradiation. Type 446 showed decrease after irradiation. Types 304, 309, and 347 showed 5% increase in resistance.

107. "Radiation effects on reactor material-metals," C. R. Sutton and D. O. Lelser, Nucleonics R. No. 9, 8, 13-6 (1954)

Type 316, 347, and 410 steels, density increased with radiation. Believed associated with austenitic - ferritic transition of some of the metal, indicated by magnetic susceptibility measurements.

108. "Antiferromagnetism in metals," R. H. Tredgold, Proc. Phys. Soc. 67 H 1018-20 (1954)

Maintains that any material with a narrow partly filled energy band will show either antiferromagnetism or ferromagnetism at sufficiently low temperatures.

109. "Magnetic properties of uranium hydride and deuterides," Wlodzimierz Trzbiatowski, Alfred Sliwa and B. Stalinski, Roczniki Chem. 28, 12-20 (1954)

UH_3 below $174^\circ K$ } Exhibit ferromagnetic properties
 UD_3 below $172^\circ K$ }

110. "Magnetic behavior and band-filling in aluminum-manganese and silver-lead alloys," E. Vogt, Appl. Sci. Res. 4B, 34-42 (1954) (German)

$M_n Al_6$ magnetic susceptibility is much lower than compounds of higher or lower M_n content. $M_n Al_6$ is a peritectic phase.

	293°K	83°K	
$M_n Al_6$	18	22.4	may suscept.,
$M_n Al_6$	140	188	$X_A \times 10^6$

Pb does not affect the suscept. of Ag up to 2% Pb.

111. "Some aspects of the quantum-mechanical theory of ferromagnetism. Critical review of existing theory," S. W. Vonsovski, Izvest. Akad. Nauk. S. S. S. R. Ser. Fiz. 18 312-18 (1954)

". . . III antiferromagnetism of transition elements S. V. Vonsovkeii Ibid 328-38.

English translation exists.

112. "The magnetic susceptibility of chromium," Friedrich Wagen-knecht, Z. Anorg. und Allgem. Chem., 275, 59-64 (1954)

Electrolytically prepared. Finds suscept. 24% less than previously reported.

Deviations of other investigators from present value are probably due to presence of O_2 , which cannot be removed. Corrections for contribution of agate (due to grinding) and of $Cr_2 O_3$ made.

Value $+2.05 \times 10^{-6}$ 1 susc./gr.

113. "Transformation kinetics of the α phase in an iron-chromium alloy with 48% chromium," Ewald Baerlecken and Heinz Fabritius, Arch. Eisenhuettenw. 26, 679-86 (1955)

Phase FeCr is antiferromagnetic at temps. below 400°C.

114. "Some magnetic properties of dilute ferromagnetic alloys," I. G. Bates, D. Schofield, W. Suchsmith, Phil. Mag. 46, 621-31 (1955)

115. "The magnetic susceptibility of metallic neodymium," L. F. Bates, S. J. Leach, R. G. Loasby, and K. W. H. Stevens, Proc. Phys. Soc. 68B pp. 181-2 (1955)

Investigated over 290-1000°K.

Purity: 99.81% - Li 0.1%, Fe 0.7%. Others, less than .01%.

116. "The magnetic susceptibility of cupric oxide," Henri Bizelle and Belling Tsai, Compt. rend. 241 182-4 (1955)

Measurements made from 4°K to 400°K. No discontinuity observed at about 230°K, contrary to Honda and Ishiwara's observations. (See CH 10, 720, temperature dependence of susceptibility: Decreases with increasing temp. to 100°K, then starts to increase, reading a flattened maximum at ~ 230°K. From 4°K rise in susceptibility with decreasing temperature is rapid.

117. "Paramagnetism of the actinide group," B. Bleaney, Discussions Faraday Soc., No. 19, 112-18 (1955)

Theoretical discussion.

118. "The relationship between temperature and magnetic susceptibility of tin-lead alloys," E. S. Borovik and L. F. Shum, Uchenje Zapiski Khar'Kov Univ. 49 Trudy Fiz. Otdel Fiz. Mat. Fakul'Teta 4, p. 151-4 (1953); Referat. Zhur. Khim. 1955, No. 6140.

20, 40, 62, 80, 90 P6.

119. "Magnetic properties of erbium metal," J. F. Elliot, S. Fegvalt, and F. H. Spedding, Phys. Rev. 100, 1595-6 (1955).

Permeability nonconstant with field strength above ferromagnetic Curie point of 20°K (although metal paramagnetic in this region).

120. "Empirical bond additivity method for the calculation of diamagnetic susceptibility of simple organic molecules," C. M. French and D. Harrison, J. Chem. Soc. 1955, 1990-6.

Correction terms take form of bond interactions. Results compared with recent experimental values. Few serious deviations noted for "relatively simple" compounds.

121. "High temperature magnetic properties of cerium," Françoise Gaume-Mahn, Compt. Rend. 241, 286-8 (1955)

Measurements made from 290-1033°K.

Curie-Weiss law not followed for temperature greater than 300°K, 500-1000°K results depend on thermal history slightly. Sharp change noted 940-980°K which diminished on successive reheatings.

Additions of Mg lowers transition temperature, decreases magnitude of sharp change.

122. "Magnetic properties of uranium hydride," Dieter M. Gruen, J. Chem. Phys. 23, 1708-10 (1955)

123. "Magnetic behavior of intermetallic phases of the Na-Tl type," W. Klemm and H. Tricke, Z. Anorg. U. Allgem. Che., 283, 162-8 (1955)

1) Na Tl -116×10^{-6} 4) Li Al $+7 \times 10^{-6}$

2) Li Zn 2×10^{-6} 5) Li In -2×10^{-6}

3) Li Cd 6×10^{-6} 6) Na In -30×10^{-6}

The above are molar susceptibilities.

2, 3, 4, 25 are very nonmagnetic

124. "Magnetic determination of the shape of the coherence zones in the segregation from supersaturated copper-iron mixed crystals," A. Knappwost, Z. Physik Chem 4, 364-75 (1955)

Cu-Fe mixed crystals. Precipitation of antiferromagnetic intermediate phase observed. Can be converted to ferromagnetic phase by cooling in liquid nitrogen.

125. "Existence of a magnetically characteristic intermediary phase in the separation from supersaturated copper-chromium mixed crystals," Adolf Knappwost and Hans Zeiger, Naturwissenschaften 42, 296-7 (1955)

Specimens annealed in H and quenched from 600-1000°C. Mag. susceptibility determined is a function of concentration up to 1 percent Cr, and temperature from 600-1000°C. Susceptibility is linear with Cr.concentration up to composition limit of homogeneous phase, then becoming independent of composition when the alloy becomes heterogeneous. Authors find evidence for separation of Cr in antiferromagnetic form for the 0.3 wt percent alloy.

126. "Magnetic susceptibility of hafnium and manganese," C. J. Kriessman, Jr. and T. R. McGuire (U. S. Naval Ordnance Lab., White Oak, Md.), Phys. Rev. 98, 936-7 (1955)

4.2 -1670°K Temp. range

$0.42 \pm 01 \times 10^{-6}$ mu/gr. hafnium.

Slight pos. dependence on temperature.

127. "Paramagnetic susceptibility measurements on palladium-silver alloys," Ebbe Kronquist, Arkiv Fysik. 10, pp. 49-57 (1955)

Palladium and some palladium-rich alloys. Measurements from room temperature to 1000°K. No appreciable change on cold-working noted. Experimental results compared with Stoner's collective electron theory. Proc. Roy. Soc. A165 372 (1938)

128. "Ferromagnetism in noble-metal alloys containing manganese," F. A. Otter, P. J. Flanders, and E. Kloholm, Phys. Rev. 99, 600, J. Franklin Inst. 260 75-6 (1955)

Electrical resistives determined as well as magnetic properties. Author believes that probably all noble-metal alloys which contain $\geq 8\%$ manganese are ferromagnetic.

129. "Paramagnetic properties of austenitic alloys with different chromium contents," V. I. Prosvich and S. Yu Sigolaev, Izvest, Akad. Nauk. S. S. S. R., Otdel-Tekh. Nauk. 1955, No. 7, 96-100.

Hysteresis of susceptibility noted with maximum value at 300-400°C. with complete reversibility noted at 20°C and above 600°C. Increasing chromium content increases hysteresis. [This behavior is suggestive of antiferromagnetism.]

130. "Neutron and diffraction studies of the magnetic structure of alloys of transition elements," C. G. Shull and M. K. Wilkinson, Phys. Rev. 97 304-10 (1955)
Fe-Cr, Ni-Fe, Co-Cr, Ni-Mn. Magnetic moment detected.
131. "The susceptibility of $\text{CuCl}_2 \cdot \text{H}_2\text{O}$ powder in the antiferromagnetic and paramagnetic states," L. C. Van der Marel, Q. Van den Broek et al, Physica, 21 685-94 (1955)
Neel temperature of 4.33°K .
132. "Magnetic susceptibility measurements on germanium between room temperature and liquid hydrogen temperature," A. Van Itterbeek, L. de Greve and W. Duchateau, Appl. Sci., Research, 4B, 300-8 (1955)
"Large" variation due to paramagnetic term at liquid H temp.
133. "Proof of the interpretation of the magnetic properties at elevated temperatures of the rhombohedral sesquioxides of titanium, vanadium, chromium, and iron (Ti_2O_3 , V_2O_3 , Cr_2O_3 , and Fe_2O_3)," Jules Wucher. Compt. Rend. 241, 288-90 (1955)
Author believes that the magnetic behavior of these compounds can be explained by assuming that a transition takes place from an antiferromagnetic ordering of the crystal network to a "molecular" antiferromagnetism above a certain temperature, Good agreement with exper. values.
134. "Deviations from the Curie-Weiss law in cupric compounds," J. Phys. Radium, 17, 134-9 (1956)
Curie-Weiss law obeyed with negative Curie temperatures. Range investigated was $90-1200^\circ\text{K}$. CuCl_2 , CuBr_2 , CuO .
135. "Magnetic susceptibility of copper metal at low temperature," Raymond Bowers, Phys. Rev. 102, 1486-8 (1955)
$$\chi_{\text{gram}} = \left(-.083 + \frac{.023}{T} \right) \times 10^{-6}$$

Temperature dependence much smaller than previously reported.
136. "Investigation of the superconductivity of hafnium," Robert A. Hein, Phys. Rev. 102, 1511-18 (1956)
Magnetic susceptibility measurements at very low temperature, $4.22-0.08^\circ\text{K}$.
137. "Magnetic phenomena in the disintegration of copper-cobalt mixed crystals," A. Knappwost and F. Ulrech, Z Physik. Chem 6, 151-61 (1956)
Cobalt cumuli of about 20 Angstroms are spontaneously magnetized. No signs of antiferromagnetic intermediate stage as observed in Cu-Fe mixed crystals.

138. "Magnetic properties of Mg_2Sn ," L. L. Korenblit and H. P. Kolesnikov, Zhur. Tekn. Fiz., 26, 941-6 (1956)

X is "very small." Sample with highest electrical conductivity $\sigma = 6.1 \text{ ohm}^{-1} \text{ cm}^{-1}$

Paramagnetic effect determined: ie = X - X high ohm sample.

139. "Magnetic properties of B-uranium hydride," S. T. Lin and A. R. Kaufman, Phys. Rev. 102, 640-6 (1956)

Hysteresis loops, coercive force given at 161.1, 75, 4.2°K; 170°K to 4.2°K, reduced spontaneous mag. vs. reduced temperature. (T/T Curie)

140. "Diamagnetism of organosilicon compounds," R. Mathure and C. L. Hanekar, Chemistry and Industry, 1956, 767-8.

No anomalies mentioned.

141. "Magnetic properties of $MnAu_4$," A. J. P. Meyer, Compt. Rend., 242, 2315-18 (1956)

Two phases: γ - base-centered cubic, stable above 400°K,
metastable at room temperature

γ' - quadrilaterally deformed f. c. e. stable below 400°K

Phase	Ferromag. Curie PT	Paramag. Curie Temp.	Mag. Mom. (Bohr)
γ	361°K	373°K	4.85
γ'	123°K	203°K	4.65

142. "Magnetic properties, antiferromagnetism, and ferromagnetism of $MnAu_2$," A. J. P. Meyer and D. Taglong, J. Phys Radium. 17, 457-65 (1956)

Discusses transition from nonmagnetic to ferromagnetic state upon reaching a critical magnetizing field. (10,000 Oe at 100°K).

143. "Paramagnetism in the γ phase in copper-manganese alloys," A. P. Meyers, Can. Jour. Phys., 34, 527-34 (1956)

Less than 25% (at.) Mn; - Curie-Weiss temperature dependence observed. Mn 30-40%, deviations from C. W. law at low temperature. Mn > 60%, < 70%, straight line on C. W. plot but weak temperature dependence. 70-80% Mn; minimum in susceptibility noted 900-950°. 90% Mn; continuous increase with temperature.

144. "The magnetic properties of the chromium-tellurium-selenium system," Ichiro Tsubokawa, J. Phys. Soc. Japan. N, 662-5 (1956)

Cr ($Te_{1-x} Se_x$) system. Ferromagnetism observed $0 \leq x \leq 0.8$. Compounds outside range are antiferromagnetic.

145. "Diamagnetism and paramagnetism of metallic mixed crystals. VII: α phases of copper and silver with B-group elements," E. Vogt and H. Friedewold, Ann. Physik 17, 281-92 (1956)
- See: Landholt-Borstein, Vol. I T1. 1, 1950 p. 394, cf
- CA. 49-13299h (Chemical Abstracts)
48-8601i
146. "Magnetic susceptibility of chromium II," Friedrich Wagenknight, Z. Physik Chem 7, 332-41 (1956)
- Corrections for oxide can be obtained only from large number of samples with differing oxide content.
147. "Superexchange and the magnetic properties of palladium between 80°K and 1600°K," Jules Wucher, Compt. rend. 242, 1143-5 (1956)
- Between 700-1600°K suggest the expression $(X_m + 20)(T + 90) = 0.250$ (c. g. s.)
Theoretical discussion; equation derived which agrees with experimental observation within 3 percent in temperature range 100-1600°K.
148. "Spontaneous magnetization in Mn-Ga-C alloys," Canadian Journal Phys. 35 No. 7, 819-822 (1957)
149. "The antiferromagnetism of manganese-copper alloys," G. E. Bacon et. al. Proc. Roy. Soc. (London) Ser. A, 241 223-238 (Aug. 7, 1957)
150. "New type of magnetic transition in $Mn_3ZnC.$," B. N. Brockhouse and H. P. Meyers, Can. Jour. Phys. 35, No. 3 313-323 (Mar 1957)
- Ferromagnetic, but anomalously 231°K.
151. "Paramagnetic properties of dilute palladium-cobalt alloys," J. P. Burger and J. Wucher, Compt. rend. 245 No 25, 2230-3 (Dec, 1957)
- Measurements made to 1000°K 1, 2, 4 percent cobalt. Rev. from Curie-Weiss law observed.
152. "Properties of palladium - rhodium alloys," F. E. Hoare and J. Preston, Nature 180, 334 (Aug. 1957)
153. "Magnetic properties of UMn_2 , S. T. Lin and A. R. Kaufman, Phys. Rev. 108, No 5, 1171-74 (Dec. 1957)
154. "Temperature dependence of the magnetic susceptibility of silver-zinc alloy," L. Meyer and D. Weiner, Phys. Rev. 108 No 6, 1426-7 (Dec 15, 1957)

155. "Specific heat and magnetic susceptibilities of alloys of cerium with lanthanum at low temperatures," L. M. Roberts and J. M. Lock, Phil. Mag. 2 No. 18 311-319 (June 1957)
156. "Magnetic properties of Cu-Mn alloy." K. Yoshida, Phys. Rev. 106 No. 5 893-898 (June, 1957)
- S-d interaction and the polarization of conduction electrons investigated in Cu-Mn alloy.
157. "Magnetic properties of dilute magnetic alloys, and of the rare-earth metals," J. Appl. Phys 29 No 3, 520-521 (March, 1958)
- Theoretical discussion.
158. "The magnetic susceptibilities of alloys of cerium with thorium," L. F. Bates and M. M. Newmann, Proc. Phys. Soc. 72, Pt 3, 345-52 (Sept. 1958)
- 90, 71, 60, 42, 20, 10, 5 at. percent Ce in the 90°K-700°K- sharp decrease in suscept. at low temp. -correlates with resist. changes. Above room temp., Curie-Weiss law dependence.
159. "Precipitation and magnetic annealing in a copper-cobalt alloy," J. J. Becker, J. Appl. Phys. 29, No 3 317-318 (Mar. 1958)
- 2 percent cobalt in copper.
160. "Electrical and magnetic behavior of dilute alloys: Co in Cu, Mn in Cu," I. S. Jacobs and R. W. Schmitt, Physica 24, Suppl., S-174 (Sept 1958), also pg. 2682.
161. "Ferromagnetism of a zirconium-zinc compound." B. T. Mathias and R. M. Bozorth, Phys. Rev. 109, No. 2, 604-5 (1958)
- Compd. Zr Zn₂ was found to be ferromagnetic below 35°K.
162. "The magnetic properties of a series of nickel-copper alloys," A.J. P. Meyer and C. Wolf, Compt. rend. 246 No 4, 576-579 (French) (Mar 1958)
163. "Low residual induction in high aluminum-iron alloys," D. Pavlovie and K. Foster, J. Appl. Phys 29, No 3 368-9 (1958)
- 10-16 percent (wt) aluminum. Ratio of residual induction to induction at 100 Oe.05-0.10 at composition having crystal anisotropy. Values for both quenched and furnace-cooled specimens.
164. Deleted.
165. "Completely nonmagnetic alloy for instrumentation in magnetic fields," E. W. Pugh, Rev. Sci. Instr. 129, No 12, 1118-19 (Dec 1958)

High purity (low Fe conc.) Alloy 96.3% Cu-3.7 Ni is described. Magnetic moment exactly zero at room temperature. 15-350°K, mass diamagnetic susc. less than $.004 \times 10^{-6}$ (pure Cu $.080 \times 10^{-6}$).

10% increase in content of nickel leads to decrease in mass susceptibility of $.01 \times 10^{-6}$. 0.0025% Fe gives positive contribution to Cu with strong Curie-Weiss type temp. dependence; magnitude is roughly 0.02×10^{-6} at 50°K.

166. "Magnetic susceptibility of copper-nickel and silver-palladium alloys, at low temp." E. W. Pugh and K. M. Ryan, Phy. Rev. Vol III No.4, 1038-42 (Aug. 1958)

167. "Magnetic properties of holmium and thulium metal," Rhodes, Legvold, Phys. Rev. 109, No 5 1547-1550 (Mar. 1958)

Rare earth metals; see Cycle C for mechanical props.

168. "Magnetic properties and the structure of metals," W. Sucksmith, Brit. Jour. Appl. Phy. Suppl. No 6 S24-S27 (1958)

168B. "Gd-La and Gd-Y alloys," W. C. Thoburn, S. Legvold and F. H. Spedding, Phys. Rev. 110 No 6, 1298-301 (June 1958)

Some alloys of high Gd content are ferromagnetic. (Pure gadolinium is ferromagnetic.) Lower concentration alloys exhibit para-antiferromagnetic transitions.

169. "Magnetic susceptibility and electrical resistivity of Au-Mn alloys," J. Phys. Chem. Solids N, No 1-3 46-54 (Sept. 1959)

170. "Method for determination of the normal magnetization curve for very low permeability materials," Electrotechnica 46, No 3, 193-9 (Mar. 1959)

Might be adapted coercive force or remanence measurements. Some values may be reported.

171. "The diamagnetic susceptibilities of some paraffins," W. R. Angus, G. I. W. Llewellyn and G. Stott, Trans. Far. Soc. 55 Pt. 6 887-90 (June 1959)

172. "Magnetic properties of dilute alloys, magnetic interaction, and antiferromagnetisms in alloys of the type noble metal-transition metal," H. Blandu and J. Fried, J. Phys. Rad. 20 No 2-3, 160-8 (1959).

173. "Magnetization of compounds of rare earths with platinum metals," R. M. Bozorth et al., Phys. Rev. 115, No 6, 1595-6 (Sept. 15, 1959)

174. R. M. Bozorth, Edit., Magnetic Properties of Metals and Alloys American Soc. Metals, Cleveland, Ohio (1959)

Bibliography included on various ferromagnetic alloys.

175. "The magnetic susceptibility of vanadium between 20 and 293°K," B. G. Child, Phil. Mag., 4 1120-1130 (1959)

176. "Properties and state of metal atoms in certain organo-metal compounds," Ya G. Dorfman, Dokl. Akad Nauk S. S. S. R. 125 No 4 765-6 (1959)

When computing diamagnetic susceptibilities, allowance must be made for "the paramagnetic component of the whole molecule."

177. "Atomic magnetic moments, Curie-point exchange energy, and paramagnetic susceptibility of ferromagnets," F. M. Gal'perin, Acad. Science U. S. S. R., Bul. Phys. Ser. (English translation) 23, No 3 391-6 (1959).

178. "On the properties of the rare-earth metals," P. O. de Gennes, Compt. rend. 247, No 21, 1836-8 (1959)

Theoretical - discusses the possibility of conduction electron spin-coupling of mag. moments of ions. Derives expression relating Curie point with other quantities.

179. "Magnetic susceptibility and electrical resistivity of Au-Mn alloys," A. Giansoldati, J. O. Linde, and G. Borelius, Phys. Chem. Solids 11, (1959)

180. "The silver-based Heusler alloys," E. V. Hal, Phil. Mag. (Eighth Ser.) 4, 730-44 (June, 1959)

These alloys are ferromagnetic alloys of silver, aluminum, and manganese.

181. "The antiferromagnetic structure of Ni-Mn," O. S. Kasper and J. S. Kovel, J. Phys. Chem. Solids Vol 11, No 3-4, 231-8 (Oct 1959)

182. "Ferromagnetism and antiferromagnetism in disordered Ni-Mn alloys," J. S. Kouvel et al, J. Phys. Radium 20, No 2-3, 198-202 (1959)

Suggests a coexistence of ferromagnetic and antiferromagnetic states.

183. "Magnetic susceptibility of solids," J. A. Krumhansl, J. Appl. Phys. 30, No 8 1183-6 (Aug. 1959)

Review, primarily concerns semiconductors.

184. "Magnetic susceptibility of iron ditelluride," J. P. Llewellyn, T. Smith, Proc. Phys. Soc. 74, No 475, Pt. 1, 65-74 (1959)

185. "Magnetic susceptibility of close-packed, hexagonal gold-indium alloys," T. B. Massalski, L. Meyer, and P. Weiner, Phys. Rev. 115, No 3, 301-21 (July, 1959)

Made at 300°, 77°, 4.2°, 1.2°K

186. "The magnetic susceptibility of silver-manganese solid solutions between 100°K and 500°K," P. P. Morris and I. Wilton, Proc. Phys. Soc. 73 Pt 3, 422-32 (Mar, 1959)
187. "Magnetic susceptibility of Ce-Th alloy," T. Murao, Prog. Theor. Phys. 22, No.2 307-9 (Aug. 1959)
188. "Magnetic susceptibility of iron-chromium alloys," M. M. Newman and K. W. H. Stevens, Proc. Phys. Soc. 74, 290-296 (1959)
Magnetic susceptibility as a function of temperature, Fe content.
189. "Magnetic susceptibility of thorium metal in the range 130-300°K, J. F. Smith and J. D. Greinen, Phys. Rev. Vol 115, 884-885 (1959)
190. "Some magnetic properties of dilute ferromagnetic alloys," W. Sucksmith, J. Physics Rad. 20, No. 2-3, 290-94 (February, 1959)
191. "Theory of weak ferromagnetism," E. A. Turov, Zh. eksper. teor. fiz. 36, No 4 1254-8 (Apr. 1959)
English trans: Soviet Physics JETP, New York, 36 (9) No 4 890-3
192. "On the magnetic behavior of aluminum and aluminum-solid solutions," R. Ungelback and E. Vogt, (German) Acta Metall. 7 445-et seq. (July, 1959)
193. "Measurement on the magnetic susceptibilities of Ag-Mn and Cu-Mn alloys," A. Van Itterbeek, R. Pollentier, and W. Pellaers, Appl. Sci. Res. B 7, No 5, 329-37 (1959)
Concentration of ferromagnetic impurities determined magnetically. Otherwise alloys are paramagnetic. Room temp.-liquid hydrogen temp.
194. "Fundamental questions in magnetism," J. H. VanVleck. Paper from Magnetic properties of metals and alloys, pp 1-17; Amer. Soc. Metals; Novelty, Ohio. (1959)
Review.
195. "Magnetic investigation of solid solutions of gold with titanium and vanadium, rich in gold," E. Vogt, D. Gerstenberg, Ann. Phys. 4, No 1-5 145-153 (1959)
Covers 90 to 906°K. Ti contribution is paramagnetism independent of temp. and proportional to Ti concentration. V contribution partly temp. independent paramagnetism, partly Curie-Weiss, temperature dependent paramagnetism. For V, neither of these effects is proportionally related to concentration.
196. "Magnetic study of Cu - Fe alloys," E. Scheil, E. Wachtel, A. Kalkul, Ann. Phys. 4 No 1-5, 58-65 (1959)
Iron precipitates as γ iron from supersaturated Cu-Fe solutions (paramagnetic). By plastic deformation at low temperatures can be transformed to some extent to ferromagnetic α -iron.

197. "Magnetic properties of brass," H. Zeiger, Metall 13, 1025-1027 (1959)
 Mag. suscep. of mixed binary Cu-Zn crystals. Author finds ferromagnetism, which can be eliminated by pickling.
198. "Magnetism and magnetic properties," J. P. L. Literature Search No. 186. Jet Propulsion Lab., Cal. Inst. Tech. (Jan. 1960)
 Includes information 5 years previous to date.
199. "Properties of alloys with superparamagnetic precipitations (Fe and Co amalgams, Cu-Co alloys with 2% Co, Ni-Mn alloys with more than 25% Mn)," (German) Solid-state physics in electronics and telecommunication, 3 Magnetic and optical properties, Pt 1, 210-222 (1960)
200. "Physical properties of niobium, tantalum, molybdenum and tungsten," B. B. Argent, G. J. C. Milne, J. Less Common Metals 2, No 2-4, 154-62 (1960)
 Magnetic susceptibility, 10 - 295°K.
 Zone-refined specimens used (high purity).
201. Delete
202. "Magnetic behavior of polycrystalline neodymium, holmium, and erbium from 300 to 1500°K," S. Arojas and K. S. Miller, Jour. Appl. Phys. Supp. 31, 325 s - 325S (1960)
203. "Importance of indirect interaction in theory of transition metals and rare earths," A. A. Berdyshev, B. V. Karpeno, Physics of Metals and Metallorgraphy 8, No. 3 1016 et seq. (1960).
204. "Magnetic analysis of the precipitation of iron from beta brass," Acta Metallurgica 8 823-832 (1960).
205. "The possibility of anomalous magnetic properties in macro-molecules," V. L. Ginzburg and F. M. Fain, Dokl. Acad. Nauk. S.S.S.R 131 No. 4, 785-8 (April 1, 1960).
206. "Thermomagnetic study of dilute alloys of Pd - Cr - hydrogen system," J. P. Burger, J. Wucher, Compt. rend 251, No. 23 2667-9 (1960).
 Curie point varies linearly with chromium concentration.
207. "Magnetic susceptibility of vanadium-chromium solid solutions," B. G. Childs, W. E. Gardner and J. F. Penfold, Phil. Mag, 5, 1267-1280 (1960).

208. "Electrical and magnetic properties in alloys," R. B. Coles.
Paper from The Physical Chemistry of Metallic Solutions, Intermetallic Compounds, Symposium, Vol. 1, 34-59; Chemical Publishing Co., Inc., New York (1960).
209. "Ferromagnetism in Pd-rich palladium-iron alloys," J. Crangle, Phil. Mag. 5 335-342 (1960).
1.25 - 15.25 Fe from 20 - 400° K Curie point as a function of composition.
210. "Band structure of transition metals and their alloys," J. B. Goodman, Phys. Rev. 120, 67-83 (Oct. 1, 1960).
Band structure and magnetic properties; Pauli paramagnetism, antiferromagnetism, ferrimagnetism, and ferromagnetism.
211. "Magnetic susceptibility of some diamagnetic alloys," W. G. Henry and J. L. Rogers, Can. Jour. Phys 38, 908-926 (1960).
Have behavior of solid solutions of many compositions.
212. "Magnetic properties of Cr - Ge alloys," S. P. Margolin and E. G. Fakidov, Fiz. Metallo. i Metallovedenie 9, 823-827, (1960).
Effect of composition, temperature on magnetization and susceptibility.
213. "Mechanism of antiferromagnetism in dilute alloys," A. W. Overhauser, Phys. Chem. Solids, 13, 71-80 (1960).
214. "Analysis of magnetic interaction in alloys of Pt with iron-group transition metal alloys," Hiroshi Sato, J. Appl. Phys, Suppl., 31, 327s-329s (1960).
215. "Magnetic susceptibilities of nonferromagnetic transition metals," Masao Shimizu and Tehesi Takahashi, J. Phys. Soc. Japan 15 2236-42 (1960)
216. "Contribution to the magnetic properties of some B-8 type phases; CoSb, Co Sn_{0.7}, Ni Sb, Co_x Ch_{1-x} Sb and Cr_{0.75} Fe_{.25} S6," Hans Schmid, Cobalt, pp. 26-32 (June 1960).
217. "Magnetic properties of manganese-copper alloys," R. Street, Journal of Applied Phys., Suppl. 31, 310-317 s (1960).
218. "The magnetic susceptibility of Ag-Mn and Cu-Mn solid solution between 1.2 and 368° K," A. Van Itterbeek et. al, Appl. Sci. Res., 8 (1960).
219. "Thermal remanence and isothermal remanence in magnetization of Pd₃ Mn₂ alloy," R. Wendling, (French) Compt. rend. 250, No. 12, 217-33 (1960)
Alloy antiferromagnetic after quenching. Shows remanence after appropriate annealing.

220. "Magnetic properties of Cr_2As and Cr_2Sb ," M. Yuruji, J. Phys. Soc. Japan, **15**, 2007-2012 (1960)
- Thermomagnetic properties.
221. "Magnetic properties of B8 type compounds in manganese - Tin system," M. Asanuma, Phys. Soc. Japan, Jour. **16** R65-R66 (1961)
222. L. F. Bates, Modern Magnetism, 4th Ed. Cambridge Univ. Press. (1961) 514
223. "Critical temperatures of binary alloys with one magnetic component," G. M. Bell, W. M. Fairbairn, Phil. Mag. **6**, No. 67 907-35 (1961)
224. "Susceptibilities and negative Knight shifts of intermetallic compounds," A. M. Clogston and V. Jaciarunara, Phys. Rev **121**, No. 5 1357-62 (Mar 5, 1961)
- Vanadium with other transition elements.
225. "Magnetic susceptibility and electrical resistance of homogenous and heterogenous iron-copper alloys," Cornelius Berhout, Z. Metallkunde **53**, 179 - 186 (1961)
- 0.11 - 3.0 Fe percent. Measurements made during annealing (0.66 percent Fe) and after varying degrees of cold-rolling; anisotropy of susceptibility noted.
226. "Study of the alloys of transition elements. Final report, 1953-1961," U. Illinois College Engr., Paul A. Beck, AROD Rept. no. 618:23 ASTIA AD 266-280 (Prob 1961)
- Magnetic susceptibility discussed.
227. "Superconductivity and ferromagnetism in the system Gd-Ru_2 , Th-Ru_2 ," R. M. Bozorth, B. T. Mathias, and D. D. Davis. Paper from Seventh International Conference on Low-Temperature Physics, Proceedings pp 385-389 Univ. Toronto Press (1961)
228. "The properties of Ti-Ni and associated phases," W. J. Bueler and R. C. Wiley (U. S. Nav. Ord. Lab., WT. Oak, Md.), ASTIA AD 266-607 (Aug 3, 1961) 91 pages
- Magnetic susceptibility determined.
229. "Thermodynamic properties of solid solution, Pt. 3. Copper-rich solid solutions of copper + zinc + manganese," G. A. Chadwick and B. B. Argent, Faraday Soc., Trans. **57**, 519-624 (1961)
- Magnetic susceptibilities also determined - with Sucksmith ring balance.
230. "Magnetic susceptibility and electron-spin resonance studies in dilute Mg-Mn and Al-Mn alloy at low temperatures," E. W. Collings and K. T. Hedgecock, Seventh International Conference on Low Temperatures Physics, Proceedings p. 259-60 Univ. Toronto Press, Canada (1961)

231. "Magnetic properties of chromium between 0-350°C," E. W. Collings, F. T. Hedgecock, and A. Siddayu, Phil Mag. 6, 155-158 (1961)
Antiferromagnetic transition at $39. \pm 0.5^\circ\text{C}$.
232. "Magnetic investigation of pure manganese and several of its alloys," H. W. Cooper, H. S. Arrot, H. W. Paxton, J. Appl Phys. 32, No 12 2506-12 (Dec, 1961)
233. "Magnetic properties of a polycrystalline alloy, Cu + 22.8 at % Manganese," I. G. Fakidov and B. V. Znamenski, Zhur. eksp. teor. fiz., 40, 1522-23 (1961)
234. "Feasibility study on the preparation of paramagnetic polymers based on ferrocene type compounds," W. Flavell ASTIA AD-267-609
Yardley Research Labs, Ltd. (Gt. Brit.). Final report No. I, 1 Nov 60 - 31 Oct 61 58 p (Nov 27, 1961). 47 references.
235. "Antiferromagnetism in dilute atoms of cobalt in copper," R. Fournier and L. Weil, J. Phys Soc. Jap 17, Suppl. B-1, 118-21 (Mar 1962). Magnetism and crystallography conference.
236. "Low field De Haas-Van Alphen effect in zinc," Alfred S. Joseph (Case Inst. Tech.), ASTIA Accession No. AD 273-017 OTS \$6.60 34 p. (Nov. 1961)
25 references.
237. H. Kajimi, R. S. Tebble, D. E. G. Williams, Proc. Royal Soc. Ser. A 260, No 1301, 237-50 (1961)
Susceptibility (paramagnetic) measured for range 20 - 1800°C for Ti, Zn, Hf, V, Nb, Ta, Mo, W, Re, Rh, Lu, Pt.
238. "The ferromagnetic - antiferromagnetic properties of copper-manganese and silver-manganese alloy," J. S. Kouvel, Phys & Chem Solids, 21, 52-70 (1961)
239. "Abrupt magnetic transition in Mn Sn_2 ," J. S. Kouvel, C. C. Hartelue, Phys Rev 123, No 1, 124-5 (July 1, 1961)
Magnetic susceptibility and electrical resistivity.
240. "Ferrocene polymers, a literature review, Pt I," W. A. Lee, 15 p. Royal Aircraft Est. (Gt. Brit.) Rept. No. Chem 525 (Sept 1961) ASTIA Access. AD 269-708
The preparation and properties of addition, condensation, and recombination polymers of ferrocene are reviewed. General lack of information. Uses claimed for some polymers - lubricants, adhesives, rubbers, and plastics. Magnetic properties of some of the polymers discussed. 49 references given.

241. Honeywell Research Center, Hopkins, Minn. "Magnetic remanence in dilute alloys." Final report. O. S. Lutes and J. L. Schmidt, ASTIA AD 267-609 (25 Oct 1961) 22 p. OTS Price \$2.60.
- Cu-Mn, Au-Cr found to be ferromagnetic. 0.6 - 40°K temperature range investigated.
242. "The Van Vleck temperature-independent magnetism of metals," L. E. Orgel, Phys & Chem. Solids, 21, 123-124 (1961)
243. "Magnetic susceptibility of materials commonly used in the construction of cryogenic apparatus," G. L. Salinger, J. C. Wheatley, Rev. Sci. Apparatus 32, 872-74 (July 1961)
- Measurements in 1.6° to 4.2°K temp. range. Says any lot of stainless steel should be tested individually. (Stainless steel Fe - Cr - Ni)
244. "Magnetic susceptibility of chromium and chromium - Fe alloys," Masao Shimizu and T. Takahusii, J. Phys. Soc. Japan 16, 1544-48 (1961)
245. "Magnetic susceptibilities of aluminum-rich transition metal intermetallic compounds," M. A. Taylor, Phys. Soc., Proc. 78, Pt. 6 cil, No 505, pp 1244-1254 (1961)
246. "Magnetic investigation of gold-chromium alloys," Ernst Wachte and U. Vetter, Z. Metalkunde, 52, 525-529 (1961)
- Composition ranges investigation 7.5 - 29.2 at % cn. Temp. range 173-1000°K.
247. "Absence of antiferromagnetism in molybdenum," S. C. Abrahams, J. Phys. Chem. Solids 23 1348 (Sept 1962)
248. Materials in Design Engineering, Materials in Selector Issue. Mid-Oct, 1962, pp. 154-155
- Gives susceptibility of several titanium alloys, as 1.00005 at 20 oersteds. Tensile properties also given.
249. "Diamagnetic susceptibilities of the elements characterized by paired electrons in the outer shells," R. Aynand, Compt. rend. 255 No 8, 1257-9 (Aug, 1962)
250. "Diphenyl propyl hydrazyl; transition to antiferromagnetic state," Z. Phys. 159, No 4, 384-7 (1960)
- Only reference in bibliography dealing with possible magnetic ordering (i.e. anti,-ferri,- ferromagnetism) in organic compounds.

251. "Anisotropic superexchange interaction and weak ferromagnetism," J. Muriya, Phys. Rev 120, No 1, 91-8 (Oct 1960)

Discusses α -Fe₂O₃, MnCO₃, Cr Fe₃

252. "Magnetism of dilute solutions of iron-group elements in platinum metals," R. M. Bozorth, D. D. Davis and J. H. Wernick, J. Phys. Soc Japan 17, Suppl. B-1, 115-17 (Mar 1962)

253. W. J. Buehler, R. L. Wiley, Tran A.S.M. 55, No 2, 269-76 (June 1962)

Titanium - nickel alloys, quench-hardenable, paramagnetic.

254. "Ferromagnetism and antiferromagnetism in nonferrous metals and alloys," J. Crangle, Metallurgical Reviews, 7, No 26, 133-174 (1962)

255. "Electric and magnetic properties of copper-gold and hydrogenated palladium alloys, with small additions of transition metals," E. Daniel, Phys & Chem Solids 23, 975-83 (1962)

256. M. V. Dekhtyor, Fiz. Tverdogo Tela. 4, No 3, pp (Mar 1962)

Antiferromagnetic properties of Ni₃Mn alloy. Temperature dependence of remanent magnetization and Neel compensation point in ordered alloy. Antiferromagnetic ordering of spins can explain relationship between remanent magnetization and quenching temperature.

257. "Low temperature study of the electronic band structure of metal and their dilute alloys," W. L. Gordon, T. G. Eck, ASTIA accession No -AD 273-018 (Jan 1962)

DeHaas-van Alphen effect and related phenomena. Some susceptibility measurements

258. "Localized magnetic moments in metals," A. J. Freeman, ASTIA AD 293-835 (Nov 1963) 6p

Susceptibility measurements on system Rh-Mo.

259. "Effect of heat treatment and plastic deformation on paramagnetic susceptibility of Cu-Ni alloys," L. E. Hedman, R. D. Mattuck, Phys and Chem. Solids 23, 955-61 (1962)

Electrical resistivity also determined for some of the alloys.

260. Invar/Behavior and magnetic moment of the γ -phase of iron-palladium alloy," H. Kussmann and K. Jessen, J. Phys. Soc. Japan Suppl. B-1, 130-9 (Mar 1962)

261. "The paramagnetic susceptibility of some b.b.c. transition-element alloys and its temperature dependence," S. Laniguchi, R. S. Tebble and D. E. G. Williams, J. Phys Soc. Jap. 17, Suppl. B 139-42 (Mar 1962)

Measurements made from 20 - 1350°C.

262. "Review of fundamental developments related to susceptibility," Mulay, Anal. chem. 34 (no 5) 343 R-61R p. 360-12 (April 1963)

Large bibliography included.

263. "Magnetic properties of Mn-Zn alloy," Y. Nakagawa, S. Saikai, and T. Huni, J. Phys. Soc. Japan 12, Suppl. B-1, 168-71 (Mar 1962)

264. "Magnetic susceptibility of cupric oxide," M. O. Keeffe, F. S. Stone, Phys. & Chem. Solids 23, 261-6 (1962)

Below 140°K, 2×10^{-6} (per gram).

Rises to broad max. of 3.4×10^{-6} at 540°K. "antiferromagnetic superexchange" proposed to explain results, with Neel temperature of 230°K.

265. "Collective electron metal magnetism," D. Rhodes, E. P. Woldfarth, Phil. Mag. 7 No. 88 1817-24 (1962)

Theoretical.

266. "Magnetic interactions between manganese atoms in metals," H. Sato, A. Arrot, J. Phys. Sci. Jap. 17, Supp. B-1, 147-51 (Mar. 1962)

267. "Appearance of a weak ferromagnetism in fine particles of antiferromagnetic materials," W. J. Shule and V. P. Deetscreek, Magnetism and Magnetic Materials, Plenum Press, N. Y. (1962)

Possible magnitude of effect should be investigated, since the number and type of antiferromagnetic compounds and alloy is considerably greater than the number and type of antiferromagnetic compounds.

268. "Electrical and magnetic properties of organic solids," 11 p. Gordon Tollin (Univ. Arizona, Tucson) (Nov. 1962) - Contract AF 19(604) - 8475 AFCRL - 62 - 1116 - N63 - 12731 (STAR. NO.)

Optical and magnetic properties in flavin semiquinones, flavinphenol complexes. Unpaired spin density determined for some of the compounds.

269. "Temperature dependence of the magnetic susceptibility of Mn-Cu alloys," D. L. Valkov, P. H. Phenichkin and G. P. Karpocheva, Zh. eksper. teor. fiz, (U.S.S.R.) 43 No. 2 (8), 370-5 (Aug. 1962) (Russian)

Temp. dependence 77°K - 1250°K

Mn content 5.70 to 91.2 at %

270. "Knight shifts and magnetic susceptibility in vanadium alloys with Ti, Cr, and Tc," D. O. Von Ostenburg et. al., Phys. Rev. **128**, No. 4, 1550-4 (Nov. 1962)
271. "Recrystallization textures and magnetic properties of copper-nickle-iron alloys," R. Wakagonne, T. Yamamoto, Electrotechnia Laboraturi (Tokyo) Bul. **26**, No. 1 23-6 (Jan. 1962)
272. "Review of modern methods of determining impurities in copper and copper alloys," - O. Werner, Metall. **16**, No. 11 (1962)
- Magnetic method mentioned.
273. "Extraordinary Hall effect in paramagnetic gold alloys," M. D. Blue, J. Appl. Phys. **33**, No. 10, 3060-3. (1963)
- Concerns Ni, Co, Te, Mn additions up to 5 percent. Some magnetic susceptibility measurements.
274. "The magnetic susceptibilities of vanadium-based solid solutions containing titanium, manganese, iron, cobolt, and nickel," B. G. Childs, W. E. Garner and J. Penfold, Phil Mag **8** (8th Ser.) No. 87, 419 et seq, (1963)
- These alloys are paramagnetic.
- Magnetic Properties (Cycle B, Ref. 275-304)
275. P. Pascal, Compt. Rend. **149**, 342-5 (1908 ?)
- Topic: additivity of magnetic properties.
276. J. H. Van Vleck, Theory of Electric and Magnetic Susceptibilities (London, New York) (1932)
277. International Critical Tables 6, 354-366 (1929)
- Paramagnetic and diamagnetic susceptibilities of organic, inorganic compounds, alloys.
278. "Effect of small quantities of magnesium on the allotropic transformation of metallic cerium," Compt. rend. **223** 78-9 (1948)
- Magnetic susceptibility, solubility measurements up to 4 percent magnesium.
279. "Magnetic properties of palladium - base alloys," Compt. rend. **229**, 1309-10 (1949)
- Cu, Ag, Au form solid solutions with palladium (at least over comp. range investigated). Pb is soluble up to 14 percent, Sb up to 13 percent. Graph of paramagnetic Curie temperature versus "electron concentration" of added metal (at percentage time true valence). Results compared with Ni-base alloys.

280. "Magnetic properties of cast stainless steel," E. A. Schaefer, Alloy Casting Bulletin No. 13 (Aug. 1949)
- 280B. "Magnetic properties of Elgiloy," 2 Aug., 1950 D. I. Gordon, U. S. Naval Ord. Lab. Unpublished report.
281. R. M. Bozorth, Ferromagnetism, Van Nostrand, New York (1951)
282. "Magnetic characteristics of nonmagnetic metallic materials, permeability and coercive force in strong fields, 100-200 oersteds," M. R. Gross and H. C. Ellinghausen, E. E. S. Report 4E(1) 66904, 4P (1166918 NS-011-083, NS-013-118) (1951)
- An extensive study. Part I.
283. "Magnetic characteristics of nonmagnetic metallic materials, comparison in strong and weak fields," M. R. Gross, E. E. S. Report 4P (2) 66918 NS-001-083 - WS-013-118. (1951)
- Part II of an intensive study.
284. "The magnetic susceptibility of hafnium, gadolinium, and manganese," C. J. Kriessman, Jr. and T. R. McGuire, Phys. Rev. 90, p. 374 (1951)
285. "Ferromagnetism of certain gadolinium-magnesium alloys," Francoise Gaume-Mahn, Compt. rend. 235, 352-4 (1952)
- 72-84% Gd-single crystals. Curie point (in "weak fields") of 102°K, 84-100% - Curie pt. 300°K. Other data.
- | | <u>Moment (Bohr mag)</u> | <u>Curie (temp)</u> |
|-----------------------|--------------------------|---------------------|
| Paramagnetic (78-84%) | 6.87 | 114°K |
| Ferromagnetic | 7.49 | 102°K |
- 285B. "The measurement of magnetic characteristics of 'nonmagnetic' materials," D. I. Gordon, May 1952, NAVORD 2415 N63-80772
286. "Antiferromagnetism and ferrimagnetism," L. Neel, Proc. Roy. Soc. 65 No. 39, 869-85 (1952) (Nov. 1)
- Review of knowledge up to 1952. Bibliography.
287. "Magnetic behavior of rhenium associated with palladium," Jules Wucher and Nicolas Perakis, Compt. rend., 235, 419-21 (1952)
288. "Magnetic investigation of the nature of the cumuli by separation in the system-copper-iron," A. Knappwost and G. E. Bockstiegel Z. Elektrochem, 57, 700-9 (1953) (See CA 47, 32016, cold rolling and ferromag. cumuli.) Specimens contain 0.3, 0.5, 0.7, 1.0, 1.3 and 2.0% F by wt. quenched from 1030° (F or C?) Tempered samples;

Kinetics of the formation of Fe-rich cumuli at 400° are observed. They are anti-ferromagnetic. After quenching at liquid nitrogen temperature, they become ferromagnetic.

289. "Antiferromagnetism in cupric oxide," Phys. Rev. 94, 781 (1953) B. N. Brockhouse.
290. "The magnetic susceptibility of nickel-copper and nickel-chromium alloys," J. E. Goldman and Arrott, Phys. Rev. 94, 782 (1953)
291. "Magnetic properties of the elements niobium, tantalum, and rhenium," Acta. Chem. Scand. 8, 558-62 (1954)

Element	X gram $\times 10^{+6}$
Nb	2.35 - (3.53×10^{-4}) T ($^{\circ}$ K)
Ta	0.860 - (6.8×10^{-5}) T
Re	56.* (79 - 471 $^{\circ}$ K)

*(9% difference with two samples)

292. "Search for antiferromagnetism in the silicides V_3Si and Mo_3Si ," Phys. Rev. 95, 280-1 (1954)

Degree of antiferromagnetic alignment is very small, if any exists.

293. "Magnetizabilities of binary magnesium alloys and their interpretation from the standpoint of electron theory of metals," Z. Physik, Chem. 202, 352-78 (1954)

Studies the system $M_g Cu_2 - M_g Si_2$, and $M_g Al_2$. Known as Laves phases, j.

294. "Magnetic susceptibility of α and β brass," J. P. L. Bibliography No. 186, Magnetism and Magnetic Phenomena (1960)

Measurements at 77 $^{\circ}$ K series of copper-zinc alloys. 0-47.6% to atomic Zn. Ag-Cd. - 30% Cd. Susceptibility for Cu-solutions ranges from -0.085 (gm^{-1}) to -0.191×10^{-6} for 47.6% Zn. No temp. dependence noted. Refers to theory proposed by Henry and Rogers, Physic. Abstracts, 1957, 4547

295. "The colors of nickel in glasses of various types and their implications concerning glass structure - III. The absorption spectra of nickel in various solutions and in certain organic compounds, also the magnetic properties of nickel in the various experimental glasses in relation to the state of nickel in the different glasses," H. Moore and H. Winkelman, J. Soc. Glass Tech., 39 287-313T (1955, 1956)

- 295B. "Effect of iron on the magnetic properties of beryllium-copper," 24 May 1956 Tech. Rept. No. NGF-T-27-56

296. P. W. Selwood, Magnetochemistry, 2nd Ed. (New York., London 1956.)

297. Deleted
298. "The structure and properties of some ternary alloys of manganese, zinc, and carbon," R. G. Butlers and H. P. Myers, Phil. Mag. 40, 132-43
- Face-centered cubic structure. 20 at %C 10-20 at %Zn, 70-60 %Mn Ferromagnetic. Optimum compound Mn_3ZnC .
299. "Paramagnetism and distribution of the electrons in the definite compounds $NiAl_3$, $CoAl_4$, $FeAl_3$, $MnAl_6$, and $CrAl_7$."
- $CrAl_7$ - less than that of free Al, 0.355×10^{-6}
- $NiAl_3$ - feeble paramagnetism 0.609×10^{-6}
- [Find Article]
300. "Proceedings of the sixth conference on magnetism and magnetic materials," J. Appl. Phys., Supp., 32, No. 3, 340s
- Topic: rare-earth metal compounds with manganese. Curie points (ferromagnetic) are:
- Y Mn_5 - $490^\circ K$
- Sm Mn_5 - $440^\circ K$
- Gd Mn_5 - $465^\circ K$
- $T_6 Mn_5$ - $445^\circ K$
- Dx Mn_5 - $430^\circ K$
- Ho Mn_5 - $425^\circ K$
- En Mn_5 - $415^\circ K$
301. "Ferromagnetic impurities in metals," F. W. Constant, Rev. Mod. Phy. 17, No. 1
302. "Effect of precipitation phenomena in the temperature range of embrittlement at 425° upon some magnetic properties of iron-chromium alloys," Edward Baerlecken and Heinz Fabritius, Stahl U. Eisen 75, 1774-83
- No mention of any nonmagnetic phases. Effect of temperature and cold-working on ferromagnetic properties.
303. "An isothermal anneal study of quenched and cold-worked copper-palladium alloys," F. E. Jaumob, Jn. and A. Sawatsky, Acta. Met. 4, 127-44
- Magnetic susceptibility of disordered Cu-Pd alloys increase when cold-worked at room temperature. Resistivity decreases.

304. "Dependence of paramagnetic susceptibility on short-range-order parameter in binary alloys," R. D. Mattuck, J. Phys. Chem. Solids (Gt. Brit.) 23, 1637-49
Theoretical discussion.
305. Mechanical and Physical Properties (Cycle C, 305-352), "Workhardening of metals; general theory," A. F. Freudenthal, J. Franklin Inst. 248, No. 6 (Dec. 1949)
Bibliography included.
306. "Beryllium and beryllium alloys," J. T. Richards, J. of Metals 3, No. 5, 799-86 (1951)
Alloy systems: precious metals, titanium, zirconium. Bibliography.
307. U. S. Bureau of Stand. Cir N 520, May 7, 1952 206 p G. W. Geil, N. L. Carwile
Tensile properties of copper, nickel and some copper-nickel alloys at low temperature.
308. "Constitutions of aluminum-chromium-zinc alloys of low chromium content," A. R. Harding and G. V. Raynor, J. Inst. of Metals, 86 Pt. 8 435-48 (1952)
Zinc (diamagnetic) rich alloys; chromium add. 9.5 to 2 percent. Bibliography.
309. "Investigation of alloys of 'five nine' (purity) zinc," W. Hofman, et al. Z. Metallkunde 43, M 12, 417-21 (1952) Zn-Al, Zn-Al-Cu alloys.
310. "Magnetic testing methods in metal industry," W. Jellinghaus, Metall. 7 No. 17-18 669-78 (1953)
Paramagnetic and diamagnetic materials; measuring methods and equipment - phase diagrams of number of ferrous and nickel alloys.
- 310B. Woldmann, Engineering alloys (1954)
311. "Mechanical properties of beryllium-copper at subzero temperatures," J. T. Richards, R. M. Brek, J. of Metals 6, No 5 547-80 (1954)
Beryllium-cobalt-copper and beryllium-zinc-copper.
- 311B. J. S. Kasper, Theory of alloy phases, Amer. Soc. Metals Pub., Cleveland, Ohio (1956)
- 311C. M. Hansen, Constitution of binary alloys, 2nd Ed, McGraw-Hill, N. Y., London (1958)
312. Mechanical properties of intermetallic compounds, J. Westbrook, (Editor) Wiley, N. Y. (1960)
313. "On resistivity of intermetallic phases of Nb, Ta, Mo, and W with other transition metals," Iron Age 183, No 25, 114-15 (June 23, 1960)

314. Metallurgy of Hafnium, Ed. by P. E. Thomas, E. T. Hayes, U. S. Atom. Energy Comm., Naval Reactors Div. (1960) 383 p (Avail. Sup. Doc., Wash., D. C., \$1.50)
315. "Some new alloy metals," Mech. World 140, No. 3486 27-28 (1960) Age-hardened Cu-base alloys as substitute for Be-Cu spring alloy: 10Ni - 1.55; - 4 Al. Turbine wheels; 16 Cr - 25 Ni - 6 Mo. High-strength bronze 97.5 Cu - 1.9 Ni - 0.6 Si
316. "Molybdenum," Richard F. Allen, Cornell Engineer, 26, Nov., pp. 36-41 (1960)
Review of physical and mechanical properties of molybdenum.
317. "Physical properties of the rare earth metals," A. A. Duane, The Rare Earths, Ch. 13, 177-189 Wiley, New York (1961)
318. "Konstitution der ternaren metallischen system," Compilation edited by M. Goertler, E. Anastaraudis, No. 12, 56 p (1961) also No. 13, 31 p.
No. 12. Cu and two metals from Fe, Mn, Ni, P, S, Si; also data on Al-Cb, Al-Ti, Fe-Ti, Fe-W, Ni-Ni, Mo-Si and many others.
319. Metal Selector - Steel 149, No. 16, 51-532 (Oct. 16, 1961). Stated to be the most up-to-date single source of information on metals and alloys. Both ferrous and non-ferrous alloys included.
320. "New aeronautic materials," H. Buckle, Technique Moderns, 53, 53-64 (1961)
W-Re-Ta, Os, Mo, Cb, Ru, Hf, Rh, Cr, V, Zr, Pt, Ti, Be, graphite, Mo-Re, W-Re, Ni-Cr, Mo Si₂, B₄C, W, Ti N, Ta B₂, TiC, CbC, Hf C.
Mechanically tested - 160 to 2900°C.
Mechanical and physical properties tabulated; 11 ref.
321. "Niobium, molybdenum, tantalum and tungsten. - A Summary of their properties with recommendations for research and development," R. Syrri Advisory Group for Aeronautical Research and Development, Paris (France). AGARDograph 50, 130 p (1961). ASTIA No. AD-274-036, 1500 ref.
322. Metals Handbook, 8th Ed. Vol. I. Properties and Selection of Metals, American Soc. Metals, Metal Parks, Ohio (1961). Nonferrous alloys 935-1197.
(Magnetic properties listed under subheading G.)
323. "Preparation and properties of some hydrocarbon-soluble cerium and iron compounds," (NRL, Wash., D.C.) ASTIA. AD-266-599 [Prob 1961 Div. 4] [Cerium and iron compounds are generally paramagnetic; hydrocarbons, plastics diamagnetic.]

324. "Effect of the space environment on plastics - a summary with annotated bibliography," Arthur H. Landrock, July 1962, 88 p., 202 ref. (Plastics Rept. R) OTS \$2.25
N 63 - 10170 [From scientific & tech. aerospace reports]
325. Defense Metals Information Center, Columbus, Ohio. Bibliography on metals AD-273-184 62-2-3 (1962)
326. "Development of palladium-base alloys," D. W. Rhys and R. D. Berry, Metallurgia, 66, No. 398, 255-63 (1962)
327. "Thermal and electrical conductivity of copper-manganese alloys," M. K. Gupta, F. Banerjee, W. M. L. Tech. J. 4, No. 4 12-16 (Nov. 1962)
328. Titanium-aluminum compound, tensile strength at 700°C. A63-12718 06-18
Check 1963 issues of either International Aerospace Abstracts or Sci. Tech. Aerospace Reports.
329. "Orientation of paramagnetic and diamagnetic rods in magnetic fields," A. R. Jaufen, Am J. Phys 19, No. 5, 275-9 (1951)
330. AD 275-039 ASTIA (TAB 3-3-62) Bibliography, Steel, Metals, Alloys, Mechanical properties.
331. B. Ya. Pines, I. G. Ivanov, Fiz. Tverdogo Tela, 4, No. 8 (Aug 1962) English translation in Soviet Physics, Solid State, 4, No. 8 (Feb 1963) p. 1543-8
High temperature, mechanical properties of copper-nickel alloys.
332. "New magnesium alloy 2 percent lighter than standard alloys." - Materials in design engineering. March, 1963
A magnesium-lithium alloy. Tensile strength about 10,000 psi.
333. "Defense metals information center selected accessions," AD-299-269 (Feb., 1963)
Comp. by Patricia B. Plate (Contract AF 339616) 7747 Proj. 2 (8-3975)
334. "Recent worldwide technological advances in polymers, plastics, synthetic fibers, organic and inorganic materials and metals," AD-276-709, AD-276621.
- 334B. "Bibliography. - Polymers, plastics, synthetic fibers, literature review," N63-10073
335. "Materials for space exploration: 2) nonmetallic materials for spacecraft," G. F. Pendirtz (NASA Langley Research Ctr.), 10 p., 16 ref. N63-11517 [Prob. 1962]
336. Colin J. Smithels, Metals Reference Book p. 749-64 Butterworth, Wash., D. C. (1962)
Page 764, list of approx. 12 nonmagnetic stainless steels.

337. "Studies of the mechanical strength of glass," C. Symmers, J. B. Ward, B. Sugarman, Phys. & Chem. of Glasses, 3, No. 3, 76-83 (June 1962)
- Etching with HF produces specimens with mean strength of 250-300,000 psi.
338. "Tensile behavior of intermetallic compound Ag Mg," P. L. Wood, J. H. Westbrook, Met. Soc. A.I.M.E. Trans., 224, No. 5, 1034-37 (1962)
- Paramagnetic element with diamagnetic element
339. Compilation of tensile properties of high-strength alloys. J. E. Campbell, Battelle Memorial Institute, DMIC Memo 150 (April 23, 1962)
340. "Tensile properties of polycrystalline cadmium and some cadmium alloys in range -196 to 200°C," W. J. McGilegart, Journal Inst. Metals 91, Pt. 3, (Nov. 1962)
341. Columbium-hafnium binary alloys for high-temperature service, H. R. Babitzke, G. Hsai, H. Kato, U. S. Bureau Mines report. Investigation 6101 - 1962, 17 p.
342. "Survey of intermediate phases in transition metal alloys," Y. L. Vao, Met. Soc. AIME trans. 224, No. 6, 1146-53 (Dec 1962)
343. "Investigation on copper-zirconium alloys," U. Z. Wicker, Metall. 16, No. 5, 9, 11. (three articles) May 1962, p. 409-12, Sept. p. 864-70, Nov. p. 1110-13.
- Solubility of zirconium in high-purity copper. Hardness and elec. cond., and magnetic measurements.
344. U. Zwicker, Z. Metallkunde, 53, No. 11 709-14 (Nov. 1962) Age-hardening and mechanical properties of copper-titanium alloys. Intermediate phases $Ti_2 Cu_7$. Continuous and discontinuous precipitation.
345. "Production and properties of grain-stabilized platinum and platinum alloys," J. R. Knight, B. Taylor, Powder Metallurgy 10, 108-18, (1962)
- Rm. temperature tensile, and stress rupture results from 1250-1460°C.
- [Weakly paramagnetic]
346. "On equilibrium diagram of recent system bismuth-rhodium," R. G. Cross., W. Hume-Rothery, J. Less. Common Metals 4, No. 5 (Oct. 1962)
- [Bismuth diamagnetic, rhodium paramagnetic]
347. V. M. Amonenko et. al., Fi₃ metallov i metallovedenie 14 No. C, 852-C (Rec 1962)
- X-ray investigation of solubility of Ti, Zn, Y, and Ni.

348. "Intermetallic phases in commercial beryllium," H. P. Rooksby, J. Nuclear. Matls 7, No. 2, Nov. 1962 p. 205-211

Heat treatment with regard to phases Be_3Fe , Be_3Al .

[Beryllium is a diamagnetic element]

- 348B. E. Pelzel, P. Paschen, Metall. 16, No. 8, 750-752 (1962)

[Mechanical properties of a zinc-copper-titanium alloy.]

349. "Order-disorder transformation in Cd-rich Mg-Cd alloys." G. S. Ramath, R. S. Craig, W. E. Wallace, Met. Soc. AIME Trans. Vol. 227 No. 1, 26-31 (Feb. 1963)

Recent information on diamagnetic metals mixed with paramagnetic metals

350. "Deformation and fracture of polycrystalline cadmium," M. S. Stuboft and M. Gensamer, Met. Soc. AIME Transactions, 227, No. 1, 10-80 (Feb. 1963)

Effect of temperature and magnesium content, grain size on strength and ductility between -140 , 199°C , 15.35% Mg.

351. Modified metals, Mech. World Vol. 143 No. 3524, pp. 103-104 (Mar. 1963)

Some discussion of the possibility of using high-strength organic or metallic fibers to reinforce weak metals such as lead.

352. "High-strength aluminum alloy," J. H. Mack Jr., H. Y. Hunsicher, J. of Metals, 15 No. 3, 216-24 (1963)

Room temp. strength and notch toughness of different commercial aluminum alloys. Properties of experimental Al-Zn-Mg alloys discussed, with tensile strength approaching 100,000 psi at room temp.

N64-28212

TESTING OF NONMAGNETIC MATERIALS

E. Levy

INTRODUCTION

To date, most measurements of the magnetic properties of "nonmagnetic" materials have been performed in large magnetic fields (>1000 gauss). (References 1-25.) Unfortunately, these methods do not produce data useful to individuals concerned with materials in fields of the magnitude encountered on earth (0.5 gauss) or in space ($<10^{-4}$ gauss). (See Reference 26 for a discussion of the dependence of magnetic permeability on field strength.)

The purpose of this report is to describe work performed at the Goddard Space Flight Center on methods of measuring the magnetic properties of "nonmagnetic" materials in low magnetic fields (0.5 gauss). Before actual experimentation began, a literature survey of various test methods was conducted. A bibliography resulting from the survey is included at the end of the report.

TEST METHODS

The literature search indicated two feasible test methods (described here as Methods II and III). Work on these began early in the program. A third technique (Method I) was attempted at a later date. In all, three test apparatus have been set up and developed to various stages.

1: FORCE METHOD

E. A. Johnson and W. E. Steiner have described (27) a technique for measuring the magnetic susceptibility of materials in low magnetic fields in which the force existing between a permanent magnet and the specimen is a measure of the susceptibility of that specimen.

Apparatus—The apparatus consisted of two identical cylindrical Alnico magnets 2.5 mm in diameter and 8 mm long, held 4.2 cm apart by a phosphor bronze wire. Centered on the wire between the magnets was a 6-mm-diameter plane mirror. The magnet, mirror, and wire configuration was suspended by a 10-cm quartz fiber with a diameter of 7 to 8 microns (Figure C-8).

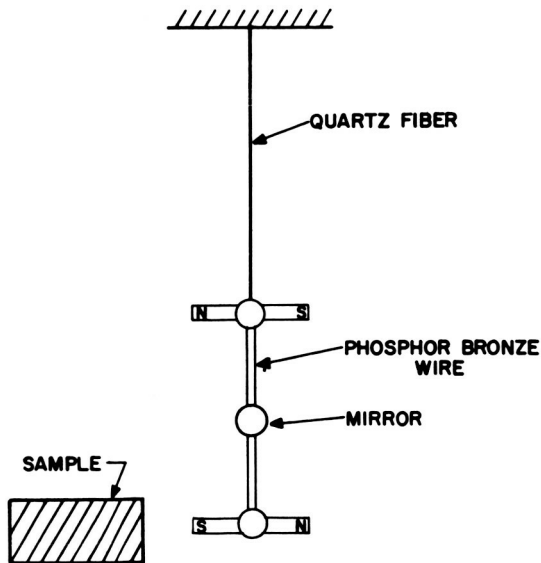


Figure C-8—Astatic Magnetometer, Schematic Diagram

A specimen placed near a pole of one of the two magnets caused a rotation of the quartz-fiber suspension, the angle of rotation being measured by a mirror, lamp, and scale arrangement. For small angles, the susceptibility of the specimen was proportional to the amount of angular rotation.

An astatic galvanometer (Figure C-9), identical to that described above, was obtained from the Coast and Geodetic Survey for the magnetic measurements to be performed at the Goddard Center.

Discussion—At the time of the writing of this report, no data had been collected. Following is a description of the proposed experimental procedure.

- (1) Determine the magnetic field strength at various distances from the poles of the magnets, using a Hewlett-Packard Company 3529 A magnetometer.
- (2) Calibrate the instrument by placing standards in a position corresponding to the desirable field strength and observing the scale deflection. (See References 7 and 28 for discussion of standards.) Standards must be enclosed in containers having the same geometry as the unknown specimens.

According to Johnson and Steiner (27), the astatic magnetometer has a maximum sensitivity of 2×10^{-8} electromagnetic cgs units per mm of scale deflection. It must be

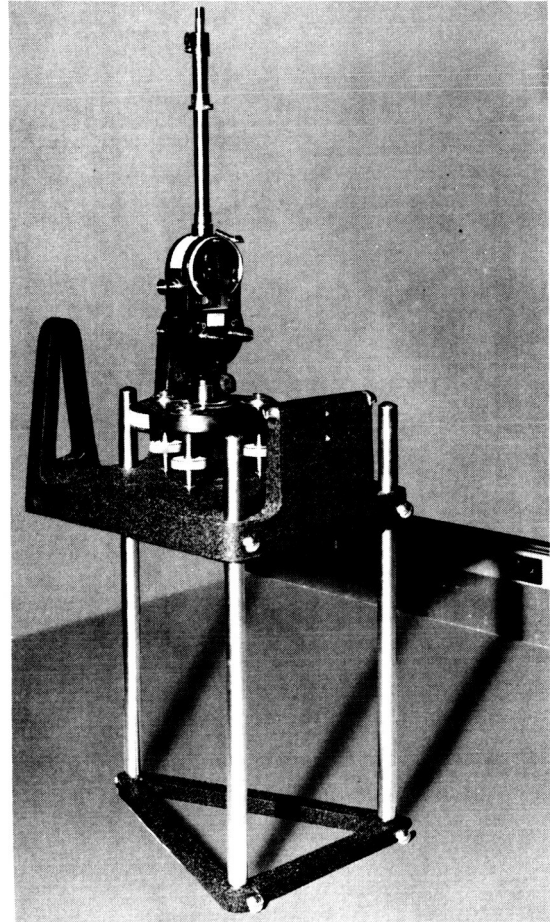


Figure C-9—Astatic Magnetometer

noted, however, that this sensitivity will occur only if the specimen is placed at the minimum distance from one of the poles of the Alnico magnets. The field at such a position will probably be several magnitudes greater than that which is desirable. Moving to a position of lower field strength will reduce the sensitivity to a value less than that stated previously.

II: AC INDUCTION METHOD

Depending upon the change of induction of a coil in an alternating magnetic field when a specimen is placed within the coil, the ac system is similar to those described by Norder (29) and by Collinson, Molyneux, and Stone (28).

A uniform periodically alternating magnetic field is established within a primary coil. Two identical series-connected oppositely wound coils located within the primary ideally will generate zero total voltage. A specimen placed within one of the two secondaries will create an imbalance voltage, this voltage being a measure of the permeability of the specimen.

Apparatus—The primary coil consisted of 280 turns of #16 magnet wire wound on 5.5-inch o. d., 15-inch-long, 1/8-inch-thick acrylic tubing. The secondaries each contained three 250-turn layers of #27 magnet wire wound over the middle 4-inch section of a 1-inch i. d., 20-inch-long coil form. The secondary coils were each fabricated by wrapping fiberglass sheet around a 1-inch-diameter mandrel, winding the 750 turns, and then building up the coil wall with layers of epoxy resin and fiberglass sheet to a 1/8-inch thickness. The primary and secondary coils are shown in Figure C-10. A complete circuit diagram is shown in Figure C-11.

During manufacture, one of the coils was damaged; it was therefore impossible to perform experiments with the ac induction apparatus.

Discussion—Broersma (30) has derived an equation relating susceptibility to imbalance voltage. Hence, permeabilities may be calculated directly (30) or determined indirectly through calibration. If the system is calibrated, standards must be geometrically identical to the samples; i. e., 1-inch-diameter by 6-inch-high cylinders. The standards used could be the same as those chosen for calibration of the astatic magnetometer.

The major disadvantage of an ac induction system is the eddy-current problem. Three effects of frequency of alternation of the electromagnetic field are:

- to reduce the permeability of the material to a value lower than the dc permeability
- to increase the resistance to a value greater than the dc resistance
- to cause a phase shift of the signal through the material

A preliminary investigation (see Appendix C-2) has led to the conclusion that, for most materials, errors due to eddy-currents would be negligible at $f \leq 10$ cps.

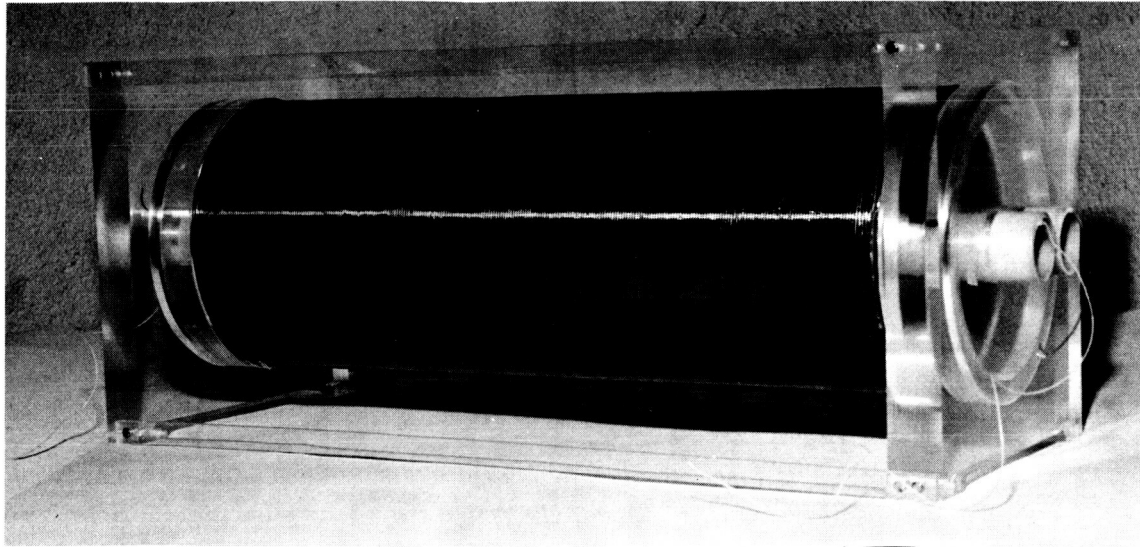


Figure C-10-AC Induction Primary and Secondary Coils

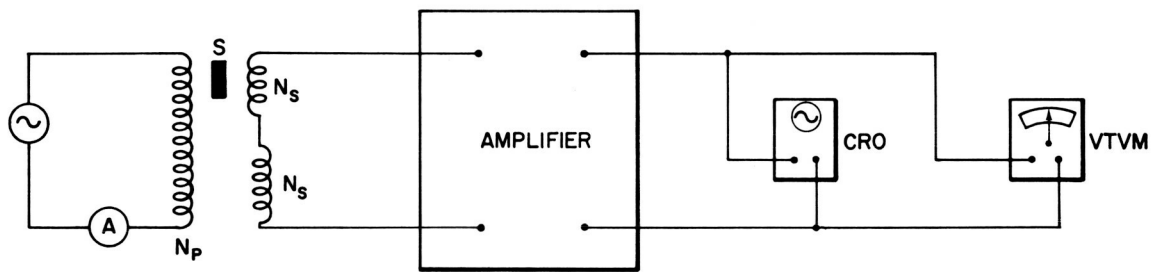


Figure C-11-AC Induction Apparatus, Schematic Diagram

III: DC INDUCTION METHOD

In May 1952, Gordon and Pasnak of the Naval Ordnance Laboratory published a report (31) describing measurement of the magnetic properties of "nonmagnetic" materials in low magnetic fields.

The apparatus (Figure C-12) consisted of a search coil, N_s , in the uniform steady magnetic field established within a primary solenoid, N_p , M , a variable mutual inductor, was adjusted for zero deflection of the galvanometer scale upon a change of the magnetic field. Placing the specimen in the search coil caused a deflection of the galvanometer, the

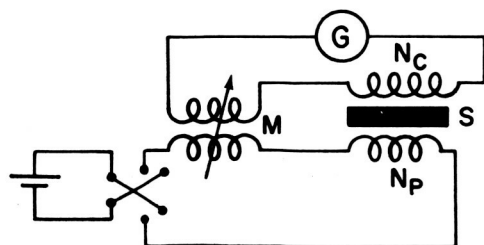


Figure C-12-Magnetic Measurement Apparatus Used at NOL

permeability being proportional to this deflection. Gordon and Pasnak have shown that the permeability is given by

$$\mu = 1 + \frac{C K_2 d}{H N_s A_m}$$

where

- μ = permeability (cgs)
- C = a constant depending upon the method of change of the field
- K_2 = galvanometer constant (see Appendix B for determination of K_2)
- d = galvanometer scale deflection (mm)
- H = field strength (gauss)
- N_s = number of turns on search coil
- A_m = cross sectional area of sample (cm²)

Preliminary Apparatus—An apparatus similar to that described previously was fabricated at GSFC for the Summer Workshop program.

The primary coil, 3400 turns of #31 magnet wire, was wound on a 2.25-inch-diameter by 20.75-inch-long coil form. The search coil consisted of 2000 turns of #28 magnet wire wrapped around a 1.01-inch i. d., 1.12-inch o. d., 5.5-inch-long form. In addition to the search coil, a third coil, used to generate the signal to balance or null the system, was designed to fit within the primary solenoid. The compensating coil contained 2200 turns of #32 wire wrapped around a 1.25-inch diameter 7-inch-long form. In each case the coil form was machined from phenolic tubing. The coils are shown in Figure C-13.

A Leeds and Northrup 2285D ballistic galvanometer was used for measuring the output of the search coil and compensating coil. This device, equipped with a plano-convex lens having a focal length of 1 meter, was placed 1 meter from a lamp and scale (Figure C-14). To minimize effects due to mechanical vibrations, the entire galvanometer system was set up on a mechanically isolated block. The measuring circuit is shown in Figure C-15.

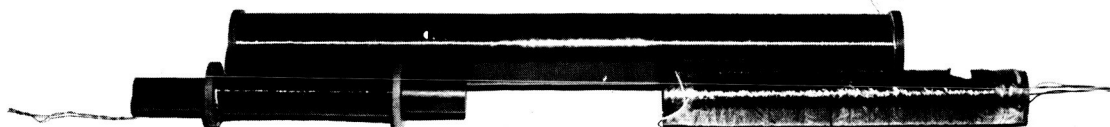


Figure C-13—DC Induction Coil System

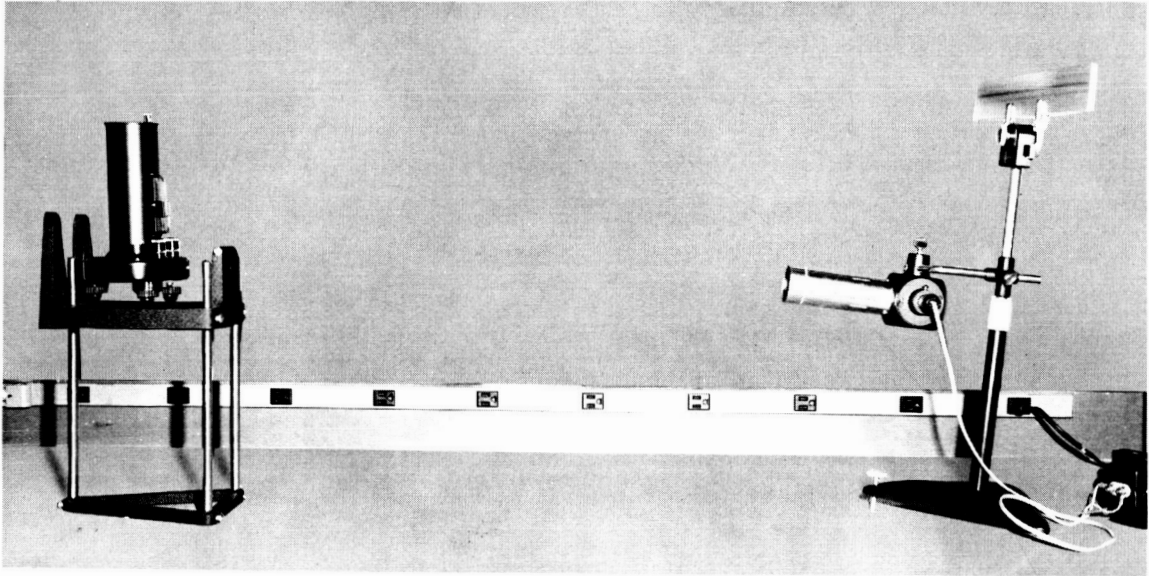


Figure C-14—Galvanometer, Lamp, and Scale

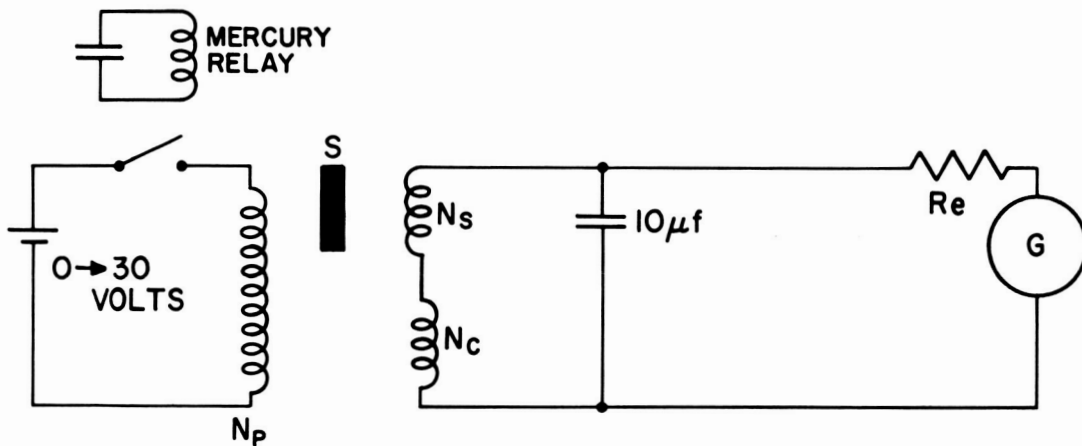


Figure C-15—Preliminary DC Circuit, Schematic Diagram

If a switch in the primary circuit of a transformer is suddenly closed, thereby causing a current to flow in the primary, a pulse is generated in the secondary. Remembering that the circuit is a combination of coil resistances, inductances, and capacitances, the pulse will be underdamped, overdamped, or critically damped, depending on the relative values of the circuit elements. It was found that the pulses generated in the search and compensating coils were underdamped. To eliminate the possibility of errors due to eddy-current losses from the high-frequency oscillations of the underdamped pulses, the $10\mu f$ capacitor shown in Figure C-15 was inserted to critically damp the induced pulse.

Resistance, R_e , was added to critically damp the mechanically oscillating galvanometer. This minimized the time required for the galvanometer to return to rest following a measurement, and also decreased the zero shift of the galvanometer.

The system of Figure C-15 was calibrated and found to have a sensitivity of 4.3×10^{-4} mm/maxwell turn. Hence it was capable of indicating permeabilities as low as 1.11 (cgs) in a field of 0.5 gauss.

It was originally hoped that the apparatus would be sensitive enough to permit measurement of extremely low permeabilities ($\mu < 1.001$ cgs). To achieve this, four methods for improvement were considered:

- Increase N_s —This would have required an unrealistic number of turns on the secondary.
- Increase the field strength—This would have violated the conditions of the problem.
- Obtain a more sensitive ballistic galvanometer—Gordon and Pasnak obtained a sensitivity of 4×10^{-3} mm/maxwell turn with the Leeds and Northrup 2285E ballistic galvanometer.
- Amplify the signal.

It was decided to add an amplifying circuit to attain the desired sensitivity. A three-stage triode RC-coupled amplifier (Figure C-16) was built and tested. It was found that, for faithful reproduction of the induced pulse, coupling capacitors greater than $C = 1 \mu f$ were required. The time constants of the resulting RC combinations were many magnitudes larger than the actual induced pulsewidth. Hence, the RC-coupled amplifier was unsatisfactory. At this point in the investigation, insufficient time remained for further experimentation.

Conclusions Regarding the AC Method—It is believed that a dc difference amplifier would provide a workable solution to the sensitivity problem. (See Reference 32 for

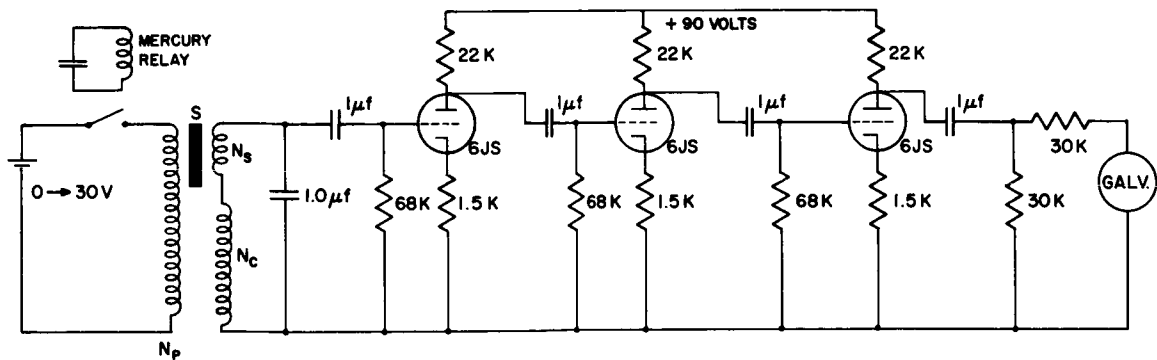


Figure C-16—RC-Coupled Amplifier with DC Apparatus

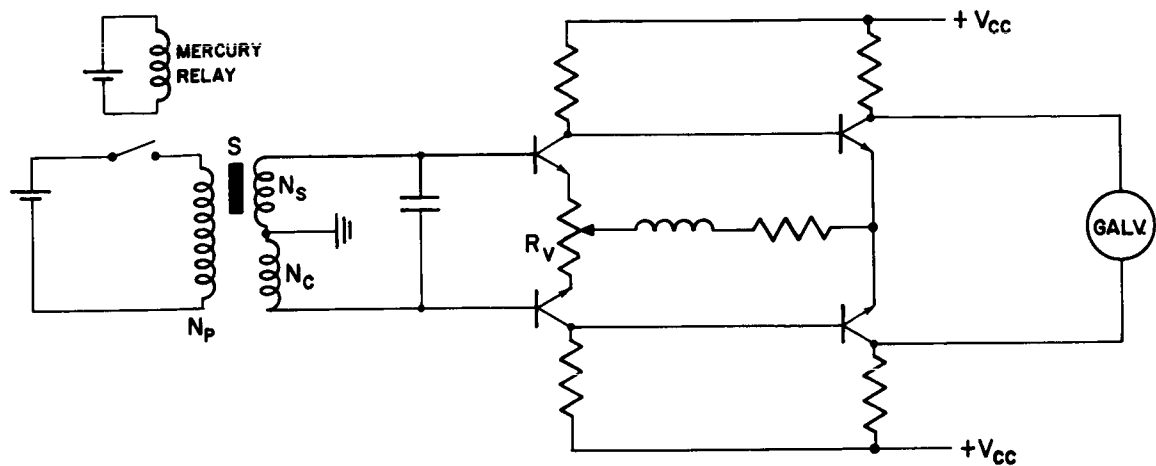


Figure C-17—Difference Amplifier, Schematic Diagram

discussion of dc difference amplifiers.) The search coil and compensation coil would form the two inputs to the amplifier (Figure C-17); the ballistic galvanometer, the load. Balance of the amplifier and coils would be obtained by regulating R_v .

CONCLUDING REMARKS

The astatic magnetometer has been used successfully by the Department of Terrestrial Magnetism for measuring magnetic properties of materials. The apparent disadvantage to using this method for 0.5-gauss measurements is the possibility of insufficient sensitivity. The equipment should be calibrated before any definite conclusions are drawn.

Although the author was unable to collect data while using the ac induction apparatus, it is felt that the results obtained from similar techniques justify further analysis of the system.

The dc induction apparatus in its present state is incapable of measuring low permeabilities. It is felt, however, that the development of a stable high-gain amplifier compatible with the system would provide the apparatus with sensitivity adequate for low permeability measurements.

BIBLIOGRAPHY

1. Smith, E. V. , "Simple form of balance for the rapid measurement of magnetic susceptibilities," *Journal of Scientific Instruments*, 38, 466-468 (Dec. 1961).
2. Singer, J. R. , "Magnetic susceptibility balance using a null technique," *Rev. Sci. Instr.* , 30 (12) 1123-1124 (1959).
3. Itterbeek and Labro, "Magnetic susceptibility of zinc and brass between room temperature and 1.2°K," *Physica* 28, 721-726 (1962).
4. Neogy, D. and Lal, R. B. , "A sensitive magnetic balance for measuring absolute susceptibility of single crystals and dilute solutions," *J. Sci. Indus. Res.* , 21b, 103-107 (March 1962).
5. Dutta Roy, S. K. , "An improved method of measuring the absolute susceptibilities of single crystals over wide ranges of temperatures," *Ind. J. Physics* 29, 429-445 (1955).
6. Senftle, F. E. , Lee, M. D. , Monkewicz, A. A. , Mayo, J. W. , and Pankey, T. , "Quartz helix magnetic susceptibility balance using the Curie-Cheneveau principle," *Rev. Sci. Instr.* , 29 (5) 429-432 (May 1958).
7. Thorpe, A. and Senftle, F. E. , "Absolute method of measuring magnetic susceptibility," *Rev. Sci. Instr.* , 30 (11) 1006-1008 (Nov. 1959).
8. Candela, G. A. and Mundy, R. E. , "Absolute magnetic susceptibilities by the Thorpe-Senftle method," *R. Sci. Instr.* 32, 1056-7 (Sept. 1961).
9. Candela and Mundy, "Absolute magnetic susceptibilities by the Gouy and the Thorpe-Senftle methods," *IRE Trans. Instr.* I-11 (3 and 4) (Dec. 1962).
10. Sucksmith, W. , "An apparatus for the measurement of magnetic susceptibility," *Phil. Mag.* , 8, 158-165 (1929).
11. Lundquist, N. and Myers, H. P. , "Strain gauge balance for ferromagnetic and paramagnetic measurements," *J. Sci. Instr.* 59, 154-5 (1962).
12. Chen, W. K. , Koch, F. B. , and Siverstsen, J. M. , "Transducer-operated balance for making magnetic susceptibility measurements," *Rev. Sci. Instr.* 31 (10) 1157-8 (Oct. 1960).
13. Meyer, L. and Weiner, D. , "Temperature dependence of the magnetic susceptibility of α -silver-zinc-alloys," *Phys. Rev.* 108 (6) 1426-7 (Dec. 15, 1957).

14. McGuire, T. and Lane, C., "Magnetic susceptibility balance for use at liquid helium temperatures," *Rev. Sci. Instr.* 20 (7) 489-491 (July 1949).
15. Bamford, C. R. and Charnock, H., "An apparatus for measuring magnetic susceptibility of glasses up to their annealing temperatures," *Phys. and Chem. of Glasses*, 1 (5) 143-147 (Oct. 1960).
16. McMillan, J. A., "Equipment for the determination of magnetic susceptibilities," *Amer. J. Phys.* 27(5) 352-354 (May 1959).
17. Fereday, R. A., "An improved method for the comparison of small magnetic susceptibilities," *Proc. Phys. Soc.* 43, 383-393 (1931).
18. Heyding, R. D., Taylor, J. B., and Hair, M. L., "Four-inch shaped pole caps for susceptibility measurements by the Curie method," *Rev. Sci. Instr.* 32 (2) 161-163 (Feb. 1961).
19. Wolf, W. P., "Force on an anisotropic paramagnetic crystal in an inhomogeneous field," *J. Applied Phys.* 28 (7) 780-1 (July 1957).
20. Gerritsen, A. N. and Damon, D. H., "Problems arising in the measurement of small magnetic forces at low temperatures by the Faraday method," *Rev. Sci. Instr.* vol. 33 (3) 301-7 (March 1962).
21. Gill, S., Malone, C., and Downing, M., "Magnetic susceptibility measurements of single small particles," *Rev. Sci. Instr.* 31 (12) 1299-1303 (Dec. 1960).
22. Gordon, R. G., "Magnetic susceptibility measurements of small samples," *Rev. Sci. Instr.* 33 (7) 729-731 (July 1962).
23. Hedgcock, F. T., and Muir, W. B., "Susceptibility servobalance for measurements on metals of extremely low resistivities," *Rev. Sci. Instr.* 31 (4) 391-94 (April 1960).
24. Hedgcock, F. T., "Magnetic susceptibility of dilute Cu alloys at low temperatures," *Phys. Rev.* 104 (6) 1564-7 (Dec. 15, 1956).
25. Bowers, R., "Magnetic susceptibility of sodium metal," *Phys. Rev.* 100 (4) 1141-4 (Nov. 15, 1955).
26. Sinnott, M. J., "The solid state for engineers," New York, John Wiley and Sons, Inc. (1958).
27. Johnson, E. A., and Steiner, W. F., "An astatic magnetometer for measuring susceptibility," *Rev. Sci. Instr.* 8, 236-8 (July 1937).
28. Collinson, D. W., Molyneux, L., and Stone, D. B., "A total and anisotropic magnetic susceptibility meter," *J. Sci. Instr.* 40, 310-12 (1963).

29. Norder, W., "Induction apparatus for the continuous measurement of magnetic susceptibility," *Rev. Sci. Instr.* 31 (8) 849-851 (Aug. 1960).
30. Broersma, S., "Inductance apparatus for diamagnetic measurements," *Rev. Sci. Instr.* 20 (9) 660-663 (S, 1949).
31. Gordon, D. and Pasnak, M., "The measurement of magnetic characteristics of 'nonmagnetic' materials," USNOL report NAVORD 2415 (May 1952).
32. Greiner, R. A., "Semiconductor devices and applications," New York, McGraw-Hill Book Company, Inc. (1961).
33. Bozorth, R. M., "Ferromagnetism," Princeton, N. J., D. Van Nostrand Company, Inc. (1951).
34. Smith and Wiedenbeck, "Electrical measurements," New York, McGraw-Hill Book Company, Inc. (1959).

ADDITIONAL REFERENCES

35. Barker, J. R., "The testing of brass and other constructional materials for ferromagnetic impurities," *J. Sci. Instr.* 25, 363-4 (Oct. 1948).
36. Mooney, H., "Magnetics in geology," *Electronics*, 143-5 (Oct. 1953).
37. Mooney, H., "Magnetic susceptibility measurements in Minnesota," *Geophysics* 16, 531-543 (1952).
38. Mooney, H. and Bleifuss, R., "Magnetic susceptibility measurements in Minnesota," *Geophysics* 17, 383-393 (1953).
39. Bollin, E. M., "Lunar surface and subsurface magnetic susceptibility instrumentation," *IRE Trans. Instr.* 102-106 (Dec. 1962).
40. Zahn, C. T., "New absolute null method for the measurement of magnetic susceptibilities in weak low-frequency fields," *Rev. Sci. Instr.* 34 (3) 285-291 (March 1963).
41. Salinger, G. L. and Wheatley, J. C., "Magnetic susceptibility of materials commonly used in the construction of cryogenic apparatus," *R. Sci. Instr.* 32: 872-4 (July 1961).
42. Balsley, J. R. and Buddington, A. F., *Am. Jour. Sci. Bradly Volume*, 258-A p 6-20 (1960).
43. Girdler, R. W., "The measurement and computation of anisotropy of magnetic susceptibility of rocks," *Royal Astr. Soc. Geophys. J1.* 5 (1) 34-44 (1961).

44. Burakov, K. S. and Dianov-Klokov, V. I., "A high-sensitivity magnetic susceptibility meter," Bull. Acad. Sci. USSR, Geophys. Ser. 2, 148-149, Feb. 1962 (published May 1962).
45. Mulay, L. N., "Instrumentation and some analytical applications of magnetic susceptibility," Anal. Chem. 34 no. 5, 343R - 361R (April 1962).
46. Palmer, T. M., "Recent trends in magnetic measurements," Proceedings of the IRE, Australia, 739-747 (October 1960).
47. Bates, "Modern magnetism," New York, Cambridge University Press (1939).
48. Kelsall, G. A., "Furnace permeameter for alternating-current measurements at small magnetizing forces," J. Optical Soc. Amer. 8, 669-674 (1924).
49. Frei, K. and Bernstein, H. J., "Method of determining magnetic susceptibilities by NMR," J. Chem. Phys. 37 (8) 1891-2 (Oct. 15, 1962).
50. Johnson, E. A., Murphy, T., and Michelsen, P. F., "A new high-sensitivity remanent magnetometer," Rev. Sci. Instr. 20 (6) 429-434 (June 1949).
51. Sanford, R. L., and Cooter, I. L., "Basic magnetic quantities and the measurement of the magnetic properties of materials," NBS monograph 47 (May 21, 1962).
52. Stout, M. R., "Basic electrical measurements," New Jersey: Prentice-Hall, Inc. (1960).

APPENDIX C-2

CALCULATION OF EFFECTS OF EDDY-CURRENTS IN CYLINDRICAL SAMPLES

- Assume: (1) the magnetic permeability of the material is independent of field strength
 (2) the sample is homogeneous
 (3) the sinusoidally varying field is parallel to the axis of the cylindrical sample

According to Bozorth (33),

$$\frac{L_{ac}}{L_{dc}} = \frac{\mu_{ac}}{\mu_{dc}} = \frac{2}{\theta} \frac{\text{ber } \theta \text{ bei}' \theta - \text{bei } \theta \text{ ber}' \theta}{\text{ber}^2 \theta + \text{bei}^2 \theta}$$

$$\frac{\Delta R}{\omega L_{dc}} = \frac{2}{\theta} \frac{\text{ber } \theta \text{ ber}' \theta + \text{bei } \theta \text{ bei}' \theta}{\text{ber}^2 \theta + \text{bei}^2 \theta}$$

where L = inductance of material

μ = permeability of material

ber and bei functions = combinations of Bessel functions of the first and second kinds

$$\theta = \pi d \sqrt{\frac{2\mu f}{\rho}}$$

$$\Delta R = R_{ac} - R_{dc} \text{ (ohms)}$$

d = diameter of rod (cm)

f = frequency of field (cps)

ρ = resistivity of rod (abohms)

$$\omega = 2\pi f$$

Table C-2 (33) shows several solutions of the equations above.

It is apparent that the severity of the eddy-current problem is increased as a , μ , and f increase and as ρ decreases.

Table C-3, also from Bozorth (33), lists the electrical resistivities of several of the most conductive materials.

Table C-2—Eddy-Current Effects as a Function of θ

θ	$\frac{\mu_{ac}}{\mu_{dc}}$	$\frac{\Delta R}{\omega L_{dc}}$
0	1.000	0
0.1	1.000	.001
0.2	.999	.005
0.4	.997	.020
0.6	.980	.045
1.0	.928	.122
1.4	.833	.221
1.8	.712	.312

Table C-3—Electrical Resistivities

Element	ρ -microhm-cm	Temp. °C
AG	1520	20
Cu	1673	20
Au	2190	0
Al	2655	20
Ca	3430	0
Na	4200	0
Mg	4460	20
Rh	4500	20

Considering a rod of silver, let

$$d = 2.54 \text{ cm}$$

$$\mu < 1.000 \text{ (cgs)}$$

$$\rho = 1520 \text{ abohms}$$

$$f = 10 \text{ cps}$$

Hence

$$\theta = 0.956$$

and

$$\frac{\mu_{ac}}{\mu_{dc}} = 0.980$$

The error in μ due to eddy-currents is 2 percent. Since silver at room temperature has a lower resistivity than other materials, the calculated 2-percent error becomes the largest error attributable to eddy-currents to be expected.

APPENDIX 2

CALIBRATION OF BALLISTIC GALVANOMETER

The circuit shown in Figure C-18 was used for calibration of the ballistic galvanometer.

$$K_2 = \frac{MI \cdot 10^7}{d} \quad (34)$$

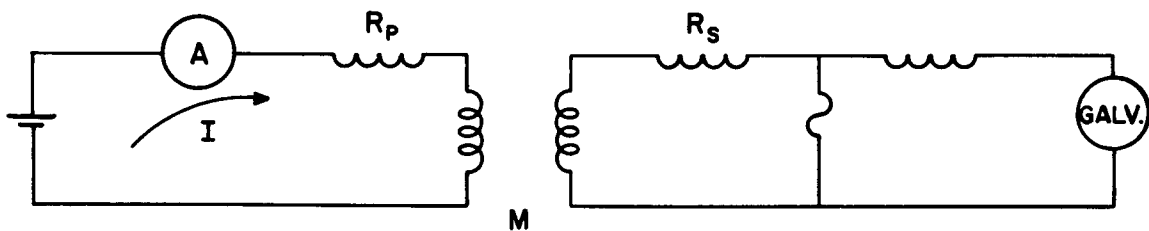


Figure C-18—Galvanometer Calibration Circuit, Schematic Diagram

where

K_2 = galvanometer constant (maxwell turn/mm)

d = galvanometer scale deflection (mm)

I = current in primary (amps)

M = mutual inductance (henries)

R_p and R_s = variable resistances (ohms)

It is important that R_p and R_s be adjusted to the values making the primary and secondary circuit resistances of the calibrating system respectively equal to those of the measuring circuit.

FOUR-CIRCULAR-COIL SYSTEM

D. L. Waidelich and M. Speiser

BRAUNBEC SYSTEM

Much information on the four-circular-coil system is available at present^(1, 2). The four-circular-coil system being constructed at Greenbelt, Md., uses the parameters first calculated by Braunbek⁽³⁾ and later by McKeehan⁽⁴⁾. The parameters calculated by Braunbek were given to five significant figures. While those of McKeehan were in six significant figures. It appeared that seven or eight significant figures were needed to resolve the doubt in the sixth figure. The computer program used previously⁽²⁾ was adapted to this need, and the results are given in Table C-4 and Figure C-19.

As indicated in Table C-4, the ampere-turns of both the No. 1 and No. 2 coils are equal. The coefficient A_8 has been defined previously⁽²⁾. The homogeneity is defined as the ratio of the diameter of the sphere of homogeneity within which the field does not vary more than 0.001 percent from that at the center, to the diameter of the largest coil in the system. In this case, then,

$$A_8 \left(\frac{2Z}{\text{DIA1}} \right)^8 \frac{\sin^4 \alpha_1 \sin^4 \alpha_2}{(\text{DIA2}/\text{DIA1})^4} = 10^{-5} \quad (1)$$

where

$$\tan \alpha_1 = \frac{\text{DIA1}}{2(\text{D1})}, \quad 0^\circ \leq \alpha_1 \leq 90^\circ$$

$$\tan \alpha_2 = \frac{\text{DIA2}}{2(\text{D2})}, \quad 0^\circ \leq \alpha_2 \leq 90^\circ$$

and the homogeneity is

$$\left(\frac{2Z}{\text{DIA1}} \right) = 0.23311270 \quad (2)$$

The field constant is the flux density at the center of the coil system in terms of the

Table C-4—Parameters for the Braunbek Coil System

DIA1	=	1.00
D1	=	0.13901407
DIA2	=	0.76389940
D2	=	0.38194970
(NI) ₂	=	(NI) ₁
A ₈	=	2.2446903
Field Constant	=	1619.3190 gamma-meter radius per ampere turn
Homogeneity	=	23.322270%

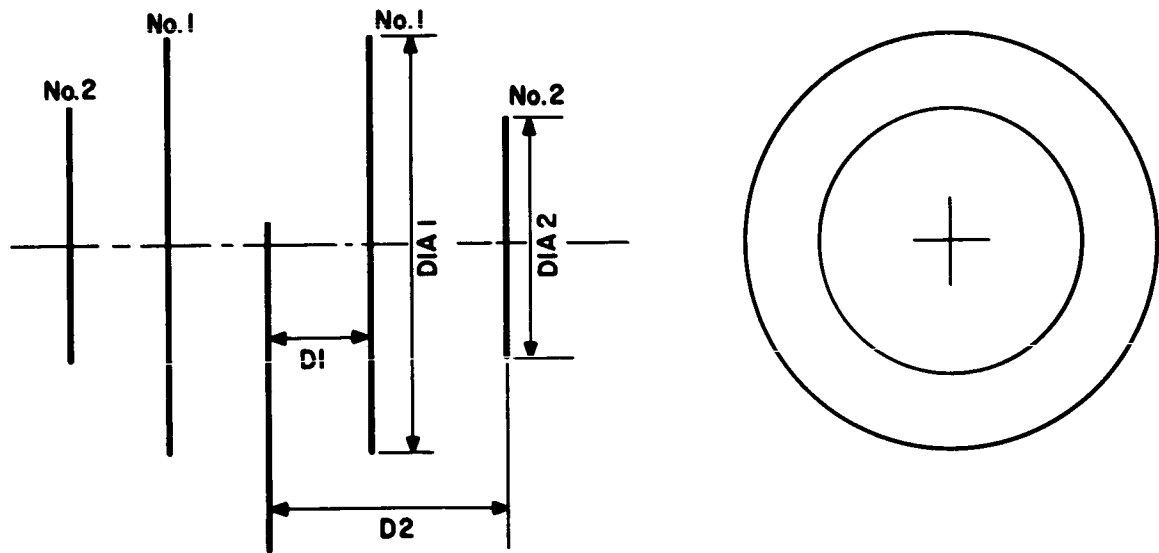


Figure C-19—Four-Circular-Coil System

ampere-turns and the radius of the No. 1 coil. It is obtained from the a_0 term for the magnetic field along the axis⁽²⁾. In this case, the field constant is 1619.3190 gamma-meter radius per ampere-turn.

SYSTEM WITH OPPOSING CURRENTS

In the previous works^(1,2) on four-circular-coil systems, it was decided to concentrate on systems in which the currents in both No. 1 and No. 2 coils were in the same direction, as these would produce a larger field constant and would generate almost all the previously known solutions. It was known, however, that Scott^(5,6) had used a system in which the current in the No. 1 coil had a direction opposite to that of the No. 2 coil. An opportunity was presented to investigate this case in more detail, using a computer program slightly modified from that used previously^(1,2). The results are presented in Table C-5. The quantities x_1 and x_2 are defined by $x_1 = \cos \alpha_1$ and $x_2 = \cos \alpha_2$ where α_1 and α_2 are given by (1). The diameter of the No. 1 coil, DIA1, is assumed to be unity, while the other symbols are the same as defined in Table C-4 and Figure C-19. Notice that when $x_2 = 0.59170$ (one end point), only the No. 1 coil is effective, and thus the system is essentially a Helmholtz pair. As x_2 is decreased, both the No. 1 and No. 2 coils move in the direction away from the origin, with the No. 2 coil always between the origin and the No. 1 coil. The No. 2 coil is always smaller than the No. 1 coil. Also, as x_2 is decreased: the magnitude of the ampere-turn ratio increases, the field constant decreases, and the homogeneity increases. At $x_2 = 0.51938$ (the other end point), the No. 1 and No. 2 coils become coincident with opposite and equal currents. This makes the field constant zero.

Table C-5—Parameters for Systems With Opposing Currents

x_1	x_2	D1	DIA2	D2	$(NI)_2/(NI)_1$	Field Constant	Homogeneity	Remarks
0.44721	0.59170	0.250	0.00	0.00	0.00	899.17	0.00	End Point
0.45885	0.580	0.25821	0.29187	0.10390	-0.0029665	899.07	0.068685	
0.47879	0.560	0.278268	0.52408	0.17712	-0.049497	782.85	0.14226	
0.49876	0.540	0.28772	0.74174	0.23794	-0.25158	564.10	0.18895	
0.51175	0.5270	0.29783	0.89778	0.27836	-0.60828	274.25	0.22668	
0.51825	0.52050	0.30299	0.98428	0.30000	-0.92958	47.234	0.25172	
0.51938	0.51938	0.30389	1.00	0.30389	-1.00	0.00	0.24980	End Point

This particular four-coil system has the advantages that the homogeneity is very high and the access space is large, but it has the disadvantage that the field constant is small.

MAGNETIC-FIELD INTENSITY

The magnetic-field intensity of the four-circular-coil system was calculated by obtaining expressions for the field intensity of one coil at a time (as shown in Figure C-20), then adding the intensities of the four coils together (Figure C-21). The details of the calculation are presented in Appendix C-3. The method is essentially the same as that employed by V. E. Williams and J. C. Cain⁽⁹⁾.

A computer program was developed, and the plotted results of the gradient of the axially-directed H field with $(NI)_1 = (NI)_2$ appear in Figure C-22. The positive and negative lobes indicate the regions where the magnetic field is greater and less, respectively, than that found at the origin. The numbers 10,

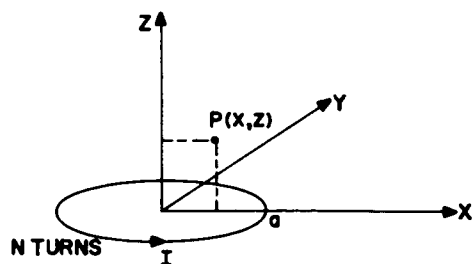


Figure C-20—Geometry for One Circular Coil

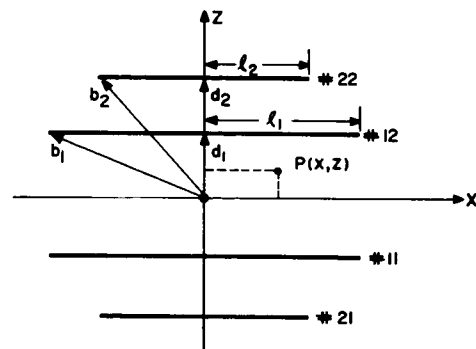


Figure C-21—Geometry of the Four-Circular-Coil System

50, and 100 are understood to be in terms of 10^{-5} . Thus, the -10 curves indicate the locus of points along which the magnetic field intensity differs from that at the origin by 10 parts in 10^5 , or within which the field varies less than 0.01 percent of the field at the origin.

Now, Figure C-22 of this report on four-circular-coil systems, and Figure C-28 of the report on four-square-coil systems, afford an excellent means of comparing and contrasting them. From these figures, it is immediately apparent that the circular system yields a considerably greater volume of homogeneity than does the square system: whereas the -10 curves cross the z and x -axes of the circular-coil system at about 0.32 and 0.35 respectively, the corresponding values in the square-coil system are 0.33 and 0.27. On this basis alone, the circular-coil system appears superior to the square-coil system.

INDUCTANCE

If a three-orthogonal-axis coil-system is used, the position of the field vector may be rotated by using alternating currents in the coil system. To determine how much alternating voltage is required demands knowledge of the inductance of the four-coil system. Total inductance may be determined by calculating the self-inductance of each of the four coils and adding to this the mutual inductances between each possible pair of coils. These various inductances were calculated by means of known formulas⁽¹⁰⁾; details are given

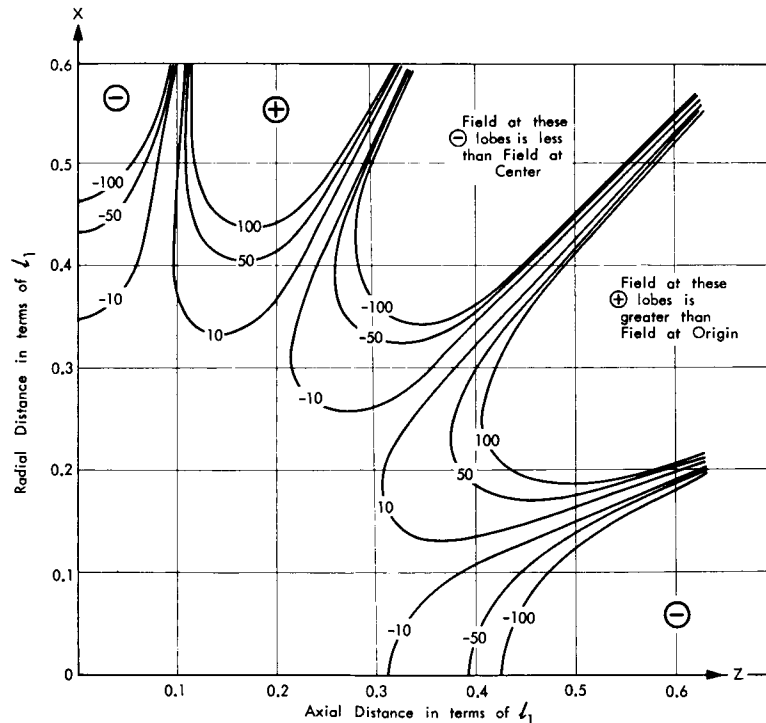


Figure C-22—Plot of Magnetic-Field Intensity,
Four-Circular-Coil System

in Appendix C-4. The geometry for one coil and for two neighboring coils is shown in Figure C-23. The Braunek system parameters were used in these calculations.

RESULTS: VERTICAL OR Z-AXIS COIL SYSTEM

$$\begin{aligned} \ell_2 &= 102.133'' = a \\ \ell_1 &= 133.700'' = A \\ d_1 &= 37.172'' \\ d_2 &= 113.064'' \\ b &= 2.230'' \\ c &= 0.603'' \\ N_1 &= N_2 = N_3 = N_4 = 24 \text{ Turns} \end{aligned}$$

$$\begin{aligned} L_1 &= 9.681 \text{ mh} \\ L_2 &= 13.218 \text{ mh} \\ L_{12} &= 1.337 \text{ mh} \\ L_{13} &= 0.549 \text{ mh} \\ L_{14} &= 0.169 \text{ mh} \\ L_{23} &= 1.976 \text{ mh} \end{aligned}$$

$$L \text{ Total Self Ind.} = 2L_1 + 2L_2 = 45.798 \text{ mh}$$

$$L \text{ Total Mutual Ind.} = 4L_{12} + 4L_{13} + 2L_{14} + 2L_{23} = 11.834 \text{ mh}$$

$$L \text{ Total} = 57.632 \text{ mh}$$

$$L \text{ Mutual} = 20.5\% L \text{ Total}$$

RESULTS: NORTH-SOUTH OR H-AXIS COIL SYSTEM

$$\begin{aligned} \ell_2 &= 99.181'' = a \\ \ell_1 &= 129.835'' = A \\ d_1 &= 36.097 \\ d_2 &= 109.795'' \\ b &= 2.230'' \\ c &= 0.603'' \\ N_1 &= N_2 = N_3 = N_4 = 26 \text{ Turns} \end{aligned}$$

$$\begin{aligned} L_1 &= 10.968 \text{ mh} \\ L_2 &= 15.016 \text{ mh} \\ L_{12} &= 1.524 \text{ mh} \\ L_{13} &= 0.624 \text{ mh} \\ L_{14} &= 0.193 \text{ mh} \\ L_{23} &= 2.252 \text{ mh} \end{aligned}$$

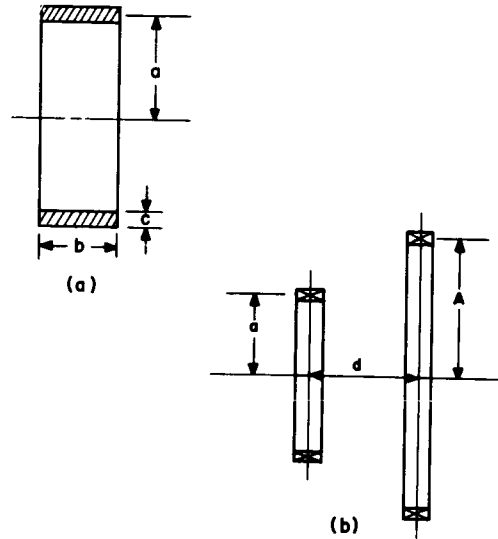


Figure C-23—Coil Geometry Used in Calculating (a) One Coil, (b) Two Neighboring Coils

$$L \text{ total self ind.} = 2L_1 + 2L_2 = 51.968 \text{ mh}$$

$$L \text{ total mutual ind.} = 4L_{12} + 4L_{13} + 2L_{14} + 2L_{23} = 13.490 \text{ mh}$$

$$L \text{ total} = 65.458 \text{ mh}$$

$$L \text{ mutual} = 20.6\% \text{ total}$$

RESULTS: EAST-WEST OR D-AXIS COIL SYSTEM

$$l_2 = 96.232'' = a$$

$$l_1 = 125.975'' = A$$

$$d_1 = 35.024''$$

$$d_2 = 106.531''$$

$$b = 2.230''$$

$$c = 0.603''$$

$$N_1 = N_2 = N_3 = N_4 = 28 \text{ turns}$$

$$L_1 = 12.320 \text{ mh}$$

$$L_2 = 17.592 \text{ mh}$$

$$L_{12} = 1.715 \text{ mh}$$

$$L_{13} = 0.704 \text{ mh}$$

$$L_{14} = 0.217 \text{ mh}$$

$$L_{23} = 2.534 \text{ mh}$$

$$L \text{ total self ind.} = 2L_1 + 2L_2 = 59.824 \text{ mh}$$

$$L \text{ total mutual ind.} = 4L_{12} + 4L_{13} + 2L_{14} + 2L_{23} = 15.178 \text{ mh}$$

$$L \text{ total} = 75.002 \text{ mh}$$

$$L \text{ mutual} = 20.2\% L \text{ total}$$

As can be seen from these results, the total inductance of such systems is considerable; and the total mutual inductance, far from being negligible, is always above 20 percent of the total inductance of the system.

The question also arises as to the magnitude of the mutual inductance of the three orthogonal systems. If two circular filaments are perpendicular to each other so that their axes intersect at the center of either, the mutual inductance, being proportional in this case to $\cos 90^\circ$, will be zero.

However, as shown in reference 10, page 204, if the coils are perpendicular to each other but their axes do not intersect at the center of either, then the mutual inductance is given by

$$M = x \left[a_1 + a_2 \frac{P_2(x)}{x} + a_3 \frac{P_3(x)}{x} + a_4 \frac{P_4(x)}{x} + \dots \right] \quad (3)$$

where the P_n are zonal harmonics and the a_n are constants. This expression would mean that additional voltages would appear in, say, the z -axis system, from the alternating currents flowing in the H - and D -axis systems. The centers of the systems on the three orthogonal axes should coincide, and the effect of the mutual inductance between systems should be zero. Any departure from this intersection or any departure from symmetry would mean that the current in the coil system of one axis would introduce voltages in the coil systems of the other axes.

REFERENCES

1. Waidelich, D. L. and Pittman, M. E. , "Magnetic Field Simulation" in "Final Report of the Goddard Summer Workshop Program in Simulation of Space Environment," . Publication X-320-62-193, Goddard Space Flight Center, Greenbelt, Md. , pages 5-3 to 5-15 (1962).
2. Pittman, M. E. and Waidelich, D. L. , "Three and Four Coil Systems for Homogeneous Magnetic Fields." To be published in the Transactions of the Institute of Electrical and Electronics Engineers, and also as a NASA Technical Note.
3. Braubek, W. , "Die Erzeugung Weitgehend homogener Magnetfelder durch Kreisstrome," Zeitschrift fur Physik 88, pages 399 to 402 (1934).
4. McKeegan, L. W. , "Combinations of Circular Currents for Producing Uniform Magnetic Fields," Review of Scientific Instruments 7, pages 150 to 153 (March 1936).
5. Scott, G. G. , "Compensation of the Earth's Magnetic Field," Review of Scientific Instruments 28, pages 270 to 273 (1957).
6. Scott, G. G. , "The Kettering Magnetics Laboratory," General Motors Corporation Research Laboratories Report GMR-291, Warren, Mich. (August 1960).
7. Symthe, W. R. , "Static and Dynamic Electricity," McGraw-Hill Book Co. , New York, N. Y. , pages 270-271 (1950).
8. Hastings, C. , Jr. , "Approximations for Digital Computers," Princeton University Press, Princeton, N. J. , pages 170-175 (1955).
9. Williams, V. L. and Cain, J. C. , "Homogeneous Magnetic Fields Produced by Circular Current Loops," unpublished memorandum, Goddard Space Flight Center.
10. Grover, F. W. , "Inductance Calculations," D. Van Nostrand & Co. , New York, N. Y. (1946).

APPENDIX C-3

MAGNETIC-FIELD INTENSITY OF FOUR COAXIAL CIRCULAR COILS

Consider first the magnetic-field intensity produced by a single circular coil of infinitesimal cross section, of N turns of radius a , and carrying a current I as shown in Figure C-20. Since this problem has cylindrical symmetry, it will suffice to look only at the fields in the x - z plane. At any point $P(x, z)$, in rationalized mks units, the x and z components⁽⁷⁾ of the magnetic-field intensity are given by

$$H_x(x, z) = \frac{NI}{2\pi} \frac{z}{x[(a+x)^2 + z^2]^{1/2}} \left[-K + \frac{a^2 + x^2 + z^2}{(a-x)^2 + z^2} E \right] \quad (\text{A-1})$$

$$H_z(x, z) = \frac{NI}{2\pi} \frac{1}{[(a+x)^2 + z^2]^{1/2}} \left[K + \frac{a^2 - x^2 - z^2}{(a-x)^2 + z^2} E \right] \quad (\text{A-2})$$

where K and E are the complete elliptic integrals of the first and second kind respectively, and both are functions of k^2 :

$$k^2 = \frac{4ax}{(a+x)^2 + z^2} \quad (\text{A-3})$$

Consider now the case of four coaxial circular coils of infinitesimal cross section, as shown in Figure C-21. Generalizing equations (A-1), (A-2), and (A-3) to the system of four coils, at any point $P(x, z)$, the x and z components of the magnetic-field intensity are given by

$$H_x(x, z) = \frac{N_1 I_1}{2\pi} \left\{ \frac{-(d_1 + z)}{x [(\ell_1 + x)^2 + (d_1 + z)^2]^{1/2}} \left[-K_{11} + \frac{\ell_1^2 + x^2 + (d_1 + z)^2}{(\ell_1 - x)^2 + (d_1 + z)^2} E_{11} \right] \right. \\ \left. + \frac{d_1 - z}{x [(\ell_1 + x)^2 + (d_1 - z)^2]^{1/2}} \left[-K_{12} + \frac{\ell_1^2 + x^2 + (d_1 - z)^2}{(\ell_1 - x)^2 + (d_1 - z)^2} E_{12} \right] \right\} \quad (\text{A-4})$$

$$+ \frac{N_2 I_2}{2\pi} \left\{ \frac{-(d_2 + z)}{x [(\ell_2 + x)^2 + (d_2 + z)^2]^{1/2}} \left[-K_{21} + \frac{\ell_2^2 + x^2 + (d_2 + z)^2}{(\ell_2 - x)^2 + (d_2 + z)^2} E_{21} \right] \right. \\ \left. + \frac{d_2 - z}{x [(\ell_2 + x)^2 + (d_2 - z)^2]^{1/2}} \left[-K_{22} + \frac{\ell_2^2 + x^2 + (d_2 - z)^2}{(\ell_2 - x)^2 + (d_2 - z)^2} E_{22} \right] \right\}$$

$$\begin{aligned}
 H_z(x, z) = & \frac{N_1 I_1}{2\pi} \left\{ \frac{1}{[(\ell_1 + x)^2 + (d_1 + z)^2]^{1/2}} \left[K_{11} + \frac{\ell_1^2 - x^2 - (d_1 + z)^2}{(\ell_1 - x)^2 + (d_1 + z)^2} E_{11} \right] \right. \\
 & + \left. \frac{1}{[(\ell_1 + x)^2 + (d_1 - z)^2]^{1/2}} \left[K_{12} + \frac{\ell_1^2 - x^2 - (d_1 - z)^2}{(\ell_1 - x)^2 + (d_1 - z)^2} E_{12} \right] \right\} \\
 & + \frac{N_2 I_2}{2\pi} \left\{ \frac{1}{[(\ell_2 + x)^2 + (d_2 + z)^2]^{1/2}} \left[K_{21} + \frac{\ell_2^2 - x^2 - (d_2 + z)^2}{(\ell_2 - x)^2 + (d_2 + z)^2} E_{21} \right] \right. \\
 & + \left. \frac{1}{[(\ell_2 + x)^2 + (d_2 - z)^2]^{1/2}} \left[K_{22} + \frac{\ell_2^2 - x^2 - (d_2 - z)^2}{(\ell_2 - x)^2 + (d_2 - z)^2} E_{22} \right] \right\}
 \end{aligned} \tag{A-5}$$

where Coils #11 and #12 have $N_1 I_1$ ampere turns; coils #21 and #22 have $N_2 I_2$ ampere turns; and K_{ij} and E_{ij} are the complete elliptic integrals of the first and second kind, which are functions of k_{ij}^2 :

$$\left. \begin{aligned}
 & \left. \begin{aligned}
 K_{11} &= K_{11}(k_{11}^2) \\
 E_{11} &= E_{11}(k_{11}^2)
 \end{aligned} \right\} \\
 & \left. \begin{aligned}
 K_{12} &= K_{12}(k_{12}^2) \\
 E_{12} &= E_{12}(k_{12}^2)
 \end{aligned} \right\} \\
 & \left. \begin{aligned}
 K_{21} &= K_{21}(k_{21}^2) \\
 E_{21} &= E_{21}(k_{21}^2)
 \end{aligned} \right\} \\
 & \left. \begin{aligned}
 K_{22} &= K_{22}(k_{22}^2) \\
 E_{22} &= E_{22}(k_{22}^2)
 \end{aligned} \right\}
 \end{aligned} \right\} \begin{aligned}
 k_{11}^2 &= \frac{4\ell_1 x}{(\ell_1 + x)^2 + (d_1 + z)^2} \\
 k_{12}^2 &= \frac{4\ell_1 x}{(\ell_1 + x)^2 + (d_1 - z)^2} \\
 k_{21}^2 &= \frac{4\ell_2 x}{(\ell_2 + x)^2 + (d_2 + z)^2} \\
 k_{22}^2 &= \frac{4\ell_2 x}{(\ell_2 + x)^2 + (d_2 - z)^2}
 \end{aligned} \tag{A-6}$$

Then, the total magnetic-field intensity at point $P(x, z)$ will be given by

$$H(P) = \sqrt{H_x^2(x, z) + H_z^2(x, z)}$$

The complete elliptic integrals K and E may be evaluated to a high degree of accuracy by using the following approximations⁽⁸⁾

$$K(k) = (a_0 + a_1\eta + \dots + a_4\eta^4) + (b_0 + b_1\eta + \dots + b_4\eta^4) \ell n \frac{1}{\eta} \quad (A-7)$$

$$E(k) = (1 + c_1\eta + \dots + c_4\eta^4) + (d_1\eta + \dots + d_4\eta^4) \ell n \frac{1}{\eta} \quad (A-8)$$

Where

$$\eta = 1 - k^2$$

$a_0 = 1.3862,9436,112$	$b_0 = 0.5$
$a_1 = 0.0966,6344,259$	$b_1 = 0.1249,8593,597$
$a_2 = 0.0359,0092,383$	$b_2 = 0.0688,0248,576$
$a_3 = 0.0374,2563,713$	$b_3 = 0.0332,8355,346$
$a_4 = 0.0145,1196,212$	$b_4 = 0.0044,1787,012$
$c_1 = 0.4432,5141,463$	$d_1 = 0.2499,8368,310$
$c_2 = 0.0626,0601,220$	$d_2 = 0.0920,0180,037$
$c_3 = 0.0475,7383,546$	$d_3 = 0.0406,9697,526$
$c_4 = 0.0173,6506,451$	$d_4 = 0.0052,6449,639$

First evaluate k_{ij} from (A-6); then $\eta_{ij} = 1 - k_{ij}^2$, and (A-7) and (A-8) yield K_{ij} and E_{ij} .

Now, along the axis of the coil system, $H_x = 0$; since H_z is an analytic function, it may be expanded in a Taylor series about the origin

$$H_z = \sum_{n=0,2,4,\dots}^{\infty} a_n z^n = a_0 + a_2 z^2 + a_4 z^4 + \dots$$

Where

$$a_n = \frac{N_1 I_1}{b_1^{n+1}} (1-x_1)^2 P'_{n+1}(x_1) + \frac{N_2 I_2}{b_2^{n+1}} P'_{n+1}(x_2)$$

$$P'_{n+1}(x) = \frac{d P_{n+1}(x)}{dx}$$

$P_n(x)$ is the n th order Legendre polynomial, and

$$x = \cos \alpha = d/\ell$$

The terms for odd n 's vanish because of symmetry considerations.

At the origin, $H(0, 0) = a_0$

and
$$a_0 = \frac{N_1 I_1}{b_1} (1 - x_1^2) + \frac{N_2 I_2}{b_2} (1 - x_2^2)$$

Define
$$HO \equiv \frac{a_0 \ell_1}{N_1 I_1} = (1 - x_1^2) \ell_1 + \frac{I}{b} (1 - x_2^2)$$

Where
$$b = b_2/b_1$$

At any given point $P(x, z)$, the magnitude of H is measured in terms of its magnitude at the origin. Hence, at the origin, $H_z = 1.0$, $H_x = 0$.

Now, a program was worked out evaluating the x and z components of H in the quadrant $x \geq 0$, $z \geq 0$, for the case where $I = N_2 I_2 / N_1 I_1 = 1.0$. This program used the following inputs:

$$x_1 = 0.26786779$$

$$x_2 = 0.74207042$$

$$I = 1.00000000$$

$$d_1 = 0.27802814$$

$$d_2 = 0.84566402$$

$$\ell_1 = 1.0$$

$$\ell_2 = 0.76389940$$

$$HO = 1.2886132$$

(See Figure C-22 for the graphed results.)

APPENDIX C-4

CALCULATION OF THE TOTAL INDUCTANCE OF A FOUR-CIRCULAR-COIL SYSTEM

Since all four coils are connected in series aiding, the total inductance of the system is given by

$$L_{\text{Total}} = [L_{\text{Total Self Ind.}}] + [L_{\text{Total Mutual Ind.}}]$$

$$L_{\text{Total}} = [2 L_1 + 2 L_2] + [2 L_{12} + 2 L_{13} + 2 L_{14} + 2 L_{23} + 2 L_{24} + 2 L_{34}]$$

However, since

$$L_1 = L_4, \quad L_2 = L_3$$

$$L_{12} = L_{34}, \quad L_{13} = L_{24}$$

$$L_{\text{Total}} = 2 L_1 + 2 L_2 + 4 L_{12} + 4 L_{13} + 2 L_{14} + 2 L_{23} \quad (\text{B-1})$$

Where L_i = self inductance of coil i ,

L_{ij} = mutual inductance of coils i and j .

To calculate the self-inductance of one coil, as shown in Figure C-23(a), let a be the mean radius of the turns. Then the self-inductance⁽¹⁰⁾

$$L = 0.05014 \left(\frac{2a}{b} \right) N^2 a k \quad (\text{B-2})$$

where a is in inches and L is in microhenries. The constant $K' = K - k$ (where K may be obtained from Table 36 and k from Tables 22 and 23, all in reference 10).

For the z -axis coils:

$$L_1 = 9.681 \text{ mh and } L_2 = 13.218 \text{ mh.}$$

For the mutual inductance M , in microhenries, from page 89 of reference 10:

$$M = N_1 N_2 M_0 \quad (\text{B-3})$$

where N_1 and N_2 are the number of turns on the two coils whose mutual inductance is to be calculated, and

$$M_0 = f \sqrt{A a} . \quad (\text{B-4})$$

The dimensions A and a , in inches, are as shown in Figure C-23(b); and f may be obtained from Table 13 of reference 10. For the z -axis coils

$$L_{12} = 1.337 \text{ mh}, \quad L_{13} = 0.549 \text{ mh}, \quad L_{14} = 0.169 \text{ mh}, \quad \text{and} \quad L_{23} = 1.976 \text{ mh}.$$

Using these values of self and mutual inductance in (B-1), the total inductance of the z -axis coil system is found to be

$$L_{\text{Total}} = 57.632 \text{ mh}.$$

Similar results are also presented, in the text, for the H- and D-axis coil systems.

FOUR-SQUARE-COIL SYSTEMS

M. Speiser and D. L. Waidelich

INTRODUCTION

In the production of uniform magnetic fields, it is believed that a system of square coils would have considerable structural advantages over a system of circular coils. The square coils would have the disadvantage, however, of introducing a field variation in the circumferential direction which the circular coils, in theory, do not have.

Suggestions^(1, 2) were made that a study of the four-square-coil system should be made. As a result, such a study was made⁽³⁾ and the results of this study were used to set up computer programs that produced many of the parameters needed.

ANALYSIS

The geometry of the four-square-coil system is shown in Figure C-24. It is assumed that each coil has zero cross section. The geometry of one coil of N turns is shown in Figure C-25. The magnetic field intensity along its axis, in rationalized MKS units, is given by:

$$H(z) = \frac{2}{\pi} \frac{NI}{\ell} f\left(\frac{z}{\ell}\right) \tag{1}$$

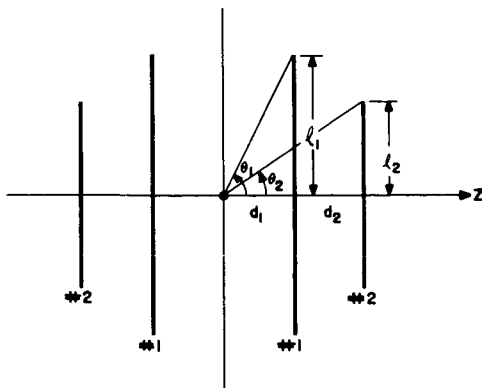


Figure C-24—Geometry of the Four-Square-Coil System

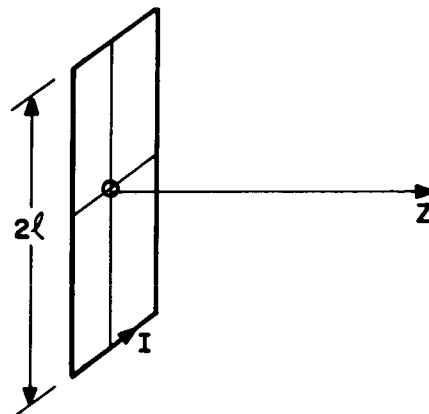


Figure C-25—Geometry of One Square Coil

where

$$f\left(\frac{z}{\ell}\right) = \frac{1}{\left[\left(\frac{z}{\ell}\right)^2 + 1\right] \sqrt{\left(\frac{z}{\ell}\right)^2 + 2}} \quad (2)$$

It may then be shown that, in the case of four square coils placed as shown in Figure C-24, the magnetic-field intensity is given by

$$H(z) = \frac{2}{\pi} \frac{N_1 I_1}{\ell_1} \left[f\left(\frac{d_1 - z}{\ell_1}\right) + f\left(\frac{d_1 + z}{\ell_1}\right) \right] + \frac{2}{\pi} \frac{N_2 I_2}{\ell_2} \left[f\left(\frac{d_2 - z}{\ell_2}\right) + f\left(\frac{d_2 + z}{\ell_2}\right) \right] \quad (3)$$

where the function f may be obtained from equation (2).

It is also possible to expand the magnetic-field intensity in a Taylor series along the z -axis and about the origin, to get

$$H(z) = H \Big|_{z=0} + \frac{z}{1!} \frac{dH}{dz} \Big|_{z=0} + \frac{z^2}{2!} \frac{d^2H}{dz^2} \Big|_{z=0} + \frac{z^3}{3!} \frac{d^3H}{dz^3} \Big|_{z=0} + \dots \quad (4)$$

$$= a_0 + a_1 z + a_2 z^2 + a_3 z^3 + \dots \quad (5)$$

where

$$a_0 = H \Big|_{z=0}$$

$$a_1 = \frac{dH}{dz} \Big|_{z=0}$$

$$a_2 = \frac{1}{2!} \frac{d^2H}{dz^2} \Big|_{z=0}$$

|

|

|

$$a_n = \frac{1}{n!} \frac{d^n H}{dz^n} \Big|_{z=0}$$

Note that, as long as the coils occur in pairs symmetric about the origin, $a_n = 0$ for odd n . Hence, equation (5) reduces to

$$H(z) = a_0 + a_2 z^2 + a_4 z^4 + a_6 z^6 + \dots \quad (6)$$

Ideally, it would be preferable to make $a_n = 0$ for all n greater than zero, in order to have the perfectly uniform magnetic-field intensity

$$H(x) = a_0 = \text{constant}$$

in equation (6). As this is impossible to do in practice, what was done was to consider the conditions necessary to make only the first three coefficients: $a_2 = a_4 = a_6 = 0$. In other words, using equation (3), the following set of three equations was derived and solved:

$$\begin{aligned} \frac{d^2H}{dz^2} \Big|_{z=0} &= \frac{4}{\pi} \frac{N_1 I_1}{\ell_1^3} f^{II} \left(\frac{d_1}{\ell_1} \right) + \frac{4}{\pi} \frac{N_2 I_2}{\ell_2^3} f^{II} \left(\frac{dz}{\ell_2} \right) = 0 \\ \frac{d^4H}{dz^4} \Big|_{z=0} &= \frac{4}{\pi} \frac{N_1 I_1}{\ell_1^5} f^{IV} \left(\frac{d_1}{\ell_1} \right) + \frac{4}{\pi} \frac{N_2 I_2}{\ell_2^5} f^{IV} \left(\frac{dz}{\ell_2} \right) = 0 \\ \frac{d^6H}{dz^6} \Big|_{z=0} &= \frac{4}{\pi} \frac{N_1 I_1}{\ell_1^7} f^{VI} \left(\frac{d_1}{\ell_1} \right) + \frac{4}{\pi} \frac{N_2 I_2}{\ell_2^5} f^{VI} \left(\frac{dz}{\ell_2} \right) = 0 \end{aligned} \quad (7)$$

Definitions of the f 's and further details of the solution are presented in Appendix C-5.

RESULTS

Some of the results of the computer solution of (7) are presented in Tables C-6 and C-7. Table C-6 gives the results for the case of the currents in the No. 1 coils flowing in the same direction as the currents in the No. 2 coils. At the upper end of the table, the No. 2 coil has a much greater size, is much farther from the origin, and has a much greater current than the No. 1 coil; at the lower end of the table, the No. 1 coil has a much greater size, is much farther from the origin, and has a much greater current than the No. 2 coil. Under Remarks are listed several solutions very close to particular solutions of special interest. When $x_2 = \cot \theta_2$ is in the vicinity of 1.00, the homogeneity is approaching a maximum and the sizes of the coils are nearly equal. When x_2 is near 1.20, the ampere-turn ratio is nearly unity. When x_2 is about 1.80, both the No. 1 and No. 2 coils lie approximately in the same plane perpendicular to the axis of the system.

Table C-7 presents the results for the case of the currents in the No. 1 coils flowing in the opposite direction to the currents in the No. 2 coils. At the upper part of the table, the coils are nearly equal in size, the homogeneity is near the maximum, but the field constant is very low because the field from the No. 1 coils nearly cancels that from the No. 2 coils. The No. 2 coils are slightly smaller and slightly closer to the origin of the system than are the No. 1 coils. The ampere-turns of the No. 2 coils are slightly less than those of the No. 1 coils. Toward the lower part of the table, the No. 1 coils are larger in size, lie much farther away from the origin of the system, and carry much more current than the No. 2 coils. The field constant has increased considerably but the homogeneity is much smaller.

Table C-6--Parameters for Systems with Currents in the Same Direction

x_1	x_2	d_1	l_2	d_2	$(N_2 I_2)(N_1 I_1)$	Field Constant, HO	Homogeneity HOMO	Remarks
0.22645	0.54451	0.22645	∞	∞	∞	-	-	End Point
0.22764	0.800	0.22764	1.45894	1.16715	8.81475	4689.8	0.21504	
0.25432	1.00	0.25432	1.01759	1.01759	2.49546	2178.6	0.27122	Coils have nearly equal size. Near maximum homogeneity.
0.29213	1.20	0.29213	0.75235	0.90282	0.99481	1486.8	0.25052	Near unity ampere-turn ratio.
0.31818	1.30	0.31818	0.65071	0.84592	0.64550	1309.5	0.23943	
0.41400	1.64	0.41400	0.38037	0.62380	0.11095	985.34	0.20067	
0.46951	1.80	0.46951	0.26068	0.46923	0.024544	895.32	0.17344	Coils nearly in the same planes.
0.54451	1.96013	0.54451	0.00	0.00	0.00	-	-	End Point

Note:

$$l_1 = 1.00 \text{ for all of Table C-6.}$$

$$x_1 = \frac{d_1}{l_1} = \text{Cot } \theta_1$$

$$x_2 = \frac{d_2}{l_2} = \text{Cot } \theta_2$$

INTEGRAL TURN RATIOS

From the results of Tables C-6 and C-7, it appears that the best results would be obtained by using systems whose values of $x_2 = \text{Cot } \theta_2$ would be in the region of approximately 0.90 to 1.30 as given in Table C-6. From practical considerations, the currents in the coils should be equal, and this then dictates an integral turn ratio for the simplest construction. A computer program was developed that would give solutions at the integral-turn ratios; several of these solutions are presented in Table C-8.

MAGNETIC FIELD CONTOURS

To determine just how much effect the square-coil shape had on the variation of the field in the circumferential direction, it was decided to calculate the field (4) for various

Table C-7—Parameters for Systems with Currents in Opposite Directions

x_1	x_2	d_1	l_2	d_2	$(N_2 I_2)(N_1 I_1)$	Field Constant, HO	Homogeneity, HOMO	Remarks
0.65558	0.65558	0.65558	1.00	0.65558	-1.00	-	-	End Point
0.65119	0.6600	0.65119	0.96274	0.63541	-0.83917	99.167	0.26590	Coils have nearly equal size. Near maximum homogeneity.
0.61369	0.700	0.61369	0.67817	0.47472	-0.16538	587.98	0.22337	
0.58798	0.730	0.58798	0.49749	0.36317	-0.038521	725.51	0.19160	
0.56411	0.760	0.56411	0.31314	0.23798	-0.0041619	788.78	0.15234	
0.54451	0.78636	0.54451	0.00	0.00	0.00	-	-	End Point

Note:

$$l_1 = 1.00 \text{ for all of Table C-7.}$$

$$x_1 = \frac{d_1}{l_1} = \text{Cot } \theta_1$$

$$x_2 = \frac{d_2}{l_2} = \text{Cot } \theta_2$$

Table C-8—Parameter for Systems with Integral Turn Ratios

N_2/N_1	x_1	x_2	d_1	l_2	d_2	Field Constant, HO	Homogeneity, HOMO
7/8	0.30122434	1.22969675	0.30122434	0.72054662	0.88605384	1427.1953	0.24715880
1/1	0.29411772	1.19880071	0.29411772	0.75366885	0.90349875	1489.3349	0.25065301
5/3	0.26973452	1.08377823	0.26973452	0.89366895	0.96853895	1806.1128	0.26453517
2/1	0.26231997	1.04494106	0.26231997	0.94833088	0.99094988	1958.1301	0.26966209
7/3	0.25662935	1.01336415	0.25662935	0.99624907	1.0095631	2107.0705	0.27405599

Note:

$$l_1 = 1.00 \text{ for all of Table C-8.}$$

$$x_1 = \frac{d_1}{l_1} = \text{Cot } \theta_1$$

$$x_2 = \frac{d_2}{l_2} = \text{Cot } \theta_2$$

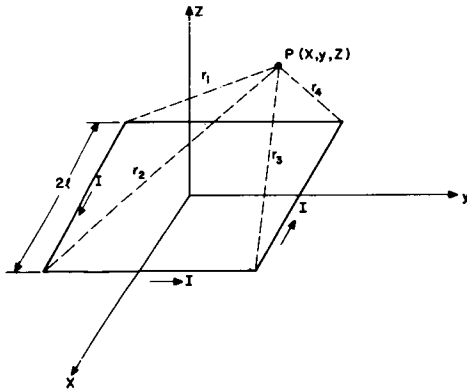


Figure C-26—Geometry for the Field-Intensity Calculations for One Square Coil

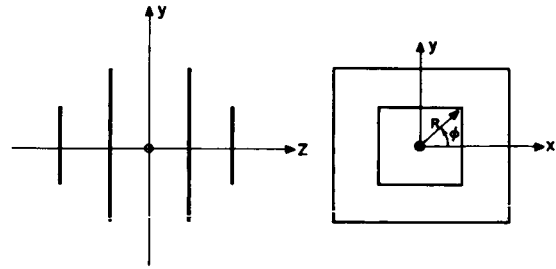


Figure C-27—Geometry for the Field-Intensity Calculations for Four Square Coils

points both on and off the axis. Then, using the calculated values of the field, contour lines of constant field intensity could be sketched. Figures C-26 and C-27 show the geometry employed in these calculations; some of the details of the method of calculation are given in Appendix C-6.

Calculations and plots of the contours were made both for the 1/1 turn ratio and for the 7/3 turn ratio. The contours shown in Figures C-28, C-29, C-30, and C-31 are those for the 1/1 turn ratio. The plane of Figure C-28 is at an angle of $\varphi = 0^\circ$ in Figure C-27. Similarly, Figure C-29 is at $\varphi = 15^\circ$; Figure C-30 at $\varphi = 30^\circ$; and Figure C-31 at $\varphi = 45^\circ$. If the field intensity at the center ($R = 0, Z = 0$) is taken as unity, then the curves of Figure C-28 labeled +10 mean that the field is $1.0 + (+10) 10^{-5}$, while that labeled -100 would have a field of $1.0 + (-100) 10^{-5}$. The field along the Z axis does not vary with the angle φ , but the field in the R direction does change. For example, when $Z = 0$ and $\varphi = 0^\circ$, the field is below unity, but when $Z = 0$ and $\varphi = 45^\circ$ the field is above unity. The negative contours along the R axis gradually disappear as φ increases, and are replaced by the neighboring positive contours which enlarge as φ increases and finally completely displace the negative contours for $\varphi = 45^\circ$. From these curves, the volume of homogeneity appears to be larger in the Z direction than in the R direction. Similar results have been obtained for the other turn ratios. Notice that these curves apply only to any one of the three orthogonal systems which eventually will be used simultaneously. The sum of the contributions from each of the three systems should be graphed, if a three-dimensional view of the contours is desired.

INDUCTANCE

In order to have the coil systems produce a rotating magnetic field, alternating currents must be introduced. As soon as this is done, the inductance of the large coils that are employed becomes an important parameter to be considered in the electrical design of the system. Consequently, a rough calculation was made to determine the order of magnitude of the total inductance of such a four-square-coil system, with $N_2/N_1 = 1.0$.

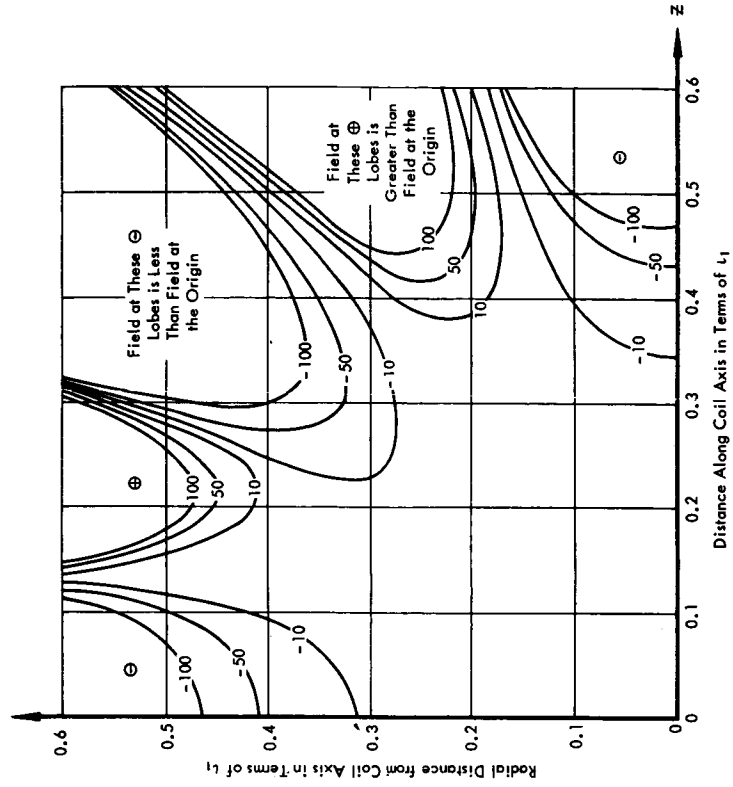


Figure C-28—Gradient of Axially-Directed H Field of a Single System of Coils with $N_2/N_1 = 1/1$ R-Z Plane at $\phi = 0^\circ$

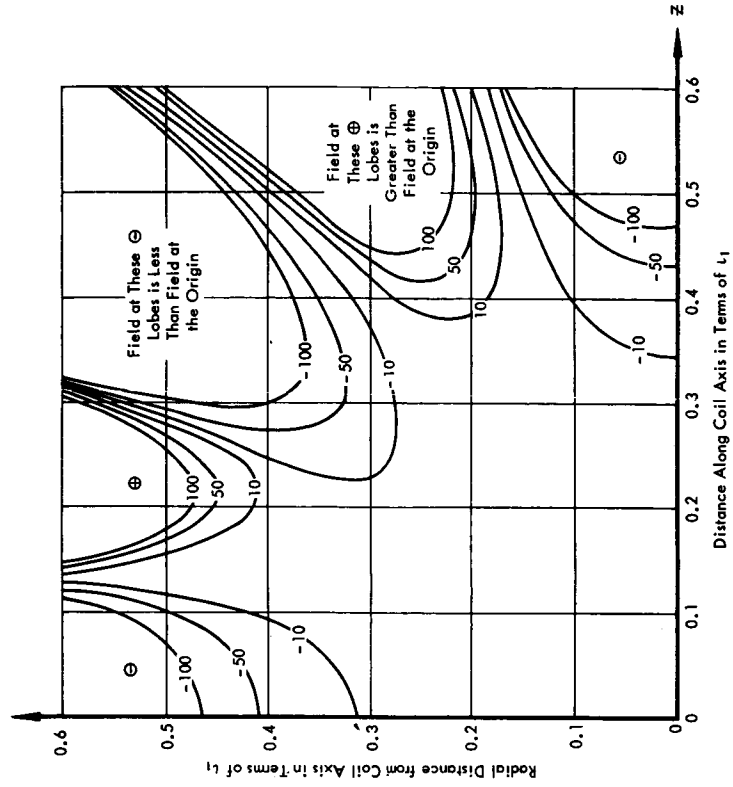


Figure C-29—Gradient of Axially-Directed H Field of a Single System of Coils with $N_2/N_1 = 1/1$ R-Z Plane at $\phi = 15^\circ$

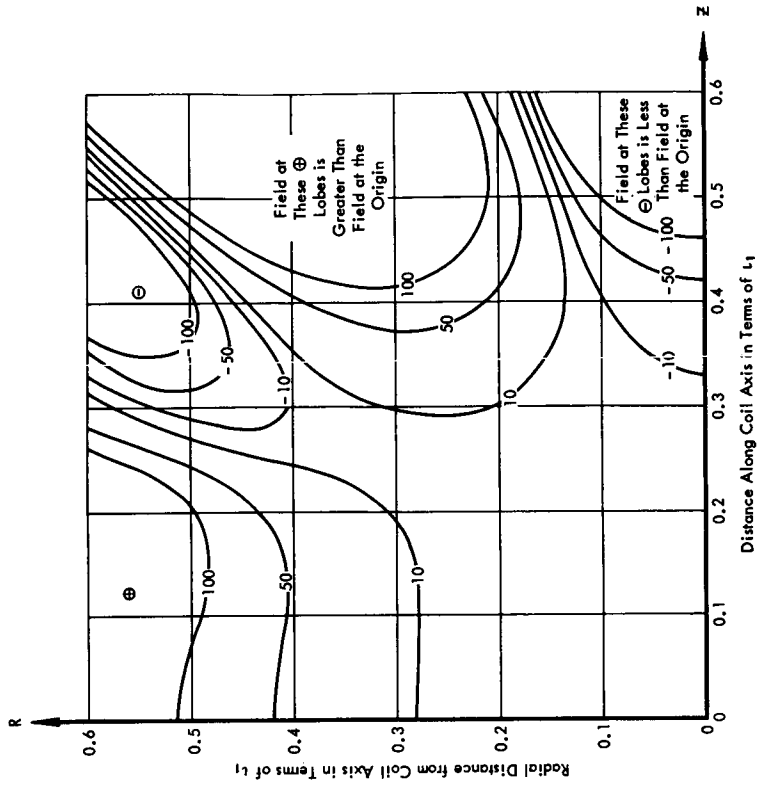


Figure C-31—Gradient of Axially-Directed H Field of a Single System of Coils with $N_2/N_1 = 1/1$ R-Z Plane at $\varphi = 45^\circ$

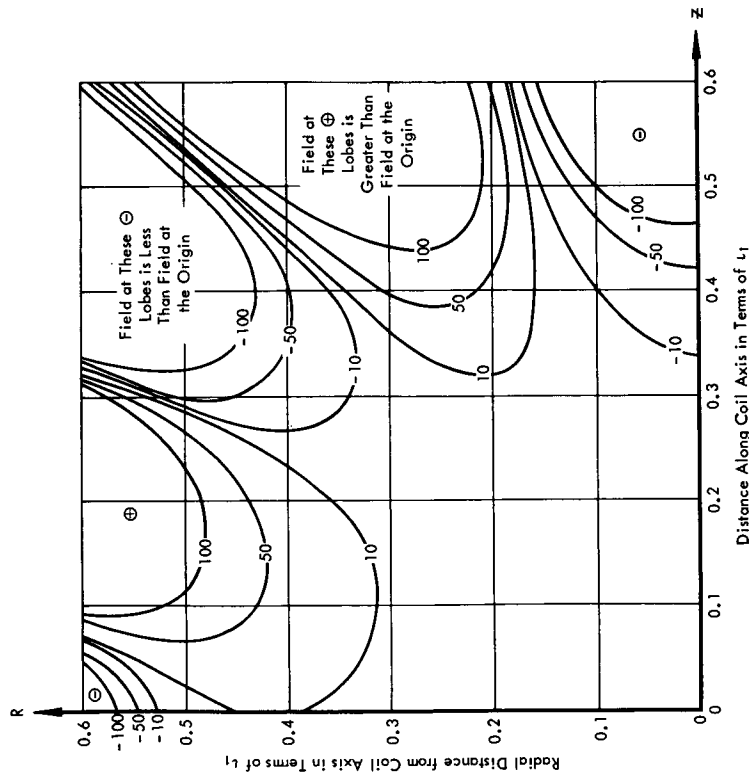


Figure C-30—Gradient of Axially-Directed H Field of a Single System of Coils with $N_2/N_1 = 1/1$ R-Z Plane at $\varphi = 30^\circ$

The inductances of the four-coil system shown in Figure C-32(a) consist of four self-inductances, L_1 , L_2 , L_3 , L_4 , and six mutual inductances L_{12} , L_{13} , L_{14} , L_{23} , L_{24} , and L_{34} . These are added in such a way as to obtain the total inductance⁽⁵⁾. The details of this calculation are presented in Appendix C-7. The total inductance for one system of four coils with an assumed 12 turns on each coil is 66 millihenries. If the three orthogonal systems of coils have their axes meeting in a common point, theoretically there should be no mutual inductance between any two of the systems.

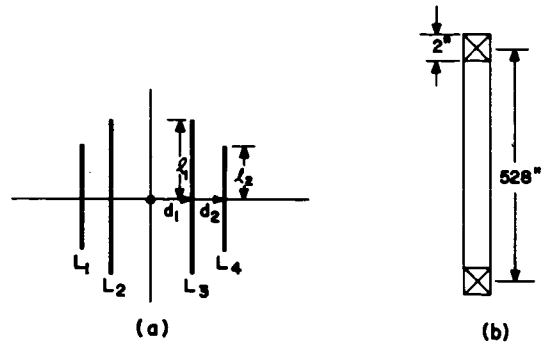


Figure C-32—Dimensions for Inductance Calculation of (a) Four-Coil System, (b) Cross Section of Single Coil

CONCLUSIONS

This report has presented the theory and some parameters of four-square-coil systems with equal currents and integral-turn ratios. The inductances of the systems seem to be comparable to those for four-circular-coil systems.

The field contours indicate that the circumferential variation is present. One possible means of reducing this circumferential variation would be to use a coil whose shape was somewhere between that of a square and that of a circle. One shape that has been suggested is that of a regular octagon.

REFERENCES

1. D. L. Waidelich and M. E. Pittman, "Magnetic Field Simulation" in "Final Report of the Goddard Summer Workshop Program in Simulation of Space Environment" Publication X-320-62-193, Goddard Space Flight Center, Greenbelt, Md., pages 5-3 to 5-15 (1962).
2. M. E. Pittman and D. L. Waidelich, "Three- and Four-Coil Systems for Homogeneous Magnetic Fields." To be published in the Transactions of the Institute of Electrical and Electronics Engineers, and also as a NASA Technical Note.
3. G. Yildirim, "Production of Uniform Magnetic Field by Using Square Coils," Research Report, University of Missouri Engineering Library (June 1963).
4. E. Weber, "Electromagnet Fields," John Wiley and Sons, Inc., New York, N.Y. (1950) pages 131 to 134.
5. F. W. Grover, "Inductance Calculations," D. Van Nostrand & Co., New York, N.Y. (1946).

APPENDIX C-5

DETAILS OF THE SOLUTIONS

The f functions of (7) are defined as

$$f^{II}(z) = \frac{d^2 f}{dz^2} = \frac{2(6z^6 + 18z^4 + 11z^2 - 5)}{(z^2 + 1)^3 (z^2 + 2)^{5/2}}$$

$$f^{IV}(z) = \frac{d^4 f}{dz^4} = \frac{12(30z^{12} + 140z^{10} + 145z^8 - 280z^6 - 678z^4 - 352z^2 + 43)}{(z^2 + 1)^5 (z^2 + 2)^{9/2}}$$

$$f^{VI}(z) = \frac{d^6 f}{dz^6} = \frac{360}{(z^2 + 1)^7 (z^2 + 2)^{13/2}} (56z^{18} + 280z^{16} - 56z^{14} - 3528z^{12}$$

$$- 10367z^{10} - 12327z^8 - 3404z^6$$

$$+ 5056z^4 + 3203z^2 - 177)$$

Defining

$$I \equiv \frac{N_2 I_2}{N_1 I_1}, \quad b \equiv \frac{\ell_2}{\ell_1}$$

$$x_1 \equiv \frac{d_1}{\ell_1}, \quad x_2 \equiv \frac{d_2}{\ell_2}$$

equations (7) take the simple form

$$\left. \begin{aligned} b^3 f^{II}(x_1) + I f^{II}(x_2) &= 0 \\ b^5 f^{IV}(x_1) + I f^{IV}(x_2) &= 0 \\ b^7 f^{VI}(x_1) + I f^{VI}(x_2) &= 0 \end{aligned} \right\} \quad (1)$$

From (1)

$$b^2 = \frac{f^{II}(x_1) f^{IV}(x_2)}{f^{II}(x_2) f^{IV}(x_1)}$$

$$I = - \frac{b^3 f^{II}(x_1)}{f^{II}(x_2)}$$

Hence, the problem has been reduced to solving the three simultaneous equations (1). As they stand, they form a set of three homogeneous equations in terms of four unknowns or variables: x_1 , x_2 , b , and I . So what must be done is to assume knowledge of one of the variables, and proceed to solve the set of three simultaneous equations in three unknowns. This was done: assuming knowledge of x_2 , a Fortran program was developed, and many solutions were obtained.

It was found that solutions existed for I positive (currents in the same direction for the No. 1 and No. 2 coils) and for I negative (currents in the No. 1 coils are opposite in direction to those of the No. 2 coils). For I positive, x_1 ranged from 0.22645 (root of f^{VI}) to 0.54451 (root of f^{II}), while x_2 ranged from 0.54451 (root of f^{II}) to 1.96013 (root of f^{VI}). For I negative, x_1 ranged from 0.65558 to 0.54451 (root of f^{II}), while x_2 ranged from 0.65558 to 0.78636 (root of f^{VI}).

To determine the volume of homogeneity of the four-square-coil system, from equation (6), note that after making $a_2 = a_4 = a_6 = 0$, it can be written as

$$\begin{aligned} H_{(z)} &= a_0 \left[1 + \frac{a_0}{a_0} z^8 + \frac{a_{10}}{a_0} z^{10} + \dots \right] \\ &= a_0 \left[1 + \left(\frac{a_8}{a_0} \ell_1^4 \ell_2^4 \right) \left(\frac{z^8}{\ell_1^4 \ell_2^4} \right) + \dots \right] \\ &= a_0 \left[1 + A_8 \frac{z^8}{\ell_1^4 \ell_2^4} + \dots \right] \end{aligned} \quad (2)$$

where

$$A_8 = \frac{a_8}{a_0} \ell_1^4 \ell_2^4$$

$$A_8 = \frac{1}{8!} \left[\frac{f^{II}(x_2) f^{IV}(x_1) f^{VI}(x_1) f^{VIII}(x_2) - f^{II}(x_1) f^{IV}(x_2) f^{VI}(x_2) f^{VIII}(x_1)}{f(x_2) f^{II}(x_1) f^{IV}(x_1) f^{VI}(x_2) - f(x_1) f^{II}(x_2) f^{IV}(x_2) f^{VI}(x_1)} \right]$$

the function f is given by equation (2), and

$$f^{VIII}(z) = \frac{d^8 f}{dz^8} = \frac{5040}{(z^2+1)^9(z^2+2)^{17/2}} (360 z^{24} + 1440 z^{22} - 7896 z^{20} - 75696 z^{18} - 244665 z^{16} - 353952 z^{14} - 22248 z^{12} + 712152 z^{10} + 1028486 z^8 + 510064 z^6 - 52584 z^4 - 91736 z^2 + 2867)$$
(3)

Define

$$\text{Homo} \equiv \frac{\text{diameter of homogeneity along } z\text{-axis}}{\text{side of largest square coil}}$$

$$\text{Homo} \equiv \frac{2z}{2\ell} = \frac{z}{\ell}$$

Now, if $\ell_1 > \ell_2$, then $\text{Homo} = \frac{z}{\ell_1}$.

If a homogeneity of one part in 10^5 is desired, then, from equation (2)

$$\left| A_8 \frac{z^8}{\ell_1^4 \ell_2^4} \right| \leq 10^{-5}$$
(4)

Then

$$\text{Homo} = \left(\frac{z}{\ell_1} \right) \leq \left[\frac{10^{-5} b^4}{A_8} \right]^{1/8}$$
(5)

Equation (5) then gives the diameter of homogeneity in terms of the largest coil dimension, within which the magnetic-field intensity is 0.001% of its value at the origin. The definition of HOMO from (5) is used as long as $\ell_2 < \ell_1$. When $\ell_2 > \ell_1$, $\text{Homo} = (z/\ell_2)$.

The field constant H_0 is defined as the field at the origin of the four-square-coil system divided by $(N_1 I_1 / \ell_1)$; i.e., the ampere turns of the No. 1 coil divided by the half-side length of the same coil. If the units of H_0 are taken as gamma-meters per ampere turn, from (3) and (4)

$$\begin{aligned} H_0 &= 400 \pi \frac{H_{z=0}}{N_1 I_1 / \ell_1} \\ &= 1600 \left[\frac{1}{(x_1^2 + 1) \sqrt{x_1^2 + 2}} + \frac{1}{b(x_2^2 + 1) \sqrt{x_2^2 + 2}} \right] \end{aligned} \tag{6}$$

APPENDIX C-6

FIELD INTENSITY CALCULATIONS

From Figure C-26, for a single square coil

$$\begin{aligned}
 r_1 &= \sqrt{(x + \ell)^2 + (y + \ell)^2 + z^2} \\
 r_2 &= \sqrt{(x - \ell)^2 + (y + \ell)^2 + z^2} \\
 r_3 &= \sqrt{(x - \ell)^2 + (y - \ell)^2 + z^2} \\
 r_4 &= \sqrt{(x + \ell)^2 + (y - \ell)^2 + z^2}
 \end{aligned} \tag{1}$$

The three components (4) of the magnetic-field intensity at the point $P_{(x, y, z)}$ are

$$\begin{aligned}
 H_x = -\frac{NIz}{4\pi} & \left[\frac{1}{r_2 (r_2 + \ell + y)} - \frac{1}{r_3 (r_3 - \ell + y)} \right. \\
 & \left. + \frac{1}{r_4 (r_4 - \ell + y)} - \frac{1}{r_1 (r_1 + \ell + y)} \right]
 \end{aligned} \tag{2}$$

$$\begin{aligned}
 H_y = \frac{NIz}{4\pi} & \left[\frac{1}{r_1 (r_1 + \ell + x)} - \frac{1}{r_2 (r_2 - \ell + x)} \right. \\
 & \left. + \frac{1}{r_3 (r_3 - \ell + x)} - \frac{1}{r_4 (r_4 + \ell + x)} \right]
 \end{aligned} \tag{3}$$

$$\begin{aligned}
 H_x = \frac{NI}{4\pi} & \left[\frac{(x - \ell)}{r_2 (r_2 + \ell + y)} - \frac{(x - \ell)}{r_3 (r_3 - \ell + y)} \right. \\
 & + \frac{(x + \ell)}{r_4 (r_4 - \ell + y)} - \frac{(x + \ell)}{r_1 (r_1 + \ell + y)} \\
 & - \frac{(y + \ell)}{r_1 (r_1 + \ell + x)} + \frac{(y + \ell)}{r_2 (r_2 - \ell + x)} \\
 & \left. - \frac{(y - \ell)}{r_3 (r_3 - \ell + x)} + \frac{(y - \ell)}{r_4 (r_4 + \ell + x)} \right]
 \end{aligned}
 \tag{4}$$

The three field components of each of the four coils of Figure C-27 are calculated. Then the x components are added to obtain the x component of the total field. A similar calculation is made for the y and z components. The total field is then the square root of the sum of the squares of the components. In almost all cases, the x and y components are sufficiently small so that the total field is essentially the same as the axial component of the field.

APPENDIX C-7

INDUCTANCE CALCULATIONS

The system to be calculated (see Figure C-32a) has a turn ratio of unity, equal currents, and dimensions:

$$l_1 = 264", \text{ i. e., } 2l_1 = 40'$$

$$l_2 = 199.1"$$

$$d_1 = 77.6"$$

$$d_2 = 238.4"$$

$$L_{\text{total}} = [L_{\text{total self ind.}}] + [L_{\text{total mutual ind.}}]$$

$$L_{\text{total}} = [L_1 + L_2 + L_3 + L_4] + [2L_{12} + 2L_{13} + 2L_{13} + 2L_{14} + 2L_{23} + 2L_{24} + 2L_{34}]$$

But since $L_1 = L_4$, $L_2 = L_3$, $L_{13} = L_{24}$, $L_{34} = L_{12}$,

$$L_{\text{total}} = [2L_1 + 2L_2] + [4L_{12} + 4L_{13} + 2L_{14} + 2L_{23}]$$

Now, the inductance⁽⁵⁾ of a rectangle of round wire is, in microhenries,

$$L = (0.008) s \left[l_n \frac{s}{\rho} - 0.524 \right]$$

where, from Figure C-32b, $s =$ side dimension in cm.

$\rho =$ radius of cross section

For L_2 , assuming N_2 turns

$$s = 2l_1 = 528"$$

$$\rho = 1"$$

$$\therefore L_2 = N_2^2 (8 \times 10^{-3}) (528) (2.54) \left[l_n \frac{528}{1} - 0.52 \right] \mu\text{h}$$

$$L_2 = N_2^2 (61.7) \mu\text{h, or } 61.7 \mu\text{h/turn}$$

If $N_2 = 12$ turns, $L_2 = 8.9$ mh.

Similarly for L_1 ,

$$L_1 = N_1^2 (44.2) \mu\text{h}$$

and if $N_1 = 12$ turns, $L_1 = 6.4$ mh.

$$L_{\text{total self ind.}} = 2L_1 + 2L_2 = 2 [N_1^2 (44.2) + N_2^2 (61.7)] \mu\text{h}$$

If $N_1 = N_2 = 12$ turns, $L_{\text{total self ind.}} = 30.6$ mh

The procedure for the evaluation of mutual inductance⁽⁵⁾ is as follows:

1. Calculate the diameter $2a$, of a circle that has the same perimeter as the given square.
2. Making use of Table 16 or 17 (of reference 5), obtain the value of f corresponding to the parameter $2a/d$ or $d/2a$, whichever < 1.0 .
3. The mutual inductance of the two equal circles is:

$$M_0 = f a$$

4. The ratio F of the mutual inductance of the coaxial squares to that of these coaxial circles is given in Table 10, reference 5, as a function of ds or s/d .

s = length of side of square

d = distance between their planes.

i.e.,
$$F = \frac{M_{\square}}{M_0} .$$

5. $\therefore M_{\square} = \frac{4s}{2\pi} f F$ = Mutual inductance of two equal square filaments of wire.

6. Given 2 coils of N_1 and N_2 turns, their mutual inductance will be given by

$$M = N_1 N_2 \frac{4s}{2\pi} f F .$$

Note: In the above formulae, s is in centimeters and M in microhenries.

Evaluation of $L_{23} : N_2 = N_3 = N$

$$d = 2d_1 = (2) (77.6) = 155.2''$$

$$s = 528''$$

The diameter $2a$ of a circle that has the same perimeter as the squares is given by:

$$2a = \frac{4s}{\pi} = \frac{(4) (528)}{3.14} = 672.6''$$

$$\frac{d}{2a} = 0.23 = \delta$$

From Table 16, reference 5, $f = 0.012$

$$\frac{d}{s} = 0.294$$

From Table 10, reference 5, approximate $F = 0.54$

$$\therefore M_{23} = (N^2) \frac{2s}{\pi} fF \mu h$$

$$M_{23} = (N^2) \left(\frac{2}{\pi}\right) (528) (2.54) (1.2 \times 10^{-2}) (0.54) \mu h$$

$$M_{23} = L_{23} = (N^2) 5.5 \mu h \text{ or } 5.5 \mu h/\text{turn}$$

If $N = 12$, $L_{23} = 0.8 \text{ mh}$

Note: The mutual inductances/turn are of the same order of magnitude as those of circular coils.

Similarly, $L_{14} = N^2 (0.4) \mu h$

and if $N = 12$, $L_{14} = 0.06 \text{ mh}$

Evaluation of $L_{12} : N_1 = N_2 = N$

Reference 5 only helps to evaluate mutual inductances of equal square loops. L_{12} will be evaluated assuming that there are two equal square loops of side dimension equal to the average of that of L_1 and L_2 . Then,

$$S = \frac{S_1 + S_2}{2} = \frac{398.2'' + 528''}{2} = 463.1''$$

Diameter $2a$, of circle of same perimeter as these squares

$$2a = \frac{4s}{\pi} = 589.9''$$

$$d = d_2 - d_1 = 238.4 - 77.6 = 160.8$$

$$\frac{d}{2a} = 0.27 \equiv \delta .$$

From Table 16, reference 5, $f = 0.01$

$$\frac{d}{s} = 0.35 .$$

From Table 10, reference 5, $F = 0.52$

$$\therefore L_{12} = (N^2) \frac{2s}{\pi} fF = (N^2) \left(\frac{2}{\pi}\right) (463.1) (2.54) (10^{-2}) (0.52)$$

$$L_{12} = (N^2) (3.9) \mu\text{h} \quad \text{or} \quad 3.9 \mu\text{h/turn} .$$

If $N = 12$, $L_{12} = 0.6 \text{ mh}$.

Similarly, for L_{13} : $L_{13} = N^2 (1.3) \mu\text{h}$ and for $N = 12$, $L_{13} = 0.2 \text{ mh}$.

Results

$$L_1 = N_1^2 (44.2) \mu\text{h}$$

$$L_2 = N_2^2 (61.7) \mu\text{h}$$

$$L_{12} = N_1 N_2 (3.9) \mu\text{h}$$

$$L_{13} = N_1 N_2 (1.3) \mu\text{h}$$

$$L_{14} = N_1^2 (0.4) \mu\text{h}$$

$$L_{23} = N_2^2 (5.5) \mu\text{h} .$$

$$L_{\text{total self ind.}} = 2L_1 + 2L_2 = (N_1^2 + N_2^2) (211.8) \mu\text{h}$$

$$\begin{aligned} L_{\text{total mutual ind.}} &= 4L_{12} + 4L_{13} + 2L_{14} + 2L_{23} \\ &= [N_1 N_2 (20.8) + N_1^2 (0.8) + N_2^2 (11.0)] \mu\text{h} \end{aligned}$$

$$L_{\text{total}} = [N_1^2 (212.6) + N_2^2 (222.8) + N_1 N_2 (20.8)] \mu\text{h} .$$

If $N_1 = N_2 = N$,

$$L_{\text{total}} = N^2 (0.46) \text{ mh.}$$

If $N = 12$, $L_{\text{total}} = 66 \text{ mh.}$

THE SIX-CIRCULAR-COIL SYSTEM

M. Speiser and D. L. Waidelich

INTRODUCTION

The six-circular-coil system which could be used to produce a very uniform magnetic field has the great advantage of a very large volume of homogeneity, but also has the disadvantage of a structure more complicated than the four-coil system. In view of the possibility that this system may be used in the larger magnetic facility planned for Goddard, it was decided to attempt an analysis of the system even though such an analysis was conceded to be much more difficult than that for the four-coil system.

The first attempt⁽¹⁾ at a solution ended in failure, probably because of troubles in the computer program. Two other attempts at a solution were then made, the first leading to a computer program that seem too complex (although it probably could have been made to work) and the second leading to a successful computer program.

ANALYSIS

The geometry of the six-coil system is shown in Figure C-33. The theoretical analysis that was carried out assumed the ideal condition in which these coils are infinitesimally thin. Analysis of the more realistic case in which the coils have finite thickness will possibly come later.

Now, consider the p^{th} coil of a system of coils, carrying current i_p , and having N_p number of turns, as shown in Figure C-34.

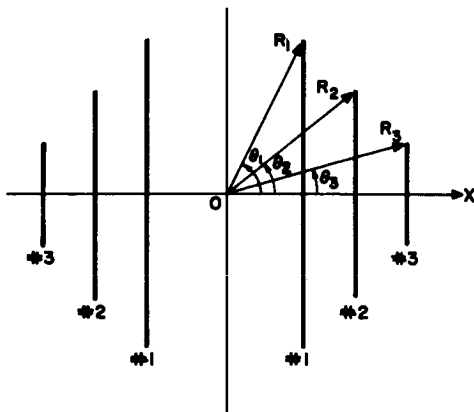


Figure C-33—Geometry of the Six-Coil System

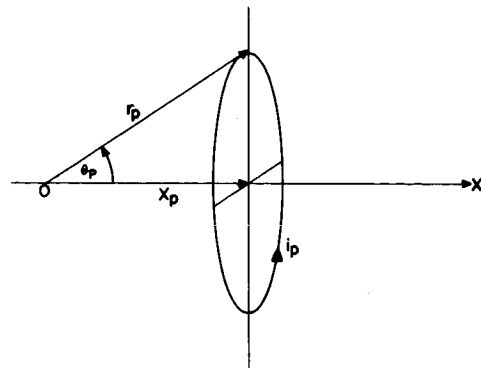


Figure C-34—Geometry for a Single Coil

The H field⁽¹⁾ along the x-axis, in Gaussian units,

$$H(x) = \frac{2\pi}{c} \sum_{n=0}^{\infty} x^n \left[\sum_p N_p i_p \frac{(1 - \mu_p^2)}{r_p^{n+1}} P'_{n+1}(\mu_p) \right] \tag{1}$$

where $\mu_p = \cos \theta_p$, $P_n(\mu_p)$ is the Legendre polynomial of order n, and

$$P'_n(\mu_p) = \frac{dP_n(\mu_p)}{d\mu_p}$$

As long as the coils occur in pairs symmetrical about the origin, the parity of the Legendre polynomials will eliminate the bracketed term of the equation (1) for odd n, so that the equation may be written as

$$H(x) = \sum_{n=0}^{\infty} a_{2n} x^{2n} = a_0 + a_2 x^2 + a_4 x^4 + \dots \tag{2}$$

This is the Taylor series expansion of H along the x-axis and about the origin.

Ideally, $a_2 = a_4 = a_6 = \dots = 0$, in order to have a perfectly uniform magnetic field.

$H(x) = a_0 = \text{constant}$, in equation (2). However, since this is physically impossible, what was done was to find the conditions necessary to make only the first five coefficients ($a_2, a_4, a_6, a_8,$ and a_{10}) all equal to zero. The five resulting simultaneous equations are solved as indicated in Appendix C-8.

RESULTS

The two quantities $x_2 = \cos \theta_2$ and $x_3 = \cos \theta_3$ were used as the independent variables and could be plotted as shown in Figure C-35. To prevent duplication of solutions, it was

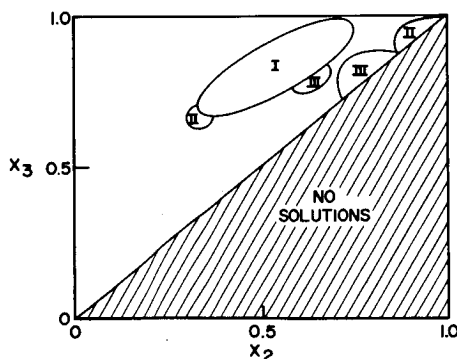


Figure C-35—Region of Possible Solutions

decided that $0.0 < x_2 < x_3 < 1.0$; this meant that no solutions were found in the shaded area of Figure C-35. From the known solutions and from solutions developed by the first computer program of Appendix C-8, solutions were available at various points in the $x_2 - x_3$ plane of Figure C-35. The second computer program of Appendix C-8 was then used to develop further solutions along straight lines radiating from the known solutions. Any kind of curve could have been used, but the straight lines were the easiest to use. Also, the work on the six-coil solutions was curtailed to permit

completion of work on the four-square-coil system to be completed; a spiral curve which had been contemplated was dropped when the available time appeared limited.

The solutions obtained lie within the approximate boundaries sketched in Figure C-35. These boundaries are dictated by the inequality for x_1 , x_2 , and x_3 , and also by the points at which s and t become negative. This last corresponds to radii which are purely imaginary. The Roman numerals within the various boundaries correspond to the various special cases:

- I: All currents in the same direction
- II: Current in the No. 2 coil is in the opposite direction to those in the No. 1 and No. 3 coils
- III: Current in the No. 3 coil is in the opposite direction to those in the No. 1 and No. 2 coils
- IV: Current in the No. 1 coil is in the opposite direction to those in the No. 2 and No. 3 coils

The two III regions of Figure C-35 probably should link up, but the one attempt to do this failed. Attempts were made to obtain the boundaries analytically, so far with little success. Knowledge of the theoretical boundaries would be especially useful in deciding whether some region had been omitted entirely.

Four solutions have been selected from those computed to illustrate the various cases, and to bring out some of the more useful properties. These solutions are given in Table C-9. DIA1, DIA2, and DIA3 are the diameters of the No. 1, No. 2, and No. 3

Table C-9—Computed Solutions for the Six-Coil System

No. of Solution	1	2	3	4
X1	0.14529	0.81448	0.31879	0.13655
X2	0.48827	0.860	0.816	0.292
X3	0.82161	0.941	0.8216	0.7747
DIA1	1.00	1.00	1.00	1.00
DIA2	0.99871	1.1301	0.41177	0.45074
DIA3	0.81765	1.00002	0.37493	0.25994
D1	0.073424	0.70190	0.16817	0.68922
D2	0.27939	0.95226	0.29063	0.68806
D3	0.58923	1.3904	0.27018	1.5923
J3	1.8372	-8.8532	0.49377	-89556.
J3	2.5566	27.637	-0.25320	-38912.
Field Constant	2.7703	0.22533	0.95801	21166.
Homogeneity	0.47687	0.50987	0.28537	0.20079

coils, with $D1a$ taken arbitrarily as unity. $D1$ is the distance of the No. 1 coil from the center of the coil system and $D2$ and $D3$ are similar distances for the No. 2 and No. 3 coils. The field constant is the field intensity in ampere-turns per meter at the center of the coil system per ampere-turn per meter for the No. 1 coil where the distance in meters is the radius of the No. 1 coil. To change the field constant to gammas per ampere-turn per meter, it is necessary to multiply by 400π . The homogeneity is defined as the ratio of the distance along the axis of the system within which the variation is less than 10^{-5} of the field at the center, to the diameter of the largest coil.

The No. 1 and No. 2 solutions of Table C-9 were selected because they have quite high homogeneities, much higher than the 0.36 that had been given previously⁽¹⁾. In fact, a homogeneity of more than 0.62 was the largest found so far, but the corresponding system is not practical because two of the coils are almost coincident and have almost equal and opposite currents. The No. 1 solution of Table C-9 has all three currents flowing in the same direction and probably could be constructed; the only trouble might be that the spacing $2(D1)$ between the two No. 1 coils seems rather small. The No. 2 solution of Table C-9 has rather large spacing and all three coils have almost the same diameter. The current in the No. 2 coil is in a direction opposite to that in the No. 1 and No. 3 coils. The spacing between coils is much larger, and the homogeneity is above 0.50. The field constant is small, however, and this is probably a result of the reversed current in the No. 2 coil.

The No. 3 and No. 4 solutions were included in Table C-9 as examples of other cases involving reversed currents. No. 3 has the current in the No. 3 coil reversed from that in the No. 1 and No. 2 coils. The homogeneity, however, is quite low and the No. 3 coil is slightly closer to the center of the system than is the No. 2 coil. The No. 4 solution has the current in the No. 1 coil reversed from that in the No. 2 and No. 3 coils. The No. 1 and No. 2 coils are nearly the same distance from the center of the system, with the No. 2 coil slightly closer. The current ratios are so high that the No. 1 coil carries almost no currents. The field current is very high because the ampere-turns on the No. 1 coil are so low. Again, the homogeneity is low.

Many other solutions are available in the various parts of Figure C-35. Possibly there is more than one solution for a given pair of x_2 and x_3 ; this would mean that, at that pair of values for x_2 and x_3 , x_1 might have two or more different values leading to two or more entirely different solutions. This has not been observed as yet.

CONCLUSIONS

A computer solution of the six-circular-coil system has been made. The results indicate a much higher volume of homogeneity than had been expected.

It is suggested that the solution should be completed, particularly as far as the boundaries are concerned. There is the possibility that even higher homogeneities might be

found than those encountered so far. Solutions giving integral ratios of the ampere-turns in each of the coils are also needed. An analysis of the effect of finite cross section of the coils would also be helpful.

The solution for the six-square-coil system should be carried out also, because this system would undoubtedly have advantages in construction.

REFERENCE

1. D. L. Waidelich and M. E. Pittman, "Magnetic Field Simulation" in "Final Report of the Goddard Summer Workshop Program in Simulation of Space Environment," Publication X-320-62-193, Goddard Space Flight Center, Greenbelt, Md., pages 5-3 to 5-15 (1962).

APPENDIX C-8

SOLUTION OF THE EQUATIONS

When the five coefficients of (2) a_2 , a_4 , a_6 , a_8 , and a_{10} are put equal to zero, the following equations result

$$f_3(x_1) + y f_3(x_2) + z f_3(x_3) = 0$$

$$f_5(x_1) + y s f_5(x_2) + z t f_5(x_3) = 0$$

$$f_7(x_1) + y s^2 f_7(x_2) + z t^2 f_7(x_3) = 0$$

$$f_9(x_1) + y s^3 f_9(x_2) + z t^3 f_9(x_3) = 0$$

$$f_{11}(x_1) + y s^4 f_{11}(x_2) + z t^4 f_{11}(x_3) = 0$$

where

$$y = j_2 r_2^3 \frac{(1 - x_2^2)}{(1 - x_1^2)}, \quad z = j_3 r_3^3 \frac{(1 - x_3^2)}{(1 - x_1^2)}$$

$$x_i = \cos \theta_i, \quad i = 1, 2, 3 \quad s = r_2^2, \quad t = r_3^2$$

$$j_2 = \frac{N_2 I_2}{N_1 I_1}, \quad j_3 = \frac{N_3 I_3}{N_1 I_1}$$

$$r_2 = \frac{R_1}{R_2}, \quad r_3 = \frac{R_1}{R_3}$$

and the functions f are the derivatives of the Legendre polynomials except for a constant

$$f_3(x) = 5x^2 - 1 = \frac{2}{3} P_3'(x)$$

$$f_5(x) = 21x^4 - 14x^2 + 1 = \frac{8}{15} P_5'(x)$$

$$f_7(x) = 429x^6 - 495x^4 + 135x^2 - 5 = \frac{16}{7} P_7'(x)$$

$$f_9(x) = 2,431 x^8 - 4,004 x^6 + 2,002 x^4 - 308 x^2 + 7 = \frac{128}{45} P'_9(x)$$

$$f_{11}(x) = 29,393 x^{10} - 62,985 x^8 + 46,410 x^6 - 13,650 x^4 + 1,365 x^2 - 21 = \frac{256}{33} P'_{11}(x).$$

Equations (A-1) form a system of five equations in seven unknowns or variables: x_1 , x_2 , x_3 , y , s , z , and t . The unknowns could also be regarded as three angles x_1 , x_2 , x_3 ; two ampere-turns ratios j_2 and j_3 ; and two radii ratios r_2 and r_3 . Hence, two of the variables could be assumed and the other five could be obtained by the solution of the five equations of (1). The equations are difficult to solve exactly, as they are quite nonlinear in x_1 , x_2 , x_3 , s and t . It was decided to choose the two quantities, x_2 and x_3 , and then solve for the five quantities, x_1 , s , t , y and z .

The first step was to choose the values of x_2 and x_3 which were not changed for the remainder of this particular solution. Then a value of x_1 was selected and the first four equations of (1) were solved for s , which resulted in a sixth-degree polynomial in s . From this point on, two somewhat different computer programs were developed.

The first program obtained all the positive roots of the polynomial in s . Then t was calculated for each of the roots of s ; if one or more values of t were positive, then these corresponding values of t and s were kept, but all other t 's and s 's were discarded. The y and z were also calculated and substituted in the last equation of (1) to give

$$g(x_1) = f_{11}(x_1) + ys^4f_{11}(x_2) + zt^4f_{11}(x_3). \quad (2)$$

Then x_1 is changed slightly and the whole process is repeated to produce a second $g(x_1)$. Suppose the first value of x_1 is x_{11} and the corresponding value of g_1 is $g_1(x_{11})$. Similarly, that for the second value of x_1 is x_{12} , and $g_1(x_{12})$. Using a straight-line approximation, a closer approximation to the correct value of x_1 should be

$$x_{13} = \frac{x_{12} g(x_{11}) - x_{11} g(x_{12})}{g(x_{11}) - g(x_{12})}. \quad (3)$$

This was continued until the difference between two successive values of x_1 became small. This value of x_1 , together with the original values of x_2 and x_3 and the calculated s , t , y and z , constitute one solution.

The second program is somewhat different from the first in that a known solution is used. Two of these known solutions are in the literature ⁽¹⁾ and two others with the x 's at the roots of f_9 and f_{11} had been obtained from (1). The x_1 , x_2 , x_3 , and s from one of these known solutions are taken, except that the x_2 and x_3 are changed slightly. The first four equations are then solved by use of an approximation method for a new s , and the method of equations (2) and (3) is used to produce a new x_1 . This new solution is

close to, but not exactly at, the location of the known solution. If the new solution is used as a starting point, a second new solution can be obtained. This process can be repeated time after time to develop a whole series of new solutions.

ANALYSIS OF FOUR-COIL SYSTEMS OF FINITE COIL-WINDING AREA

George Rinard

INTRODUCTION

Recently analytical work has been done in order to determine the dimensions of coil systems necessary to produce uniform magnetic fields. Most of the work considered only filaments of zero cross sectional area for the coils, as little was known of the effects of the physical size of the windings. Because coil systems can be built with a fairly high degree of precision, it was decided to examine more closely the dimensions for the realistic case.

The field on the axis was found by direct integration over the winding area; this field was then expanded about the origin in a Taylor series expansion. For a four-coil system, the expressions were found that make the first three non-zero terms vanish; homogeneity was then based on the coefficient of the eighth order (fourth non-zero) term. This process was very similar to that for the ideal case, once the expression for the axial field was found. Early results using the angles specified by the Braunbek solution seemed to indicate measurable deviations from the ideal case because of winding size; however, the ratio of ampere-turns could not be made exactly equal to unity. Using a new method, it was possible to iterate for any desired ampere-turn ratio and ratio of solenoid length. The results of this analysis are given following the mathematical development, for circular and square solenoids.

A cross sectional view of one coil is given in Figure C-36. The axial field at point P due to the filament of width du is given by (1), where n = turns per unit length, and i = amperes per turn.

$$dh = \frac{ni a^2 du}{2 (a^2 + \mu^2)^{3/2}} \quad (1)$$

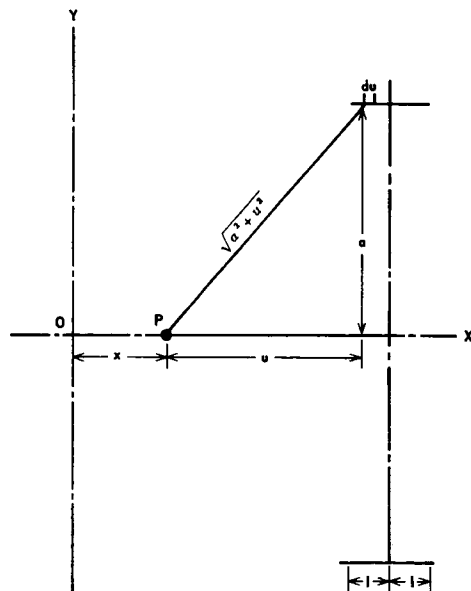


Figure C-36—Cross Sectional View of Circular Or Square Solenoid

Integrating over the winding

$$H = \int_{u_1}^{u_2} \frac{n i a^2 du}{2 (a^2 + u^2)^{3/2}} .$$

Where

$$u_1 = d - x - \ell$$

$$u_2 = d - x + \ell$$

or

$$H = \frac{ni}{2} \left\{ \frac{d - x + \ell}{\sqrt{a^2 + (d - x + \ell)^2}} - \frac{d - x - \ell}{\sqrt{a^2 + (d - x - \ell)^2}} \right\} . \quad (2)$$

For the four-coil case, the field at P is given by (3), where the subscript 1 refers to the inner two coils and 2 to the outer two coils.

$$H = \frac{n_1 i_1}{2} \left\{ \frac{d_1 + \ell_1 - x}{\sqrt{a_1^2 + (d_1 + \ell_1 - x)^2}} - \frac{d_1 - \ell_1 - x}{\sqrt{a_1^2 + (d_1 - \ell_1 - x)^2}} + \frac{d_1 + \ell_1 + x}{\sqrt{a_1^2 + (d_1 + \ell_1 + x)^2}} - \frac{d_1 - \ell_1 + x}{\sqrt{a_1^2 + (d_1 - \ell_1 + x)^2}} \right\} \\ + \frac{n_1 i_2}{2} \left\{ \frac{d_2 + \ell_2 - x}{\sqrt{a_2^2 + (d_2 + \ell_2 - x)^2}} - \frac{d_2 - \ell_2 - x}{\sqrt{a_2^2 + (d_2 - \ell_2 - x)^2}} + \frac{d_2 + \ell_2 + x}{\sqrt{a_2^2 + (d_2 + \ell_2 + x)^2}} - \frac{d_2 - \ell_2 + x}{\sqrt{a_2^2 + (d_2 - \ell_2 + x)^2}} \right\} . \quad (3)$$

This is the expression that must be differentiated eight times with respect to x in order to specify the Taylor series coefficients.

Let

$$f_0(z) = \frac{z}{\sqrt{a^2 + z^2}}$$

$$r_1 = \frac{d_1 + \ell_1}{a_1} \quad s_1 = \frac{d_1 - \ell_1}{a_1}$$

$$r_2 = \frac{d_2 + \ell_2}{a_2} \quad s_2 = \frac{d_2 - \ell_2}{a_2}$$

$$T = \frac{n_2 i_2}{n_1 i_1} \quad b = (a_1/a_2)^2 .$$

Equation (3) becomes, when evaluated at $x = 0$,

$$H_0 = \frac{n_1 i_1}{2} [f_0(r_1) - f_0(s_1) + f_0(r_2) - f_0(s_2)] \quad (3a)$$

Expanding the field about the origin in terms of a Taylor series,

$$H = \sum_{n=0}^{\infty} A_n X^n \quad (4)$$

where

$$A_n = \frac{1}{n!} \left[\frac{d^n (H)}{dx^n} \right]_{x=0}$$

(the odd terms drop out because of symmetry).

The conditions for A₂, A₄ and A₆ to vanish can be shown to be

$$[f_2 (s_1) - f_2 (r_1)] + Tb [f_2 (s_2) - f_2 (r_2)] = 0 \quad (4)$$

$$[f_4 (s_1) - f_4 (r_1)] + Tb^2 [f_4 (s_2) - f_4 (r_2)] = 0 \quad (5)$$

$$[f_6 (s_1) - f_6 (r_1)] + Tb^3 [f_6 (s_2) - f_6 (r_2)] = 0. \quad (6)$$

Let $C_{mm} = [f_m (s_n) - f_m (r_n)]$.

Solving (4), (5) and (6)

$$T = -\frac{1}{b} \frac{C_{21}}{C_{22}} \quad (7)$$

$$b = \frac{C_{41}}{C_{42}} \frac{C_{22}}{C_{21}} \quad (8)$$

$$C_{61} - \left(\frac{C_{41}}{C_{42}} \right)^2 \left(\frac{C_{22}}{C_{21}} \right) C_{62} = 0. \quad (9)$$

Equation (9) is a function of d_1/a_1 , d_2/a_2 , ℓ_1/a_1 and ℓ_2/a_2 . By specifying both ℓ_1/a_1 and ℓ_2/a_2 ; d_1/a_1 can be found for a given d_2/a_2 .

The solution of equation (9) requires an iteration process on a computer. Once d_1/a_1 and d_2/a_2 are known T can be found from (7). Another iteration is necessary to find the specified turns ratio $(T)/(\ell_2/\ell_1)$. A third iteration is required to produce ℓ_2/ℓ_1 which in general is made equal to the turns ratio.

The geometry for one square coil is shown in Figure C-37. The cross section (Figure C-36) also applies here. The field at point P due to the filament of width dn along one side of the coil is

$$\begin{aligned}
 dH &= \int_{z_1}^{z_2} \frac{n i d u}{4\pi} \frac{\sin \alpha}{r^2} dz \\
 &= \frac{n i du}{2\pi \sqrt{a^2 + u^2}} \frac{a}{\sqrt{u^2 + 2a^2}} .
 \end{aligned} \tag{10}$$

The total x-directed field due to four sides is

$$dH_x = \frac{2 ni}{\pi a} \frac{1}{1 + (u/a)^2} \frac{a}{\sqrt{u^2 + 2a^2}} . \tag{11}$$

Integrating with respect to u

$$H_x = \frac{2 ni}{\pi} \tan^{-1} \frac{z}{\sqrt{2 + (u/a)}} \quad \left\{ \begin{array}{l} u = d - x + \ell \\ u = d - x - \ell . \end{array} \right. \tag{12}$$

Let $f_0(z) = \tan^{-1} \frac{z}{\sqrt{2 + z}}$, $(H_x)_0$ then becomes

$$(H_x)_0 = \frac{2ui}{\pi} [f_0(r_1) - f_0(s_1) + f_0(r_2) - f_0(s_2)] . \tag{12a}$$

(12a) is the square coil equivalent of (3a). Equations (4) through (9) are the same for the square coil case. The functions $(f_u(z))$ were worked out and found to agree with those given by Garrett⁽¹⁾ for the circular coil. To find $(f_n(z))$ for the square coils, it was only necessary to notice that the expression for (H) in the ideal case was the same as (dH/dx) in the solenoid case.

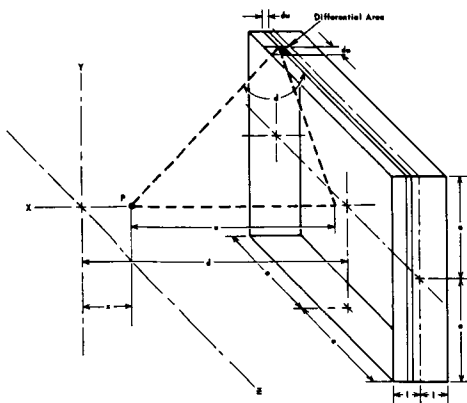


Figure C-37—Geometry for Square Solenoid
C-126

An analysis of the case dealing with coils of rectangular winding cross section was also attempted. Axial field derivatives through the eighth were determined and relationships necessary to make $A_2 = A_4 = A_6 = 0$ were found. A computer program did not yield satisfactory results, however, and time did not allow further pursuit of a solution to the problem.

In the analysis of the solenoid case, solutions were found in a range where A_8 changes sign, implying that this term might

be made to vanish. However, the program failed to converge on the $A_g = 0$ solution, so that a new approach may be necessary here. The general indication of the results in this case is that very long solenoids are required, and therefore are not suitable for a magnetic test facility.

RESULTS

Some special cases for circular and square solenoids of short length are presented in Table 1. "Ideal" refers to coils of zero winding area, and "#1 Finite" and "#2 Finite" to two short solenoid cases. The dimensions are all expressed normalized to the radius of the number one coil and to the half side length of the number one coil for the square case. The two values of ℓ_1/a_1 represent half-coil lengths of 1.5 inches ($2\ell_1 = 3$ inches) and 3.375 inches ($2\ell_1 = 6.75$ inches) normalized to 20 feet. "Change for Ideal" represents deviation from the ideal dimensions necessary to keep $A_2 = A_4 = 0$ when short solenoids are considered. Deviations are also normalized to the same base as the actual dimensions and for this reason may appear misleadingly small. In Table 1 a normalized dimension of 10^{-4} represents an actual dimension of 0.024 in. For example, a change in d_2/a_1 of 0.0007077, for the second case given for 7/3 turn ratio, represents a 0.17 in. change. This deviation from the ideal seems to be measurable and should probably be considered if this system is used. It is noted that some of the deviations from the ideal are increases and some are decreases, and that they do not seem to be linear with the change in coil length. Therefore, once the physical size of the winding has been determined on the basis of the allowable inductance and heating of the coil, it is suggested that another solution be made for this case. Solutions given in Table 1 should be considered only as examples.

POSSIBILITIES FOR FURTHER STUDY

Other problems along this line that may be of practical importance, either for a test facility or otherwise, are:

1. Examination of the solenoid case, concentrating more fully on the longer coils and the possibility of making $A_g = 0$
2. Disc-wound coils, where each turn is placed directly on top of the preceding one; these have not been examined much in the past and may offer new advantages
3. Examination of the system considering rectangular-winding cross section, to determine if a solution is possible and what effect coil depth has on the coil placement and field uniformity.

Table C-10—Comparison of Solenoid Dimensions to Those for the Ideal Case

COIL SYSTEM

	d_1/a_1	d_2/a_1	a_2/a_1	l_1/a_1	l_2/a_1
Circular Coils (Ampere turns ratio = 1)					
Ideal	.27802809	.84566325	.76389898	0	0
#1 Finite	.27805658 (+.00002849	.84574397 +.00008072	.76390684 +.00000786	.00625 ← change from ideal)	.00625
#2 Finite	.27817220 (+.00014411	.84606873 +.00040548	.76393712 +.00003814	.0140625 ← change from ideal)	.0140625
Square Coils (Ampere turns ratio = 1)					
Ideal	.29411772	.90349875	.75366885	0	0
#1 Finite	.29414552 (+.00002780	.90357538 +.00007663	.75367630 +.00000745	.00625 ← change from ideal)	.00625
#2 Finite	.29425913 (+.00014141	.90388849 +.00038974	.75370676 +.00003791	.0140625 ← change from ideal)	.0140625
Square Coils (Ampere turns ratio = 5/3)					
Ideal	.26973452	.96853895	.89366895	0	0
#1 Finite	.26975822 (+.00002370	.96864786 +.00010947	.89365307 -.00001588	.0625 ← change from ideal)	.01041666
#2 Finite	.26985424 (+.00011972	.96908946 +.00055051	.89358847 -.00008048	.0140625 ← change from ideal)	.0234375
Square Coil (Ampere turns ratio = 7/3)					
Ideal	.25662935	1.0095631	.99624907	0	0
#1 Finite	.25664655 (+.00001720	1.0097022 +.00001391	.99619685 -.00005222	.0625 ← change from ideal)	.01458333
#2 Finite	.25671748 (+.00008813	1.0102708 +.0007077	.99598978 -.00025929	.0140625 ← change from ideal)	.0328125

REFERENCE

- (1) M. L. Garret, J. Appl. Phys. 22, 1091, (1951).

PROJECT D: Causes and Effects of Radiation Damage

CONTENTS

	<u>Page</u>
INTRODUCTION	D-1
R. B. Heller	
ENERGY AND TIME BETA-RAY SPECTRA OF FISSION PROJECTS U ²³⁵ AND Pu ²³⁹ BY FISSION NEUTRONS	D-3
R. B. Heller	
METAL WHISKERS	D-9
J. A. Anderson	
EXPERIMENTAL METHOD FOR OBSERVING (TRANSITION GROWTH OF GRAPHITE WHISKERS)	D-17
Appendix A: Ultrahigh-Speed Cinemicrography	D-21
Appendix B: Bibliography	D-27
J. M. Canter and R. B. Heller	
THE EFFECT OF ACCUMULATED HYDROGEN ON CIRCUITRY EMBEDDED IN POLYURETHANE FOAM	D-31
L. L. Mohr	
THE EFFECT OF LOW-ENERGY PROTONS ON SEMICONDUCTOR JUNCTIONS	D-37
R. L. Johnston and R. B. Heller	

ILLUSTRATIONS

<u>Figure</u>		<u>Page</u>
D-1	Beta Rays from U ²³⁵ Fission, by Fission-Spectrum Neutrons	D-3
D-2	Beta Rays from U ²³⁸ Fission, by 14-Mev Neutrons	D-4
D-3	Decay Scheme	D-4
D-4	Variation of Fission Electrons with Altitude after July 6, 1962, Test Shot	D-7
D-5	Experimental Setup for Observing Transition Growth of Graphite Whiskers	D-18
D-6	Test Cell for Observation Experiment	D-19
D-7	Filament for Observation Experiment	D-19
D-8	Holder for Observation Experiment	D-19
D-9	Polyurethane Foam Analytical Sample, Before and After Compression	D-31
D-10	Apparatus for Removal of Gases from Polyurethane Foam, Schematic Diagram	D-32
D-11	Apparatus for Removal of Gases from Polyurethane Foam	D-32

<u>Figure</u>		<u>Page</u>
D-12	Test Module Before Potting	D-34
D-13	Test Module After Potting	D-34
D-14	Circuit for Measurement of Current in Test Modules	D-35
D-15	Potential Step of a Solar Cell	D-37

TABLES

<u>Table</u>		<u>Page</u>
D-1	Available Ultrahigh-Speed Framing Cameras	D-22
D-2	Hydrogen Infusion Data	D-33

SUMMER WORKSHOP 1963

Program Outline and Team Participants

PROJECT D: Causes and Effects of Radiation Damage

Study Topics

- D-1 Beta spectra calculation
- D-2 Whisker growth
- D-3 Foam environment of circuitry
- D-4 Effect of low-energy protons on semiconductor junctions

TEAM D

<u>Academic Personnel</u>	<u>Goddard Personnel</u>	<u>Code</u>
Dr. Robert B. Heller	Dr. Raymond D. Waddel	630
PRINCIPAL INVESTIGATOR	STAFF ADVISOR	
Richard L. Johnston	Dr. Wilmot N. Hess	640
John A. Anderson	William F. Cahill	640
Joseph M. Canter	Allan D. Silver	642
Lester L. Mohr	Dr. Henry E. Frankel	623
	Roland L. Van Allen	631
	Virgil L. Cleveland	325
	NSF Summer Science Student David Chang	

PROJECT D: CAUSES AND EFFECTS OF RADIATION DAMAGE

R. B. Heller

INTRODUCTION

Project D of the 1963 Summer Workshop has concerned itself with four areas that relate to the effects of radiation on matter:

- Synthetic Beta-Ray Spectra from Nuclear Explosions
- Whiskers
- Electrical Property Changes of Polyurethane
- Low-Energy Proton Junction Effects in Semiconductors

These areas were chosen in an attempt to serve GSFC without needless duplication of existing efforts.

Discussion with various GSFC operational and theoretical groups revealed the need for input data for various analytical problems relating to radiation damage. Similar needs for surveying problem areas in whisker growth and low-energy proton effects led to suggestions for fruitful types of new experiments.

Reasons for choosing the four areas, Goddard's concern with each problem, and the manner of carrying out each effort are discussed in the following paragraphs.

A. SYNTHETIC BETA-RAY SPECTRA FROM NUCLEAR EXPLOSIONS

The need for more precise values of the beta rays from nuclear explosions has long been recognized.

The July 9, 1962, high-altitude nuclear explosion of a 1.4-megaton bomb perturbed the naturally existing Van Allen belts. Injection and subsequent trapping of the charged beta rays given off by the fission fragments from U^{235} and U^{238} occurred. This explosion produced, as expected, an artificial radiation belt; however, the intensities in this radiation belt were considerably higher than were expected. It took a number of months to start getting some grasp of the characteristics of the new radiation belt. Many study groups have been and still are correlating beta-ray measurements taken before with those taken after July 9, 1962. These groups could benefit from a more precise determination of the beta rays from explosive types of fission fragments. This input data exists only from extrapolated results obtained experimentally from reactors. Such data

are deficient in short-time and complete energy information, making complete analysis of the belts' characteristics ambiguous.

Project D has synthesized the complete time and energy beta-ray spectrum expected from various nuclear explosions. This can be used as practical input data. In addition, Project D, in anticipation of future testing by nuclear powers of plutonium air-defense weapons, is synthesizing its beta spectrum for GSFC's future use. This will be reported in a Technical Note to be issued later.

Preliminary analysis of Project D's results from U^{235} and U^{238} show them to be in excellent agreement with satellite-measured results and capable of explaining early as well as long-time effects on the Van Allen belt.

In addition, the calculation of the beta spectrum received stimulus from the existing efforts to theoretically determine the changes in optical properties of lenses bombarded by fission-fragment electrons.

B. WHISKERS

The general area of spontaneous and induced metallic whisker growth and the role radiation damage may play in inducing such growth have been investigated by Project D.

A complete survey of the literature is present for GSFC use. A feasible experiment is outlined for future consideration. This experiment is aimed at studying means of stopping whisker growth and not at finding or verifying the basic mechanisms that cause it.

C. ELECTRICAL PROPERTY CHANGES OF POLYURETHANE

The effect of proton irradiation on the electrical properties of the polyurethane-foam "environment" found in all potted circuitry was studied by Project D.

A means was found of simulating the gas-accumulating properties of protons stopped in hydrogenous matter.

D. LOW-ENERGY PROTON JUNCTION EFFECTS IN SEMICONDUCTORS

A reduction in junction self-voltage (V_{oc}) of diode semiconductors due to low-energy protons has been recently reported. Independently, reports of hydrogen accumulation near the surface of diodes resulting from low-energy proton bombardment have been noted. Project D did a simple series of tests aimed at determining the correlation between both these observed effects, namely, reduction of self-voltage at the junction, and hydrogen-bubble accumulation after bombardment.

ENERGY AND TIME BETA-RAY SPECTRA OF FISSION PRODUCTS OF U^{235} AND Pu^{239} BY FISSION NEUTRONS

Robert B. Heller

INTRODUCTION

In 1960 the author made a calculation of the energy-time beta spectra from fission for the Weapons System Evaluation Group of the Department of Defense. In performing this calculation, it was necessary to synthesize the beta spectra from the decay of the fission fragments of U^{235} by fission neutrons and of U^{238} by 14 Mev neutrons. For this original calculation it was necessary to calculate the decay constants and end point energies of more than 50 percent of the 412 possible fission fragments. Where experimental data were lacking about the forbiddenness or shape of the beta spectra from an isotope, values were chosen to agree with the Ft values of Feingold. It is common practice to assume 100-percent beta transitions (energy-wise) between isotope ground states whenever experimental evidence is lacking. Although this assumption is incorrect, because gamma rays are needed to account for the total gamma energy from fission, it was nevertheless used as a first attempt. These calculated results as shown in Figures D-1 and D-2 agreed very well with those of Cameron and King⁽²⁾, but they were always suspect because of the one-step transition used.

The purpose of the present calculation was twofold. First, it recalculated the original work done in 1960, using a two-step transition model for the allowable energy Q_0 for the transition. Figure D-3 shows the decay scheme used.

Second, it expanded the scope of the problem in conjunction with the Naval Radiological Defense Laboratory to include other fissile material undergoing controlled fission of the

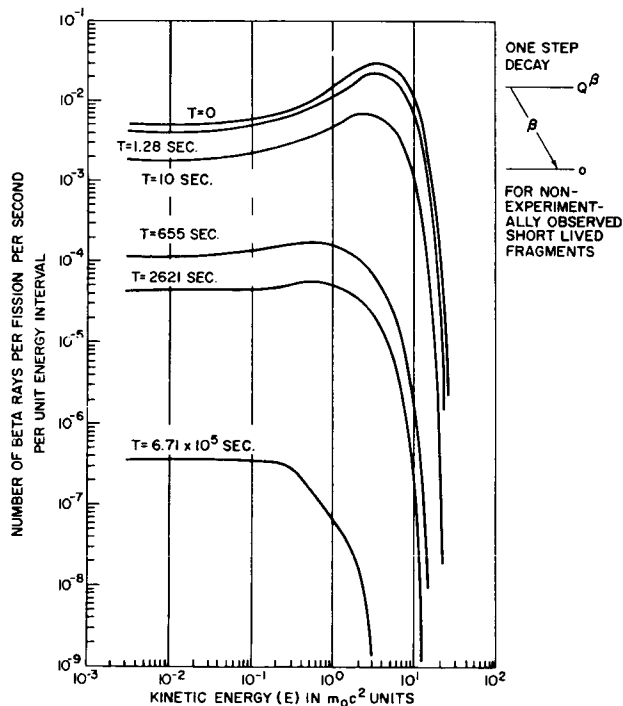


Figure D-1—Beta Rays from U^{235} Fission by Fission-Spectrum Neutrons

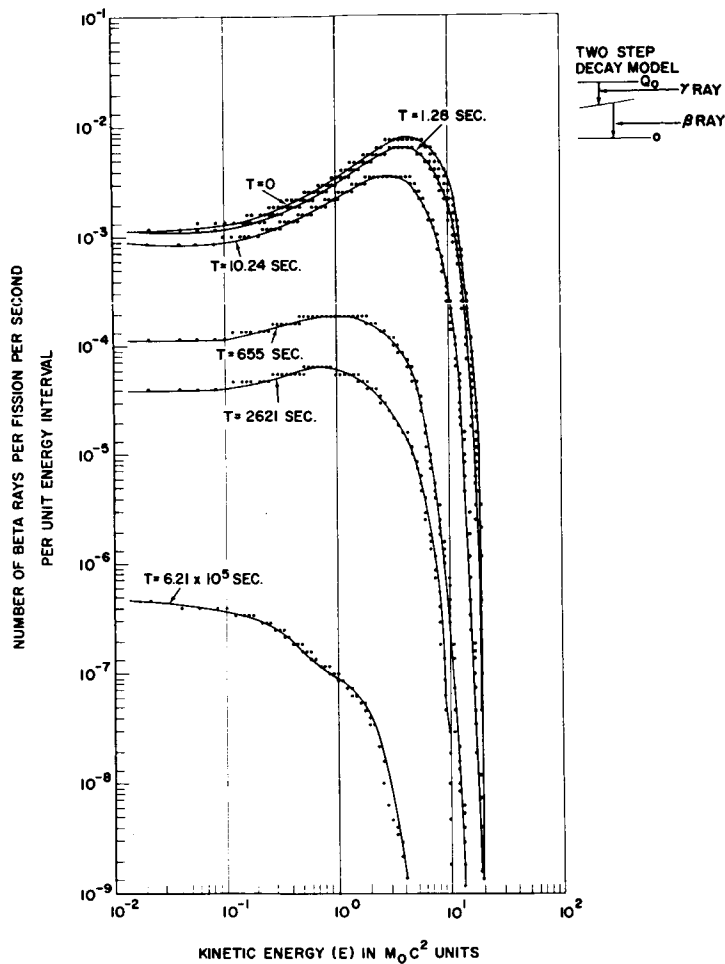


Figure D-2—Beta Rays from U²³⁸ Fission, by 14-Mev Neutrons

reactor type. The object of this joint undertaking was to produce a universal computer-program code to encompass the entire range of fission from explosions to controlled-reactor operation. This later joint effort will not be pursued or published in this report. Pertinent parts presented by Dr. Ora Hersch of USNRDL have been included in our calculations. Parts of Dr. R. Heller's program presented at USNRDL are being used in their computations.

THEORETICAL MODEL AND METHOD OF COMPUTATION:

To save space, the IBM-7090 FORTRAN program for this model

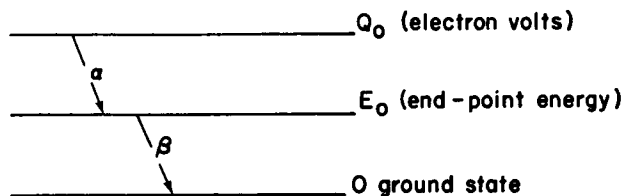


Figure D-3—Decay Scheme

and method of computation will not be reproduced here, but a reprint will be made available to cognizant organizations. A short outline will be given of the basic concepts used.

METHOD:

The disintegration rate $\beta_j(t)$ for the j^{th} fission fragment of a chain was generated by solving the following differential equation for the decay chain:

$$\frac{dA_j}{dt} + \lambda_j A_j = \lambda_{j-1} A_{j-1}$$

where

$$\beta_j(t) = \lambda_j A_j(t)$$

and $A_j(t)$ is the amount of the j^{th} isotope at time t , and $j = 1, \dots, i_0$.

The equation expresses the rate of change of an isotope (A_j) with decay constant λ_j , in terms of all previous members of a chain and their decay constants.

$\beta_j(t)$ was then multiplied by a function $\rho_j(E)$ which gives the probability that the decay yields a beta ray with kinetic energy E .

$$\rho_j(E) = \frac{E(E^2 - 1)^{1/2} (E_0 - E)^2 F(z+1, E) g^2 \zeta}{\int_1^{E_0} E(E^2 - 1)^{1/2} (E_0 - E)^2 F(z+1, E) g^2 \zeta dE} \quad (1)$$

E = beta energy in rest mass ($M_0 C^2$) units

E_0 = beta end point energy in rest mass ($M_0 C^2$) units

$F(z+1, E)$ = energy correction term due to the Coulomb distortion of an electron wave amplitude in the Coulomb field of the nucleus

g = Fermi's fundamental coupling constant

$$\zeta = |C_v|^2 \cdot |\langle 1 \rangle|^2 + |C_A|^2 \cdot |\langle \sigma \rangle|^2$$

a coefficient in the general expression indicating a nuclear matrix element mixture of vector and pseudovector coupling.

The product $B_j(t) P_j(E)^{dE}$ gives the number of beta rays at a given energy and time from the j^{th} isotope, in the energy range between E and $E + dE$.

This product is then double summed over all known or postulated members of a specific fission chain with mass number A , then summed over A ranging from 72 to 162 so that

$$\beta(E, t) = \sum_A \sum_j \beta_j(t) \rho_j(E) \quad (2)$$

INPUT DATA:

Equation 2 requires input data of two general categories:

a. The initial fission abundance $A_j(0)$ of the isotopes by chain mass number A and by charge distribution z within the chain A . This plus the decay time constants suffice to calculate $\beta_j(t)$.

b. The beta-ray end-point energy E_0 , plus the forbidden degree of the beta transition. These factors enable the calculation of the probability function $\rho_j(E)$.

A complete compilation of all the data used in our calculations will be reproduced in tabular form in a Technical Note to be issued later. The estimated total chain and independent fission yields for the various neutron-induced fission processes was taken from U. S. Naval Radiological Defense Laboratory Report USNRDL-TR-633, March 5, 1963. In this report most total chain yields were taken from Katcoff's compilation⁽¹⁾. Fractional chain yields were determined for each value of z in the mass chain A , in the region of the most probable charge in fission, z_p , for that mass number. The values for z_p for thermal neutron fission of U^{235} were taken from Coryell⁽²⁾. Unique values are not given for z_p in the neighborhood of shell and subshell closures and their conjugates; instead, z_p values were calculated by linear plots between the extreme points of the double-value region of z_p . Fractional chain yields for other fissile material and neutron energies were found by using Coryell's prescription for the change in z_p ⁽²⁾, (Δz_p) . From the values obtained for z_p and Δz_p , together with Gleudenin's charge dispersion⁽²⁾ curve, the values for fractional chain yield were found for each mass number A .

All calculations are based on 10^4 simultaneous fissions occurring under various conditions.

DISCUSSION:

Goddard Space Flight Center's interest in these calculations stems from the high-altitude test shot of July 9, 1962, which injected into the earth's field quantities of fission electrons. The spectrum was measured at various altitudes, shown in Figure D-4.

The spectrum at $R = 1.3 R_e$ is "similar" to that obtained from controlled-reactor fission products at a time of approximately 20 seconds of the fission. The other spectra, at larger R , correspond to later times. Very little is known experimentally about the energy-time spectra, and most of this knowledge comes from 'pulsed' reactors covering times from greater than 1 second to about 5 minutes.

These results were limited by detector energy interval sensitivity and did not extend sufficiently into the low beta energies. Consequently, it is not clear that the experimental setup could have indicated the rise in the number of betas (at short times after fission) in going from the low- to the high-energy region.

It is shown that the calculated spectrum shown in Figure D-2 contains the measured results given by Dr. Hess in Figure D-4.

It should be emphasized that these calculated results are good for any time after fission.

CONCLUSION:

Both the one-step and two-step decay transition models yielded results that differed only in magnitude. It can be concluded that the fission-fragment beta spectrum is not very sensitive to the model of radioactive decay.

The results that can be generated by the $B(E, t)$ functions can be used as good practical input data for all reactor and explosion problems.

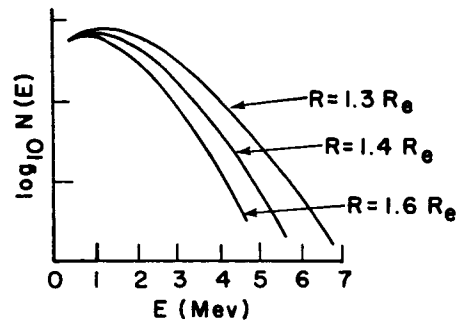


Figure D-4—Variation of Fission Electrons with Altitude after July 6, 1962, Test Shot

METAL WHISKERS

N64-28218

John A. Anderson

INTRODUCTION

Metal "whiskers" are filamentary crystal growths on the surface of metals and crystalline solids with a length-to-diameter ratio of about 10^3 - 10^4 . The observation of metal filaments⁽¹⁾ was previously reported by Ercker in 1574, Boyle in 1661, and Mellar⁽²⁾. Significant research in the area of whisker growth began in 1948 at Bell Telephone Laboratories when the development of shorted circuits in some miniaturized telephone equipment was found to be caused by these filaments.

Spontaneous whisker growth⁽³⁻⁶⁾ has been observed in the metals zinc, cadmium, lead, tin, antimony, silver, copper, and some aluminum alloys containing copper, nickel, and tin. Growth from silver and copper occurred only in the presence of sulfur. The rate of growth for spontaneously growing tin whiskers is about 10^{-8} cm/sec.^(7, 8). A specific growth rate for all metal whiskers cannot be stated as growth rates have been found to vary with different metals⁽⁵⁾. Although many whiskers have reached a length of more than 10 mm, it is not known to what length a whisker may develop. Many long specimens may have been dislodged as a result of air currents or mechanical shock⁽⁵⁾.

As whiskers are usually found on electroplated metals, the inhibition of their growth was attempted by adding organic chemicals to the electroplating bath⁽⁸⁾. This was not successful. Application of supplementary coatings after electroplating was also tried⁽⁵⁾. The whiskers easily penetrated coatings of hard wax and lacquer. Thermosetting plastics inhibited the growth of whiskers, but, after a short period of time, developed cracks through which the whiskers emerged. Other methods of preventing whisker growth have been tried, such as coplating a small amount of lead or arsenic with tin; variation of the substrate metal; oil immersion of electrical equipment; annealing, coldworking, and preliminary corrosion of the metal surface. Not one of these methods will completely eliminate the possibility of whisker growth.

INDUCED GROWTH

Induced growth of whiskers occurs at a faster rate than spontaneous growth. Some of these processes are electrodeposition⁽⁸⁾, the application of pressure to the specimen surface⁽⁹⁾, controlled supersaturation of vapor over a suitable surface⁽¹⁰⁻¹⁵⁾, the heating of metals⁽⁶⁾, and the reduction of metal salts on a suitable substrate^(7, 13, 16-18).

Fisher et al.⁽⁹⁾ have found that the growth rate can be accelerated 10^4 times by the application of pressure to the specimen surface.

Observation of metal whiskers has shown that they increase their length by the addition of material to the whisker tip, or by the addition of material to its base. It is accepted that these two types of growth proceed by different mechanisms. Many mechanisms have been proposed^{(9-13), 17, (19-22)}; of these, it is generally accepted that growth from the solid phase is based on a screw dislocation mechanism. The dislocation loops breaks through the surface, leaving a closed step one atomic unit high on the surface, and each successive loop increases the step one more atomic unit.

For growth from the vapor phase, the whisker is believed to inherit screw dislocations^(13, 23) from the condensing surface, or an impure particle⁽²³⁾ is believed to generate one. The atoms condense from the vapor phase onto the sides of the whisker, then migrate to the tip where they are incorporated around a screw dislocation. All mechanisms imply that, after growth, whiskers contain either no dislocations or only a single axial dislocation.

MECHANISMS FOR GROWTH

In the growth of whiskers, there is an induction period which varies with the type of crystal; this is believed to be the time it takes for the dislocation loops to pile up before breaking through the surface⁽²¹⁾. The growth rate of whiskers is governed by the rate of diffusion of material to the vicinity of the whisker base. Pressure can affect this diffusion time. The temperature dependency of whisker growth may be considered on the basis of the rate of material diffusion⁽²⁴⁾: an increase in temperature results in an increase in the rate of diffusion. This accounts for the greater growth length and thickness observed at higher temperatures⁽²¹⁾. The effect of temperature on whisker growth can also be partially explained on the basis of stress-relieving and metal purity. In the case of cold-rolled and preannealed copper⁽²⁴⁾, at temperatures below 300° C, it would be reasonable to assume that the dislocation stress fields have been sufficiently reduced to permit the dislocations to move more easily.

ENERGY SOURCES FOR GROWTH

Several sources of energy for the growth of whiskers should be considered. F. C. Frank⁽²⁵⁾ proposed that the surface may oxidize to a depth sufficient to make the net surface free energy negative. Thus, an initial microscopic protrusion would tend to grow in order to expose more surface for oxidation. This source of energy could possibly hold for the growth of some whiskers, as they have been observed to grow faster in pure oxygen than in air^(3, 24); however, this energy source would not hold for all whiskers, as metals that do not undergo oxidation have been observed to grow whiskers⁽²⁶⁾. C. Sines⁽²⁷⁾ suggests that a probable source of energy is the release of elastic strain energy

from microresidual stresses in a polycrystalline medium due to the anisotropy of thermal expansion. J. Franks⁽²¹⁾ and other authors generally accept the idea that the source of energy for whisker growth is either external pressure or internal strain within the crystal lattice. If the filament is free or almost free of dislocations, and the bulk material is filled with dislocations, the energy of distortion of the crystal lattice becomes available for whisker growth. The acceleration of growth by a compressive stress has been explained as the effect of the stress gradient in accelerating the diffusion of the metal in the bulk to the base of the whisker^(9, 28). It is plausible that energy release due to residual stresses can promote whisker growth.

PROPERTIES OF WHISKERS

The majority of the work on metal whiskers within the last decade has been concerned with their properties and possible uses. This was prompted by the observation that the strength of whiskers was unusually high^(8, 29). The strength of whiskers has been measured by bend tests or tensile apparatus^(7, 8, 29-40); results of these tests showed that the whiskers deformed at pressures which were close to what had been theoretically predicted, but not observed, for crystals. Nadgarny⁽³⁵⁾ gives the characteristic properties of whiskers as: large elastic deformation up to several percent; stress-strain and bending curves in the plastic region different from those for ordinary crystals; several peculiarities of phase transitions, such as the anomalous existence of high-temperature phases at low temperatures; slower rates of oxidation, evaporation, and dissolution, and higher coercive forces (e. g., iron) than those usually observed. The strength of whiskers has been found to decrease as the whisker thickens. This tends to support the theory of dislocation mechanism in which the final whisker now has at least a pair of axial dislocations. Smith and Randle⁽⁴¹⁾ found that tin whiskers contain some imperfections, but fewer than bulk crystals. Coleman and Cabreen⁽³³⁾ found that whiskers of Zn and Cd contain many dislocations. Pearson⁽³⁰⁾ concluded that high strength does not always imply absence of dislocations. As the size increases, the probability of dislocations and weakness increases, thus giving rise to an average decrease in strength.

Screw dislocations of equal magnitude and opposite signs may annihilate each other under an applied stress, as observed by Muller⁽⁴²⁾ and by Dragsdorf and Johnson⁽¹⁷⁾. This has made their detection difficult, and actually has caused workers to speculate that whiskers contained no dislocations⁽⁴³⁾.

MAGNETIC PROPERTIES

Whiskers have helped to eliminate the discrepancy in the predicted magnetic-field strength required to nucleate domain wall⁽⁴⁾, and coercive forces required for domain-wall motion^(44, 45). Crystal defects cause the formation of extraneous domain boundaries in strong magnetic fields, giving rise to errors in the results. With metal whiskers

(usually iron), a single domain wall can be studied at high field strength and at very rapid reversal of magnetization. As whiskers deviate from the ideal state and develop imperfections, the magnetic properties also become less than optimum⁽³⁵⁾. This applies particularly to the spread in magnitude of the coercive force and its dependence on whisker diameter and dislocations in the whisker. Surface films are known to enhance the strength of normal crystals⁽⁴⁶⁾. In air, all whiskers with the exception of gold and ionic crystals⁽³⁵⁾ are probably entirely covered with an oxide film. Films on iron⁽⁴⁷⁾ and zinc⁽³⁰⁾ whiskers have been observed experimentally. As decreasing whisker diameter is accompanied by increasing strength due to film, the strength of whiskers has in some circles been attributed to this effect⁽⁴⁹⁾.

USES OF WHISKERS

Whiskers of mercury^(42, 50, 51) have been used as field emitters by growing them in a field-emission tube. Using this method, Parker and Harly⁽⁵²⁾ have studied the vapor-phase kinetics of potassium whiskers. These experiments suggest that the mechanism for tip growth is one involving the adsorption of metal atoms on the sides of the whiskers and their consequent diffusion to the tip where they are incorporated around an emerging screw dislocation.

EFFECTS OF RADIATION

Neutron radiation of tin-plated, cold-rolled specimens by S. M. Arnold⁽⁵³⁾ has clearly shown substantial enhancement of whisker growth.

Our present concern with radiation as a factor in growth of whiskers stems from measured proton, electron, and gamma-ray fluxes in outer space and their potential effect on vital electronic components. As most of these circuits are usually internal to the spacecraft, the problem to be investigated is twofold: One is the long-term effect on system reliability from just the spontaneous growth of whiskers that can cause electrical shorts; the other is the reduction expected in system lifetime if short circuits caused by whiskers can be accelerated by radiation-induced screw dislocations.

Except for the most energetic of the known proton, electron, and cosmic particles, a circuit internal to a spacecraft is most likely to be affected by gamma-ray-produced screw-dislocation defects; the outer skins and module coverings afford reasonable shielding against protons and electrons.

It is clear that radiation should have some effect on whisker growth. Radiation that is sufficiently energetic is known to produce defects in solids. It is generally accepted that the energy for whisker growth arises from stresses which are the result of defects in a crystal lattice. Therefore, radiation may supply enough energy to initiate whisker growth, enhance it, or completely disturb the lattice⁽²¹⁾ and inhibit its growth.

A proposed experiment is the observation of the growth of crystals passing through a whisker stage with the use of high-speed photography. This experiment was outlined at the second progress report meeting of the Summer Workshop. By performing these experiments, we may be able to learn more about the mechanism of whisker growth and consequently propose means to inhibit its growth to an appreciable extent.

Having studied the problem of metal whiskers, we conclude that the complexity of the problem requires more study before any definite conclusions can be made. No means has been found to completely inhibit whisker growth; no experiment has been performed to clearly illustrate or ascertain the mechanism of growth. If the growth of whiskers arises from crystalline imperfections, problems of whisker growth will always be present, as nature tends to "abhor" perfect crystals. Recent works seem to be concerned with uses of whiskers. This appears to be a good area for research. As electrical equipments are being miniaturized, the use of metal whiskers in these systems might be applicable.

Bibliography

1. Daremus, Roberts, and Turnbull (ed.), Growth and Perfection of Crystals (Cooperstown Conference), John Wiley and Sons, New York, 1958, p. 15.
2. K. C. Compton et al., Corrosion 7, 327 (1951).
3. Ibid. p. 334.
4. S. S. Breener, Scientific American, July 1960.
5. S. M. Arnold, proceeding of the 1954 Elect. Comp. Symp., pp. 38-44.
6. S. E. Koonce and S. M. Arnold, J. Appl. Phys. 24, 365 (1953).
7. S. S. Breener, Science 128, 569 (1958).
8. C. Herring and J. K. Galt, Phys. Rev. 85, 1060 (1952).
9. Fisher et al., Acta Met. 2, 368 (1954).
10. G. W. Sears, Acta Met. 1, 457 (1953).
11. Ibid. 3, 361 (1955).
12. Ibid. p. 367.
13. S. S. Brenner, Ibid. 4, 62 (1956).
14. R. V. Coleman and G. W. Sears, Ibid. 5, 131 (1957).
15. J. H. How, Phys. Rev. 55, 578 (1939).

16. J. Amick, J. Appl. Phys. 25, 1204 (1954).
17. R. D. Dragsdorf and R. T. Johnson, J. Appl. Phys. 33, 727 (1962).
18. Riper and Roth, Phys. Rev. 92, 503 (1953).
19. G. W. Sears et al., Acta Met. 2, 727 (1954).
20. Ibid., J. Chem. Phys. 26, 1549 (1957).
21. J. Franks, Op Cit. 6, 103 (1958).
22. G. W. Sears, Acta Met. 4, 258 (1956).
23. J. D. Newkirk and G. W. Sears, Acta Met. 3, 110 (1955).
24. W. R. Lasko and W. K. Tice, J. Electrochem. Soc. 109, 211 (1962).
25. F. C. Frank, Phila. Mag. 44, 854 (1953).
26. C. R. Morelock, Acta Met. 10, 160 (1962).
27. G. Sines, J. Physical Soc. of Japan 15, 1199 (1960).
28. R. R. Hasiguti, Acta Met. 3, 200 (1955).
29. Frank B. Cuff and L. Mcd. Schetky, Scientific American, July 1955.
30. G. L. Pearson et al., Acta Met. 5, 181 (1957).
31. S. S. Brenner, J. Appl. Phys. 27, 1484 (1956).
32. R. S. Eisner, Acta Met. 3, 419 (1955).
33. R. V. Coleman et al., J. Appl. Phys. 28, 1360 (1957).
34. J. E. Gordon, Nature 179, 1270 (1957).
35. E. M. Nadgarnyi, Soviet Physics Uspekhi 5, 462 (1962).
36. W. W. Webb and W. D. Forgeng, Acta Met. 6, 462 (1958).
37. J. E. Gordon, See (1), p. 219.
38. S. S. Brenner, See (1), p. 157.
39. R. Bacon, Bull. Am. Phys. Soc. 3, 108 (1958).
40. S. S. Brenner, J. Metals 12, 748 (1960).
41. Smith and Randle, J. Appl. Phys. 29, 679 (1958).

42. Robert Gomer, J. Chem. Phys. 28, 457 (1958).
43. W. W. Webb et al., Phys. Rev. 108, 498 (1957).
44. R. W. Deblois and C. P. Bean, J. Appl. Phys. 32, 253 (1961).
45. R. W. Deblois, J. Appl. Phys. 29, 459 (1958).
46. R. Roscoe, Phila. Mag. 21, 399 (1936).
47. J. V. Lauconis and R. V. Coleman, J. Appl. Phys. 30, 1364 (1959).
48. P. B. Price, Proc. Roy. Soc. London 206A, 1251 (1961).
49. N. Cabrera and P. B. Price, See (1), p. 204.
50. A. J. Melmend and R. Gomer, J. Chem. Phys. 30, 586 (1959).
51. Ibid. 34, 1802 (1961).
52. R. L. Parker and S. C. Hardy, Ibid. 37, 1606 (1962).
53. S. M. Arnold, See (1), p. 108.

EXPERIMENTAL METHOD FOR OBSERVING TRANSITION GROWTH OF GRAPHITE WHISKERS

J. M. Canter and R. B. Heller

N64-28219

Graphite is a convenient material on which to observe whisker growth. A means has been devised to quickly grow and observe graphite whiskers, with the idea of eventually developing methods to destroy them or inhibit their growth. The findings may then be applied to the study of metal whisker growth. Rapid growth which passes from whisker to crystal stage has the advantage of enabling numerous experiments to be performed within a reasonable amount of time. It is anticipated that a few of the many thousands of photographed sequences will contain information on the creation of defects in the whisker and its subsequent participation in normal crystal growth.

Graphite whiskers have been grown in a dc carbon arc,⁽¹⁾ under an inert atmosphere at 92 atmospheres pressure. The carbon atoms condense, forming a cylindrical matrix of polycrystalline graphite on one of the electrodes. Graphite whiskers are found inside the graphite matrix.

The whiskers thus formed are from 1-5 μ in diameter, and may reach several cm in length. They appear to be scrolls or tubes of sheet graphite. This is an anisotropic structure, differing from the structure of whiskers formed on the common metals.

Carbon filaments have also been observed to grow in blast furnaces.^(2,3) Their structure and form seem to imply that these are not pure whiskers, but may be the result of the growth of imperfect whiskers.

Dr. Heller has had some experience with the deposition of graphite from gaseous and liquid hydrocarbons. Extruded graphite lamp filaments are found to be rather irregular, leading to the formation of "hot spots" which reduce the life of the bulb. It was found that, if the filament was fired in a gaseous hydrocarbon atmosphere, crystalline graphite was preferentially deposited on the "hot spots."

This is the basis of the method proposed here. An electric current is passed through a selected graphite filament. The hydrocarbon atmosphere in the immediate vicinity of a constriction (perhaps chosen to contain a whisker) is broken down and the carbon atoms deposit on both the whisker and its surroundings. It is anticipated that the pressure and temperature required for the growth of whiskers will be critical; the optimum conditions will have to be experimentally determined.

Once these parameters are determined, observations of crystal growth may be made. This will require the use of ultra-high-speed photography, as can be seen from a simple calculation. The magnification required will be of the order of 1000x. We expect a growth rate of the order of 0.1 cm/sec. At 1000x, this means a velocity of 100 cm/sec at the focal plane of the camera. The resolution of the camera is about 300 lines across the 1-cm frame; we should like the image blur due to growth to be at least as small as that due to imperfect spatial resolution. Hence, the exposure time must be at most 1/30,000 sec, implying a framing rate of 3.3×10^5 frames/sec. It would be advantageous to reach rates higher than this, because the incremental growth rate may be greater than the average rate.

Details of the choice of camera, light source, etc. may be found in an appendix to this report. The experimental arrangement is diagrammed in Figure D-5. The camera views through a standard microscope, a cloth bellows excluding extraneous light. The filament is enclosed in a glass tube with an optical flat viewing port. Should pressures of many atmospheres be required, a metal chamber will have to be used; glass is preferable, however, because it allows more flexibility in lighting. Figure D-5 shows a 1:1 relay lens used to form a real image of the event at the focus of the microscope objective. This will be necessary because it may not be possible to get the 1000x objective close enough to the growth area. A pyrometer (not shown) may be used to measure the filament temperature.

It has been determined that, at these high powers, only a laser beam can supply sufficient intensity for adequate illumination. The polarized laser beam may also be of advantage to better show the details of the event. There remains the question whether the high-intensity short-duration (100- μ sec) beam will seriously disturb the experiment. A condensing lens and iris will be used to regulate the light.

A possible design of the test cell and filament mounting is shown in Figures D-6, D-7, and D-8.

Although the photographs thus obtained will not be of great resolution, it is anticipated that, given a large number of sets of pictures, the experienced human operator

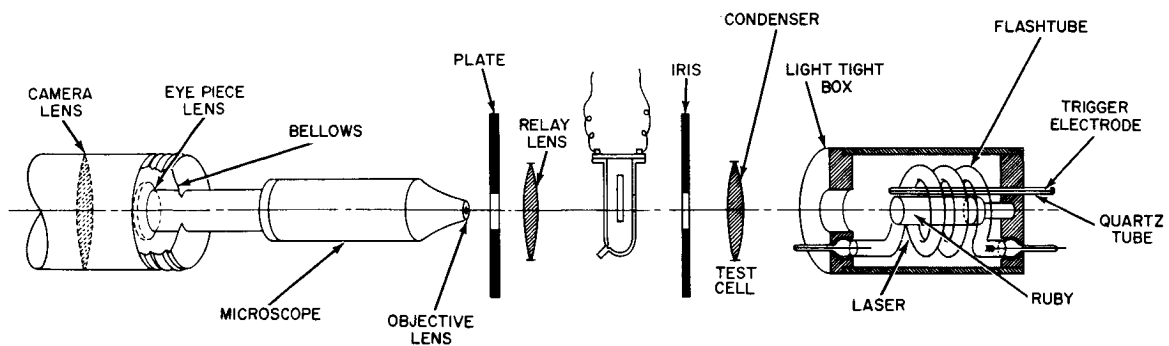


Figure D-5—Experimental Setup for Observing Transition Growth of Graphite Whiskers

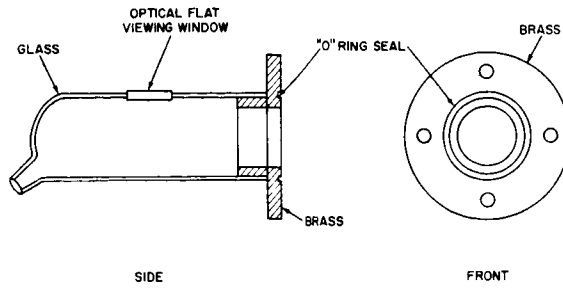


Figure D-6—Test Cell for Observation Experiment

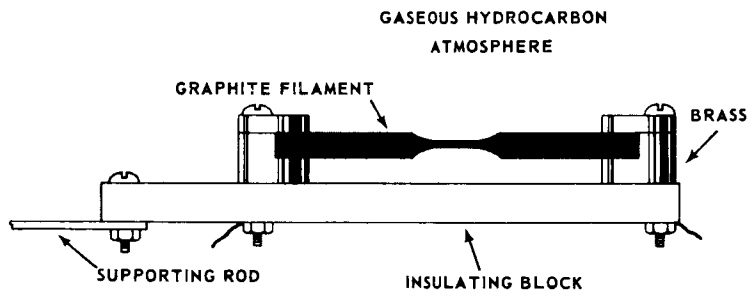


Figure D-7—Filament for Observation Experiment

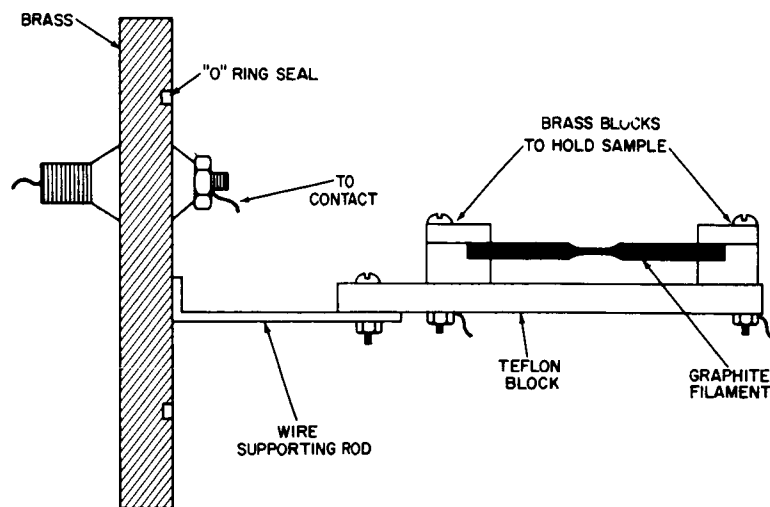


Figure D-8—Holder for Observation Experiment

will be able to make significant observations. From these observations, it is hoped that methods may be devised to reduce the growth rate of whiskers normal to the parent surface. Observations of possible surface motion of deposited carbon may clear up the question of whether a surface mass-transport mechanism plays any role in the growth or destruction of whiskers. The setup described above may also be used for other related experiments (e. g. , the study of the effect of current pulses of varying duration and magnitude on the growth of whiskers).

REFERENCES

1. Bacon, Roger, J. Appl. Phys. 31, 283 (1960).
2. Hofer, L. J. E., E. Sterling, J. T. McCartney, J. Phys. Chem. 59, 1153 (1955).
3. Davis, W. R., R. J. Slawson, G. R. Rigly, Nature 171, 756 (1953).

APPENDIX A

ULTRAHIGH-SPEED CINEMICROGRAPHY

THE CAMERA

Ultrahigh-speed photography is defined as the recording of sequences of photographs at rates of 10^5 frames per second and up. This definition is somewhat restrictive in that it considers only the "framing" camera, to the exclusion of the "streak" camera. The difference between these two types is precisely what is implied: the streak camera records a smear of an event, it is resolved in only one spatial dimension, while the framing camera records individual frames. Considering the proposed application to the photomicrographic study of whisker growth, this restriction is well justified.

The ordinary movie-camera principle of moving a film discontinuously behind a rotary shutter is unsuitable for rates in excess of several hundred frames per second, because of the excessive inertial forces. Higher speeds are achieved by moving the film continuously and compensating by means of a rotary prism. This is the principle of the "Fastex" camera, and is useful up to about 50,000 frames per second.

To attain ultrahigh speeds, entirely different techniques must be used, because it becomes impossible to transport film at the necessary rates. Perhaps the simplest method is to use a number of cameras fired in sequence. A difficulty of this method is that each camera has a different viewpoint; this objection may be overcome by using a single lens and either a spinning mirror or a beam-splitter.

The spinning-mirror framing camera is the most common of the ultrahigh-speed cameras. A set of cameras is arranged in an arc of a circle, focused at a common point. A real image of the event is formed at this point by the main camera lens, and a small rapidly rotating mirror relays the image to each of the cameras in sequence. Commercially available cameras can record from 15 to 117 frames at rates up to 9×10^6 frames per second. Resolution is of the order of 30-60 lines per mm. A typical example is the Beckman & Whitley Model 189. Another interesting spinning-mirror camera is the Electro-Optical Instruments (EOI) RMC 15-F, which has the advantage of being lightweight and compact. Its major flaws are small frame size (10×15 mm) and low frame capacity (15). More details on these and other cameras may be found in Table D-1.

The "beam-splitter" camera consists of several cameras viewing simultaneously through a common lens by means of a beam-splitting arrangement. The individual cameras have their own shutters (typically, Kerr cells), which are fired sequentially by associated electronics. This camera can attain extremely high speeds; it is limited mainly by the

Table D-1
Available Ultrahigh-Speed Framing Cameras

Camera	Speed × 10 ⁶		Size (mm)	Frames		f/value	Writing Time (%)	Lines/mm	I.F. (°)	I.T. (°)	Focal Length (mm)	Notes
	Max.	Min.		Capacity	Capacity							
Beckman & Whitley 189A	4.3	.24	8×25	25		f/20	10	40	320	8,000	610	a. Interchangeable drive
	2.4	.12	16×25	25		f/20	10	40	640	16,000	610	
	1.2	.048	19×25	25		f/20	10	40	760	19,000	610	
192	1.4	.07	17×25	80		f/26	100	19	154	12,300	610	a.
Barr & Stroud Model CP5 Type CP5901	8.64		50×8	117		f/16	10	30(?)	360	42,200		a.
	4.32		50×13.5	59		f/14.5	10	30(?)	608	35,900		
	2.16		50×19	30		f/13	10	30(?)	855	26,700		
	1.73		50×19	28		f/13	10	30(?)	855	23,900		
	8.64		50×8	60		f/16	10	30(?)	360	21,100		
	1.44		50×19	22		f/13	10	30(?)	855	18,800		
Electro-Optical Instruments RMC-15 F			10×15 to 14×15									
	1.2	.02		15		f/10-f/28	40	30	189	2,830	85	a. Lightweight
Los Alamos Model 8	15.		5×13	96		f/26	40	30(?)	58.5	5,620		a.
Cordin Model F-2	1.2		19×25	25		f/20	10	30(?)	428	10,700		a.
J. Langham-Thompson Ltd. Courtney-Pratt Series 600	.15	.001	87×112	300 on 1 4×5" plate		f/4.5	100	2.5	61	18,300		b. Lenticular Plate
Sultanoff	100		100×125	300 on 1 4×5" plate		f/10	100	2.5	78.3	23,500		b. Grid Plate
Abtronics, Inc. Model 1	1		30	4		f/1.4		10	283	1,115		Image converter
Electro-Optical Instruments KFC-600	100		44.5 diam.	6		f/30	100	40-60	3,870	23,300	305	Kerr Cell, beam-splitter

a. Spinning mirror, turbine drive
b. Image dissection
c. See text

difficulty of supplying short pulses to Kerr shutters because of their high capacitance. Disadvantages include low light efficiency (caused both by the Kerr cell and the beam splitter) and low frame capacity. A commercial version is the EOI KFC-600, which consists of six Kerr-cell cameras grouped around a beam-splitter and lens. Speeds of 10^8 frames per second may be attained, with a resolution of 40-60 lines per mm on a frame 45 mm in diameter. Polaroid film may be used.

Another approach to the problem is the "image-dissection" camera, a sampling device which in its simplest form consists of a mask with an array of holes placed in front of the film in the focal plane of the camera. The mask is moved rapidly during exposure. The "frames" may be decoded after processing by the same mask, which is then moved more slowly. These cameras take several hundred frames at up to 10^8 frames/sec. The Sultanoff camera uses an optically opaque plate upon which lines have been ruled, instead of the halftone-type mask previously described. The Courtney-Pratt camera uses a lenticular plate for a mask, which greatly improves light efficiency. Instead of moving the lenticular plate, a scanning disk is used. The main flaw in these cameras is their poor resolution, of the order of a few lines per mm. There has been considerable experimentation with fiber optics, which are used to translate the two-dimensional image to one that is essentially one-dimensional. Higher resolution may be attained by using such a device; there are as yet no commercially available models.

Very great light efficiency may be attained with an image-converter tube. This is shuttered electronically, and the array of sequential frames is displayed on the face of the tube, where it may be photographed. The Abtronics Model 1 is a commercially available image-converter camera which records 4 frames at up to 10^6 frames per second. Its effective aperture is $f/1.4$. The resolution of these devices is rather poor.

Table 1 briefly summarizes the properties of various commercially available cameras. Much of the information is taken from "Engineering and Scientific High Speed Photography" by W. G. Hyzer⁽¹⁾. Only two of the entries require explanation, those entitled "I. F." and "I. T.", standing for "Information Factor" and "Information Total" respectively. The "Information Factor" is a measure of the information per frame. I have defined it as the area of the frame multiplied by the square of the resolution, divided by 10^3 for convenience. Physically, this is the number of "information cells" present per frame. The "Information Total" is the "Information Factor" multiplied by the total number of frames.

ADAPTATION TO THE MICROSCOPE

Communication with Willis Goss⁽³⁾ of EOI has indicated that the RMC-15F camera is available in a version to fit any standard microscope. It was learned that the camera was designed with this purpose in mind, although it has never been used at powers as high as 1000x.

The Beckman & Whitley Model 189 has been used by Zernow and Hauver⁽⁴⁾ and Zernow and Woffinden⁽⁵⁾ in studies of exploding wires and microcracking in glass. Magnification ranged from 5x to 200 x at framing rates up to about 10^6 frames/sec. It was not stated whether the highest magnifications were attained at the maximum framing rates, nor were any cinemicrographs at magnifications greater than 25x published. The optical system used a microscope objective in conjunction with the 24-inch lens of the 189 camera. A relay lens was used to form a real image of the event at a point where the microscope could be focused.

J. S. Courtney-Pratt and C. M. Huggins^(6,7) have published several articles on the use of lenticular-plate image-dissection cameras in cinemicroscopy. The camera described is similar to the Courtney-Pratt series 600 unit manufactured by J. Langham-Thompson, Ltd., the major difference being that it relies on actual motion of the lenticular plate with respect to the photosensitive surface rather than on a scanning disk. This is done to maximize the optical efficiency of the system. The camera is about 400 times (8-1/2 f-stops) more efficient than a spinning-mirror camera. It is claimed that magnifications as great as 2000x may be obtained, using a Vickers projection microscope.

J. S. Courtney-Pratt and D. P. C. Thackeray⁽⁸⁾, and J. S. Courtney-Pratt⁽⁹⁾ have published papers dealing with image-splitting techniques in cinemicrography. One camera described takes 8 pictures in silhouette at rates up to 5×10^5 frames/sec. At magnifications up to 200x. The other, utilizing a rotating-prism beam-splitter, takes 8 or 16 frames illuminated by transmission or reflection, at rates up to 10^5 frames/sec at 500x magnification. It would appear, however, that these cameras possess little if any advantage over a spinning-mirror camera and do have the distinct disadvantage of being unavailable commercially.

LIGHT SOURCE

Our most exacting requirement will be the light source. Lighting a non-selfluminous event for 10^6 frames/sec photography is a difficult matter: at 1000x we are pushing the state-of-the-art. It has been indicated in the literature⁽⁵⁻⁹⁾ and from communication with Mr. Goss⁽³⁾ that while we could get away with "conventional" light sources, such as small xenon flash tubes or argon "bombs", at magnifications of the order of 25x, a more intense source would be necessary for our work.

The most practical means of achieving this seems to be a laser. The great advantage of a laser is that it emits a beam of parallel light, thus being effectively a point source. With the use of a condensing lens, we can regulate the intensity by varying the spot size. A bonus of the laser is that its beam is plane-polarized. It may be possible to employ this to bring out surface details of the growth process. Although any source may be polarized by a filter, it is unlikely that any other source will provide sufficient intensity to make up for losses in the polarizer. D. A. Buddenhagen of Hughes Research Labs

has indicated ⁽³⁾ that one of their packaged units can easily be modified to supply a flat-topped pulse of 100 microseconds duration. It may also be possible to extend this pulse length.

CHOICE OF CAMERA

The choice of the camera to be used requires that an intelligent compromise be made between the various parameters involved. These include maximum and minimum framing rates, resolution, frame capacity, and general versatility. The f-number is not of great concern, since the laser provides more than enough light.

All things considered, it would appear that our best choice would be a rotating-mirror camera. The KFC-600 beam-splitter camera, despite its remarkable resolution, is judged to take an insufficient number of frames. Likewise, the Abtronics Model 1 takes too few frames, besides which it has poor resolution. The two image-dissection cameras have been carefully considered, but are rejected. Both have poor resolution, as indicated by their "I. F.". The Courtney-Pratt camera can attain only 1.5×10^5 frames/sec.

Of the rotating-mirror cameras, it is felt that the Beckman & Whitley Model 189 with 1.2×10^6 frame/sec mirror will best meet our needs. Three cameras very similar to this are the Barr & Stroud CP5904 and CP5906, and the Cordin F-2; insufficient information is available at the time of writing to determine if any of these cameras possess any great advantage over the Beckman & Whitley.

The Model 189 is a proven, versatile instrument. For all its complexity, it is rather easily operated. A Beckman & Whitley drum-streak camera may be attached to the 189 and set up to take one frame every revolution of the mirror. This extends the lowest rate to about 400 frames/sec. If needed, additional mirror assemblies may be purchased and interchanged to give speeds up to over 4×10^6 frames/sec. Thus, it has a range of four decades in framing rates.

There remains the question whether it is possible to wed the 189 to a 1000x microscope. If this is not feasible, the EOI RMC-15F can definitely be used. ⁽³⁾ The only real advantage of this camera is its small size and weight; its low frame capacity and poorer resolution make it a second choice to the 189 and similar units.

The National Bureau of Standards operates a 189 camera. The possibilities of performing the experiment using their equipment should not be ignored. It is probably also possible to lease the unit; however, it would appear likely that there are enough other experiments of interest to justify purchase of the equipment.

REFERENCES

1. Hyzer, Engineering and Scientific High Speed Photography, Macmillan (1962), 132-136.
2. Ibid.
3. Goss, Willis, Electro-Optical Instruments, Private communication (Monrovia, Calif.)
4. Zernow, L. and G. E. Hauver, Proceedings at the Third International Congress on High Speed Photography, Butterworths Scientific Publications, London (1957), 305-315.
5. Zernow, L. and G. Woffindey, Exploding Wires, Plenum Press (1959), 170.
6. Courtney-Pratt, J. S. , Bell Laboratories Record (June 1961), 212.
7. Courtney-Pratt, J. S. , and Charles M. Huggins, Rev. Sci. Inst. 28, 256 (1957).
8. Courtney-Pratt, J. S. , and D. P. C. Thackeray, Proceedings of the Third International Congress on High Speed Photography, Butterworths Scientific Publications, London (1957), 81-86.
9. Courtney-Pratt, J. S. , Proceedings at the Third International Congress on High Speed Photography, Butterworths Scientific Publications, London (1957), 87-95.

APPENDIX B BIBLIOGRAPHY

CARBON WHISKERS

1. Bacon, Roger, "Growth, Structure, and Properties of Graphite Whiskers," J. Appl. Phys., **31**, 283 (1960).
2. Hofer, L. J. E., E. Sterling, J. T. McCartney, "Structure of the Carbon Deposited from Carbon Monoxide on Iron, Cobalt and Nickel," J. Phys. Chem. **59**, 1153 (1955).
3. Davis, W. R., R. J. Slawson, G. R. Rigby, "An Unusual Form of Carbon," Nature **171**, 756 (1953).
4. Fesner, P. A., A. T. Echeistova, "Electron-Microscope Study of the Growth of Lamplblack Particles," Doklady Acad. Nauk. U. S. S. R. **87**, 1029 (1952).
5. Doremus, R. H., B. W. Roberts, and David Turnbull, "Growth and Perfection of Crystals," Wiley, New York, pp. 47, 48, 197-203 (1958).

ULTRA-HIGH-SPEED PHOTOGRAPHY

6. Hyzer, W. G., "Engineering and Scientific High-Speed Photography," MacMillan (1962).
7. Courtney-Pratt, J. S., "Review of Methods of High-Speed Photography," Reports on Progress in Physics **20**, 379 (1957).
8. Lunn, George H., "A General Survey of High-Speed Photographic Techniques," J. S. M. P. T. E. **71**, 915 (1962).
9. Kapany, N. S., "Role of Fiber Optics in Ultra-High-Speed Photography," J. S. M. P. T. E. **71**, 75 (1962).
10. Hauser, S. M. et al., "A True Kerr-Cell Framing Camera," J. S. M. P. T. E. **71**, 440 (1962).
11. Goss, W. C., "Kerr Cell Framing Camera," J. S. M. P. T. E. **69**, 889 (1960).

12. Earnshaw, Kenneth B. and Charles M. Benedict, "An Ultra-High-Speed Image-Dissection Camera for Photographing Strong Shock Waves," J. Res Nat. Bur. Stds. 66C, 4 (1962).

APPLICATION TO CINEMICROSCOPY

13. Courtney-Pratt, J. S. and Charles M. Huggins, "Construction and Performance of a High-Speed Cinemicrograph," Rev. Sci. Inst. 28, 4 (1957).
14. Courtney-Pratt, J. S. and D. P. C. Thackeray, "High-Speed Silhouette Micrography Using Image-Splitting Techniques," Proceedings of the Third International Congress on High-Speed Photography, Butterworths Scientific Publications, London (1957).
15. Courtney-Pratt, J. S., "High-Speed Micrography Using Image-Splitting Techniques," Proceedings of the Third International Congress on High-Speed Photography, Butterworths Scientific Publications, London (1957).
16. Courtney-Pratt, J. S., "High-Speed Photography and Micrography," Bell Laboratories Record, June (1961).
17. Zernow, L. and G. Woffinden, "The Cinemicroscopic Observation of Exploding Wires," Exploding Wires, Plenum Press, New York (1959).
18. Zernow, L. and G. E. Haover, "High-Speed Cine-Micrography and Space-Time Resolved Spectrography," Proceedings of the Third International Congress on High-Speed Photography, Butterworths Scientific Publications, London (1957).

LIGHT SOURCE

19. Courtney-Pratt, J. S., "Some Uses of Optical Masers in Photography," J. S. M. P. T. E. 70, 509 (1961).
20. D'Haenens, I. J. and D. A. Buddenhagen, "Lasers and Their Applications," J. S. M. P. T. E. 71, 828 (1962).
21. Lengyel, Bela A., Lasers, Generation of Light by Stimulated Emission, Wiley, New York (1962).
22. Shimoda, K., T. Yajima, and F. Shimaza, "High-Speed Photography Using Ruby Optical Masers," Sci. Pap. Inst. Phys. Chem. Res. (Japan) 56, 201 (1962).
23. Sewell, R. G. S., L. N. Cosner, H. W. Wedaa, and R. Gallup, "High-Speed Explosive Argon Flash Photography System," J. S. M. P. T. E. 66, 21 (1957).

24. Winning, C. H. and H. E. Edgerton, "Explosive Argon Flashlamp," J. S. M. P. T. E. 59, 178 (1952).
25. Bagley, Charles H., "Submicrosecond High-Intensity Light Source," Rev. Sci. Inst. 30, 163 (1959).

The Proceedings of the Sixth International Congress on High Speed Photography is not available at the time of writing. It was published in July 1963, by H. D. Tjeenk Willink & Zoon, N. V. (Haarlem, Netherlands). The following papers appear to be of particular interest:

26. Frungel, Frank, "Laser-Blitze in der High-Speed Photography."
27. Edgerton, Harold E., John C. Goncz, and Paul W. Jameson, "Xenon Flash Lamp Limits of Operation."
28. Zernow, Louis, and George Woffinden, "Cinemicrographic Study of Electrically Exploded Metal Foils."

N64-28220

THE EFFECT OF ACCUMULATED HYDROGEN ON CIRCUITRY IMBEDDED IN POLYURETHANE FOAM

Lester L. Mohr

INTRODUCTION

The work reported here was undertaken to determine whether bombardment of polyurethane foam by protons and a resulting accumulation of hydrogen in the foam could cause changes in the electrical characteristics of the foam which might be mistaken for changes in the electrical characteristics of circuits which had been embedded or "potted" in the foam. Assuming that protons with energy spectra similar to those of space sources might cause charges in the organic structure of polyurethane molecules, or might cause accumulation of occluded gases (mostly hydrogen or hydrogenous in nature), experiments were designed to simulate and to determine the effect of typical voltages in producing parasitic currents, directly attributable to breakdown of the foam environment, which could be confused with electrical-component damage caused by irradiation.

author

DEVELOPMENT OF HYDROGEN TREATMENT PROCEDURE

It was assumed that the proton flux stopped in the polyurethane foam, plus molecules of hydrogen formed by collision, would slowly accumulate in some of the closed cells in the foam.

The first step was to develop a method of infusing a significant amount of hydrogen into the cells of some polyurethane foam, and the simplest way to do this was to subject the foam to hydrogen gas under pressure. Foam samples were made (Figure D-9) in cylinders measuring 5.5 cm in diameter and 13 cm in length, with densities of from 8 to 10 pounds per cubic foot. Each sample in turn was placed in a chamber having a volume of about 4 cubic feet; the chamber with the enclosed sample was

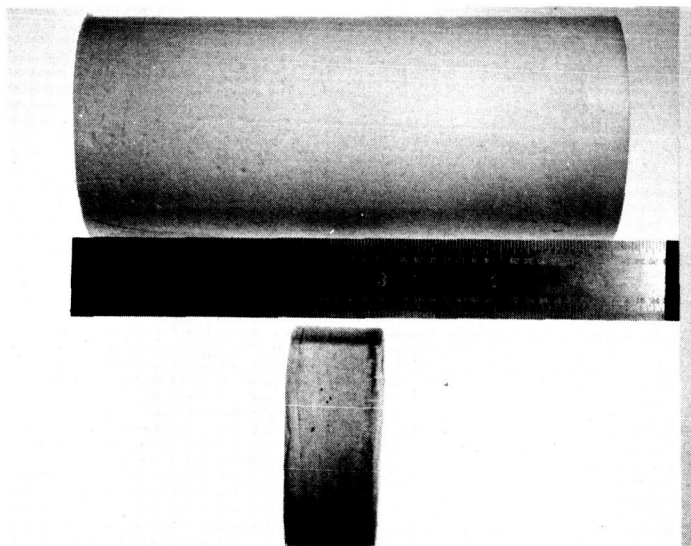


Figure D-9—Polyurethane Foam Analytical Sample,
Before and After

evacuated to a pressure usually below 50 microns of mercury for various lengths of time. When the chamber was evacuated, hydrogen was introduced until a given pressure was reached. The sample was left in the pressurized chamber for a specified period for each test run.

To determine how much hydrogen had been infused into the foam sample, an apparatus was constructed (Figure D-10) to compress the sample, force out the gas, and collect it. Figure D-11 is a photograph of the apparatus, basically a cylinder and piston with a

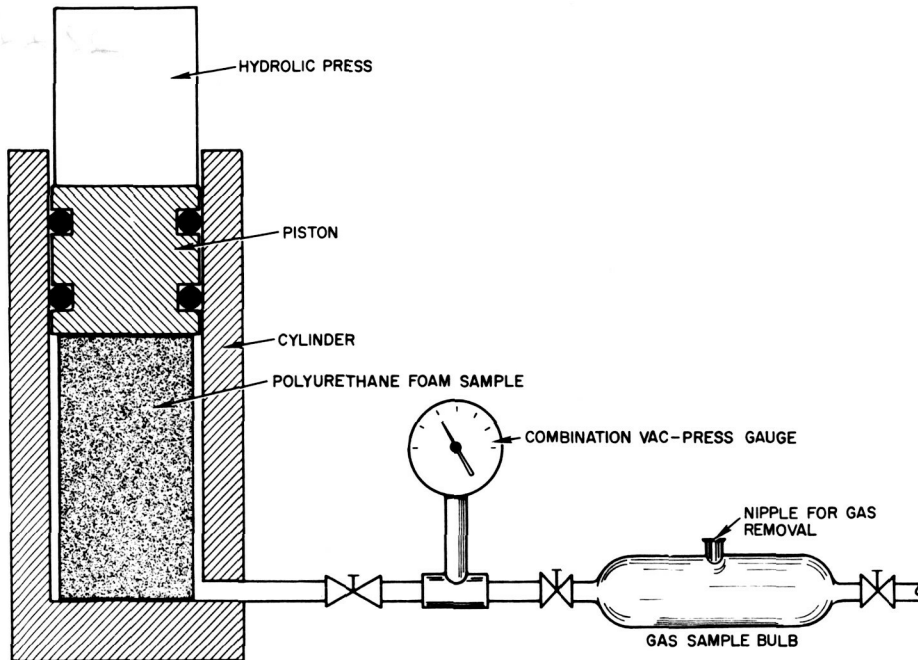


Figure D-10—Apparatus for Removal of Gases from Polyurethane Foam, Schematic Diagram

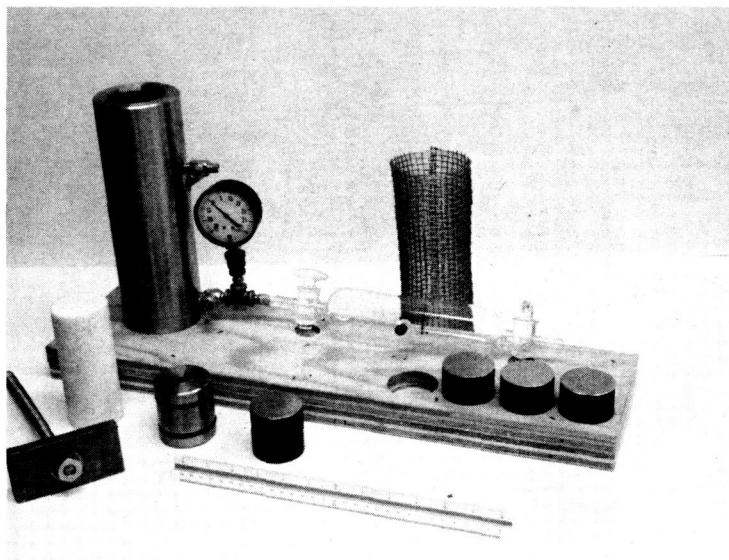


Figure D-11—Apparatus for Removal of Gases from Polyurethane Foam

Table D-2
Hydrogen Infusion Data

Run No.	Sample No.	Density of Sample (lb/ft ³)	Time for H ₂ Infusion (hours)	Pressure of H ₂ (psi gauge)	Millimoles H ₂ from sample after treatment	Notes	
2	2	7.6	0	0	0.0	Untreated sample H ₂ pressure near 1 atm.	
13	13	9.5	5	1	2.3		
10	10	8.2	3	20	7.1		
7	7	9.8	4	20	6.7		
8	8	9.4	24	20	5.2		
5	5	8.9	1	30	6.5		
4	4	8.8	3	30	6.7		
12	12	10.0	4	30	4.8		
6	6a	9.4	5	30	6.0		Immediate analysis Analysis after 2 hours outgassing
	6b	9.2	5	30	1.3		
11	11a	9.2	5	30	8.1		Immediate analysis Analysis after 1-1/2 hours outgassing
	11b	9.8	5	30	3.0		
3	3	9.0	19	30	6.4		Repeat of Run #3
9	9	8.9	19	30	6.5		
1	1	8.9	48	30	10.0		
14	14	9.8	19	30	6.4	Treatment of Test Module A	
15	15	9.8	5	30	4.8	Treatment of Test Module B	
16	16	9.5	19	30	3.0	Treatment of Test Module C	
17	17	10.0	19	30	7.0	Treatment of Test Module D	

gas-collecting bulb attached so that it can collect the gas evolving from the compressed foam sample. Each sample was put into the cylinder; the gas-tight piston was placed above it and forced down by a hydraulic press, compressing the sample to one-tenth its original volume. Gas forced from the sample flowed into the collecting bulb, and the gas pressure was measured with an attached gauge. The gas was analyzed by means of two Fisher gas partitioners, which are basically gas chromatographs which can be used to find the percentage of hydrogen when the carrier gas is argon. Given the volume of gas in the bulb, the pressure of gas, the fraction of hydrogen in the sample, and the room temperature, the millimoles of hydrogen expressed from the sample can be calculating by using the ideal gas law.

Table D-2 gives the results of many test runs performed in the manner described. The amount of hydrogen infused into the foam sample does not appear to be directly proportional to the length of time or the amount of pressure to which the foam is subjected. However, only one run was performed at a pressure below 20 psi gauge; it is possible that saturation is reached at a point below 20 psig, so that no proportionality was seen. Pressure of 30 psi gauge for any period over an hour was sufficient to infuse a considerable

amount of hydrogen into the sample; 6 millimoles of hydrogen or more was infused at this pressure, representing from 40 to 75 percent of the gas removed from the sample. This amount was sufficient for testing purposes, and 30 psi gauge was chosen as the pressure to be used for testing the potted modules.

CONSTRUCTION OF TEST MODULES

To determine the effect of hydrogen in closed cells of polyurethane foam upon circuitry embedded in the foam, four test modules were constructed with open circuits extending into the foam environment. Each module consisted of a printed circuit board measuring 5 by 2 inches with six open circuits on it; two circuits were gold strips, the other four wires on standoffs (Figure D-12). The parallel conductors were 1/32 to 1/16-inch apart. After completion of the circuits, the entire board was potted in polyurethane foam, the finished module (Figure D-13) measuring 5 inches in length, 2 inches in width, and 1 inch in depth.

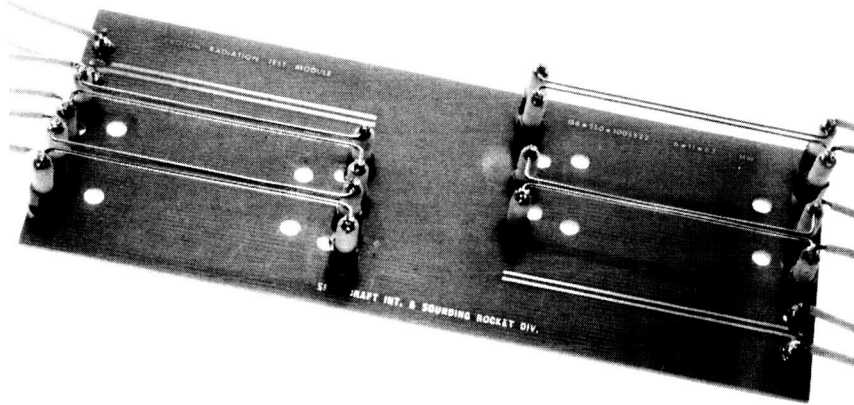


Figure D-12—Test Module Before Potting



Figure D-13—Test Module After Potting

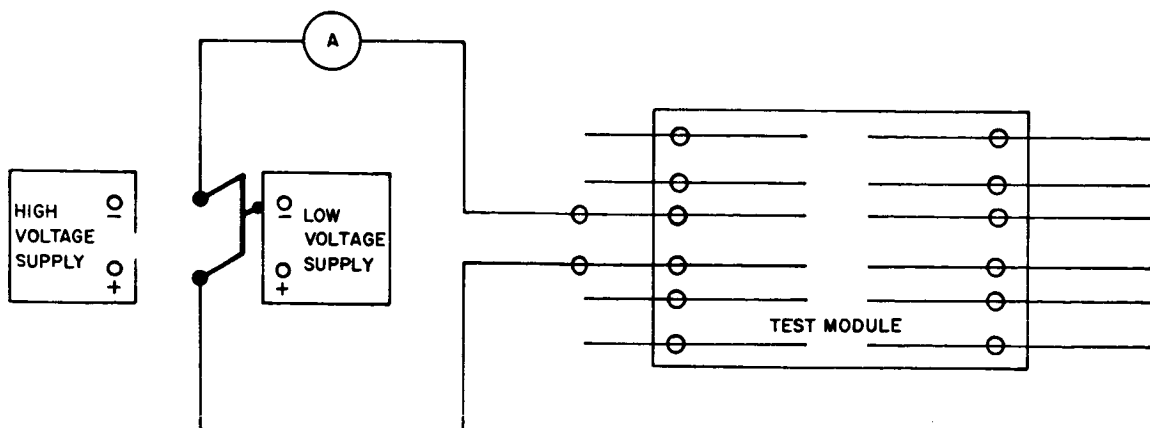


Figure D-14—Circuit for Measurement of Current in Test Modules

TESTING OF MODULES BEFORE TREATMENT

A simple circuit (Figure D-14) was devised to determine whether parasitic circuits might occur when hydrogen accumulates in the foam between two conductors. For purposes of comparison, the current on the modules was measured before and after treatment with hydrogen under pressure. Potentials of 10, 20, 80, 500, and 1000 volts were obtained from a low-voltage dc power supply or a high-voltage supply. Currents were detected by a Hewlett & Packard 425A voltmeter-ammeter, using the millimicroampere range to avoid interference which occurred when the micromicroampere range was used. When the circuits on the modules were tested before treatment, no significant currents were found even when the 1000-volt potential was used.

TREATMENT AND TESTING OF MODULES

After the untreated modules had been measured for leakage currents, they were treated with hydrogen under the conditions shown in Table D-2. Cylindrical foam samples for gas analysis were placed in the pressure chamber along with the modules so that the amount of hydrogen in the modules could be determined. After treatment, the module was removed from the pressure chamber and its current was measured within 10 minutes. Results of test runs 11 and 6 showed that considerable hydrogen remained in the foam samples after 2 hours had elapsed; therefore, most of the hydrogen probably remained in the accompanying modules after the 10-minute measuring period. Measurements of current after hydrogen treatment did not differ significantly from measurements before treatment, remaining in the 10^{-9} ampere range they had before being subjected to pressure. Currents of this magnitude are insignificant and would not affect the function of circuits in a satellite.

PROTON IRRADIATION OF MODULE

Originally, plans included proton bombardment of an analytical sample and a test module to determine how much hydrogen might be produced by such a bombardment, and what effect it would have on an operation of the circuit. However, calculations attempting to approximate the range of protons of about 5 Mev (the spectrum available to us) indicated that, at this energy, proton penetration into the polyurethane would be about 0.3 cm. To achieve deeper penetration into the sample, a much higher energy proton would need to be used, and protons of such energy were not available for experimentation.

HYDROGEN ACCUMULATION IN POLYURETHANE FOAM

It appears doubtful that a significant amount of hydrogen would accumulate in polyurethane foam under conditions which a satellite would meet in space, unless it encountered sustained proton storms. Generally no attempt is made to make the satellites gas-tight; therefore, any hydrogen produced in the foam would be likely to diffuse from the foam. As the range of protons of greatest flux in space (low-energy particles) is very short, any substance surrounding the foam-embedded circuitry probably would prevent the protons from reaching even the foam. Very rough calculations indicate that it might take a great length of time to accumulate a significant amount of hydrogen in the foam, even if the foam were completely exposed to incident radiation and sealed in a gas-tight container.

CONCLUSIONS

It seems clear that accumulation of hydrogen in the polyurethane foam environment of satellite circuitry would have no effect on the circuitry. However, hydrogen would probably never accumulate to a significant extent. The results of this experiment certainly do not rule out other changes in the electrical circuits, such as carbonized thermal spikes, which might occur because of radiation, but hydrogen accumulation appears to be no problem.

The author is grateful for the technical assistance of John Unger, Space Power Technology Branch, who performed most of the hydrogen analysis.

THE EFFECT OF LOW-ENERGY PROTONS ON SEMICONDUCTOR JUNCTIONS

R. L. Johnston and R. B. Heller

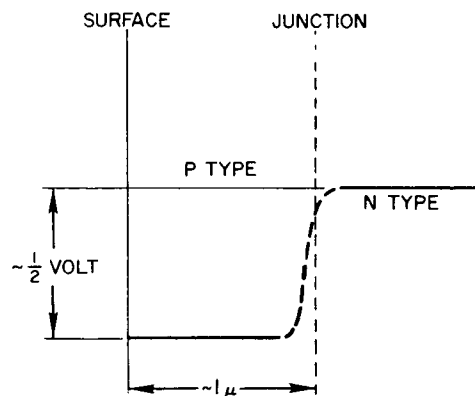
INTRODUCTION

It has been observed experimentally that silicon (Si) solar cells, when bombarded with heavy charged particles, suffer a decrease in their short-circuit current (I_{sc}) and also in their open-circuit voltage (V_{oc}).⁽¹⁾ It has been suggested that the decrease in V_{oc} is due to a function layer effect. The initial trial calculation was to assume that the number of displacements produced by a 5-Mev proton, for instance, would be equal to the change in the concentration of donor or acceptors in the semiconducting materials. Using the ordinary expression for the capacitance in terms of these parameters, we have calculated the magnitude of the change in capacitance, assuming 10^2 protons $\text{-cm}^{-2}\text{-sec}^{-1}$ for a period of 1 year which could then be used as an experimental check. However, the magnitude of the change in capacitance due to displacements is too small to be detected by present precision instruments; neither would it account for the change in voltage observed. Also, if the protons (hydrogen) are considered as introducing a material of different dielectric constant into the junction capacitance, the quantities produced during a year's irradiation appear insufficient to produce a measurable change in the observables.

Next we considered that the effect might be due to a preferential accumulation of hydrogen in the region of the junction. A possible explanation for the accumulation of hydrogen at the junction is to consider the interaction of a proton with the potential step representation of the solar cell shown in Figure D-15.

The permanent damage that occurs is usually caused by particles that have been neutralized at an energy large in comparison with the step at the junction. Thus, the problem appears to be one of diffusion, with possibly slightly different diffusion coefficients on each side of the junction.

In considering the diffusion of hydrogen in Si, the following observations have been made. Several investigators, Johnson⁽²⁾, Thurmond et al.⁽³⁾, and Kaiser and Keck⁽⁴⁾, have found that many so-called "pure" crystals may contain



D-15-Potential Step of a Solar Cell

hydrogen and oxygen in concentrations as high as 10^{19} cm^{-3} if the crystal is grown in hydrogen atmosphere. Reiss⁽⁵⁾ has shown that the hydrogen may reside in interstitial positions in a monatomic state which would not be expected to affect the electrical characteristics of the cells. Few, if any, of the measurements reported include any information on hydrogen impurity content.

In an attempt to make some connection between measured parameters and the hydrogen content, some P/N cells with measured I-V characteristics were placed in a test chamber which was first evacuated (~ 10 microns of Hg) and later pressurized with 30 psig of 99.8-percent pure hydrogen for 18 hours. The I-V characteristics were measured within 5 hours after removal from the hydrogen atmosphere. The results are tabulated below:

Control Cells (3)			
Characteristic	Number which Increased	Number which Decreased	Average Change
I_{sc}	3	0	2.2 ma
V_{oc}	2	1	1.6 mv
P. P.	0	3	0.7 mw

Test Cells (8)				
Characteristic	Number which Increased	Number which Decreased	Average Change	Average Change in Percent
I_{sc}	7	1	2 ma	10
V_{oc}	2	6	-11 mv	2
P. P.	0	8	-1.1 mw	5

Measuring the capacitance of one cell 25 hours after removal from the hydrogen chamber, then pumping it down to $\sim 10^{-4}$ atm and exposing it to the atmosphere, produced no change in capacitance. Taking the same cell, pumping on it overnight (10μ), placing it under 30 psig of 99.8-percent pure hydrogen for 6 hours, and immediately measuring its capacitance over the same range of applied voltages, no change was observed.

Baruch and coworkers⁽⁶⁾ reported the occlusion of hydrogen at the end of the proton range in Si; we had no way of trying to test whether the formation of gas bubbles would cause a decrease in V_{oc} . If the hydrogen bubble is formed in the region of the junction, it is in a relatively strong field ($\sim 5 \times 10^4$ volts/cm) and, being polarizable, would tend to reduce the self field and hence the equivalent voltage across the junction. Trial calculations along this line led to inconclusive results.

Up to the present time we have not been able to show how the presence of hydrogen would produce the experimentally observed effect.

Bibliography

1. Diebold, J. W., Radiation Effects on Solar Cells. Thesis School of Engineering W. P. A. F. B., Ohio.
2. Johnson, O. H., Chem. Revs. 51, 431 (1952).
3. Thurmond, Guldner & Beach, Electrochem. Soc. J., 106, 603 (1957).
4. W. Kaiser, P. H. Keck, J. Appl. Phys., 28, 882 (1957). (1956).
5. Reiss, H., J. Chem. Phys., 25, 681 (1956).
6. Baruch, Constatin, Pfistar & Saintesprit, Disc. Far. Soc., 31, 76 (1961).

Excellent bibliographies on the many aspects of semiconductors are at the end of the chapters of the book Semiconductors, edited by Hannay, American Chemical Society Monograph Serial No. 140, published by Reinhold Publishing Company.

APPENDIX

I. SOLAR CELL CHARACTERISTICS

	Page
SHELF LIFETIME OF GALLIUM ARSENIDE SOLAR CELLS*	I-1
R. L. Johnston	
TEMPERATURE EFFECTS ON IRRADIATED SOLAR CELLS*	I-7
B. T. Cunningham, R. L. Sharp, and L. Slifer	

II. NATIONAL SCIENCE FOUNDATION HIGH-ABILITY
SECONDARY-SCHOOL STUDENTS IN SUMMER WORKSHOP

	Page
A FLUXGATE MAGNETOMETER	II-3
T. B. Silliman	

ILLUSTRATIONS

Figure	Page
I-1	Solar-Cell Vacuum Bakeout, Schematic Diagram I-1
I-2	Characteristic I-V of a GaAs Solar Cell I-1
I-3	Typical GaAs Solar Cell I-2
I-4	Microphotographs of Junction of GaAs Solar Cell I-3
I-5	X-Ray Photographs of Sample GaAs Solar Cells After Lapping I-4
I-6	Experimental Equipment for Monitoring Temperature Effect on Electrical Characteristics of Irradiated Solar Cells I-8
I-7	Experimental Equipment, Interior View I-9
I-8	Change in Open-Circuit Current with Temperature for Three Types of Irradiated Silicon Solar Cells I-12
I-9	Change in Short-Circuit Current with Temperature for Three Types of Irradiated Silicon Solar Cells I-12
I-10	Change in Maximum Power with Temperature for Three Types of Irradiated Silicon Solar Cells I-13
II-1	George Williams, Wheaton High School Student, at Workshop Session II-1
II-2	Single Toroidal Core Magnetometer II-3
II-3	Fluxgate Magnetometer II-4

TABLES

Table	Page
I-1	Percentage Change in Short-Circuit Current for Irradiated Solar Cells Under Tungsten or Solar Illumination I-10
I-2	Percentage Change in Short-Circuit Current for Irradiated Solar Cells at Varying Temperatures I-13
I-3	Percentage Drop in Maximum Power for Irradiated Solar Cells at Varying Temperatures I-13

SHELF LIFETIME OF GALLIUM ARSENIDE SOLAR CELLS

R.L. Johnston

N64-28221

The Solar Power Sources Section has observed a deterioration in operating characteristics of some of its GaAs solar cells during their shelf life. It was suggested that the possible causes of this deterioration might be checked during the Summer Workshop period. Possible causes are:

- Surface and volume hygroscopic effects
- Postmanufacture continued diffusion of the dopant
- Poor electrical contacts

The first item was checked experimentally accomplished by using a strip heater in a bell jar, shown schematically in Figure I-1. A series of bakeouts of several hours' duration was done under vacuum at room temperature, 50°C, 100°C, and 200°C. After each temperature, the I-V characteristics were measured. These curves for a single cell are shown in Figure I-2.

The curve labeled 4 is the initial I-V characteristic as well as the I-V curve for room temperature, 50°C, and 100°C. The curve labeled 3 is after heating to 200°C and cooling to 50°C at 15 microns, then letting up to atmospheric pressure while cooling to room temperature. The curve labeled 2 represents the same cell, scrubbed with trichlorethylene and rinsed with alcohol; the curve labeled 1 is after the cell had been

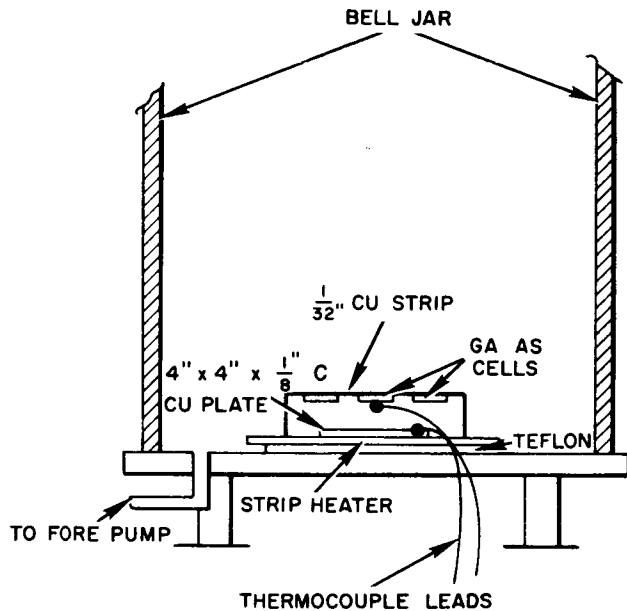


Figure I-1 - Solar-Cell Vacuum Bakeout, Schematic Diagram

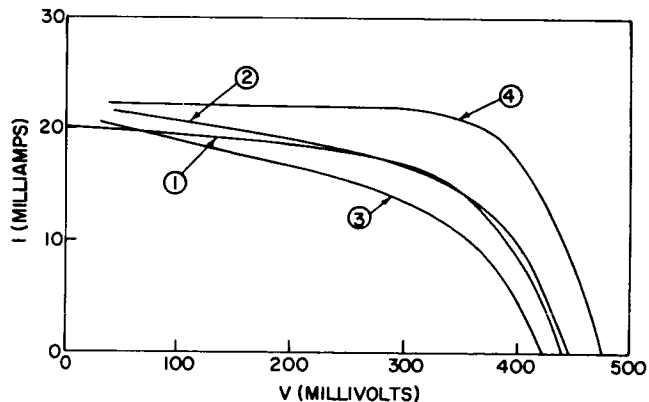


Figure I-2 - Characteristic I-V of a GaAs Solar Cell

lapped, reducing its surface area, which is expected to reduce the short-circuit current (I_{sc}). It appears that, until the temperature of 200°C was reached, no change resulted within the experimental accuracy, and then only enhanced reduction in the output. The temperature-reading thermocouple was not soldered to the cell, but was only a light pressure contact, so that the temperature reading of the thermocouple may have varied considerably from the surface temperature of the cell.

Microscopic examination of the top contacts indicated that they were good. The only observations of the lower contacts were made where the cells were lapped, in an attempt to measure the junction depth. Where observed, they appeared satisfactory. Figure I-3 is a sketch of a solar cell showing where they were lapped, indicated by the dashed line.

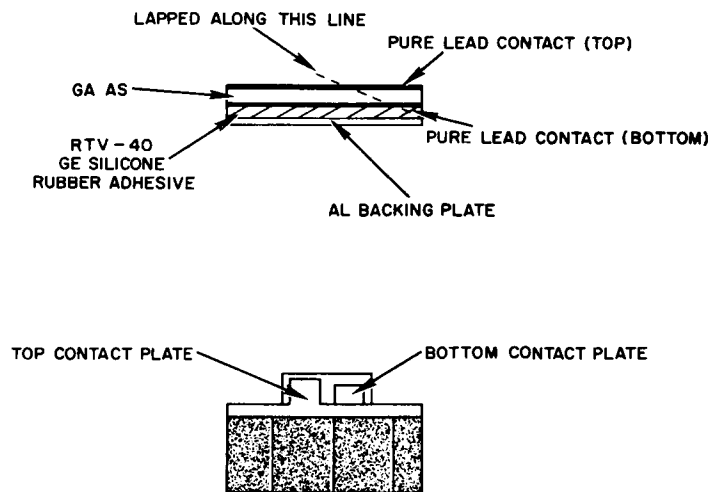
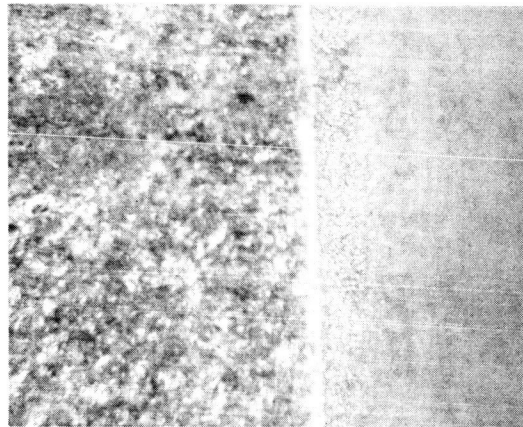


Figure I-3—Typical GaAs Solar Cell

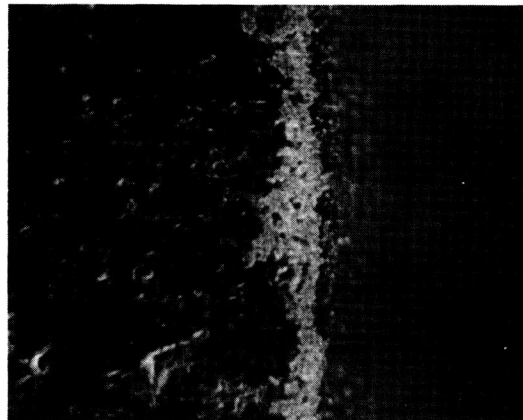
We attempted to measure the junction depth by lapping the cells at 2 - 3 degrees. No accurate measurements or positive identifications of the junction could be made. The angle was increased to 6 - 7 degrees; as no junctions were apparent, several etchants and stains were tried without success. Finally, using a method suggested by RCA (1), we were able to delineate the junction by chemiplating with copper. The plating is accomplished by placing a drop of stain on the junction and illuminating it with a bright light. The stain is a solution of copper sulfate (Cu_2SO_4) with 1 percent by volume of hydrofluoric acid (HF). The light produces electron-hole pairs which in the region of the junction can neutralize the Cu_2 and SO_4 ions, plating the Cu_2 onto the n-type material. The initial measurements were made on cells lapped with 600-grit abrasive paper. This produced an irregular edge, making it difficult to decide exactly where the junction was.

Photomicrographs of the plated junction for the 600-grit finish are shown in Figures I-4a and I-4b, of nominal 300x and 500x magnification respectively. The sketch I-4c shows the photographic arrangement with the dashed line indicating the rounded edge produced by the nap of the cloth.

The cells were later polished on a metallurgical wheel, a cloth with 6-micron diamond paste and oil. This more finely polished surface gave a well-defined junction; however, the nap of the cloth rounded the top edge, resulting in a great uncertainty as to where the top surface of the cell was supposed to be. As such, the accuracy of the measurements



A) 300X



B) 500X

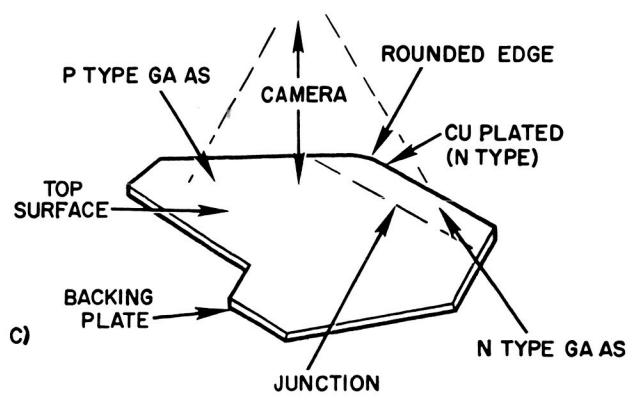


Figure I-4—Microphotographs of Junction of GaAs Solar Cell

is of the same order of magnitude. The results of the measurements are:

Cell #93	2.3 microns
Cell #12	1.6 microns

The uncertainty, for the reasons previously stated, is about 100 percent.

A more accurate method is described by McDonald and Goetzberger (2) in which measurements as small as 0.2 micron with ± 0.04 -micron accuracy can be made. Had sufficient time been available, this improved method would have been used. The method made use of presently available equipment.

After the cells were lapped, they frequently appeared to be broken more in the substrate than on the surface. Some of the breaks could be traced to surface cracks, others could not. X-ray photographs (Figure I-5) were taken in an attempt to determine whether the lapping produced any of the additional fractures; however, the presence of a nonuniform lead backing prevented the obtaining of revealing exposures.



70



71



47



103

Results of the study indicate no correlation between the suggested causes and the resulting deterioration of the GaAs solar cells. It is therefore concluded that some other phenomenon is responsible for the short "shelf life" of some of the cells.

The manufacturer has express interest in this phenomenon, asking that a number of the poor cells be returned so that a separate investigation may be conducted.

The cooperation of many GSFC personnel is greatly appreciated, especially for their advice, use of equipment, and speedy procurement of necessary items. Special thanks are due Luther Slifer and Brian Cunningham, Space Power Technology Branch; Dr. John Schutt, Thermal Systems Branch; James Munford, Fabrication Division; and Charles Madison and C.P. Michael of the Test and Evaluation Division.

Figure I-5—X-Ray Photographs of Sample GaAs Solar Cells After Lapping

REFERENCES

- (1) Bob Gold, RCA, Somerville, N.J., private communication.
- (2) McDonald, B. and Goetzberger, A., *Electrochem. Soc. J.* , 109, 141, 1962

BIBLIOGRAPHY

Transistor Technology, edited by H.E. Bridgers, J.H. Scaff and J.N. Shive. Van Nostrand, Princeton, N.J. (1958)

Electrochemistry of Semiconductors, edited by P.J. Holmes. Academic Press, N.Y. and London (1962)

Both the above contain extensive bibliographies.

N64-28222

TEMPERATURE EFFECTS ON IRRADIATED SOLAR CELLS

B.T. Cunningham, R.L. Sharp, and L. Slifer

INTRODUCTION

Numerous studies have been conducted to determine the effect of electron irradiation on silicon solar cells. In order to extend the knowledge already gained in this area, an experiment was undertaken to investigate the electrical characteristics of irradiated silicon solar cells as a function of temperature. Consultation with individuals familiar with satellite environments indicated that a temperature range of -100°C to 125°C would be appropriate.

During October and November 1962, silicon N/P and P/N "state-of-the-art" solar cells with different base resistivities were purchased from nine different manufacturers. The I-V characteristics of these cells were measured in sunlight and under a tungsten source (2800°K) at or near room temperature. Some cells from each manufacturer were then set aside as control units, some were set aside for thermal and mechanical tests, and thirty cells from each manufacturer were forwarded to the Naval Research Laboratory, Washington, D.C., for irradiation. Fifteen from each source were irradiated with 1-Mev electrons in dosages varying from 10^{11} to 10^{16} electrons/cm². The room temperature characteristics of these irradiated cells were obtained (1) and the cells were then made available for this temperature-effects study.

EQUIPMENT

The experimental equipment used to collect the data is shown in Figure I-6. By way of explanation, the unit consists of a 9-inch-diameter aluminum chamber sealed off at one end with a 3-cm circulating water bath blocked on both sides by pieces of plexiglass 1/4-inch thick. The water bath served as a filter for the tungsten source by cutting out a large amount of the undesirable infrared. The other end of the chamber was fitted with a "thermal finger", as shown in Figure I-7, which contains a 340-watt heater and 1/4-inch aluminum tubing for transferring liquid nitrogen. The front of the thermal finger, which is a relatively large heat sink, acts as a base for the test plate on which the cells are mounted.

The light source used in the experiment consisted of a 300-watt tungsten-filament reflector flood bulb. This unit was calibrated for a color temperature of 2800°K . The

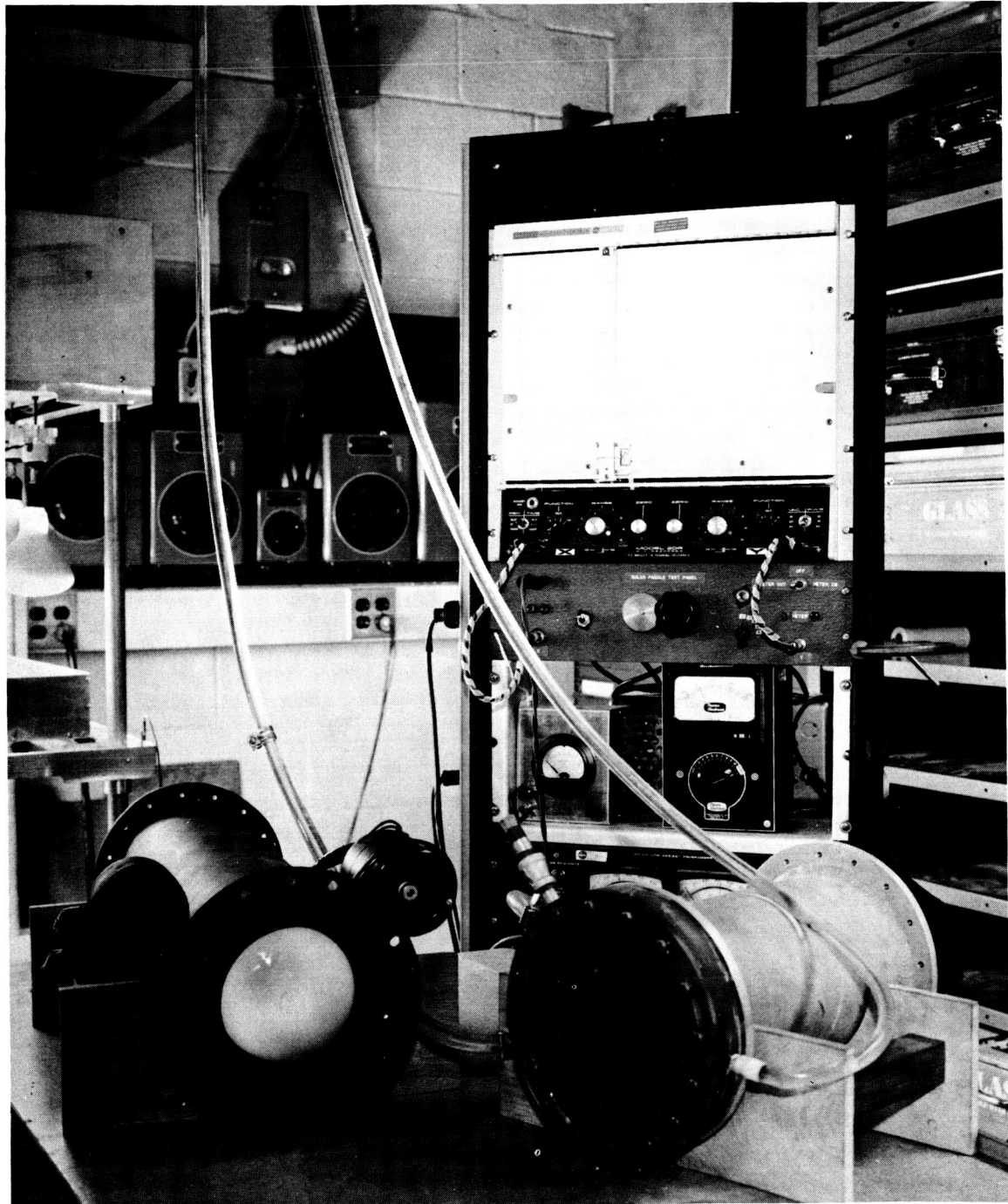


Figure I-6—Experimental Equipment for Monitoring Temperature Effect on Electrical Characteristics of Irradiated Solar Cells

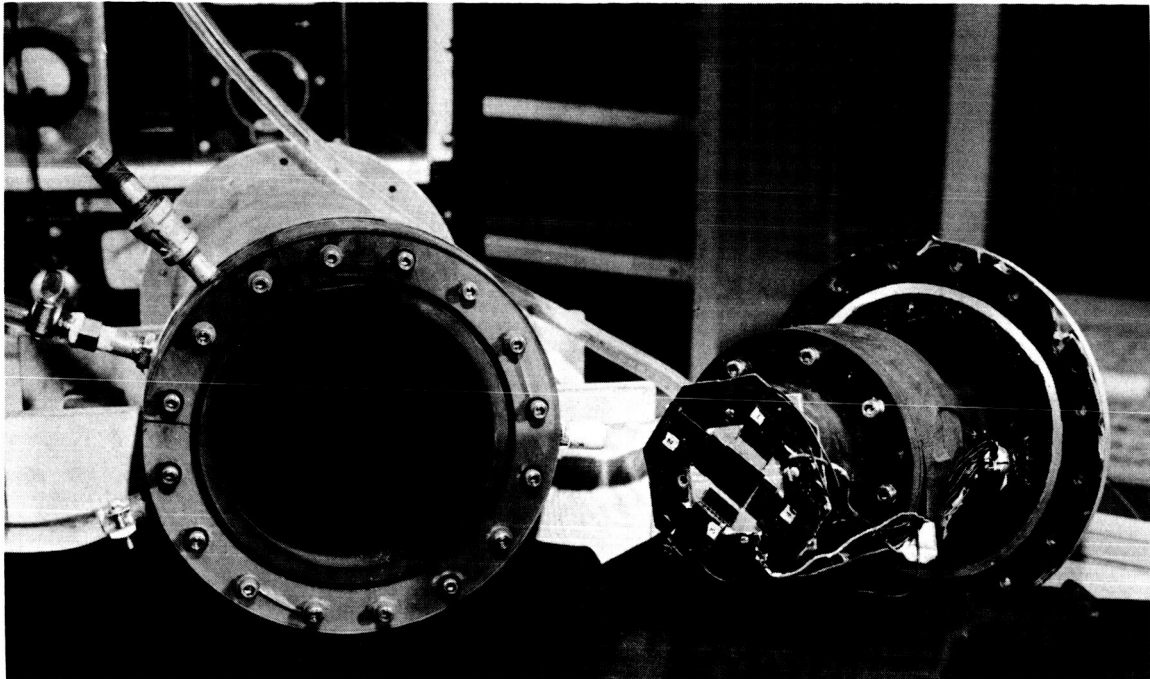


Figure I-7—Experimental Equipment, Interior View

bulb was housed in a cylindrical chamber, shown in Figure I-6, to prevent stray light from affecting the test. The bulb platform was mounted on a worm screw so that the intensity of the incident light could be adjusted by moving the source closer to or further away from the cells under test.

All surfaces exposed to the light source were coated with optical-quality black paint to prevent reflections which would disturb the uniformity of illumination. After assembly, the 6.5-square-inch test area was checked for uniformity using a standard solar cell as a detector. The uniformity of illumination was found to be within 2 percent.

When in operation, the chamber was evacuated to 35 micrometers of mercury in order to prevent frost from accumulating on the cells at low temperatures. Temperatures were monitored using three copper-constantan thermocouples calibrated over the temperature range of the tests to an accuracy of $\pm 1^{\circ}\text{C}$. An attempt was made to determine the cell-junction temperature as closely as possible. To this end the thermocouples were placed on the top (on the contact strip) and on the bottom of the cells, first, to determine if a temperature gradient existed, and second, to find out what its magnitude might be. The data obtained for the temperature gradient led to inconclusive results and further work is under way in this area. The thermocouple outputs were initially measured with a potentiometer. Later, a deflection-type pyrometer was employed, which gave results nearly as accurate as those from the potentiometer with a great saving of time. At the extremes of the temperature range, an accuracy of $\pm 5^{\circ}\text{C}$ was obtained. This accuracy improved to within $\pm 1^{\circ}\text{C}$ as room temperature was approached.

The solar-cell electrical characteristics were monitored by varying the lead resistance across the cell between 1 ohm and 2500 ohms. The current flowing with the 1-ohm load across the cell is, by accepted definition, short-circuit current, I_{sc} , while the voltage across the 2500 ohms is considered to be open-circuit voltage, V_{oc} . The complete I-V characteristics were recorded on an X-Y plotter to obtain a permanent record.

PROCEDURE AND DISCUSSION

Several months had elapsed since previous measurements had been made, hence up-to-date sets of I-V characteristics were obtained for all cells using both the filtered tungsten source and sunlight. The sun intensity was monitored with an Eppley 50-junction normal-incidence pyrhelometer. The short-circuit current of the cells was then linearly normalized to short-circuit current for a sunlight intensity of 100 milliwatts/cm². These normalized current readings were compared to the short-circuit current readings obtained from measurements made on the cells at room temperature, using the tungsten source with the illumination level set at 100 milliwatts/cm² sunlight equivalent. A standard solar cell with a known short-circuit current at 100 milliwatts/cm² sunlight input was used in setting the intensity level of the tungsten simulator to obtain such the same short-circuit current. It was found that, under the tungsten source, the same readings were obtained for nonirradiated cells, as in sunlight regardless of manufacturer. However, for N/P solar cells irradiated with dosages greater than 10¹³ electrons/cm², the percentage of change as seen under tungsten differed significantly from that seen under sunlight. For P/N solar cells, a significant difference was observed for dosages greater than 10¹¹ electrons/cm². The percentage of change in short-circuit current for solar cells irradiated at 10¹⁶ electron/cm², as measured using tungsten and sunlight, is shown in Table I-1, which categorizes the solar cells as to the base resistivity and type.

These results show the extent to which the shift in spectral response of the solar cells caused by electron irradiation (2) is a major factor to be considered when analysing data obtained from measurements on irradiated cells using a source other than sunlight. In interpreting the information presented here, it must be emphasized that tungsten is a "red" source: that is, the spectrum is a maximum in the infrared region, whereas the sun's spectrum peaks in the ultraviolet. As electron irradiation degrades the red and of the solar-cell spectral response, radiation degradation appears worse under tungsten as a source is that, as the temperature is varied, the solar-cell spectral response is changed. This topic will be treated fully in a more detailed report to follow later in 1963.

Table I-1

Base Resistivity	Type	Change Under Tungsten (%)	Change Under Sunlight (%)
10 ohm-cm	N/P	37	26
1 ohm-cm	N/P	49	37
1 ohm-cm	N/P	57	40
1 ohm-cm	P/N	76	63

Mounting of the cells was initially accomplished by heating a pre-tinned copper plate to the solder melting point. Four solar cells were then placed on the plate and the unit was removed to a cool heat sink as quickly as possible. Results using this method were poor in that, first, electrical measurements before and after mounting indicated changes in short-circuit current to be as much as 4 percent, and second, cells under test would occasionally shatter when undergoing temperature changes. To alleviate this problem, conductive epoxy was used between the cell and the test plate. Curing of the epoxy at 60°C had no measurable effect on the electrical characteristics of the cells; the epoxy held throughout the test temperature range, and no cracking of the cells was observed after institution of its use.

Cells to be tested were selected at random in groups of four and mounted on the copper plate. The cells were then placed in the chamber and the source intensity was adjusted to the "prechamber installation" value. The chamber was evacuated and the temperature lowered to -110°C. Because of the comparatively large heat sink, it was found suitable to simply let the temperature drift upward while readings were taken at the desired temperature intervals. In most cases, all four I-V curves could be obtained with a variation of only $\pm 2^\circ\text{C}$ from the desired measuring point. I-V curves were then analyzed for short-circuit current, open-circuit voltage, and maximum power.

DATA ANALYSIS

The data obtained from these measurements and its analysis and interpretation will be presented in three parts. Each part concerns one of the solar-cell parameters in the following order: open-circuit voltage; short-circuit current; maximum power.

Open-Circuit Voltage—Figure I-8 shows that, except for extremely low values of temperature, the open-circuit voltage for both irradiated and nonirradiated (control) cells decreased linearly with temperature. The coefficient of open-circuit voltage change with temperature varied between -2.22 and -2.59 millivolts per degree Centigrade, and did not appear to be related to the level of irradiation. The decrease in open-circuit voltage after a dosage of 10^{16} electrons/cm² was approximately 95 millivolts for N/P solar cells and 150 millivolts for the P/N type. These values were not dependent on temperature.

Short-Circuit Current—Figures I-9a, I-9b, and I-9c show the increase of short-circuit current with temperature for P/N solar cells, N/P solar cells with 1 ohm-cm base resistivity, and N/P cells with 10 ohm-cm base resistivity, respectively. Characteristics of N/P cells with base resistivity less than 1 ohm-cm were found to be very similar to those with base resistivity of 1 ohm-cm, and therefore are not shown. The short-circuit current vs. temperature curves were not linear, but could be approximated by linear relationships over a small temperature range, for example, in Figure I-9a, between 0°C and 100°C the coefficient of short-circuit current with temperature would be approximately 75 microamperes per degree Centigrade for a P/N cell irradiated to 10^{16} electrons/cm².

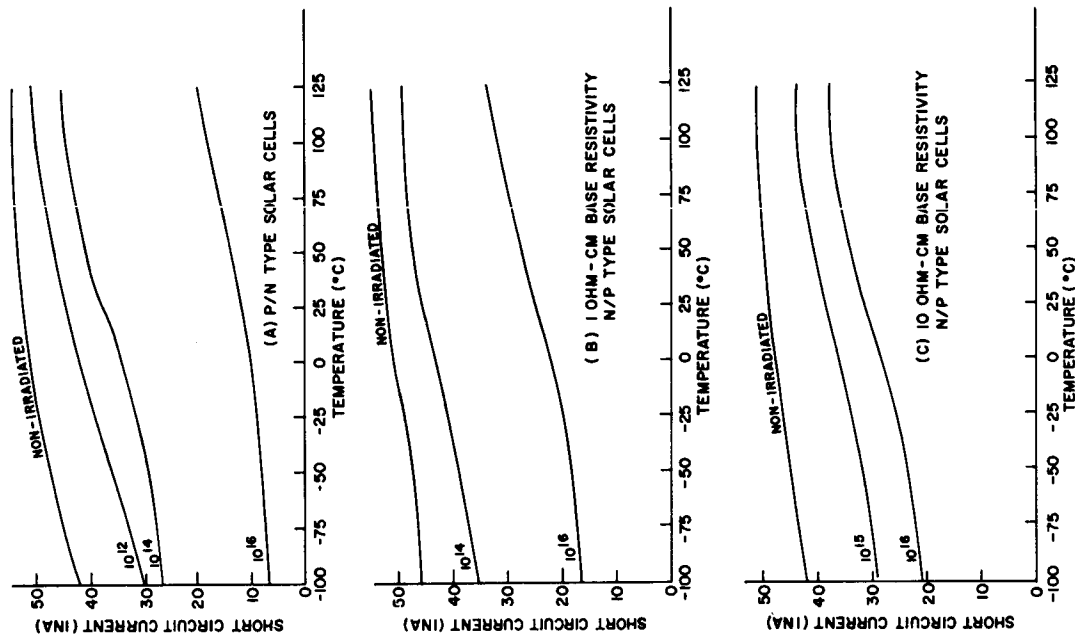


Figure 1-9—Change in Short-Circuit Current with Temperature for Three Types of Irradiated Silicon Solar Cells

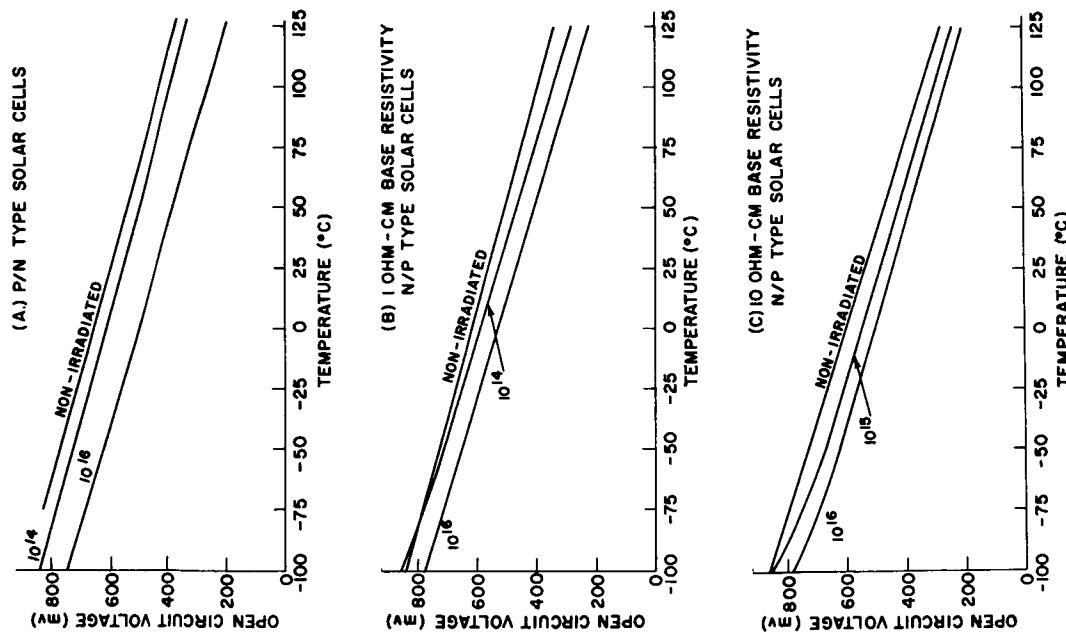


Figure 1-8—Change in Open-Circuit Current with Temperature for Three Types of Irradiated Silicon Solar Cells

Table I-2

Base Resistivity	Type	Percent Drop in Short Circuit Current		
		At -50°C	At 25°C	At 100°C
1 ohm-cm	P/N	84	78	68
21 ohm-cm	N/P	62	53	41
10 ohm-cm	N/P	47	36	26

Table I-2 illustrates the percentage drop in short-circuit current after a dosage of 10^{16} electrons/cm² at temperatures of -50°C, 25°C, and 100°C. It may be seen from this table and from the graphs of Figure I-9 that, for the entire temperature range between -100°C and 125°C, the percentage drop in short-circuit current was

greatest in the P/N cells and least in the higher base-resistivity N/P cells.

MAXIMUM POWER

Figures I-10a, I-10b, and I-10c show the variation in maximum power with temperature for P/N solar cells, N/P cells with 1 ohm-cm base resistivity, and N/P cells with 10 ohm-cm base resistivity, respectively. These graphs indicate that, in general, maximum power decreases for temperatures above -50°C. Below this temperature, maximum power is observed to increase, decrease, or remain unchanged, depending on the cell; in most cases the variation is small. Thus, maximum power does not change linearly with temperature.

Table I-3 illustrates the percentage drop in maximum power

Table I-3

Base Resistivity	Type	Percent Drop in Maximum Power (°C)		
		-50	25	100
1 ohm-cm	P/N	88	85	84
1 ohm-cm	N/P	65	57	53
10 ohm-cm	N/P	56	49	54

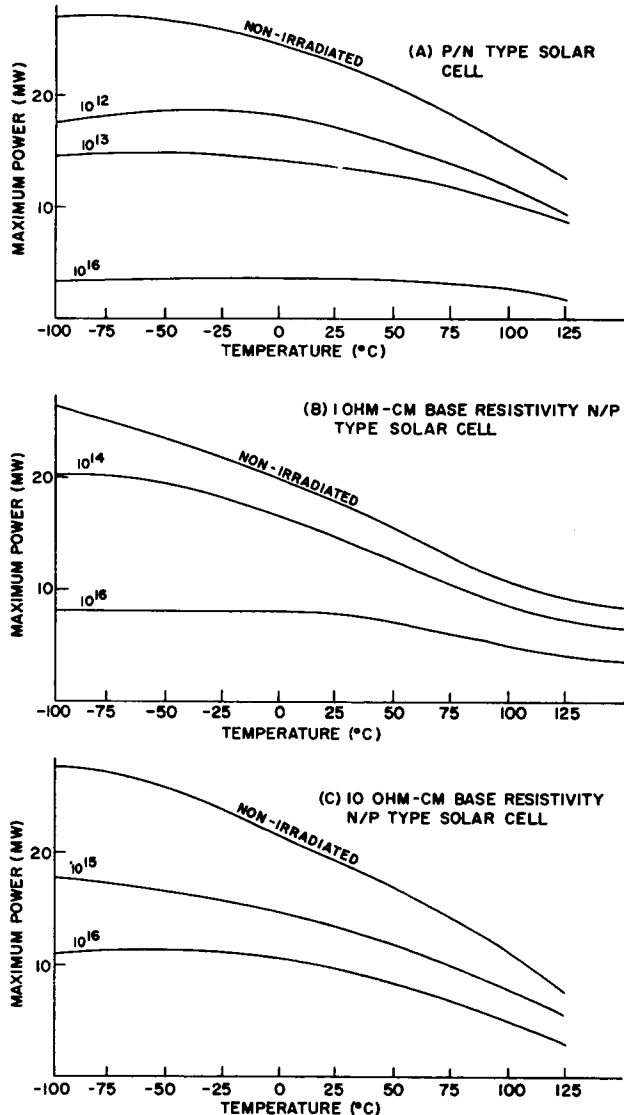


Figure I-10—Change in Maximum Power with Temperature for Three Types of Irradiated Silicon Solar Cells

after a dosage of 10^{16} electrons/cm² at temperatures of -50°C, 25°C, and 100°C. This table and the graphs of Figure I-10 show that for temperatures between -100°C and 100°C the percent drop in maximum power was greatest in P/N solar cells and least in the 10 ohm-cm base resistivity N/P cells. For temperatures between 100°C and 125°C, there appeared to be very little difference between the 1 ohm-cm and the 10 ohm-cm base-resistivity N/P solar cells. Both, however, show much less degradation than do the P/N solar cells.

CONCLUSIONS

The data obtained have led to the following conclusions:

1. Open-circuit voltage varies linearly with temperature between -75°C and 125°C for both irradiated and nonirradiated silicon solar cells. The coefficient of open-circuit voltage change with temperature is -2.22 to -2.59 millivolts per degree Centigrade.
2. For temperatures between -75°C and 125°C, irradiation does not appreciably effect the coefficient of open-circuit voltage change with temperature.
3. For temperatures between -100°C and 125°C, the degradation of short-circuit current and maximum power due to irradiation at 10^{16} electrons/cm² is greater in P/N solar cells than in the N/P type.
4. For temperatures between -100°C and 100°C, the degradation of short-circuit current and maximum power caused by irradiation at 10^{16} electrons/cm² is greater in N/P solar cells with a base resistivity of 1 ohm-cm than in the N/P cells with 10 ohm-cm base resistivity. There appears to be no significant difference between these two types of N/P cells in degradation of maximum power at temperatures from 100°C to 125°C.

REFERENCES

1. William R. Cherry and Luther W. Slifer, Solar Cell Radiation Damage Studies with 1 Mev Electrons and 4.6 Mev Protons, NASA-Goddard Space Flight Center, Greenbelt, Md. (May 27, 1963).
2. William C. Cooley and Robert J. Handa, Handbook of Space-Radiation Effects on Solar-Cell Power Systems, Washington, D.C., NASA Office of Scientific and Technical Information (1963), p. 28.

NATIONAL SCIENCE FOUNDATION HIGH-ABILITY SECONDARY-SCHOOL STUDENTS IN SUMMER WORKSHOP

A new feature of the Summer Workshop this year was the participation of four high-ability high-school students. Each was assigned to support a working team of scientists. Under the guidance of the visiting academic researchers and of Goddard permanent staff investigators, the students participated in the team's projects. Although the young men were the "leg men" of the teams, they were not errand boys; they actively participated in the research efforts and contributed in many ways to the achievement of the team goals. This was possible because of their ability to grasp new material quickly, and because of the expert instruction and guidance afforded the young men by the scientists.

This close working relationship was beneficial to all concerned. The young men were able to perform work for the scientists for which they had had no previous training. Only one of the students had had high-school physics, yet all of them were able to perform library research, calculate mathematical problems, and handle laboratory equipment. One student even constructed a fluxgate magnetometer (see following article) that was used by the scientists in their experiments on nonmagnetic materials. An indication of the student's ability to quickly grasp instruction is seen in the accompanying photograph of George Williams, Wheaton High School, explaining analytically a method for spectral irradiance at one of the workshop meetings.

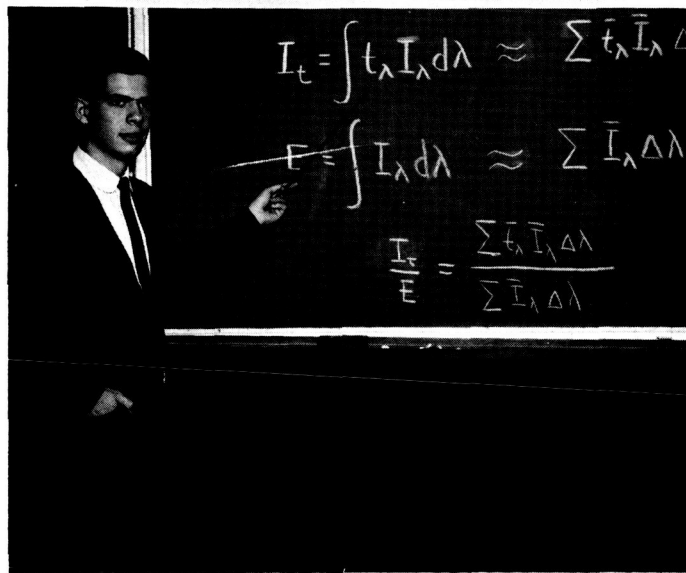


Figure II-1—George Williams, Wheaton High School Student,
at Workshop Session

The students themselves garnered many benefits from the program. Undoubtedly the experience of working closely with prominent scientists on vital work will be of enormous personal value to the students. This association, as well as the expert instruction they have received, will provide a background that will make the academic work of their senior year in high school extremely meaningful. The impact of these space-oriented students upon their fellow students in their respective high schools will be immeasurable, and there is no question but that these young men will be messengers of good will for Goddard and its work.

As one scientist commented, the use of these young men in the Summer Workshop is in accordance with President Kennedy's desire to give younger people an opportunity to work with science.

A FLUXGATE MAGNETOMETER

T. B. Silliman

The fluxgate magnetometer has two distinct advantages: first, it is very sensitive; second, it is quite portable. Figure II-2, a circuit diagram of the magnetometer, shows the two basic parts, the multivibrator and the detector. The multivibrator has two 2N43A transistors and is powered by a 12-volt mercury battery. The resistor shown has 400 ohms resistance. The multivibrator produces an alternating voltage which drives the toroidal core to magnetic saturation at a frequency of about 3000 cycles per second. The core is 4-79 permalloy and is available from Sprague, Inc. under the trade name Dynacor. Two center-tapped windings are used by the multivibrator part of the circuit, and the other two windings are used for the detector. The detector has two germanium diodes and a microammeter shunted by a 4-microfarad capacitor.

The excitation magnetic flux produced by the multivibrator in the toroidal core alternates at about 3000-cps. The voltages generated in the two detector coils are equal in magnitude and opposite in phase so that the output current in the meter is zero. When an external field is applied to the core, one side of the core has the external flux opposing the excitation flux, and the other side of the core has both fluxes aiding each other. Thus, one side is unsaturated magnetically while the other side is driven far into saturation. The result is an imbalance of voltages on the two detector coils and an output current as indicated by the meter reading.

The core was used as a probe and the meter, power supply, multivibrator

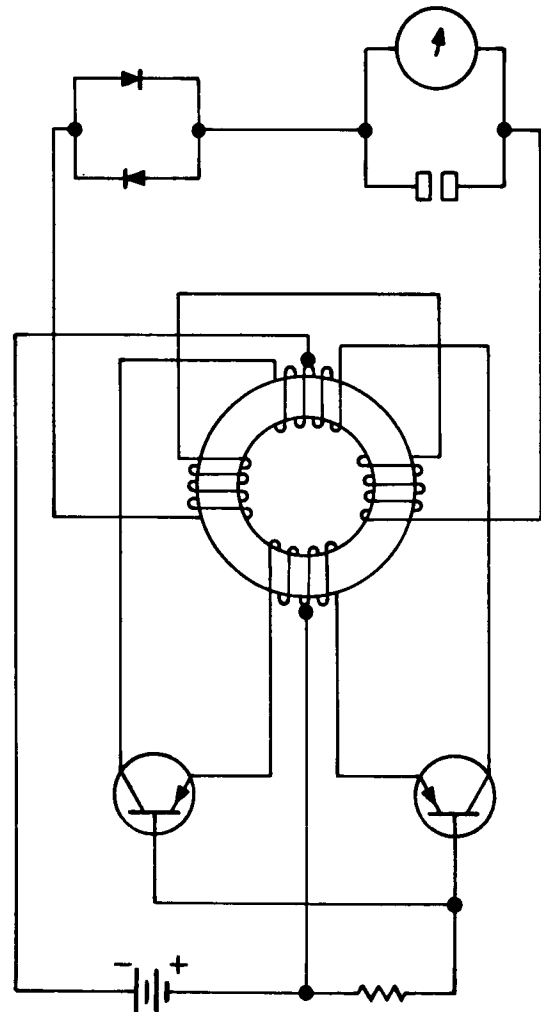


Figure II-2—Single Toroidal Core Magnetometer

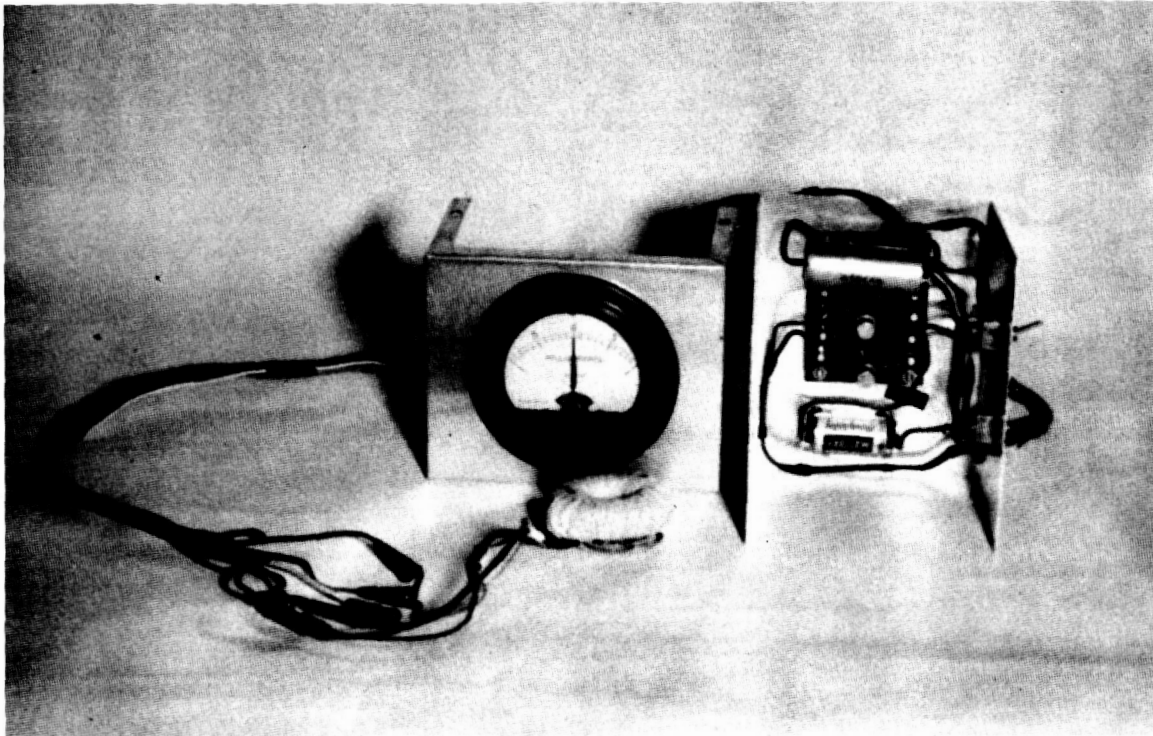


Figure II-3—Fluxgate Magnetometer

and detector were placed in a small metal box. The probe must be kept away from the box because the meter has a considerable magnetic field. To increase the sensitivity, the proper frequency of the multivibrator must be determined experimentally; this may be done by varying the number of turns of the multivibrator on the toroidal core. When a magnetometer is constructed, the detector circuit should be tuned to the second harmonic of the exciter voltage for maximum sensitivity. This is the reason for the capacitor in Figure II-2. Mercury batteries are preferred for the power supply because their voltage is more constant with respect to time. The magnetometers were calibrated by the use of a standard solenoid.

A photograph of one of the completed magnetometers is shown in Figure II-3. These magnetometers will be used to measure the magnetic field in the neighborhood of samples of nonmagnetic materials being tested. Also, it is hoped to try to use the magnetometers as a testing instrument to determine the permeability of the nonmagnetic materials.